Large Scale Molecular Simulations with Application to Polymers and Nano-scale Materials

Thesis by

Guanghua Gao

In Partial Fulfillment of the Requirements

for the Degree of

Doctor of Philosophy

California Institute of Technology

Pasadena, California

1998

(Submitted March, 1998)

To my great granny

Acknowledgements

There are so many people who made my stay at Caltech truly enjoyable. First of all, I thank my advisor, Bill Goddard, for his support and guidance.

Yongchun Tang, Siddharth Dasgupta, Naoki Karasawa, Yuejin Guo, Sue Melnik gave me much valuable help when I first joined Goddard's group and computer simulation was a new game for me. Michael Belmares collaborated with me extensively in our polymer project; K.T. Lim, Mihail Iotov, Nagarajan Vaidehi, Yue Qi, and Hao Li worked with me on the MPSim project, I thank them for sharing with me the experiences, as well as the frustration. Tahir Cagin gave me much needed help when I was trying to speed up my graduatation, I truly enjoyed the many discussions between us, scientific and philosophical.

I also thank Daqi Lu, Xinlei Hua, Jinsong Hu, Shaoyi Jiang, and Xiaoyan Chang for their freindship during the past several years.

Finally I would like to thank members of my family for their support of so many years, especially my wife, Lucy, for her companion and patience.

Abstract

There remain practical problems to predicting structures and properties of materials from first principles, though the foundation, quantum mechanics, has been established for many years. The goals of this research are to develop methods and tools that are accurate and practical, and apply them to important problems. Two aspects of the methodology are focused.

1. The development of accurate force fields based on *ab initio* quantum mechanical calculations on prototype systems. Procedures were developed on polyvinyl chloride (PVC) and successfully applied on other types of polymers. They are very important to studying of amorphous polymers materials, for which current methods have not been useful in predicting important properties (e.g. moduli and glass temperature).

2. The development of Massive Parallel Simulation (MPSim) Software. MPSim is suitable for large systems (millions of atoms). It has the ability of including environmental variables (temperature, pressure, tension, and shear) and extracting physical properties (moduli and glass temperatures). The theories and algorithms implemented are summarized in the Appendix.

These methods and tools are applied to the accurate simulation of structures and properties of amorphous polymer materials and nano-materials.

Molecular dynamics (MD) simulation on polyethylene (chapter 6) was used to develop a general strategy for predicting glass transition temperatures which is expected to be very important in polymer industry. In chapter 7, these strategies were successfully applied to three important fluoro polymers.

Single-walled carbon nanotubes (SWNT), recently discovered but not very well characterized, is an interesting new class of materials. Using an accurate force field, structures and mechanical properties of these systems are studied. Chapter 2 shows that the dominating factor for deciding stable structures and mechanical properties

is the tube size, not chirality. The behavior of (10, 10) nano-tube under bending are studied (chapter 3) based on energy of hypothetical toroids with different radii. Yielding curvature of $1/R_s$ (R_s = 183.3 (Å)) where elastic bending becomes plastic response is found. In chapter 4, closest packing of K_5C_{80} with the distribution of K atoms along tube surface similar to the stacking of stage one K_1C_8 is established as the optimum structure of K-doped SWNT crystal.

Contents

List of Figures

List of Tables

Chapter 1 Introduction

1.1 Molecular Simulations

The use of atomistic simulation to study structure, energy, physical and chemical properties of molecules provides a straightforward, reliable, and accessible avenue for many investigators in materials sciences, biotechnology, chemical technology and nanotechnology.

To provide the most rigorous and reliable predictions on new materials requires first principle quantum mechanics, the solution of *Schrödinger* equation, to obtain electronic wavefunctions. However the practical time and length scales for first-principle theory may be magnitudes too long for systems of many atoms. By averaging over the electron wave functions to obtain discrete charges, van der Waals parameters, spring constants, and etc., quantum mechanics can be approximated with molecular mechanics and molecular dynamics where coupled Newtonian equations are solved to predict the motions of systems 100 times larger and for periods 1000 times longer.

Using classical force field methods, I studied two kinds of systems, single walled carbon nano tubes (SWNT), and the amorphous polymer materials. For SWNT, I calculated the energetics, structures and mechanical properties of pure SWNT and K-doped SWNT crystal (bundle). For amorphous polymer materials simulation, I developed accurate atomistic force fields (for chloro polymers) based on quantum calculations that are required for accurate modeling of these polymer systems. Based on polyethylene, I also explored molecular dynamics procedures for predicting glass transition temperatures of amorphous polymers. By applying these procedures to fluoro polymers, we are able to correlate the experimental glass temperatures to our calculated results. All of the above systems have large amount of atoms, which cannot

be handled by current available software packages, need a new software package that can handle large atomic systems. Based on the initial version of Massive Parallel Simulation Program (MPSim), which was originally developed by K.T. Lim to handle huge atomic systems, I implemented many features that are needed for the simulations of nanotubes and amorphous systems.

1.2 Simulation of Single-Walled Carbon Nano Tubes.

As a class of quasi-one-dimensional system, single-walled carbon nanotubes, discovered by Iijima[1] and Bethune[2], have versatile properties, electro-magnetically and mechanically. Each single-walled nanotube could be regarded as a rolled graphite sheet in the cylindrical form. Generally, single-walled tubes can be characterized by two integers (n, m). Starting from a graphite sheet with the primitive lattice vectors $\vec{a}$, $\vec{b}$ making an angle of 60^o, the (n, m) tube is a cylinder with the axis running perpendicular to $n\vec{a}+m\vec{b}$, so that atoms separated by $n\vec{a}+m\vec{b}$ are wrapped onto each other.

1.2.1 Mechanical Properties of Pristine SWNTs

In Chapter 2, we present a detailed study of the energetics, structures, and mechanical properties of single-walled carbon nano tubes with different radius and different chirality: (armchair (n, n), chiral (2n, n), and zigzag (n, 0)). We used an accurate quantum mechanically derived force field to represent the interactions between the carbon atoms.[3] These interaction potentials were used earlier in studying structure, mechanical and vibrational properties of graphite, various fullerenes and intercalated compounds of fullerenes[4] and nano tubes.[5] In our studies, we employed classical molecular dynamics and molecular mechanics methods as implemented in MPSim (a massively parallel program for materials simulations) program.[6] For all three forms, we found three regions associated with two transition radii (R_1 and R_2). For tubes with circular radius smaller than R_1, only the circular form existed. The collapsed

initial structure recovered to the circular form during structural optimization. For tubes with circular radius between R_1 and R_2, there are two stable structures with the circular structure more stable. For tubes with circular radius larger than R_2, collapsed form becomes energetically favored while the circular form becomes metastable. Based on our study, we concluded that the mechanical stability of isolated SWNT is dominated by its size (radius of circular form), not by its chirality (which is a dominant factor for band structures).

1.2.2 Carbon Toroids, New Form of Carbon Molecule?

Experiments done by Dai[7] and Wang[8] illustrated the potential use of carbon nano tube as scanning microscopic probe and other high yield materials. Motivated by these exciting developments in finding new forms of carbon materials and studies of their properties, we designed the new hypothetical carbon molecules, single walled carbon nano toroids. Carbon toroids system is an ideal model to study the behavior of single walled nanotubes under bending. We can accurately correlate the behavior of the tubes to its uniform curvature. In a futuristic point of view, pure or doped (inside the tube by other elements) forms of carbon toroids could be synthesized and find its use as components of electro-magnetic devices or micro machines. For example, as nano conducting rings. In our study, we investigated the energetics and structures of (10, 10, n) toroids and found three transition radii that defines regions of different physical behavior. Bending curvature of $1/R_s$ ($R_s = 183.3$ (Å)) is the yielding point, where elastic response becomes plastic, while curvature of $1/R_b$ ($R_b = 38.9$ (Å)) corresponds to the breaking point, beyond this curvature, the tube breaks.

1.2.3 K-Doped Single-Walled Carbon Nano Tube Crystals

Perfectly packed nanotube bundles have superb mechanical properties, such as high-tensile and chemical stability. Recent work done by Thess[9] and Lee[10] on doped single-walled carbon nanotube further gives hope for developing structures useful for new

generations of nanoscale devices. In Chapter 4, we studied the K-doped single-walled carbon nanotube crystals. In our study, we explored various ways of putting K atoms into (10, 10) SWNT bundles and calculated their relative energy cost. Based on these calculation, we found the optimal stoichiometry of K doped (10, 10) SWNT crystals for doping between tubes (exo), doping inside tubes (endo) and doping both inside and within tubes (exo and endo). By looking at the best packing of exo doping, we found excellent correlation with stage one K intercalated graphite compound K_1C_8.

1.3 Simulations of Amorphous Polymers

Amorphous polymers are widely used in industry. By varying the structural unit of a polymer, or even by blending different polymers, a wide range of physical properties, including temperature stability, mechanical property, optical property and processibility can be obtained[11]. In order to create a polymer material with a set of desired properties, physics underlying the material behavior at the atomic level must be understood. We started with accurate force field development from *ab initio* calculation. Based on molecular dynamics simulations of Polyethelene, we established a strategy for predicting glass transition temperatures of amorphous polymers. This strategy is successfully applied to three important fluoro polymers.

1.3.1 Force Field Development

Currently, for polymer systems, direct *ab initio* calculations are not practical. Even with today's fast development in both hardware and software technology, this situation will not change in the near future. Thus calculations with classical force fields, parameterized based on either experimental results or *ab initio* calculations on smaller model systems, are the method of choice.

The distribution of backbone conformations and the rates of conformational transitions have a strong effect on the properties of amorphous polymer materials, such as moduli, glass temperature, dielectric constant, and diffusivity of small molecules. It

is critical that the FF leads to the correct relative energies of the minima, e.g., *trans* versus *gauche*, and of the barrier heights between them. Thus torsional FF parameters are particularly important for describing amorphous polymers. In many cases, the existence of the molecule in other local minima can be detected, but energies for these states cannot be reliably obtained from experiments. In addition, the barriers between the local minima can also not be obtained reliably from the experimental data alone. To circumvent this problem, we used *ab initio* calculations to provide the torsional potential energy surface. With the 6-31G** basis set, the torsional potentials calculated from HF wave functions are adequate. The HF calculations lead to a total torsional potential function $E^{HF}(\phi)$. The classical force fields are fitted to reproduce these energy surfaces.

Chlorinated polyvinyl chloride has become an important specialty polymer due to its relatively low cost; high glass transition temperature; high heat distortion temperature; outstanding mechanical, dielectric, and flame and smoke properties; chemical inertness; and low sensitivity to hydrocarbon costs. In Chapter 5, based on accurate quantum mechanical calculations, we developed an accurate force field for Chloro polymers that accurately describes the adiabatic backbone rotational energy surface.

1.3.2 Glass Transition of Amorphous Vinyl Polymers

For amorphous polymers, the transition from liquid-like to glass-like behavior is called the glass transition. Although various macroscopic properties around and below the glass transition temperature have been extensively investigated experimentally, the phenomena of glass transition and relaxation are not yet fully understood from molecular point of view. In chapter 6, I revisited various existing theories[12–19] on glass transition and developed a strategy for predicting glass transition temperature of amorphous polymer. The strategy is established through the analysis of trajectories of molecular dynamics simulations that are based on an accurate all atom force field.

Polymer materials containing fluorine atoms have unique properties. Compared

to the corresponding hydro-carbon analogues, they have:

- Very low surface tension and friction coefficient,
- High chemical stability to strongly acidic or basic environments,
- High thermal stability,
- Piezo- and pyro-electric properties (e.g., PVDF),
- Low refractive index.

It is important to combine, or enhance, these basic characteristics of fluoropolymers in order to develop new materials. Thus, an atomistic understanding of the mechanism and origin of these properties is essential. Fluoro polymers are very useful for many applications,[20] with

$$\text{Poly(tetrafluoroethylene) (PTFE)} : \; -(CF_2 - CF_2)_n - \tag{1.1}$$

$$\text{Poly(vinylidenefluoride) (PVDF)} : \; -(CF_2 - CH_2)_n - \tag{1.2}$$

$$\text{Ethylene} - \text{tetrafluoroethylene (ETFE)} : \; -(CF_2 - CF_2 - CH_2 - CH_2)_n - \tag{1.3}$$

serving as typical and important fluoro polymers. These three fluoro polymers provide fundamental structures that might be combined to design and develop novel fluoro polymers. Though often more complicated in practice, we consider here simple models with no branches, with all head-to-tail sequences (PVDF), and with perfectly alternating copolymer structures (ETFE).

Using a systematic annealing methodology for molecular dynamics simulations, which was explored in simulation of Polyethylene (Chapter 6), we obtain well defined glass transitions that correlate well with experimental values. In these simulation, instead of using explicit atomic force field, we used united atom force field (UAFF)

that allows more rapid calculations. The success of UAFF, suggests further the energetics of main chain dominates physical properties of amorphous vinyl polymer materials.

1.4 Development of Massive Parallel Simulation Program (MPSim)

It is now routine to carry out molecular dynamics (MD) simulations of systems (molecules, polymers, liquids, biopolymers and inorganic materials) containing thousands of atoms using commercially available software such as CERIUS[2], POLYGRAF, Discover, and AMBER. However, many important problems require explicit treatment of 10,000 to 10 million atoms (per simulation cell) with accurate treatment of long-range interactions. Examples include studies of amorphous polymers, nanoscale materials, Starburst dendrimers, and assembly/disassembly of viruses.

The Massively Parallel Simulation program (MPsim) is a general molecular mechanics and molecular dynamics package designed to handle molecular systems containing large number of atoms by taking advantage of parallel computer architectures. It has the following features:

1. It uses the most popular force fields: DREIDING[21], Universal (UFF)[22], AMBER[23], and CHARMM[24]. It can also handle all of the special force field (FF) terms allowed by commercial software such as POLYGRAF and CERIUS[2] plus other terms that have been published for specialized FFs[25].

2. Long range interactions are accurately and efficiently calculated using spline cutoffs[26], Ewald summation[27], cell multipoles (CMM)[28] and the reduced cell multipole (RCMM) method[29].

3. It contains a full complement of minimization techniques: steepest descent[30] and conjugate gradient methods[31] for both fixed cell and variable cell cases.

4. It allows full flexibility in using modern dynamics methods, including Nosé-Hoover canonical[32] and Parrinello-Rahman Gibbs dynamics[33].

5. It allows mixed mode simulations: molecular mechanics and molecular dynamics for rigid body molecules, fixed atoms, and flexible molecules. The rigid body simulation is implemented by using a quaternion representation[34].

6. It includes the Newton-Euler Inverse Mass Operator (NEIMO) method[35] to reduce the degree of freedoms for chain molecules.

7. It implements dynamic load balancing for parallel architectures[36].

8. It has a full set of analysis tools.

The MPsim program, originally developed by K.T. Lim[37], is based on the Cell Multipoles Method for non bond interactions. Many new features were added to the original version, among them,

- more force field types support, including AMBER nonbond interactions, 3-body DREIDING type hydrogen bond interactions,
- Ewald summation that is accurate and efficient for systems of medium size, with hundreds, and maybe thousands of atoms,
- stress calculation for systems with periodic boundary conditions,
- constant volume structural optimization and constant pressure optimization for periodic systems implementing either steepest descent method or conjugate gradient method,
- constant stress constant temperature (Gibbs) dynamics.

In the Appendix, I outline the physics implemented in MPSim, including energy and force expressions, the non-bond summation methods (Spline, Ewald, CMM), and the integration algorithms (dynamics and structural minimizations). Appendix A

and Appendix B detail the energy expressions, forces, stresses and second derivatives for valence and non-bond interactions. Appendix C is a detailed derivation of CMM methods, Appendix D is the derivation of Ewald summation, where I also outline the theory and algorithm for Particle-Mesh Ewald (PEM) theory[38] that can be implemented in the future. Appendix E details the theories and algorithms of steepest descent and conjugate gradient methods for structural optimization. In Appendix F, theories of NVE, NVT, NPT and rigid molecule dynamics are explained with corresponding Newtonian equations. The algorithms implemented in MPSim are explained, supplemented with flow-charts.

1.5 References

1. S. Iijima, *Nature* **354**, 1991, 56-58.

2. S. Iijima and T. Ichlhashi, *ibid* 1993, 603.

3. Y.J. Guo, Ph.D. Dissertation, California Institute of Technology 1992

4. Y.J. Guo, N., Karasawa, and W.A., Goddard III, *Nature* **351**, 1991, 464-467.

5. G. Gao, T. Cagin, and W.A. Goddard III, "Where the K are in Doped Single Walled Carbon Nanotube Crystals," (on press).

6. K.T. Lim, S. Brunett, M. Iotov, R.B. McClurg, N. Vaidehi, S. Dasgupta, S. Taylor, and W.A. Goddard III, *J. Comp. Chem.* **18**, 1997, 501.

7. H. Dai, E.W. Wong, and C.M. Lieber, *Science* **272**, 1996, 523.

8. E.W. Wong, P.E. Sheehan, C.M. Lieber, *Science* **277**, 1997, 1971.

9. A. Thess, R. Lee, P. Nikolaev, H. Dai, P. Petit, J. Robert, C. Xu, Y.H. Lee, S.G. Kim, A.G. Rinzler, D.T. Colbert, G.E. Scuseria, D. Tomanek, J.E. Fisher, and R. Smalley, E., *Science* **273**, 1996, 483-487.

10. R.S. Lee, H.J. Kim. J.E. Fischer, and A. Thess, *Nature* **388**, 1997, 255-257.

11. D. Tanner, V. Gabara, J.R. Schaefgen, "Polymers for advanced structures - an overview," *Polymers for advanced technologies, IUPAC International Symposium* 1987, 384-418.

12. P.J. Flory, *Principles of polymer chemistry,*, Ithaca, Cornell University Press 1953.

13. P.J. Flory, *Statistical mechanics of chain molecules*, New York, Interscience Publishers 1969.

14. K.S. Schweizer, "Microscopic theory of the dynamics of polymeric liquids: general formulation of a mode-mode-coupling approach," *J. Chem. Phys.* **91(9)** 1989, 5802-21.

15. D. Turnbull, M.H. Cohen, "Free-volume model of the amorphous phase: glass transition," *The Journal of Chemical Physics* **34(1)**, 1961, 120-125

16. M.H. Cohen, G.S. Grest, "Liquid-glass transition, a free-volume approach," *Physical Review B* **20(3)**, 1979, 1077-98

17. M.L. Williams, R.F. Landel and J.D. Ferry, "The temperature dependence of relaxation mechanisms in amorphous polymers and other glass-forming liquids," *J. Am. Chem. Soc.* **77**, 1955, 3701-3707.

18. J.H. Gibbs, E.A. Dimarzio, "Nature of the glass transition and the glassy state," *The Journal of Chemical Physics* **28(3)**, 1958, 373-383.

19. G. Adam and J.H. Gibbs, *J. Chem. Phys.* **43**, 1965, 139.

20. C. A. Sperati and H. W. Starkweather, Jr., *Adv. Polym. Sci.* **2**, 1961, 465.

21. S.L. Mayo, B.D. Olafson, W.A. Goddard III "DREIDING - a generic force-field for molecular simulations," *J. Phys. Chem.* **94(26)**, 1990, 8897-8909.

22. A.K. Rappe, C.J. Casewit, K.S. Colwell, W.A. Goddard III and W.M. Skiff, " UFF, a full periodic-table force-field for molecular mechanics and molecular-dynamics simulations," *J. Am. Chem. Soc.* **114(25)**, 1992, 10024-10035.

23. S.J. Weiner, P.A. Kollman, D.T. Nyuyen and D.A. Case, *J. Comp. Chem.* **106**, 1986, 230-252.

24. B.R. Brooks, R.E. Bruccoleri, B.D. Olafson, D.J. States, S. Swaminathan, and M. Karplus, *J. Comp. Chem.* **4(2)**, 1983, 187-217

25. N. Karasawa, S. Dasgupta and W.A. Goddard III, *J. Phys. Chem.* **95**, 1991, 2260.

26. H.Q. Ding, N. Karasawa and W.A. Goddard III, "Optimal spline cutoffs for Coulomb and van der Waals interactions," *Chem. Phys. Lett.* **193(1,2,3)**, 1992, 197-201.

27. N. Karasawa and W.A. Goddard III, *J. Phys. Chem.* **93(21)**, 1989, 7320-7327.

28. H.Q. Ding, N. Karasawa and W.A. Goddard III, "Atomic level simulations on a million particles - the cell multipole method for Coulomb and London nonbond interactions," *J. Chem. Phys.* **97(6)**, 1992, 4309-4315.

29. H.Q. Ding, N. Karasawa and W.A. Goddard III, "The reduced cell multipole method for Coulomb interactions in periodic-systems with million-atom unit cells," *Chem. Phys. Lett.* **196(1-2)**, 1992, 6-10.

30. E. Polak, *Computational Methods in Optimization*, New York; Academic Press, 1971.

31. W.H. Press, S.A. Teukolsky, W.T. Vetterling, and B.P. Flannery, *Nemerical Recipes in C*, Cambridge, University Press, 1992.

32. S. Nosé, "Constant temperature molecular-dynamics methods," *Progress of Theoretical Physics Supplement* **103**, 1991, 1-46.

33. M. Parrinello and A. Rahman, *J. Appl. Phys.* **52**, 1981, 7182.

34. G.S. Pawley and M.T. Dove, "Quaternion-based reorientation conditions for molecular dynamics analyses," *Molecular Physics* **55(5)**, 1985, 1147-1157.

35. N. Vaidehi, A. Jain and W.A. Goddard III, "Constant-temperature constrained molecular-dynamics - the Newton-Euler Inverse Mass Operator method," *J. Phys. Chem.* **100(25)**, 1996, 10508-10517.

36. K.T. Lim, S. Brunett, M. Iotov, R.B. Mcclurg, N. Vaidehi, S. Dasgupta, S. Taylor and W.A. Goddard III, "Molecular-dynamics for very large systems on massively-parallel computers - the MPSim program," *J. Comp. Chem.* **18(4)**, 1997, 501-521.

37. K.T. Lim, "Mega-molecular dynamics on highly parallel computers : methods and applications," Ph.D. Thesis, 1995.

38. U. Essmann, L. Perera, M.L. Berkowitz, T. Darden, H. Lee, and L.G. Pedersen, "A smooth particle mesh Ewald method," *J. Chem. Phys.* **103(19)**, 1995, 8577-93.

Chapter 2 Simulation of Single Walled Carbon Nano Tubes (SWNT)

2.1 Introduction

Carbon nanotubes were discovered in 1991 by Iijima of NEC Corporation.[1] Since then, efforts in synthesis, characterization, and theoretical investigation have grown exponentially. This is mostly due to their perceived novel mechanical and electronic properties and their tremendous potential for future technological applications. In 1993, the simplest kind of carbon nanotubes, single-walled carbon nanotubes were discovered independently by Iijima's group[2] and an IBM team headed by Bethune.[3] These SWNTs can be regarded as rolled-up graphite sheets in the cylindrical form. Some specific defect-free forms of SWNTs showed remarkable mechanical properties and metalic behavior.[4] These materials present tremendous potential as components for use in nano electronic and nano-mechanical applications, or as structural elements in various devices.

Thess and co-workers[4] later produced crystalline "ropes" of metallic carbon nanotubes with 100 to 500 SWNTs bundled into a two-dimensional triangular lattice. These tightly bundled linear "ropes" are expected to have remarkable mechanical properties, as well as superior electronic and magnetic properties. Various levels of studies were performed on the properties of SWNTs, including use of classical molecular mechanics, molecular dynamcis, and tight binding level quantum mechanical methods.[5–12]

In this chapter, we present a detailed study of the energetics, structures, and

[1]Based on "Energetics, structure, mechanical and vibrational properties of single-walled carbon nano tubes (SWNT)," **G. Gao, T. Cagin, and W.A., Goddard III**, presented on Fifth Foresight Conference on Molecular Nanotechnology

mechanical properties of single-walled carbon nano tubes with different radius and chirality (armchair (n, n), chiral (2n, n), and zigzag (n, 0)). We used an accurate force field, derived through quantum calculation, to represent the interactions between the carbon atoms.[13] These interaction potentials were used earlier in studying structure, mechanical and vibrational properties of graphite, various fullerenes and intercated compounds of fullerenes,[14] and nano tubes.[15] In our studies, we employed classical molecular dynamics and molecular mechanics methods as implemented in MPSim (a massively parallel program for materials simulations) program.[16] Molecular dynamics runs are made to anneal the structures, whereas molecular mechanics, energy and/or enthalpy minimization, are applied at the end of annealing cycle to obtain the final optimized structures. Using the analytical second derivatives of the potential energy, we also calculated the vibrational modes and frequencies of three kinds of nanotube bundles, (10, 10) armchair, (17, 0) zig-zag and (12, 6) chiral. These tubes have comparable cross section diameters, and are among the easiest to make.

2.2 Energetics and the Stability of Circular versus Collapsed Tubes

In order to assess the mechanical stability of various SWNTs, we created three chiral forms ((n, n) armchair, (n, 0) zigzag, and (2n, n) chiral) with various diameters. For each form, we studied two sets of initial structures, perfect circular cross section and elongated or collapsed cross section. For the collapsed structures, the opposit walls in the middle section are within van der Waals attraction distance and the shape of the two ends is close to circular with diameter of D $\sim$ 10.7 (Å) (Fig. 2.2). To mimic long isolated nanotube, we imposed periodic boundary condition in c-direction (tube axis). To eliminate inter tube interactions, we set the cell parameters a and b as 50 times of the circular tube diameter. Energy and structural optimizition were carried out using MPSim. Figure 2.1 is the strain energy per carbon atom

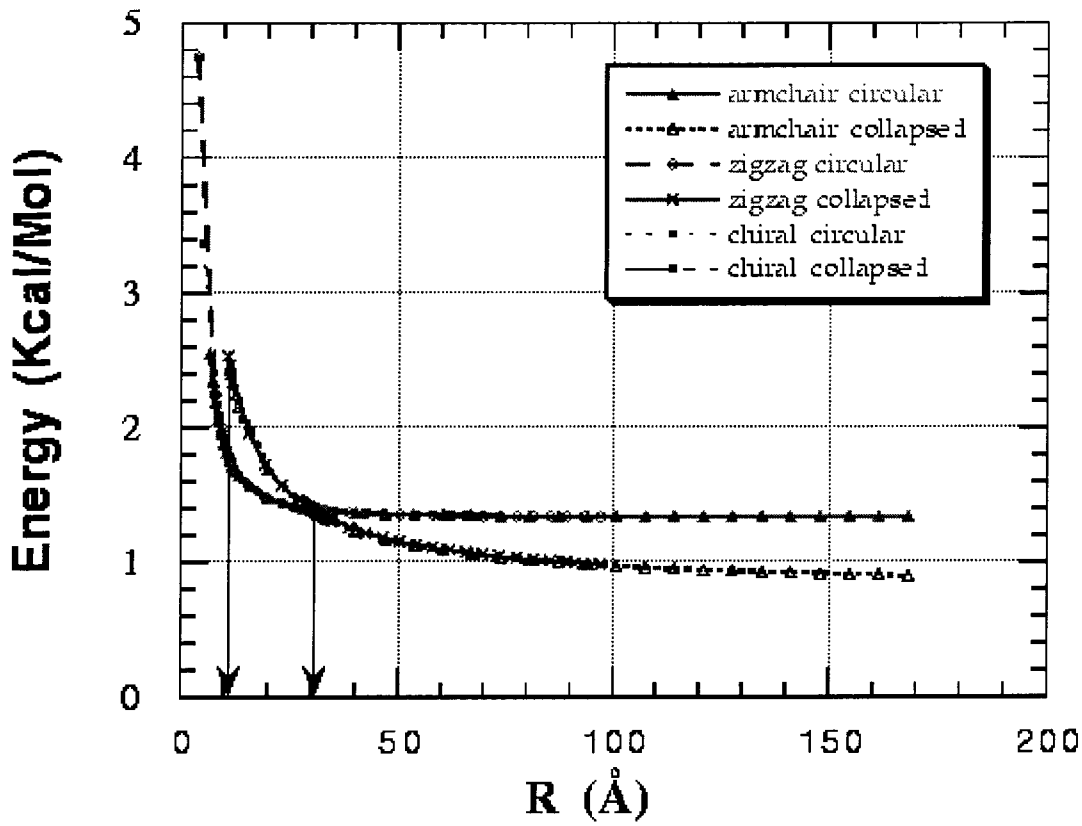

Figure 2.1: Energy per carbon atom (relative to graphite) of stable structures for (n, n), (n, 0), and (2n, n) SWNTs; R is the radius of its circular structure.

versus radius of its circular form. We put the two sets (collapsed versus circular) with three chiral forms (armchair (n, n), chiral (2n, n), and zigzag (n, 0)) on the same plot. For all three forms, there are three regions associated with two transition radii (R_1 and R_2). For tubes with circular radius smaller than R_1, only the circular form is existed, the collapsed initial structure recovered to the circular form during structural optimization. For tubes with circular radius between R_1 and R_2, there are two stable structures with the circular structure more stable. For tubes with circular radius larger than R_2, collapsed form becomes energetically favored while the circular form becomes meta-stable. The structures and radii of the first transition are:

- (n, n) armchair, R_1 is between 10.77 (Å) of (16, 16) and 11.44 (Å) of (17, 17).

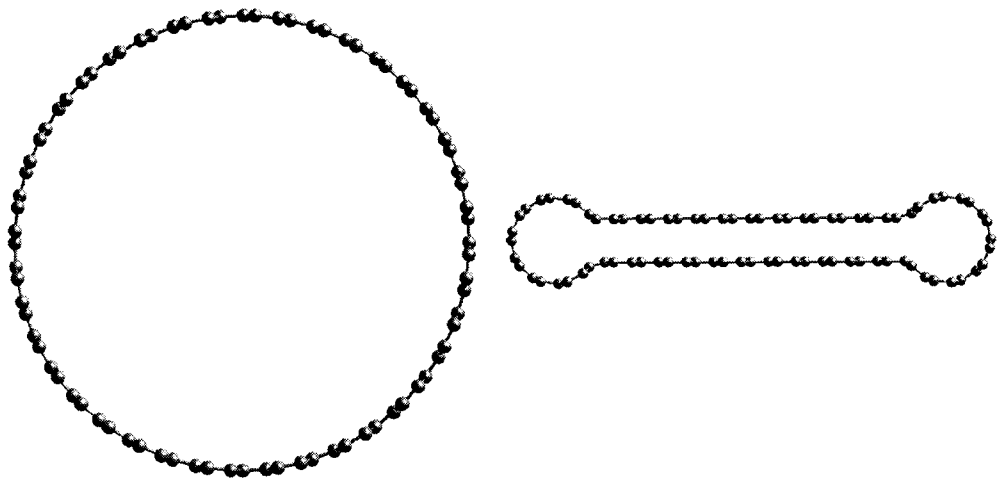

Figure 2.2: Starting structures for circular and collapsed tubes

- (2n, n) chiral, R_1 is between 10.28 Å) of (20, 10) and 11.31 (Å) of (22, 11).
- (n, 0) zigzag, R_1 is between 10.49 (Å) of (27, 0) and 10.88 (Å) of (28, 0).

The structures and the radii of the second transition are:

- (n, n) armchair, R_2 is between 29.62 (Å) of (45, 45) and 30.30 (Å) of (46, 46).
- (2n, n) chiral, R_2 is between 29.82 (Å) of (58, 29)) and 30.85 (Å) of (60, 30).
- (n, 0) zigzag, R_2 is between 29.93 (Å) of (77, 0) and 30.32 (Å) of (78, 0).

Looking at the collapsed structures of various radii along tube axis, we found that they all have two circular (or elliptical) ends of diameter D $\sim$ 10.5 (Å) and flat middle section. The inter wall distances in the flat region are close to 3.4 (Å), which is the inter layer distance of adjacent graphite sheets. The ends sections are highly strained compared to the circular form, thus cost energy. In addition to zero strain energy, the flat region is further stablized by inter layer van der Waals attractions. The relative strength of these two opposite forces dictates the two structural transformations. Shown in Fig. 2.3 are optimized structures of armchair (n, n) tubes with collapsed initial structure. The zigzag (n, 0) and chiral (2n, n) tubes are the same.

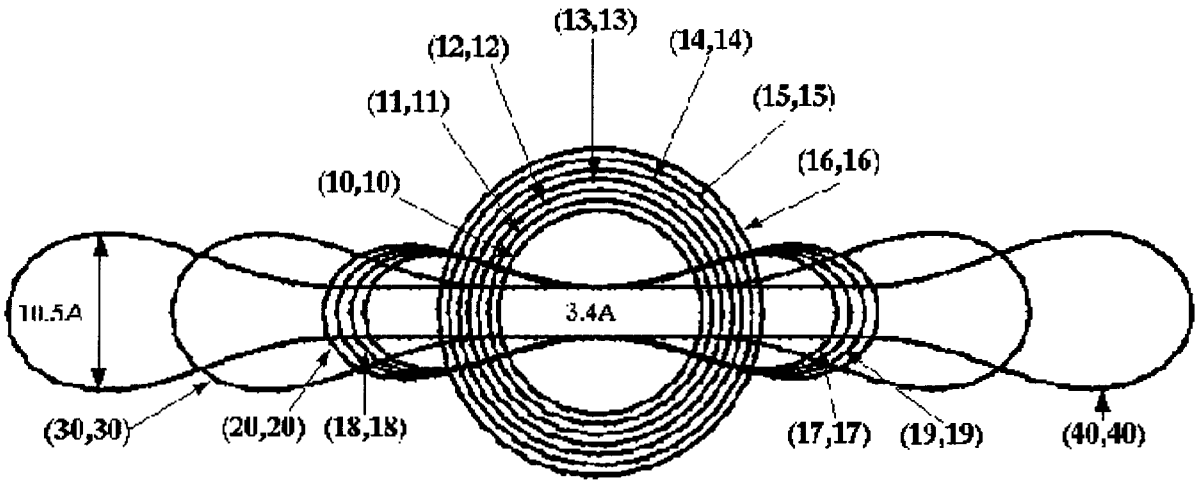

Figure 2.3: Cross section of optimum tube structures (started from collapsed form)

Based on the optimized structures and their energies of the circular form, we can model the basic energetics by approximating the tube as a membrane with a curvature of 1/R and bending modulus[17] of κ. Assuming a as the thickness of tube wall, the elastic energy stored in a slab of width L is given by $\pi\kappa La^2/(12R)$. The per atom energy can be written as

$$E_C = \frac{\pi\kappa La^2}{12RN} + E_\infty \tag{2.1}$$

where N is the number of carbon atoms per slab and E_∞ is energy per carbon atom for tubes with $R \sim \infty$, i.e., flat sheets. Considering ρ as the number of carbon atoms per unit area of tube wall, we have

$$E_C = \kappa \frac{a^2}{24\rho} \frac{1}{R^2} + E_\infty \tag{2.2}$$

Setting a as the spacing between two graphite sheets, 3.335 (Å), $R_o = 1.410$ (Å) as the C-C bond distance, we obtained $\kappa_{(n,n)} = 963.44$ (GPa), $\kappa_{(n,0)} = 911.64$ (GPa), and $\kappa_{(2n,n)} = 935.48$ (GPa). These results are plotted against the theoretical estimates in Fig. 2.4.

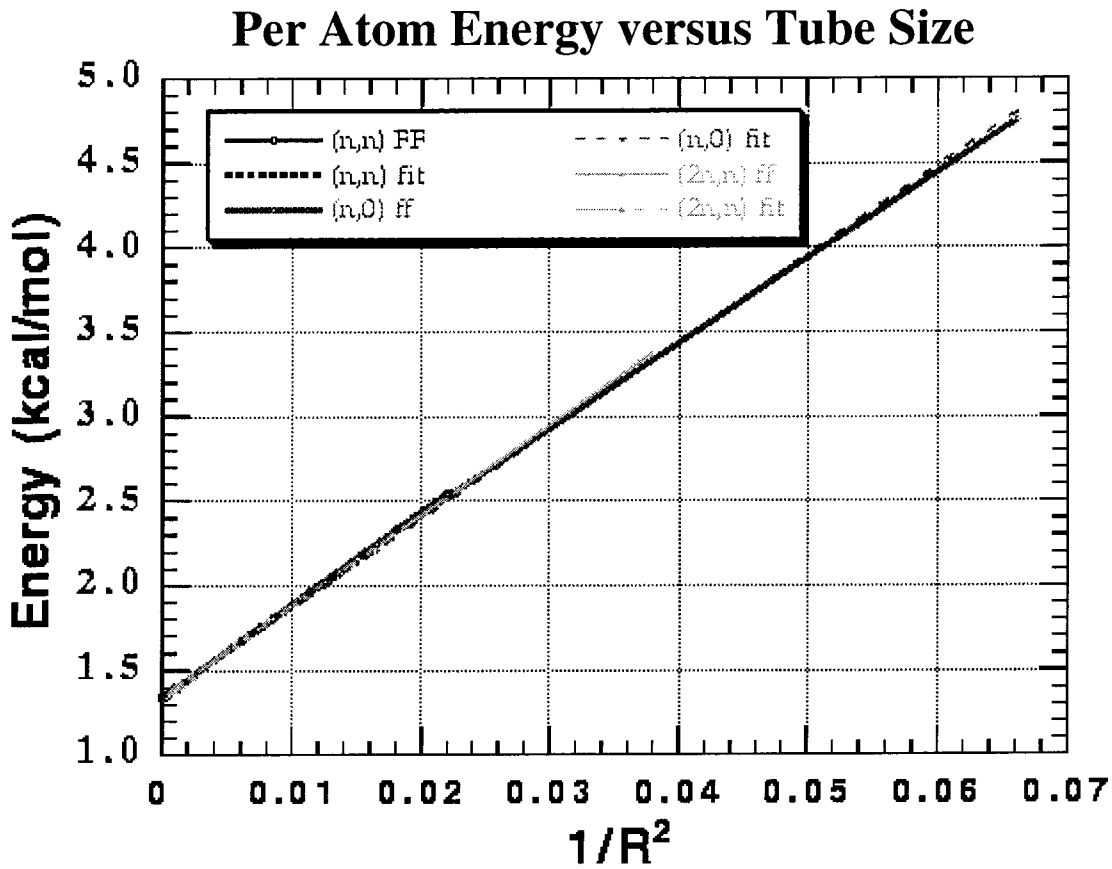

Figure 2.4: Energy per atom versus square of tube curvature

The bending modulus of sheets with different chirality suggest that the transition radius depends on the chirality, with (2n, n) transition radius larger than that of (n, 0) zigzag, but smaller than that of (n, n) armchair. That is what we expected, because the higher the bending modulus, the higher the strain energy. The (n, n) armchair has higher binding energy than that of (2n, n), while the (n, 0) zigzag has lower binding energy than that of (2n, n). However, by examining the collapsed structures closely, we also found different inter layer stacking in the collapsed region. Figure 2.5 is the side views of the two attracting layers for three cases. The inter-layer stacking patterns are different due to different chirality. The inter-layer distances are also differ slightly, with $d_{(n,n)} = 3.38$ (Å), $d_{(2n,n)} = 3.39$ (Å), and $d_{(n,0)} = 3.41$ (Å).

Energetically, inter-layer attraction of armchair is the best with per atom energy of E = 0.7336 (kcal/mol), and stacking of the opposite walls is almost identical to the graphite stacking. The inter-layer attraction in the zigzag form is the worst with per atom energy, E = 0.7439 (kcal/mol), since the carbon atoms on different layers are lined up on top of each other. The attraction energy per atom for the collapsed (2n, n) chiral nanotube is between the two. Overall, the two factors (bending modulus and van der Waals attraction) cancels out for different chirality, so that in terms of transition radius and the cross-over radius, the size of the circular tube (radius) is the dominant factor in deciding the stable forms.

2.3 Structure and Mechanical Properties of Packed SWNT Crystals

Among various conformations, the (10, 10) SWNT is the easiest to make. We studied the mechanical properties of its bulk phase (tube bundles). We also calculated the bulk properties of (17, 0) zigzag and (12, 6) chiral tubes, with cross section radii close to that of (10, 10) tube. Molecular dynamics and molecular mechanics studies led to a triangular packing as the most stable structure for all three forms. The triangular lattice parameter for armchair (10, 10) is $a = 16.78$ (Å) with density of $\rho = 1.33$ (g/cc). For the zigzag (17, 0), they are $a = 16.52$ (Å) and $\rho = 1.34$ (g/cc). For the chiral form (12, 6), they are $a = 15.62$ (Å) and $\rho = 1.40$ (g/cc). More importantly, we determined the Young's modulus along the tube axis for triangular-packed SWNTs using the second derivatives of the potential energy. They are Y = 640.30 (GPa), Y = 648.43 (GPa), and Y = 673.49 (GPa), respectively. Normalized to carbon sheet, these values are within a few percent of the graphite bulk value.

2.4 Vibrational Modes and Frequencies of SWNTs

We calculated the vibrational modes and frequencies of (10, 10) tube crystals. Due to their comparable tube radius with respect to (10, 10) tube, zigzag (17, 0) and chiral (12, 6) tube crystals are also studied. These results can be used to differentiate chiral tubes with comparable diameters. In Table 2.1, B denotes breathing mode as displayed in Fig. 2.6b, S stands for shearing mode as in Fig. 2.6c, and C stands for cyclopes as in Fig. 2.6d. The uniform compression mode is also shown in Fig. 2.6a and occurs at 186 cm^{-1} for (10, 10), which is exactly the same as the experimental frequency[18]. We tabulated the uniform compression mode and highest graphite in-plane mode in Table 2.2.

2.5 Conclusion

We presented a detailed study of structure, energetics and mechanical properties of SWNTs of varying size and chirality. The determined structure and lattice parameters for closed packed (10, 10) like nanotubes are in close agreement with observations. We also determined all vibrational modes and frequencies of bulk and isolated nanotubes using a highly accurate classical force field.

2.6 References

1. Iijima, S., *Nature* **354**, 1991, 56-58.

2. Iijima, S. and Ichlhashi, T., *ibid* 1993, 603.

3. Bethune, D.S., Kiang, C.H., Devries, M.S., Gorman, G., Savoy, R., Vazquez, J., Beyers, R., *Nature* **363**, 1993, 605-607.

4. Thess, A., Lee, R., Nikolaev, P., Dai, H., Petit, P., Robert, J., Xu, C., Lee, Y.H., Kim, S.G., Rinzler, A.G., Colbert, D. T., Scuseria, G.E., Tomanek, D., Fisher, J.E., and Smalley, R.E., *Science* **273**, 1996, 483-487.

5. Krotov, Y.A., Lee D.-H., and Louie, S.G., *Physical Review Letters* **78(22)**, 1997, 4245-4248.

6. Tuzun, R.E., Noid, D.W., Sumpter,B.G., and Merkle, R.C., *Nanotechnology* **7(3)**, 1996, 241-246.

7. Ihara, S. and Itoh, S., *Surf. Rev. Lett.* **3(1)**, 1996, 827-834.

8. Cohen, M.L., *Mat. Sci. Eng. A* **209(1-2)**, 1996, 1-4.

9. Menon, M., Richter, E., and Subbaswamy, K.R., *J. Chem. Phys.* **104(15)**, 1996, 5875-5882.

10. Hamada, N., Sawada, S. and Oshiyama, A., *Phys. Rev. Lett.* **78(10)**, 1992, 1579-1581.

11. Saito, R., Fujita, M., Dresselhaus, G. and Dresselhaus, M.S., *Appl. Phys. Lett.* **60**, 1992, 2204-2206.

12. Blase, X., Benedict, L.X., Shirley, E.L., and Louie, S.G., *Phys. Rev. Lett.* **72(12)**, 1994, 1878-1881.

13. Guo, Y.J., Ph.D. Dissertation, California Institute of Technology, 1992

14. Guo, Y.J., Karasawa, N., and Goddard III, W.A., *Nature* **351**, 1991, 464-467.

15. Gao, G., Cagin, T. and Goddard III, W.A., "Where the K are in Doped Single Walled Carbon Nanotube Crystals," (on press).

16. Lim, K.T., Brunett, S., Iotov, M., McClurg, R.B., Vaidehi, N., Dasgupta, S., Taylor, S. and Goddard III, W.A., *J. Comp. Chem.* **18**, 1997, 501.

17. Landau, L.D. and Lifshitz, E.M., *Elasticity Theory, Pergamon*, Oxford, 1986.

18. Rao, A.M., Richter, E., Bandow, S., Chase, B., Eklund, P.C., Williams, K.A., Fang, S., Subbaswamy, K.R., Menon, M., Thess, A., Smalley, R.E., Dresselhaus, G., and Dresselhaus, M.S., *Science* **275**, 1997, 187-191.

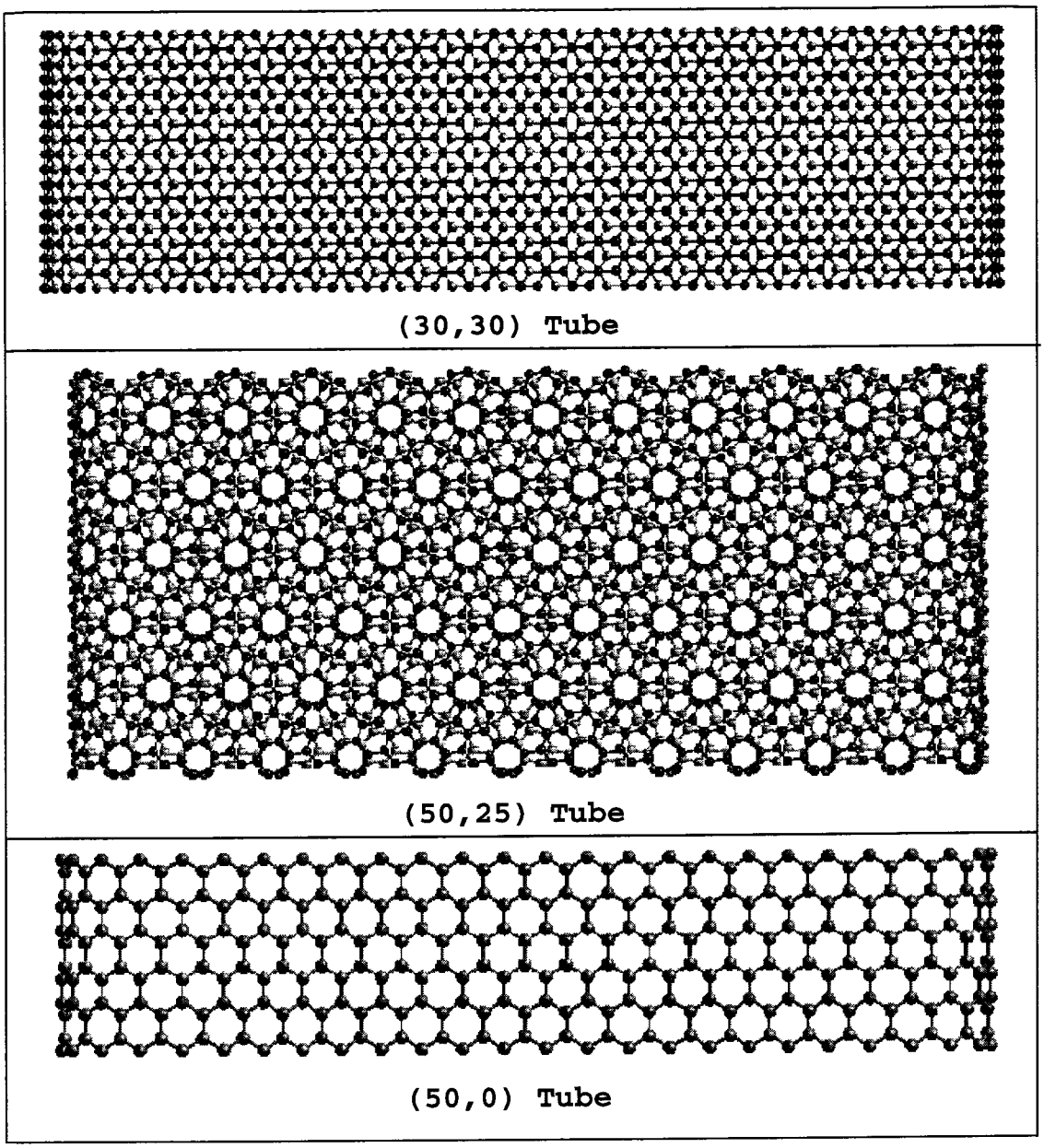

Figure 2.5: Side views of collapsed structures

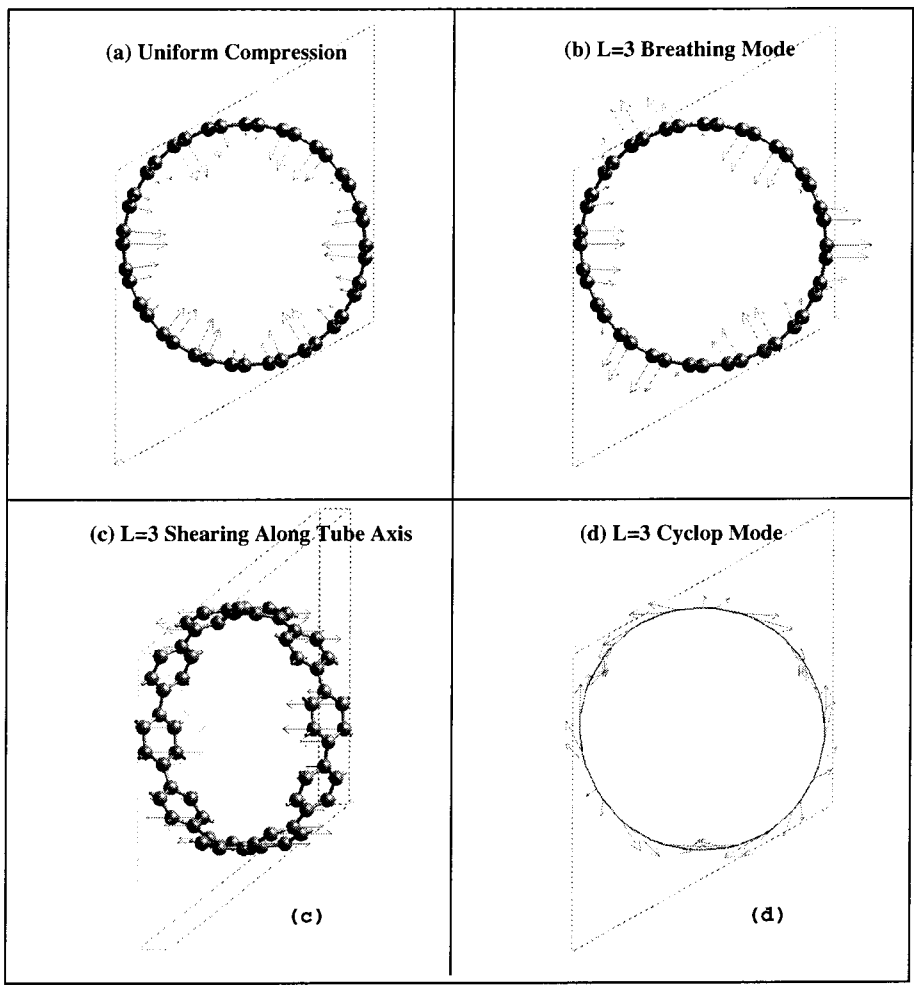

Figure 2.6: Selected vibrational modes

2.7 Tables

Table 2.1: Vibrational Modes of (10, 10), (12, 6), and (17, 0)

L	$B_{(10,10)}$	$S_{(10,10)}$	$C_{(10,10)}$	$B_{(12,6)}$	$S_{(12,6)}$	$C_{(12,6)}$	$B_{(17,0)}$	$S_{(17,0)}$	$C_{(17,0)}$
1		111	242		122	265		113	247
		112	244		122	265		113	247
2	53	223	381	59	243	412	54	227	386
	53	223	381	59	243	412	54	227	386
3	49	333	524	57	364	566	50	341	530
	55	333	530	63	364	571	57	342	535
4	127	442	671	137	483	720	128	456	675
	127	442	671	137	483	720	129	456	676
5	147	549	805	168	600	850	149	570	806
	147	549	805	168	600	850	150	570	806
6	201	652	924	229	713	976	203	683	921
	226	652	925	249	713	977	227	683	921
7	262	750		299	819	1072	267	794	1017
	272	750		299	819	1072	267	794	1017
8	328	838		360	912	1136	327	901	1091
	330	838		360	912	1136	328	901	1091
9	375	909		396			379	1002	1140
	381	909		400			385	1002	1140
10	402	939		394			434		

- Frequency in CM^{-1}.

Table 2.2: Compressing Mode and the Highest Mode

	(7, 7)	(8, 8)	(9, 9)	(12, 6)	(17, 0)	(10, 10)	(11, 11)	(12, 12)
Uniform Comp.	261	231	207	202	188	186	168	152
Highest Mode	1583	1584	1584	1585	1586	1584	1584	1584

- Frequency in CM^{-1}.

Table 2.3: Energy of Collapsed and Circular (n, n) Tubes (relative to graphite)

(n, n)	Atoms	R (Å)	$E_{circular}$	$E_{collapsed}$	(n, n)	Atoms	R (Å)	$E_{circular}$	$E_{collapsed}$
10	40	6.73	2.5418		50	200	33.66	1.3793	1.3251
11	44	7.41	2.3366		60	240	40.39	1.3641	1.2353
12	48	8.08	2.1790		70	280	47.13	1.3550	1.1715
13	52	8.75	2.0556		80	320	53.86	1.3490	1.1232
14	56	9.43	1.9571		90	360	60.59	1.3450	1.0858
15	60	10.10	1.8773		100	400	67.32	1.3420	1.0559
16	64	10.77	1.8117		110	440	74.05	1.3399	1.0313
17	68	11.44	1.7572	2.4340	120	480	80.79	1.3383	1.0109
18	72	12.12	1.7115	2.3293	130	520	87.52	1.3372	0.9939
19	76	12.79	1.6726	2.2369	140	560	94.25	1.3361	0.9791
20	80	13.46	1.6394	2.1553	150	600	100.98	1.3354	0.9659
30	120	20.20	1.4678	1.6847	160	640	107.72	1.3348	0.9552
40	160	26.93	1.4074	1.4600	170	680	114.45	1.3341	0.9452
41	164	27.60	1.4036	1.4435	180	720	121.18	1.3337	0.9362
42	168	28.28	1.4002	1.4278	190	760	127.91	1.3332	0.9284
43	172	28.95	1.3969	1.4128	200	800	134.65	1.3326	0.9211
44	176	29.62	1.3939	1.3987	210	840	141.38	1.3324	0.9146
45	180	30.30	1.3910	1.3849	220	880	148.11	1.3321	0.9088
46	184	30.97	1.3884	1.3720	230	920	154.84	1.3318	0.9035
47	188	31.64	1.3859	1.3594	240	960	161.57	1.3318	0.8984
48	192	32.31	1.3836	1.3476	250	1000	168.31	1.3317	0.8943
49	196	32.99	1.3814	1.3361	∞	∞	∞	1.3050	0.7336

- Energy in $kcal/mol$.

Table 2.4: Energy (kcal/mol) of Collapsed and Circular (n, 0) Tubes

(n, 0)	Atoms	R (Å)	$E_{circular}$	$E_{collapsed}$	(n, 0)	Atoms	R (Å)	$E_{circular}$	$E_{collapsed}$
10	40	3.89	4.7507		77	308	29.93	1.3926	1.3968
20	80	7.77	2.2446		78	312	30.32	1.3910	1.3898
21	84	8.16	2.1614		79	316	30.71	1.3894	1.3816
22	88	8.55	2.0890		80	320	31.09	1.3879	1.3743
23	92	8.94	2.0255		90	360	34.98	1.3757	1.3098
24	96	9.33	1.9697		100	400	38.87	1.3669	1.2586
25	100	9.72	1.9203		110	440	42.76	1.3604	1.2163
26	104	10.11	1.8763		120	480	46.64	1.3555	1.1818
27	108	10.49	1.8371		130	520	50.53	1.3516	1.1517
28	112	10.88	1.8019	2.5316	140	560	54.42	1.3486	1.1262
29	116	11.27	1.7702	2.4623	150	600	58.30	1.3461	1.1042
30	120	11.66	1.7416	2.3980	160	640	62.19	1.3441	1.0850
40	160	15.55	1.5623	1.9563	170	680	66.08	1.3424	1.0683
50	200	19.43	1.4788	1.7217	180	720	69.96	1.3410	1.0532
60	240	23.32	1.4333	1.5672	190	760	73.85	1.3398	1.0392
70	280	27.21	1.4058	1.4567	200	800	77.74	1.3388	1.0270
71	284	27.60	1.4037	1.4476	210	840	81.62	1.3380	1.0160
72	288	27.99	1.4016	1.4384	220	880	85.51	1.3372	1.0062
73	292	28.37	1.3997	1.4298	230	920	89.40	1.3366	0.9971
74	296	28.76	1.3978	1.4213	240	960	93.28	1.3360	0.9884
75	300	29.15	1.3960	1.4129	250	1000	97.17	1.3355	0.9808
76	304	29.54	1.3942	1.4047	∞	∞	∞	1.3050	0.7439

Table 2.5: Energy (kcal/mol) of Collapsed and Circular (2n, n) Tubes

(2n, n)	Atoms	R (Å)	$E_{circular}$	$E_{collapsed}$	(2n, n)	Atoms	R (Å)	$E_{circular}$	$E_{collapsed}$
5	140	5.14	3.3639		25	700	25.71	1.4149	1.4938
10	280	10.28	1.8579		26	728	26.74	1.4085	1.4664
11	308	11.31	1.7672	2.4559	27	756	27.77	1.4028	1.4415
12	336	12.34	1.6979	2.2969	28	784	28.79	1.3976	1.4182
13	364	13.37	1.6438	2.1660	29	812	29.82	1.3930	1.3961
14	392	14.40	1.6008	2.0572	30	840	30.85	1.3888	1.3757
15	420	15.43	1.5660	1.9660	35	980	35.99	1.3731	1.2917
20	560	20.57	1.4629	1.6690					

Chapter 3 Energetics and Structures of Single-Walled Carbon Nano Toroids

3.1 Introduction

Carbon has diverse forms of structure,[1-2] both in nature and by lab synthesize. Three dimensional diamond and two dimensional graphite sheet are the two well-known forms. In the past decade, the discoveries of zero dimensional bucky balls[3-7] and one dimensional bucky tubes[8-9] have generated great interests among researchers. Studies of the structures and properties of low-dimensional carbon molecules, theorectical[10-13] and experimental,[14-18] showed tremendous potential use of nano scale carbon material as components of electro-magnetic devices, or high yielding materials. Among them, experiments done by Dai[19] and Wang[20] illustrated the potential use of carbon nano tube as scanning microscopic probe. Motivated by these exciting development in finding new forms of carbon materials and studies of their properties, we designed a hypothetical carbon molecules, single walled carbon nano toroids. Carbon toroids system is an ideal model for studying the behavior of single walled nano tubes under bending. We can accurately correlate the behavior of the tubes to its uniform curvature. In a futuristic point of view, pure, or doped (inside the tube by other elements) forms of carbon toroids could be synthesized and find its use as components of electro-magnetic devices or micro machines, e.g., as nano conducting rings.

The carbon toroid can be chracterized by three integers (n, m, l), where (n, m) defines the single-walled nano tube that is used to construct the toroid, while l is the number of the smallest repeating units along tube axis. We investigated the

[2]Based on "Energetics and structures of single-walled carbon nano toroids," **G. Gao, T. Cagin, and W.A. Goddard III, to be published.**

mechanical property of carbon toroids to investigate the bending of (10, 10) single-walled carbon nano tube.

3.2 Optimum Structures of Toroids

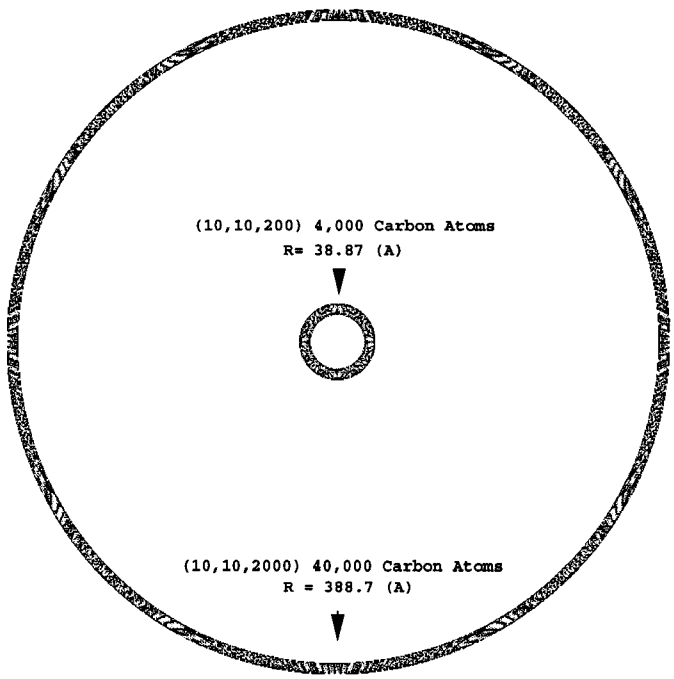

Figure 3.1: Starting structure of two toroid with different radius, the smallest stable toroid and the largest toroid used in our calculation.

We generated toroids with radius from 19.43 (Å) that is (10, 10, 100) with 2,000 atoms, to 388.69 (Å), (10, 10, 2000) with 40,000 atoms. Based on the molecular simulation forece field[21] (MSFF), their structures are optimized by using molecular mechanics and molecular dynamics. Developed for graphite and fullerenes, MSFF was proved to be very accurate in calculating vibration frequencies and predicting experimental structures. The parameters are listed in Table 3.1. Figure 3.1 shows the initial structures of two toroids, $R = 38.87$ (Å) of (10, 10, 200), and $R = 388.7$ (Å) of (10, 10, 2000).

Toroids with small radius are highly strained. To stablize the structure, harmonic bond interactions are used at the early stage of the minimization. The more accurate

Table 3.1: Force Field Parameters for Carbon Nano Tube

van der Waals[a]	R_v	D_v	Bond[b]	r_e	k_r	E_{bond}
C	3.8050	0.06920	C–C	1.4114	720.000	133.0000
Angle[c]	θ_e	k_θ	$k_{r_1\theta}$	$k_{r_2\theta}$	$k_{r_1r_2}$	
C–C–C	120.000	196.130	-72.410	-72.410	68.000	
Torsion[d]	V_0	V_1	V_2			
C–C–C–C	10.6400	0.0000	-10.6400			

[a] $E_{vdw} = D_v(\rho^{-12} - 2\rho^{-6})$ where $\rho = R/R_v$.

[b] $E = D_e(\chi - 1)^2$ with $\chi = e^{-\gamma(R-R_e)}$.

[c] $E(\theta, R^A, R^C) = \frac{1}{2}C(\cos\theta - \cos\theta_e)^2 + D(R^A - R_e^A)(\cos\theta - \cos\theta_e) + E(R^C - R_e^C)(\cos\theta - \cos\theta_e) + F(R^A - R_e^A)(R^C - R_e^C)$, k_θ, $k_{r_1\theta}$, and $k_{r_2\theta}$ are force constants with respect to θ.

[d] $E(\phi) = V_0 + V_1\cos(\phi) + V_2\cos(2\phi)$.

Morse potential that allows bond breaking are used at the latter stage of minimization. By doing so, we can avoid the bias built in when the starting structure was created. This is important for tracking down the transition radius that separates stable toroids (though highly strained) from the unstable toroids (under Morse bond interaction, the structure flies apart). Figure 3.2 is the strain energy per atom (relative to infinite long straight (10, 10) tube) versus $1/R^2$. For toroids with different radius, different final structures resulted. In the plot, we can identify three transition radii, associated with four structural regions.

For toroids with radii larger than $R_s = 183.3$ (Å) (corresponds to (10, 10, 943) toroid with 18,860 atoms), after molecular dynamics simulation and energy minimization, smooth toriod is the only stable structure. This corresponds to the elastic bending of isolated (10, 10) tub.

For toroids with radii smaller than $R_s = 183.3$ (Å) and larger than 109.6 (Å) ((10, 10, 564) with 11280 atoms), the optimum structures obtained through minimization are smooth toroids without buckles. However, after 20 pico seconds of

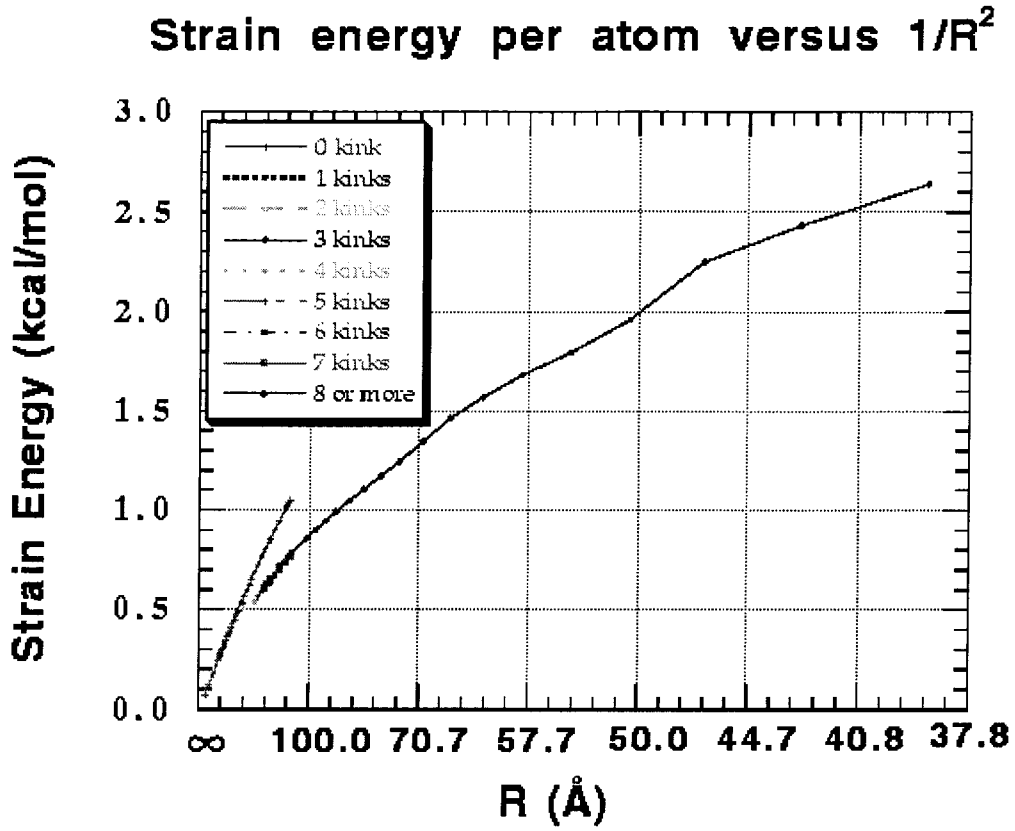

Figure 3.2: Strain energy per atom versus curvature

molecular dynamics equilibration at 300 (K), numerous small dents appeared along the inner wall. Take a snapshot of dynamics trajectory as the starting point of structural minimization, we found an interesting phenomena. During the minimization, small dents diffused along the inner tube and nucleated into larger dents when they meet. This nucleation of deformations continues, until the optimum structure resulted. The optimum structures usually have a number of buckles almost uniformly spaced along the tube.

Figure 3.3 are the snapshots at the late stage of minimization for (10, 10, 564) (toroid with radius of 109.6 (Å) and 11280 atoms). Looking at the lower left quater of each ring, we can clearly identify the diffusion of small dents. These small dents eventually moved toward the larger dent as the minimization progresses, and combined with the large dent. The snapshots are numbered according to the minimization

sequence. Snapshot with smaller numbering represents structure at earlier stage of minimization. Comparing to the smooth toroids, these structures have lower strain energy per atom. This is due to the stretching of the outer surface and compression of the inner surface. Knee like buckle relaxes compression over large region at the expense of increased local strain.

Figure 3.4 gives a close look at a buckle, which is cut out from a optimized toroid with one buckle. At the center of the buckle, tube wall collapsed completely. The closest distance between atoms in opposite tube walls is 3.3 (Å), comparable to the distance between adjacent layers of graphite. A short distance away from the collapsed point, the tube stays almost circular. Rooms created for the inner wall at the buckles relax the stretch and compression along the rest of the toroid.

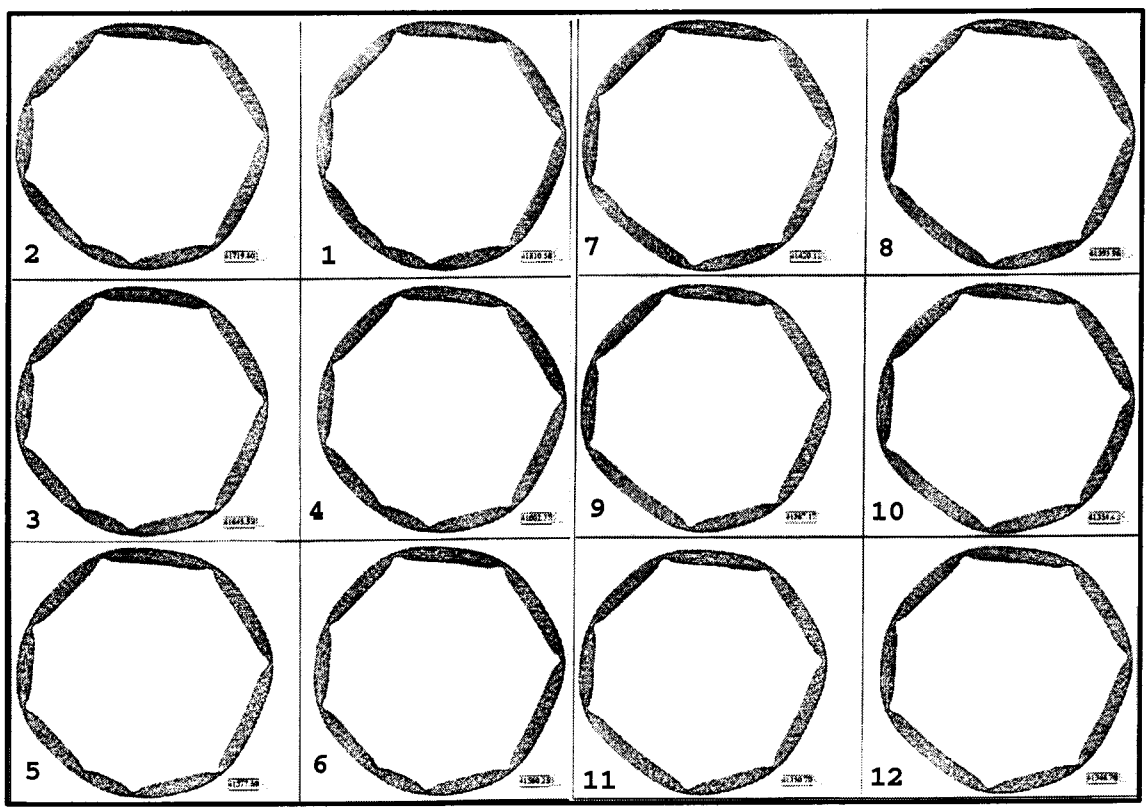

Figure 3.3: Snapshots of structural minimization; numbered according to the minimization stages to illustrate nucleation of small buckles into large buckle

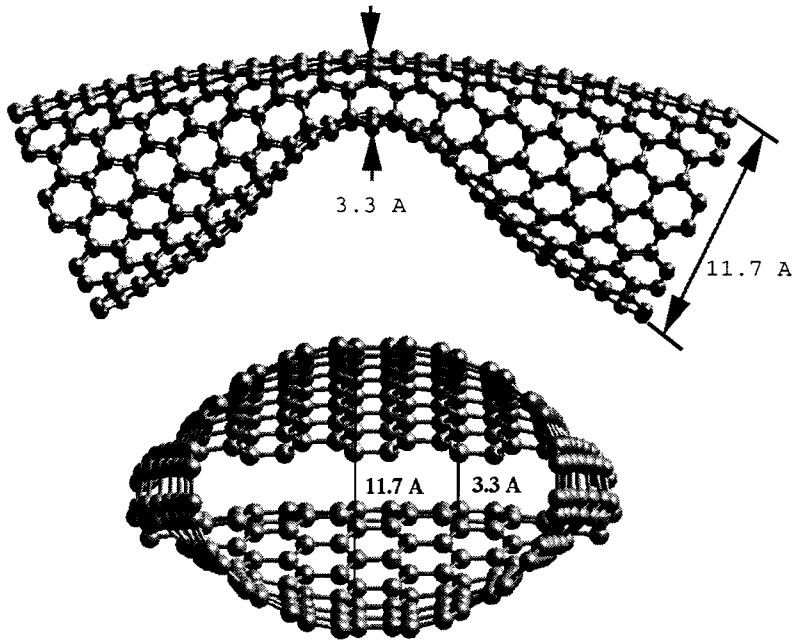

Figure 3.4: Close look at a kink

There is a strong correlation between the number of buckles and the curvature of the toroids. The higher the strain (curvature) is, the more buckles appeared in the final structure of minimization. However, for each toroid within this region, there are many stable final structures with different number of buckles, each resulted from different starting sructure. This suggests that there exist many meta stable structures for toroids in this region. The fact that the curves towards small radius in Fig. 3.2 are not smooth suggests that we are not connecting the points with optimum number of buckles. Generally, if we increase the radius (thus reduce strain) we get structures with smaller number of buckles and when we approach the smooth region, we should get only structures with single buckle.

In order to track down the transition point, we created structures with different number of buckles as starting point of minimization. The buckles are uniformly distributed along the circumferences. To create a buckle, we added artificial harmonic constraint on two atoms in the opposit wall of the tube to pull together the inner wall

and the outer wall. After the structures are minimized to lower RMS force, where the structures are stable under Morse bond interaction, we remove the constraints and switch harmonic bond potential back to Morse potential to further optimize the structures. We could just heat up the initial structures by using molecular dynamics and then anneal them down to zero temperature. However, given the size of the toroids in the transition region ($\geq$ 10,000 atoms), the long time that takes to anneal each structure, and the fact that there could be several stable structures associated with different number of buckles, it is impractical to do so. Figure 3.5 shows the transition region where smooth toroids and toroids with different number of buckles co-exist. Points with same number of buckles are connected into lines. It clearly shows the overlap and shifts of lines with different number of buckles.

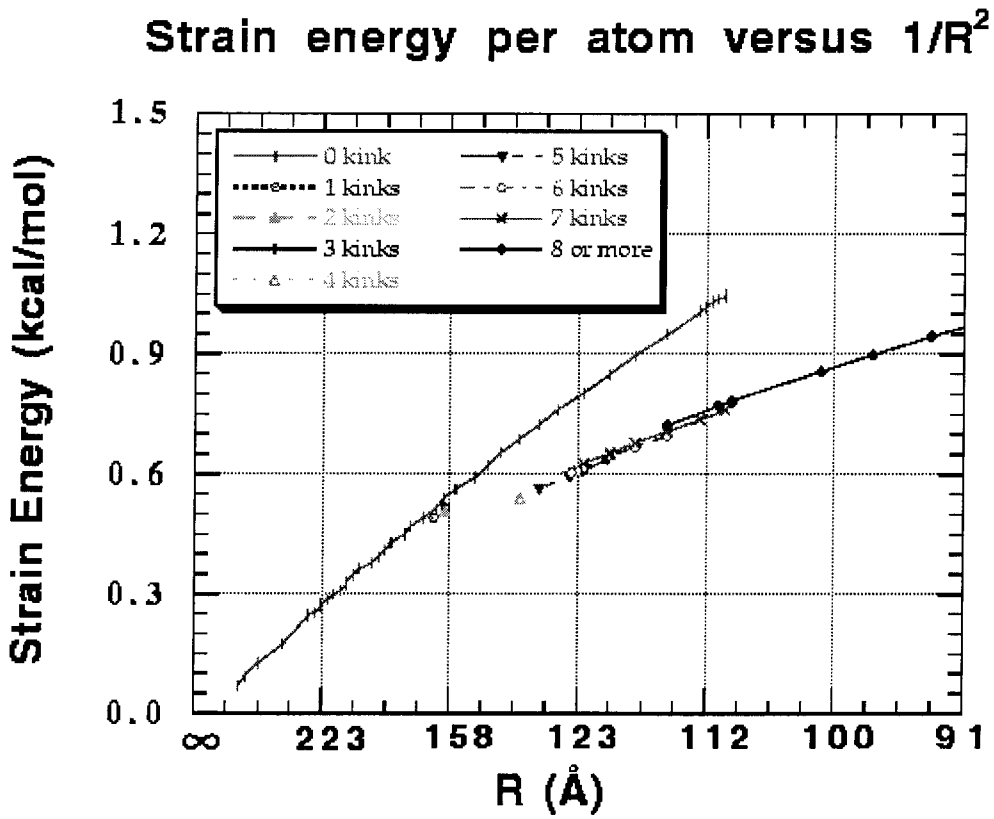

Figure 3.5: Strain energy per atom versus $1/R^2$ at the transition region where smooth toroids and toroids with different amount of buckles co-exist.

Towards the transition point beyond which smooth toroids resulted, we are able to create stable structures with four buckles, three buckles, two buckles and one buckle. At region close to the transition radius R_s, only the one buckle toroids have the smallest strain energy per atom. Figure 3.6 shows the buckled structures in this region.

If we further increase the curvature (decrease radius), at $R_k \sim 109.6$ (Å), (corresponds to (10, 10, 564) toroid with 11,280 atoms), only toroids with various number of buckles exist. At even higher curvature, the toroids are flatterned. In this region, there are no smooth toroids, due to the high strain built in the compression of inner wall and tension of the outer wall. Further decrease the radius down to the point of $R_b = 38.9$ (Å) (corresponds to (10, 10, 200) toroid with 4,000 atoms), the structure breaks and atoms fly apart in the course of minimization. Figure 3.7 shows toroids with more than eight buckles to the smallest toroid that can stand the built in strain.

3.3 Discussion

Consider the (10, 10) tube as thin elastic rods, then the toroids are rings of thin rods. Assuming κ as the Young's modulus of the (10, 10) tube, I the moment of inertia about the axis parallel to tube cross section, the strain energy of the rings are given by

$$E = \frac{1}{2}\kappa I \int (\frac{1}{R} - \frac{1}{R_o})^2 dl \tag{3.1}$$

where

$$I_y = \int x^2 df = \frac{1}{2}\int r^2 df = \frac{\pi}{4}(r_{r_{out}}^4 - r_{r_{in}}^4) \tag{3.2}$$

Taking $r_{out} = 16.70$ (Å), the inter-tube distance of (10, 10) SWNT crystals, $r_{in} = 10.5$ (Å), which assumes 13.6 (Å) as the radius of (10, 10) tube, we get Young's modulus of the 913 (GPa) for toroids of large radius, which compares to the experimental value

of 1280 $\pm$ 0.6 (GPa)[20] for multi-walled carbon nano tubes (MWNT).

3.4 Conclusion

We have investigated energetics and structures of (10, 10, n) toroids, three transition radii are found that define the regions with different stable structures. Based on classical elastic theory analysis, we calculated the modulus of different regions.

3.5 References

1. Huffman, D.R., *Physics Today* **44(11)**, 1991, 22-29.

2. Tibbetts, G.G., *Journal of Crystal Growth* **66**, 1984, 632-638.

3. Kroto, H.W., Heath, J.R., O'Brien, S.C., Curl, R.F., Smalley, R.E., *Nature* **318**, 1985, 162.

4. Krätschmer, W., Lamb, L.D., Fostiropoulos, K., and Huffman, D.R., *Nature* **347**, 1990, 354.

5. Bethune, D.S., Meijer, G., Tang, W.C., Rosen, H.J., *Chem. Phys. Lett.* **174**, 1990, 219.

6. Krätschmer, Fostiropoulos, K., and Huffman, D.R., *Chem. Phys. Lett.* **170**, 1990, 167.

7. Taylor, R., Hare, J.P., Abdul-Sade, A.K., and Kroto, H.W., *JCS Chem. Comm.* **20**, 1990, 1423.

8. Iijima, S., *Nature* **354**, 1991, 56.

9. Bethune, D.S., Kiang, C. H., Devries, M. S., Gorman, G., Savoy, R., Vazquez, J., Beyers, R., *Nature* **363**, 1993, 605.

10. Dresselhaus, M.S., Dresselhaus, G., and Saito, R., *Carbon* **33(7)**, 1995, 883.

11. Jishi, R.A., Inomata, D., Nakao, K., Dresselhaus, M.S., and Dresselhaus, G., *Journal of Physical Soceity of Japan* **63(6)**, 1994, 2252.

12. Benedict, L.X., Crespi, V.H., Louie, S.G., and Cohen, M.L., *Physical Review B* **52(20)**, 1995, 14935.

13. Robertson, D.H., Brenner, D.W., and Mintmire, J.W., *Physical Review B* **45(21)**, 1992, 12592.

14. Hulteen, J.C., Chen, H.X., Chambliss, C.K., and Martin, C.R., *Nano-Structured Materials* **9**, 1997, 133.

15. Ruoff, R.S., Tersoff, J., Lorents, D.C., Subramoney, S., and Chan, B., *Nature* **364**, 1993, 514.

16. Thess, A., Lee, R., Nikolaev, P., Dai, H., Petit, P., Robert, J., Xu, C., Lee, Y.H., Kim, S.G., Rinzler, A.G., Colbert, D.T., Scuseria, G.E., Tomanek, D., Fischer, J.E., Smalley, R.E., *Science* **273**, 1996, 483.

17. Bockrath, M., Cobden, D.H., McEuen, P.L., Chopra, N.G., Zettl, A., Thess, A., and Smalley, R.E., *Science* **274**, 1997, 1922.

18. Cowley, J.M., Nikolaev, P., Thess, A., and Smalley, R.E., *Chemical Physics Letters* **265**, 1997, 379.

19. Dai, H., Wong, E.W., and Lieber, C.M., Science **272**, 1996, 523.

20. Wong, E.W., Sheehan, P.E., Lieber, C.M., *Science* **277**, 1997, 1971.

21. Guo, Y. J., Karasawa, N., and Goddard III, W.A., *Nature* **351**, 1991, 464.

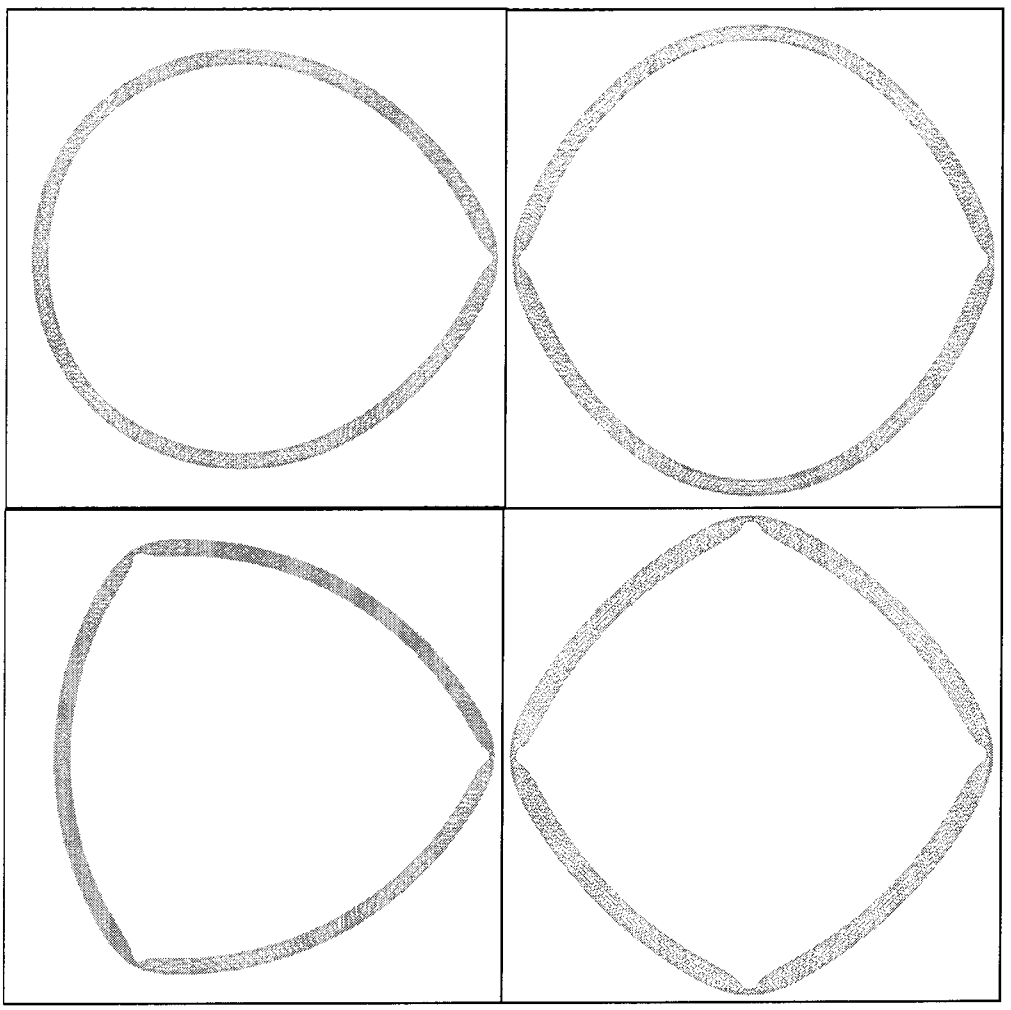

Figure 3.6: Optimized carbon toroids with 1, 2, 3, and 4 buckles. The one buckle toroid has 16,800 carbon atoms. Denoted as (10, 10, 840), the radius of its circular form is 163.3 (Å). The toroid with two buckles has 16,400 carbon atoms, (10, 10, 820), radius of its circular form is 159.4 (Å). The toroid with three buckles has 18,000 atoms, (10, 10, 900), radius of its circular form is 174.9 (Å). The toroid with four buckles has 14400 atoms, (10, 10, 720), radius of its circular form is 139.9 (Å).

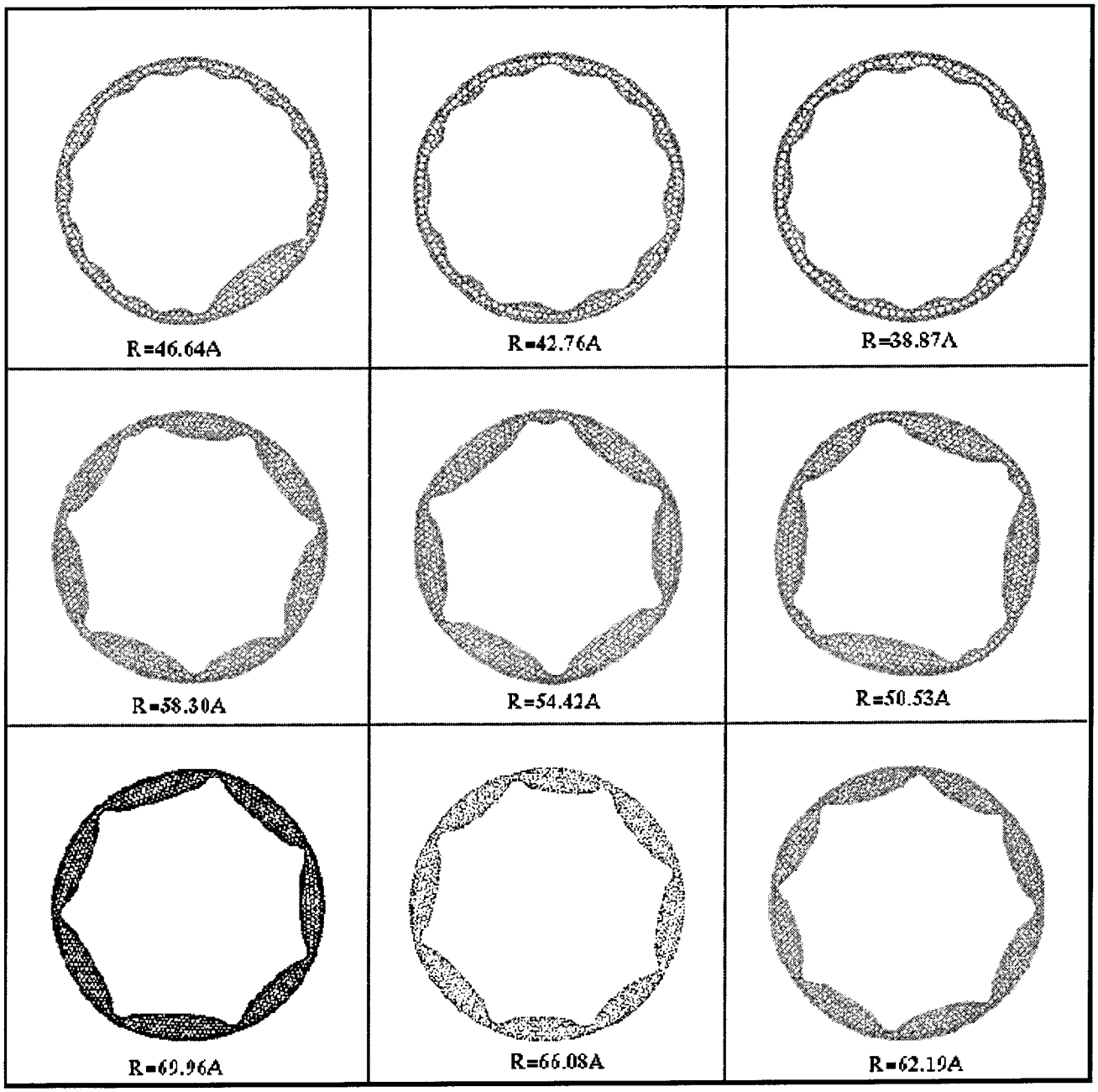

Figure 3.7: Collection of kinky toroids

Chapter 4 Structures and Properties of K-Doped Carbon SWNT

4.1 Introduction

The development of methods[1] to control the catalytic synthesis of SWNT (originally synthesized by Bethune[6] and Iijima[7]) to form ordered ropes containing 100's to 1000's of tubes gives hope for developing structures useful for new generations of nanoscale devices. The recent report that these SWNT ropes can be doped to form metallic conductors[2] gives further hope for interesting devices. Because many standard analysis techniques are difficult in the nanoscale region (10 to 100 nm), it is important to have accurate computer simulations of the structures and properties that can be correlated with observable signatures.

Lee[2] *et al.* recently showed that doping single-walled carbon nanotube (SWNT) ropes with K, Rb, or Br_2 leads to metallic conductivity. However, the structures and properties of these doped systems have not been characterized. We used theory (quantum mechanics (QM) and molecular dynamics (MD)) to predict structural properties which may help motivate and interpret experiments on SWNT/K. Assuming that the K cannot penetrate the tubes, we find the optimum stoichiometry to be KC_{16}, leading to a triangular crystal with a tube-tube spacing of 17.72 (Å), 6.1% larger than for pristine SWNT crystals. We predict the optimum structure and the associated X-ray powder diffraction pattern expected for K_nC_{80} from $n = 0$ to 10 (optimum is $n = 5$) for both triangular (closest packed) and square packing of the tubes. The Young's modulus per tube along the tube axis changes from 640 to 525

[3]Based on "Where the K are in Doped Single Walled", **G. Gao, T. Cagin, and W.A. Goddard III**, on press

GPa for $n = 0$ to 5. We also calculated the optimum structure assuming that K can penetrate inside the tubes (perhaps at defects or through open ends). This leads to an optimum stoichiometry of K_1C_{10} ($K_5^{exo}K_3^{endo}C_{80}$ with 3 inside the tube). In order to help experimentalists search for such possible interesting changes in structure, we calculated the powder diffraction and fiber diffraction patterns for all n from 0 to 11 for all the cases.

4.2 Structures and Energies of K-Doped SWNT Crystals

We used the force fields[8] developed for, and applied to, studying alkali doped fullerenes which is shown to be very accurate. In the force field, full charge transfer is assumed with each K donating one electron and the donated charges distributed uniformly among C atoms. In addition, we used QM calculations to establish the energy of nanotubes as a function of doping level. This is required to obtain absolute energies for comparing the stability as a function of n. The molecular mechanics and MD calculations exclude Coulomb and van der Waals interactions between atoms that are bonded (1-2 interactions) or share a bonded atom (1-3 interactions). To estimate the relative energy of the SWNT with different amounts of charge, we must include the effect of shielded 1-2 and 1-3 interactions. To do this we considered the absolute energy of C_{60}^{q-} as a function of n from QM[9] and added to the standard MM or MD energy a correction term of the form $E = E_0 + \lambda Q + JQ^2$; $\lambda = 413.116$ kJ/mol and $J = 4568.690$ kJ/mol are adjusted such that the total energy differences for $q = 60Q$ match the QM. These constants, λ and J, were then used for the SWNT/K calculations to obtain absolute energies.

We considered both closed packing and square packing for exo cases. For the closed packing, we started with the predicted minimized crystal structure for (10,10) SWNT crystals (triangular with $a = b = 16.70$ (Å), $c = 4.94$ (Å), $\gamma = 60°$, tube-tube

spacing of 16.70 (Å)). For square packing, we also started with the predicted optimum square packing structure with $a = b = 16.70$ (Å), $c = 4.94$ (Å), $\gamma = 90°$, tube-tube spacing of 16.70 (Å). We also considered doping inside tubes (exo) and doping both inside tupes (endo) and doping between and inside tubes (exoendo).

4.2.1 Doping outside tubes

By comparing the van der Waals radius of K atom with the distance between adjacent layers of (10,10) tube, we found $c = 4.94$ (Å) with 80 carbon atoms (two layer rings) is a reasonable starting structure. Since we have 80 carbon atoms per unit cell, we'll denote the number of K atoms with respect to 80 carbon atoms, i.e., K_nC_{80}, with $n = 1$ to $n = 10$. For each n, after calculating various stable structures, the most energetically favored structure (one tube per cell) was extended to allow more independent tubes per cell (four tubes). We then carried out 20 ps of MD at 600K to equilibrate the system and quenched the structures by minimizing the energy.[10] In these studies, we considered both triangular (closest packed tubes) and square packing of the tubes.

Square packings are considered first. For $n \leq 3$, there is only one stable structure shown in Fig. 4.1a through Fig. 4.1c. For $n = 4$ and $n = 5$, we have two stable structures after initial minimization, shown in Fig. 4.2a, Fig. 4.2b and Fig. 4.3a, Fig. 4.3b. For $n = 6$ and $n = 7$, we found three stable structures each, shown in Fig. 4.4a, 4.4b, 4.4c and Fig. 4.5a, 4.5b, 4.5c. For $n = 8$, 9 and 10, four stable structures found shown in Fig. 4.6a, 4.6b, 4.6c, 4.6d, Fig. 4.7a, 4.7b, 4.7c, 4.7d, and Fig. 4.8a, 4.8b, 4.8c, 4.8d.

After quenching the quadrupled (extend the unit cell to 2×2 of the single tube unit cell) structures, we found that $n = 1$ and $n = 2$ packing are transformed into triangular packing (closest) and the rest stays more or less orthorhombic. Figure 4.9 is the projected final structures along c axis, and Fig. 4.10 is the calculated X-ray powder patterns.

We went through the same procedure for triangular packing. Figure 4.11 is is

the projected structure along c axis for $n = 1$ to $n = 10$, while Fig. 4.12 shows the predicted X-ray powder diffraction pattern.

The energetics of varius cases are shown in Fig. 4.13; here we see that the global minimum is the triangular structure of K_5C_{80} =KC_{16}. For $n \leq 2$ the K intercalate in hollows between three tubes, whereas for $n \geq 3$ the K intercalate between pairs of tubes, just as in stage one K intercalated graphite (GIC). Indeed Fig. 4.14a and 4.14b shows that for the optimum structure, $K_5C_{80} = KC_{16}$, the K are packed in the same (2×2) pattern observed for intercalated graphite, KC_8[3], as shown in Fig. 4.15. The difference for KC_{16} SWNT is that the K can only be on the outside of the tube (vide infra), leading to half the amount of K. For $n \geq 7$ there are significant distortions of the tube shells.

We have not yet examined the dynamics for K diffusing through the SWNT to form the equilibrium structure. However, these results suggest a qualitative picture. The K fit quite nicely into the three fold hollows of the triangular cell, requiring no change in the tube packing up to $K_2C_{80} = KC_{40}$. Probably this diffusion is relatively rapid. Adding further K to form triangular K_3C_{80} requires a 13% volume expansion of the tubes, which could be a rather sluggish transformation. Since square K_3C_{80} and K_4C_{80} are nearly as stable as triangular, it may be that adding K to triangular K_2C_{80} leads to a transformation into the square phases for $n = 3, 4$. In any case, for K_5C_{80} and beyond the triangular is strongly favored over square. Thus, we expect only the expanded triangular structure in this region.

4.2.2 Doping inside and inside-and-outside the tubes

We assumed above that the K intercalate between tubes (exo K), but it is possible that the tubes have defects or open ends that would allow K to penetrate the tubes. First we calculated the case in which only endo K are allowed. This leads to energetics as in Fig. 4.13 with an optimum packing of $K_4^{endo}C_{80}$. The structures are shown Fig. 4.16 and the powder diffraction patterns are shown in Fig. 4.17. Combining the best exo packing ($n = 5$) with endo packing, we find an optimum structure of K_5^{exo} K_3^{endo} C_{80}

$= KC_{10}$. The projected structures for combined cases are shown in Fig. 4.18 and the powder patterns are in Fig. 4.19. The side and top view of K_5^{exo} K_3^{endo} $C_{80} = KC_{10}$ is shown in Fig. 4.14c and 4.14d.

4.3 Mechanical Properties and Vibrational Frequencies

The density and modulus along the tube axis are plotted in Fig. 4.20a as a function of n (for the triangular case). Here we see a dramatic break at $n = 2$, corresponding to the change in K intercalation. The Young's modulus (Fig. 4.20b) is 18% smaller for $n \geq 3$ than for $n \leq 2$. This is because of the change in area per tube. Normalizing by the number of tubes leads to modulus of $\sim$ 640 GPa, independent of n. Indeed normalizing by per projected atom along the sheet leads to the same value (1090GPa) as for graphite.

A valuable probe of the structure of nanotubes is the vibrational spectra. Indeed the assignment of the tubes in these experimental studies as (10,10) armchair was based on the observation that the strong Raman mode at 186 cm^{-1} changes dramatically with diameter of the ring and is predicted at 186 cm^{-1}, in good agreement. Consequently, we calculated the vibrational modes of the K_nC_{80} crystals for all n. In Fig. 4.21a shows the highest frequency in-plane mode for various n, and Fig. 4.21b shows the tube expansion mode (at 186 cm^{-1} in the pristine SWNT crystal). We see that the highest (in-sheet) vibration mode at 1583 cm^{-1} (observed at 1593 cm^{-1},[4] drops by 8 cm^{-1} as n increases from 0 to 5. This calculated drop of 8 cm^{-1} is consistent with experiment[5] which observes $\delta\nu = 29$ cm^{-1}. Simultaneously the intense ring expansion Raman mode observed at 186 cm^{-1} (calculated at 186 cm^{-1}) in pristine SWNT increases to 203 cm^{-1} for n=5. Experimentally[6] all modes in the low frequency region disappear for SWNT/K. These intensity changes were explained in terms of a resonance similar to that observed in KC_8 graphite. However, for SWNT/Br_2 shifts

of 74 cm^{-1} were observed. Overall we believe that these results are compatible with the observations on SWNT/K. The predicted diffraction, vibration, and modulus properties should be useful in characterizing these systems.

4.4 Conclusion

We used theory (quantum mechanics (QM) and molecular dynamics (MD)) predicted structural properties which may help motivate and interpret experiments on SWNT/K. Assuming that the K cannot penetrate the tubes, we found the optimum stoichiometry to be KC_{16}, leading to a triangular crystal with a tube-tube spacing of 17.72 (Å), 6.1% larger than for pristine SWNT crystals. We predicted the optimum structure and the associated powder diffraction X-ray pattern expected for K_nC_{80} from $n = 0$ to 10 (optimum is $n = 5$) for both triangular (closest packed) and square packing of the tubes. The Young's modulus per tube along the tube axis changes from 640 to 525 GPa for $n = 0$ to 5. We also calculated the optimum structure assuming that K can penetrate inside the tubes (perhaps at defects or through open ends). This leads to an optimum stoichiometry of K_1C_{10} ($K_5^{exo}K_3^{endo}C_{80}$ with 3 within the tube).

4.5 References

1. Thess, A., Lee, R., Nikolaev, P., Dai, H., Petit, P., Robert, J., Xu, C., Lee, Y.H., Kim, S.G., Rinzler, A.G., Colbert, D.T., Scuseria, G.E., Tomanek, D., Fisher, J.E., and Smalley, R.E., *Science* **273**, 1996, 483-487.

2. Lee, R.S., Kim. H.J., Fischer, J.E., and Thess, A., *Nature* **388**, 1997, 255-257.

3. Dresselhaus, M.S. and Dresselhaus, G., *Advances in Physica* **30**, 1981, 139-326.

4. Rao, A.M., Eklund, P.C., Bandow, S., Thess, A., and Smalley, R.E., *Nature* **388**, 1997, 257-259.

5. Rao, A.M., Richter, E., Bandow, S., Chase, B., Eklund, P.C., Williams, K.A., Fang, S., Subbaswamy, K.R., Menon, M., Thess, A., Smalley, R.E., Dresselhaus, G., and Dresselhaus, M.S., *Science* **275**, 1997, 187-191.

6. Bethune, D.S., Kiang, C.H., Devries, M.S., Gorman, G., Savoy, R., Vazquez, J., Beyers, R., *Nature* **363**, 1993, 605-607; Kiang, C.H. and Goddard III, W.A., *Phys. Rev. Lett.* **76**, 1996, 2515-2518.

7. Iijima, S. and Ichlhashi, T., *Nature* **363**, 1993, 603-605.

8. Guo, Y.J., Karasawa, N., and Goddard III, W.A., *Nature* **351**, 1991, 464-467.

9. Chang, A.H.H., Ermler, W.C., and Pitzer, R.M., *J. Phys. Chem.* **95**, 1991, 9288-9291.

10. Lim, K.T., Burnett, S., Iotov, M., McClurg, R.B., Vaidehi, N., Dasgupta, S., Taylor S., & Goddard III, W.A., *J. Comp. Chem.* **18**, 1997, 501-521.

4.6 Figures

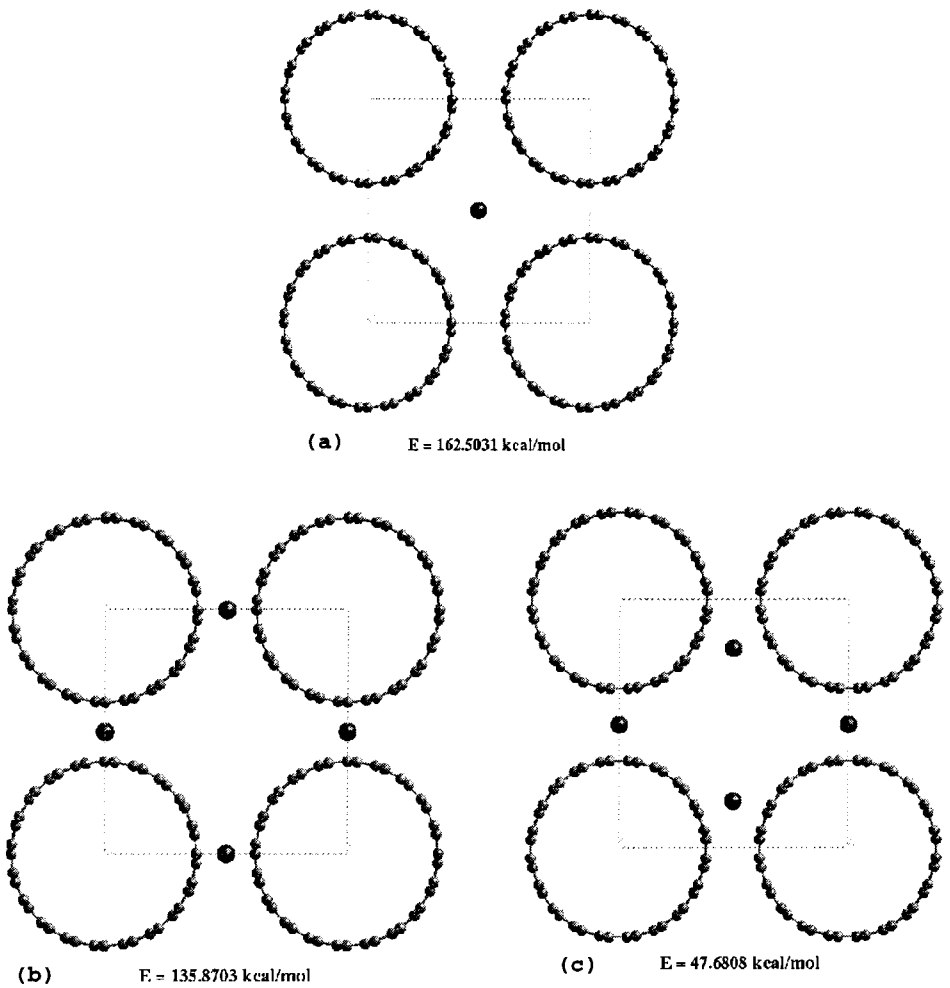

Figure 4.1: Projections of n = 1, 2, and 3 exo cases

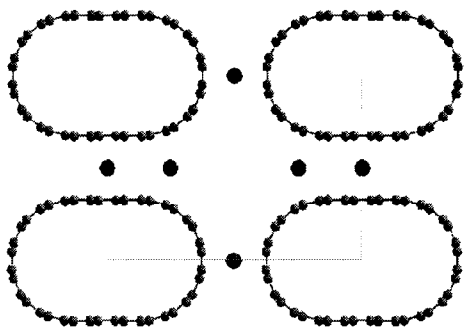

(a) E = −13.3356 kcal/mol

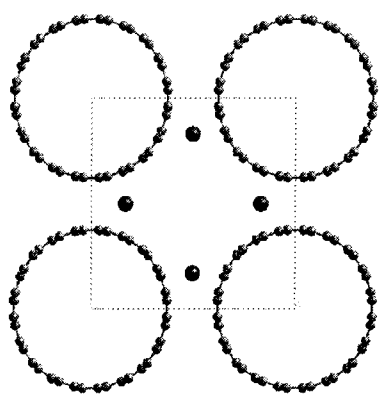

(b) E = −53.1019 kcal/mol

Figure 4.2: Projections of n = 4 exo cases

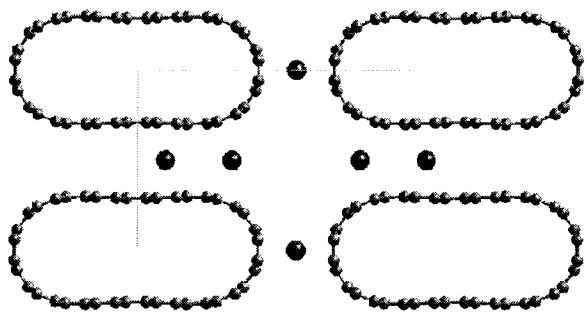

(a) E = -84.9462 kcal/mol

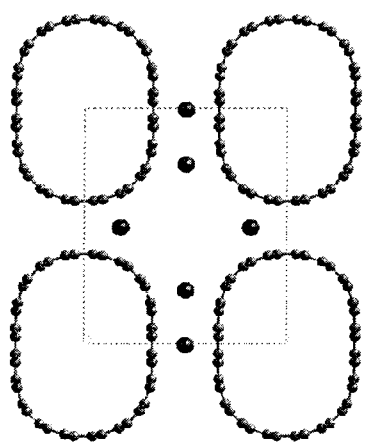

(b) E = -121.5347 kcal/mol

Figure 4.3: Projections of n = 5 exo cases

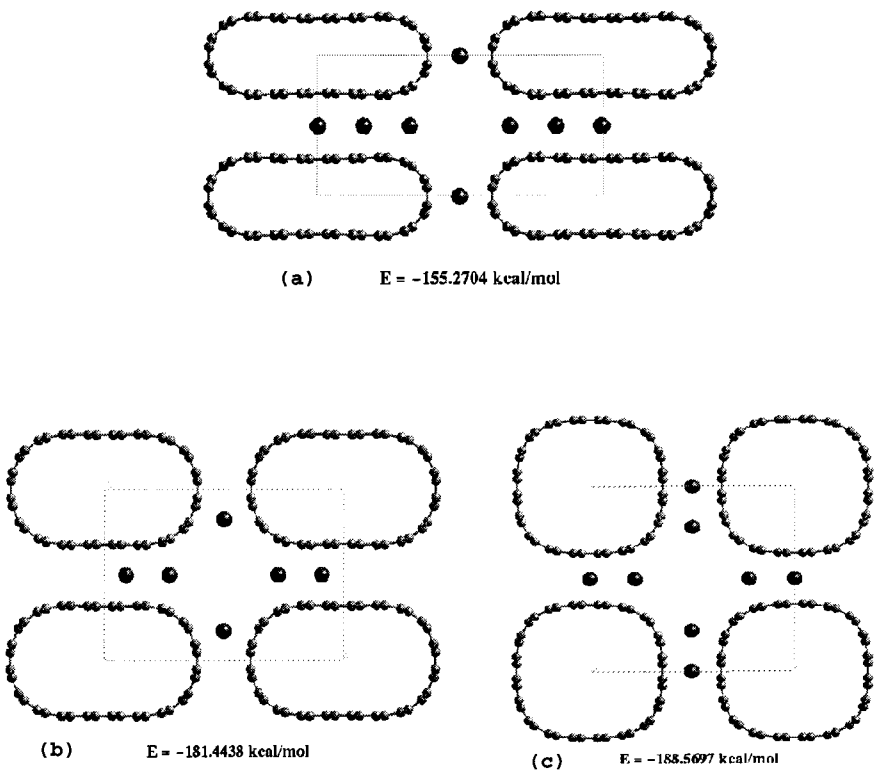

Figure 4.4: Projections of n = 6 exo cases

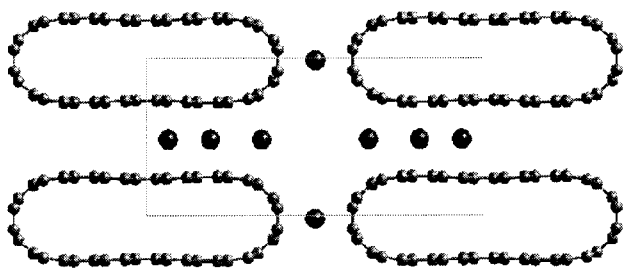

(a) E = -225.5677 kcal/mol

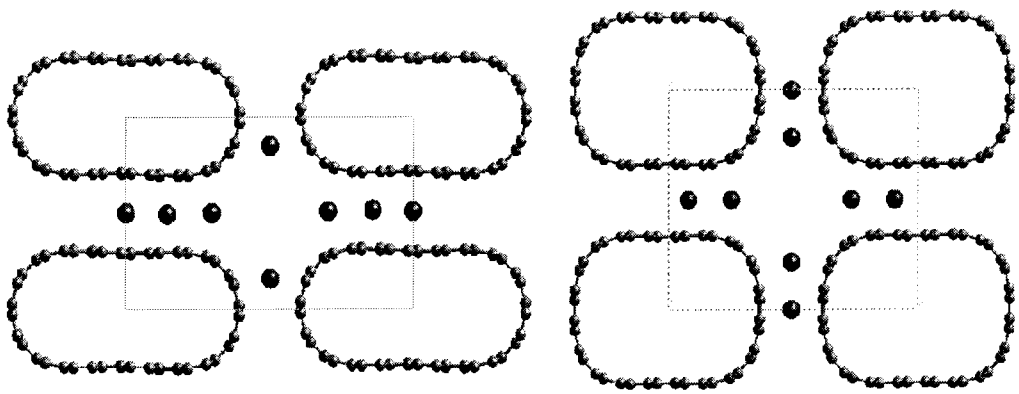

(b) E = -262.6625 kcal/mol

(c) E = -267.5824 kcal/mol

Figure 4.5: Projections of n = 7 exo cases

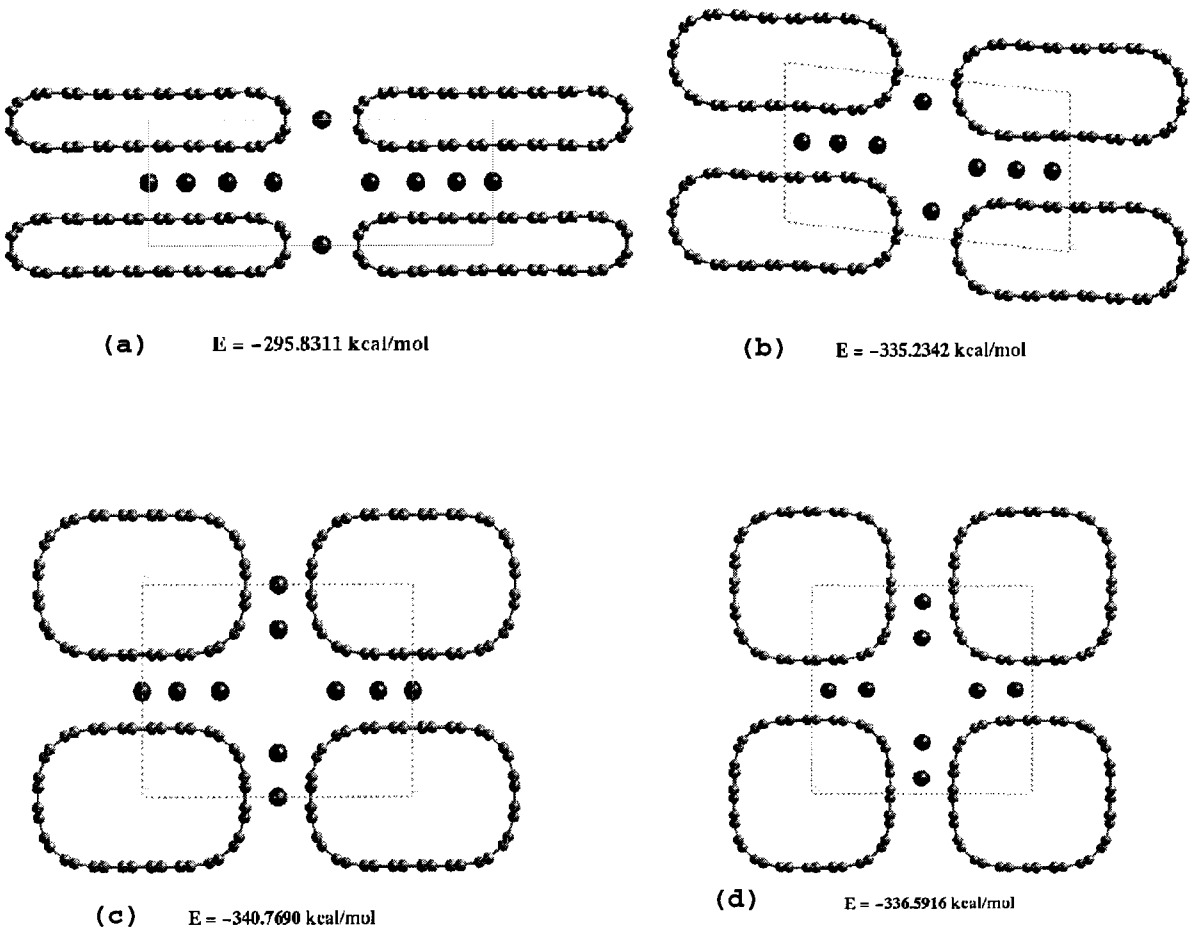

Figure 4.6: Projections of n = 8 exo cases

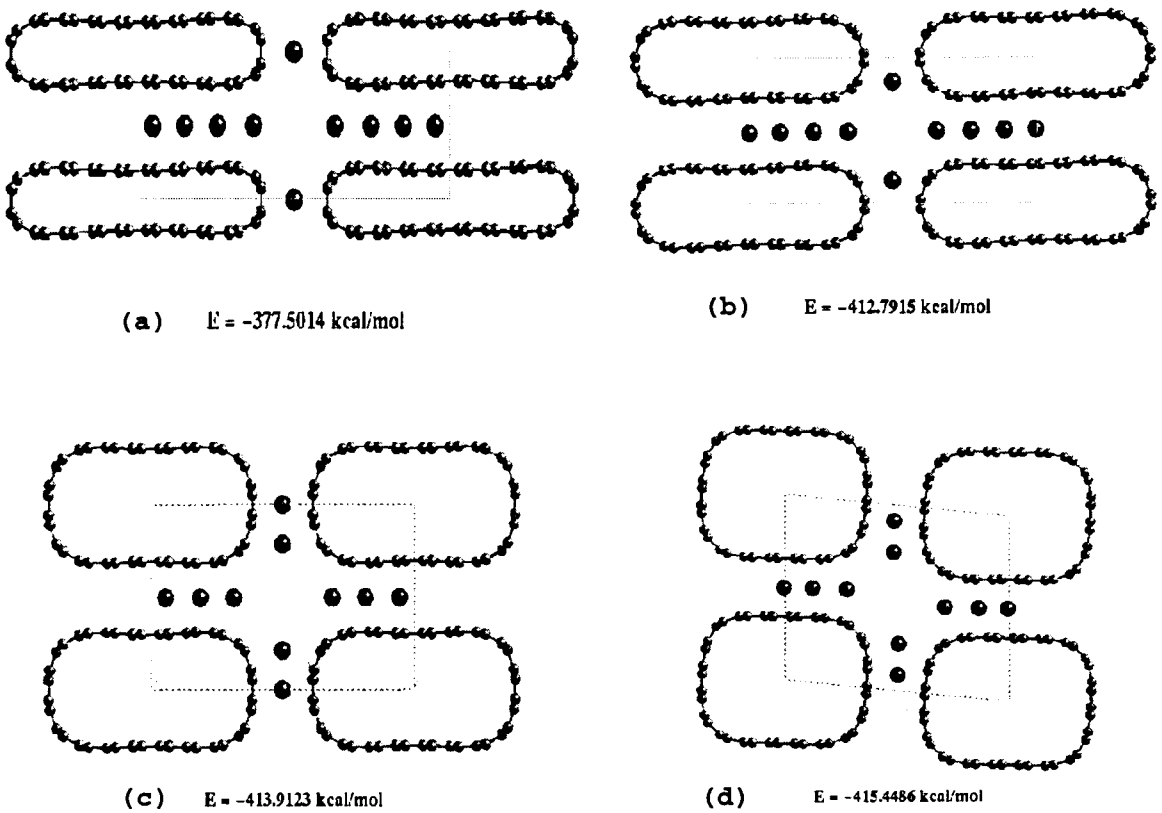

Figure 4.7: Projections of n = 8 exo cases

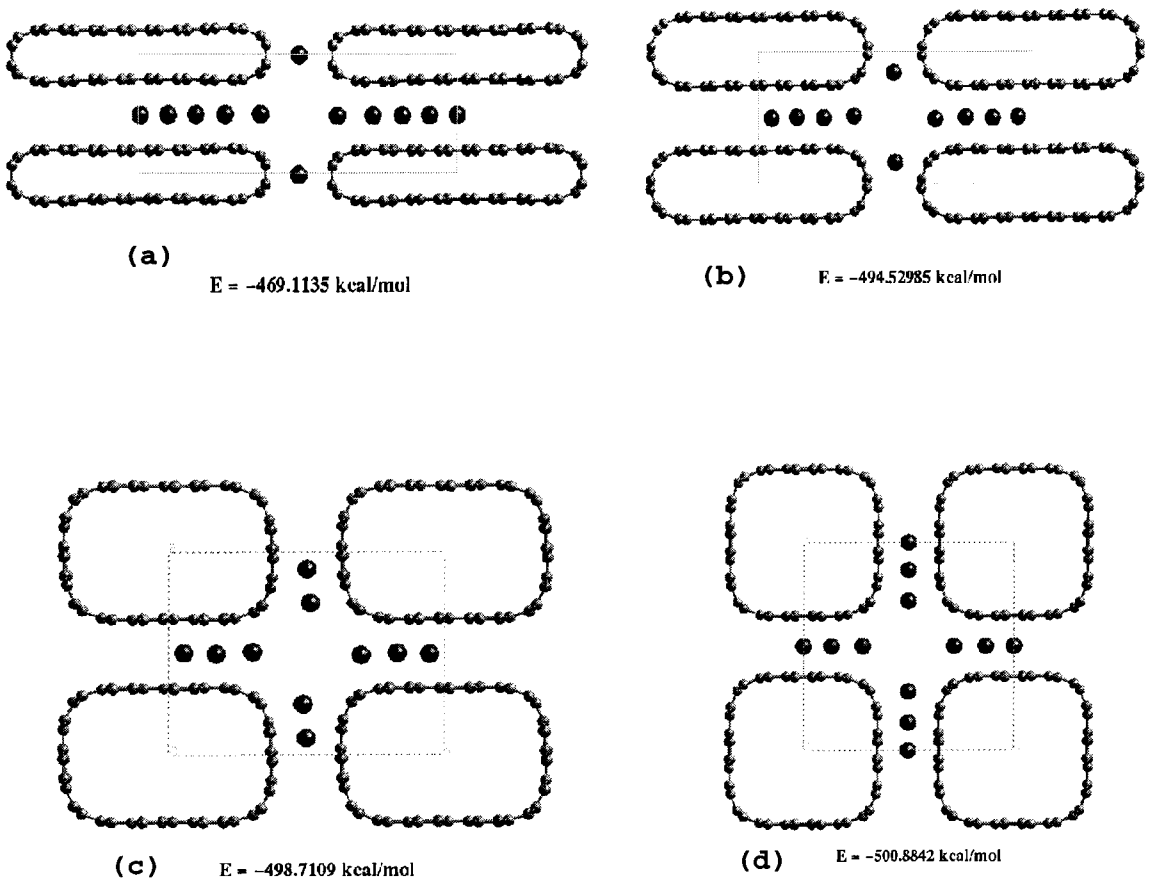

Figure 4.8: Projections of n = 10 exo cases

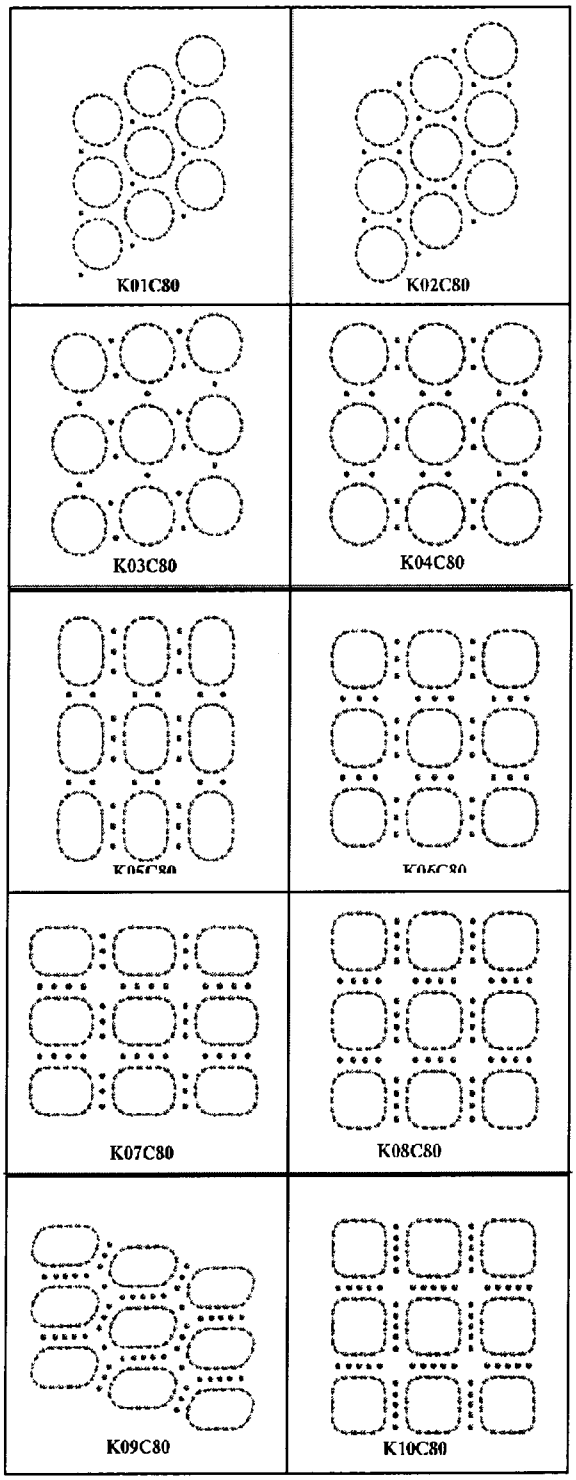

Figure 4.9: Optimum square exo packings

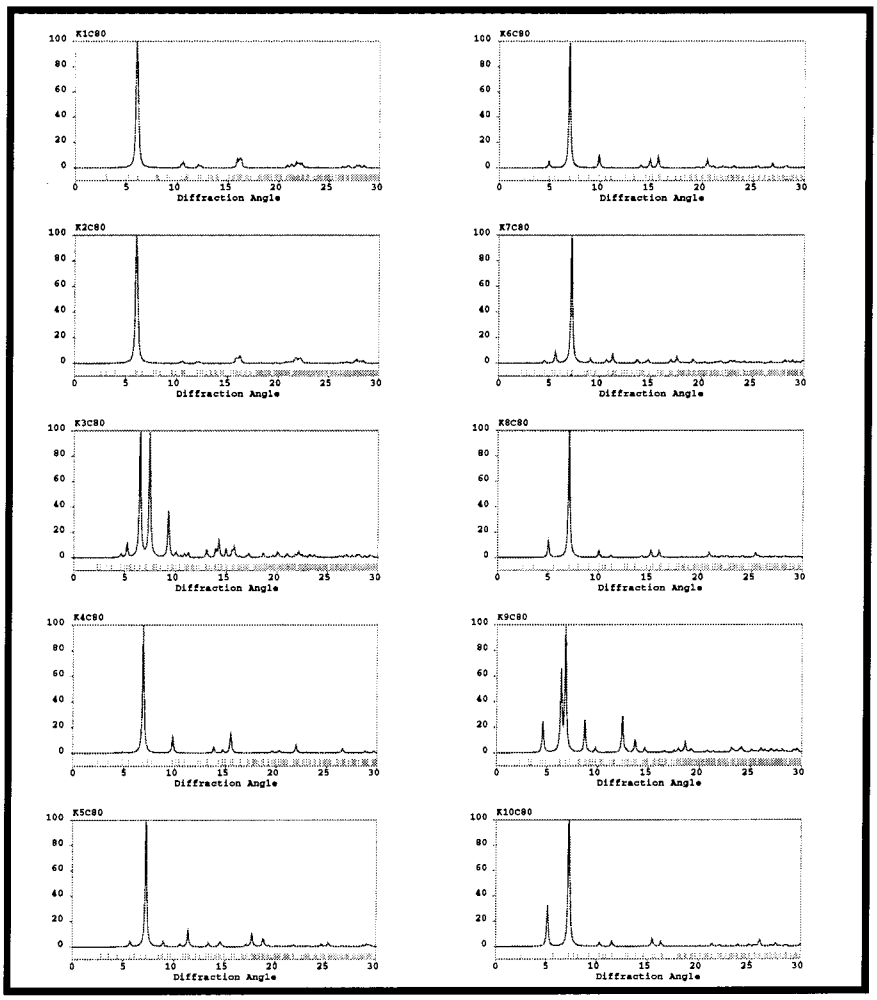

Figure 4.10: X-ray powder diffraction patterns of optimum square exo packings

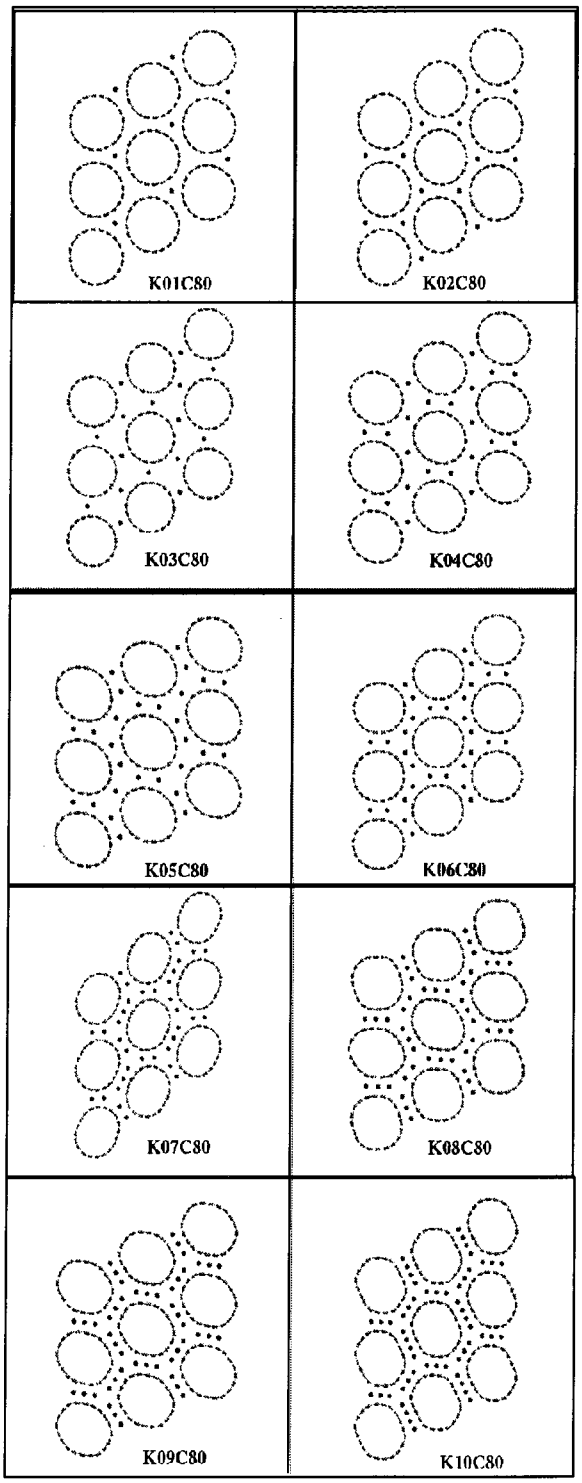

Figure 4.11: Optimum trigonal exo packings

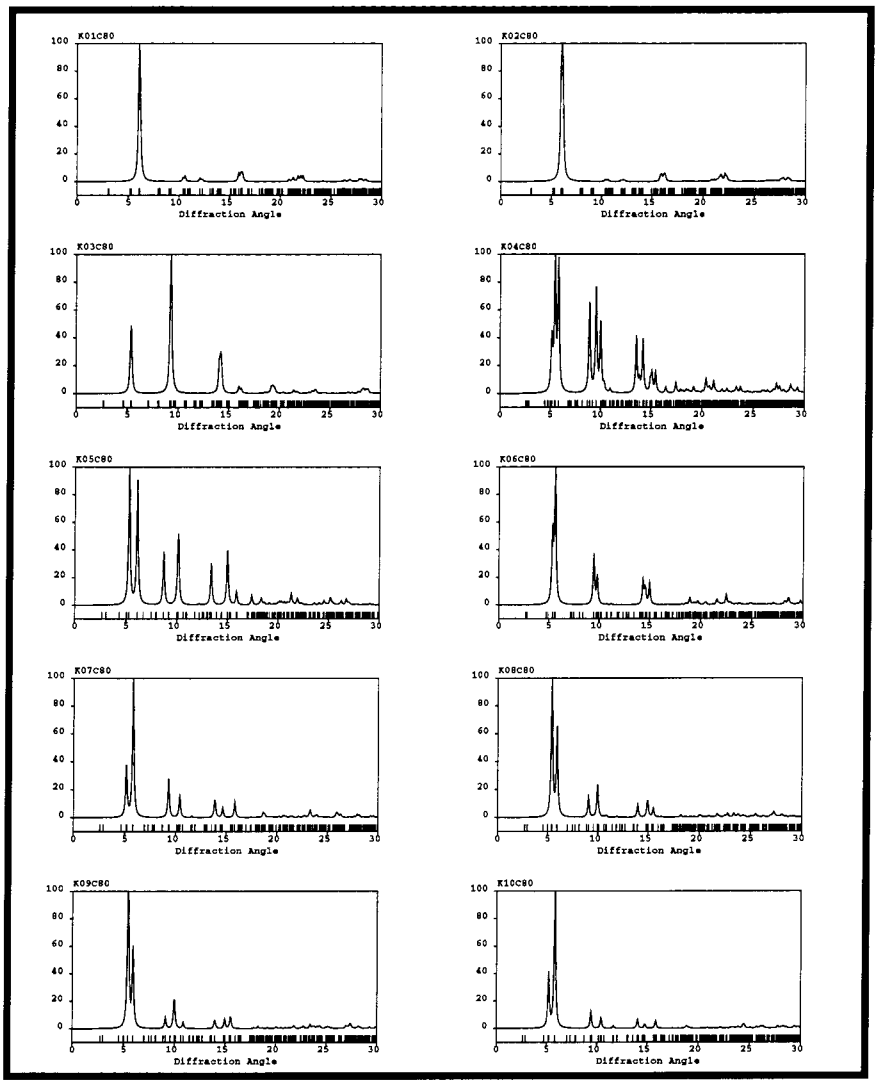

Figure 4.12: X-ray powder diffraction patterns of optimum trigonal exo packings

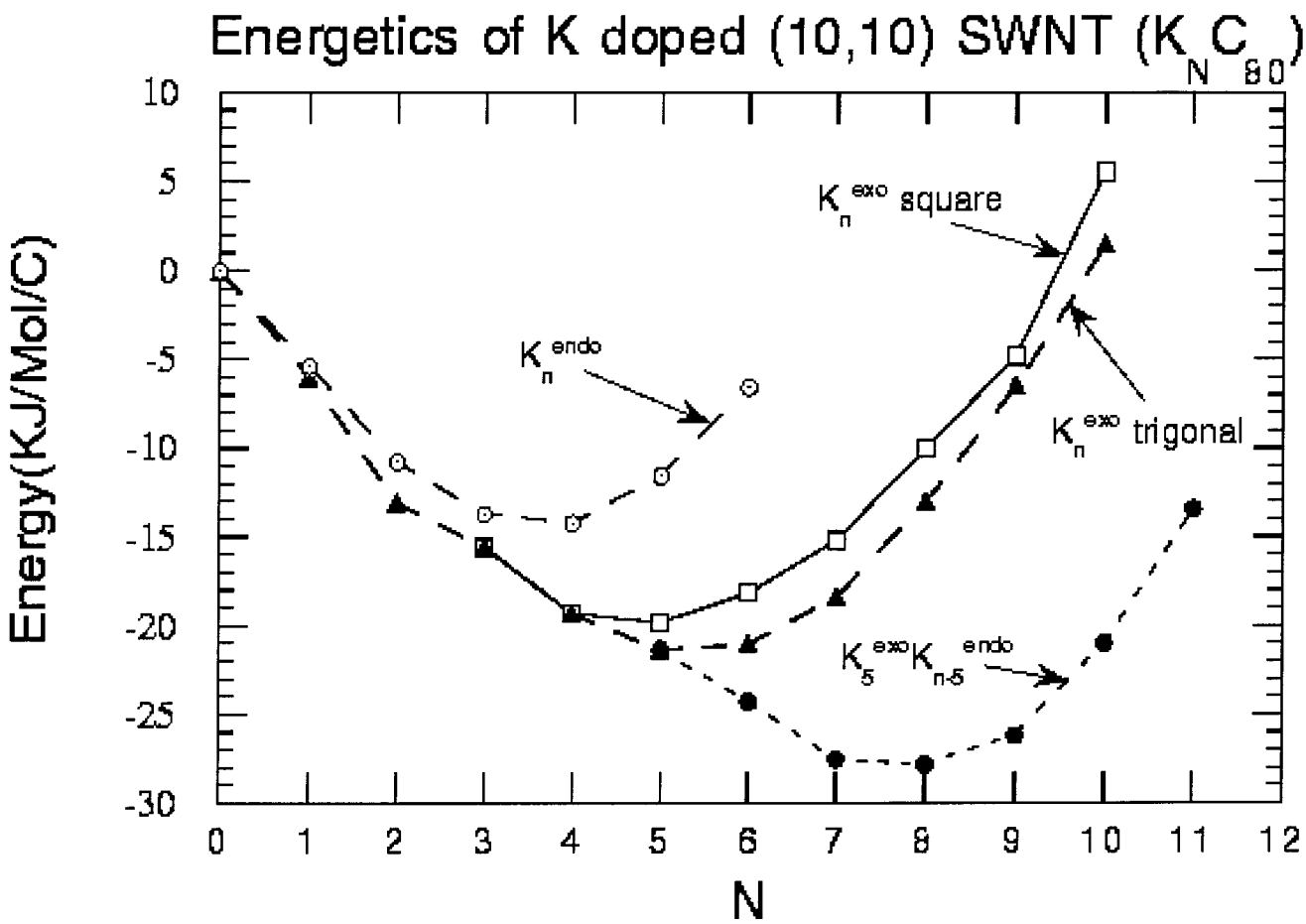

Figure 4.13: Energetics of various packings

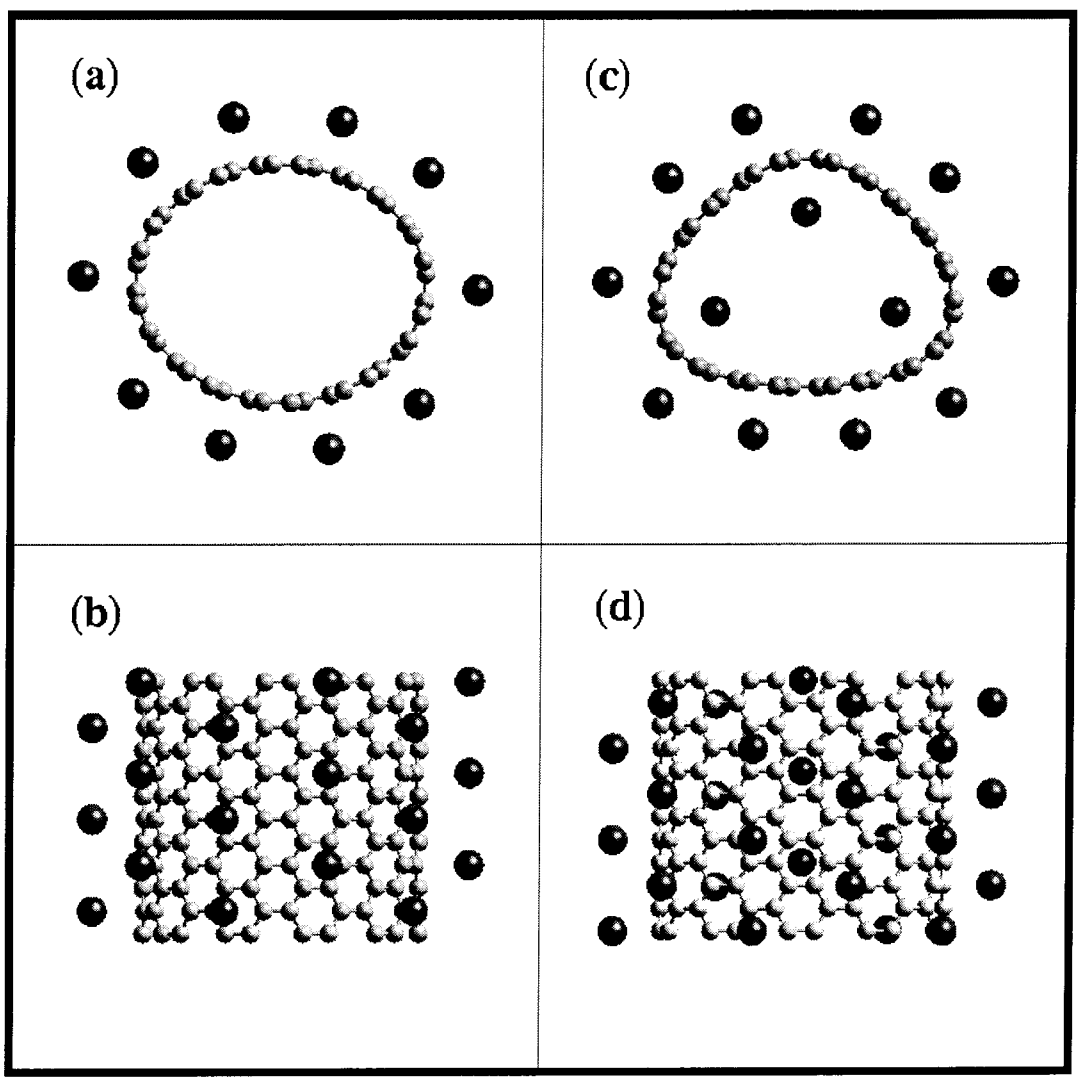

Figure 4.14: Optimum exo packing and optimum exo-endo packing

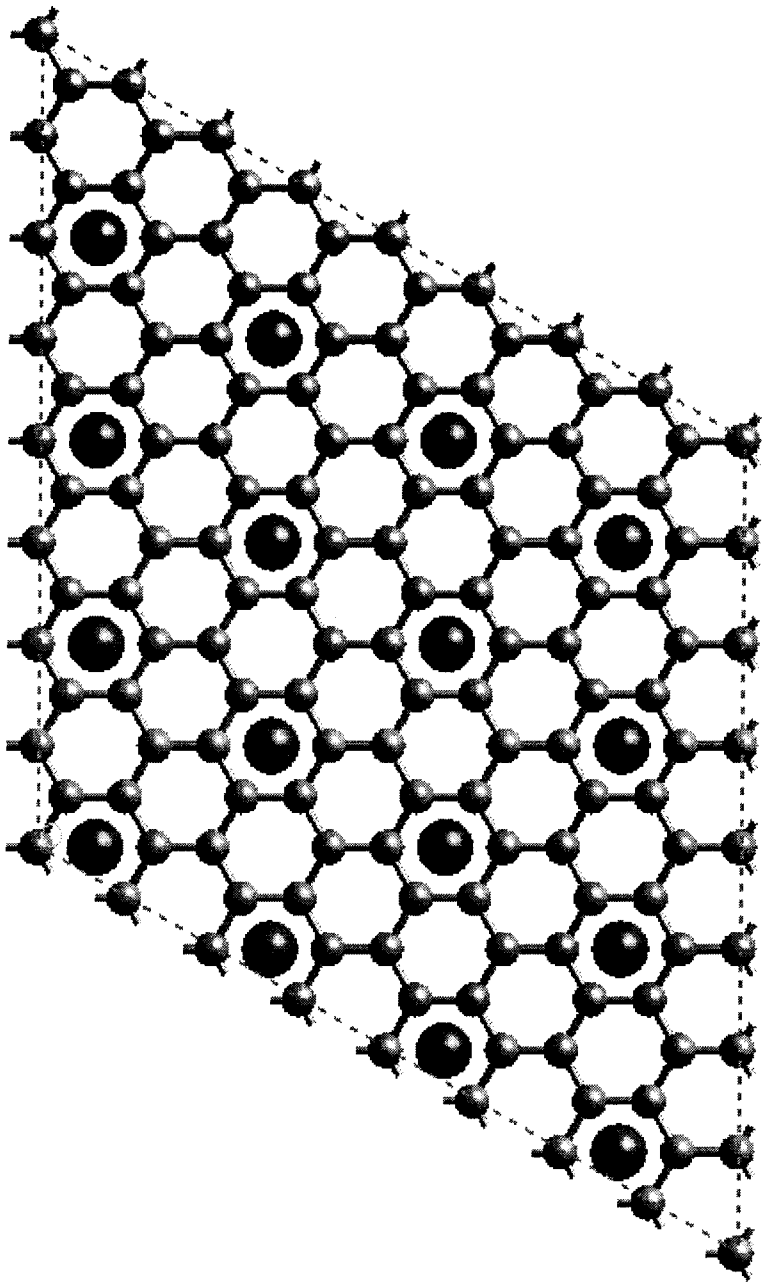

Figure 4.15: Crystal structure of stage one K intercolated GIC, K_1C_8

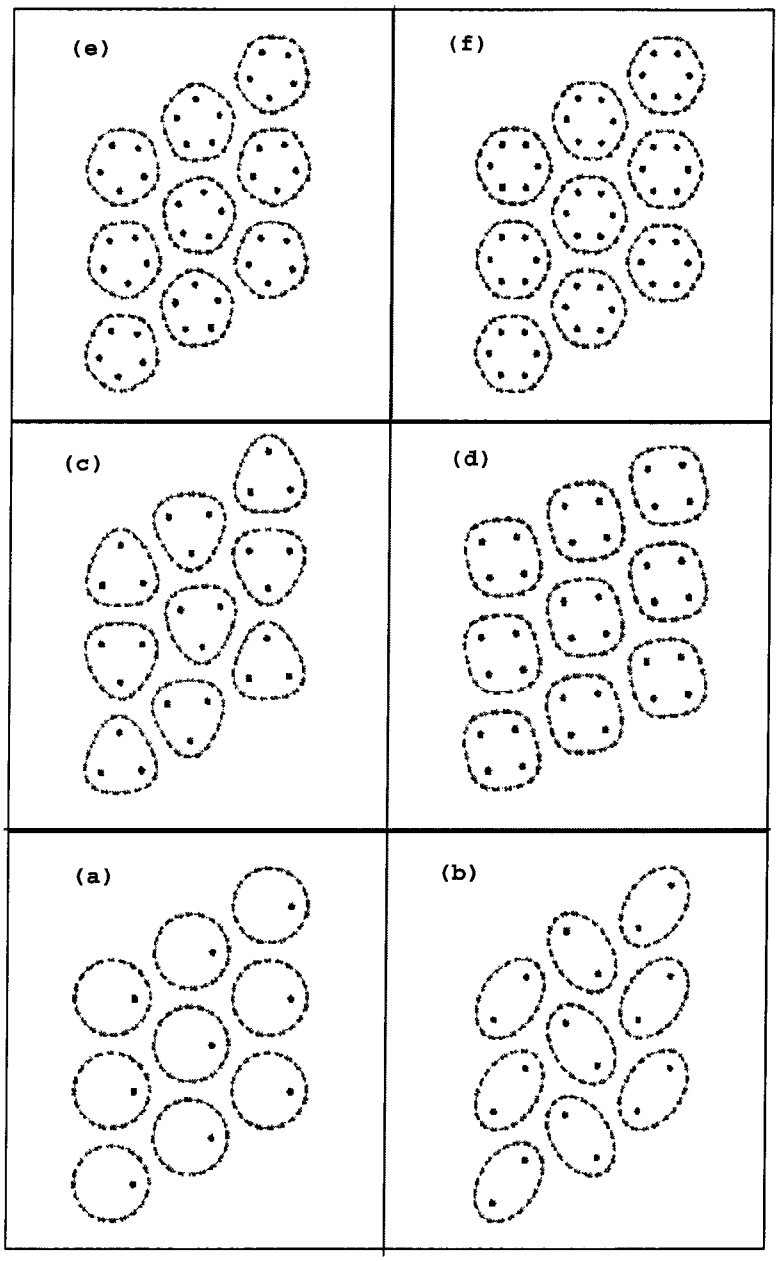

Figure 4.16: Projection of endo packings

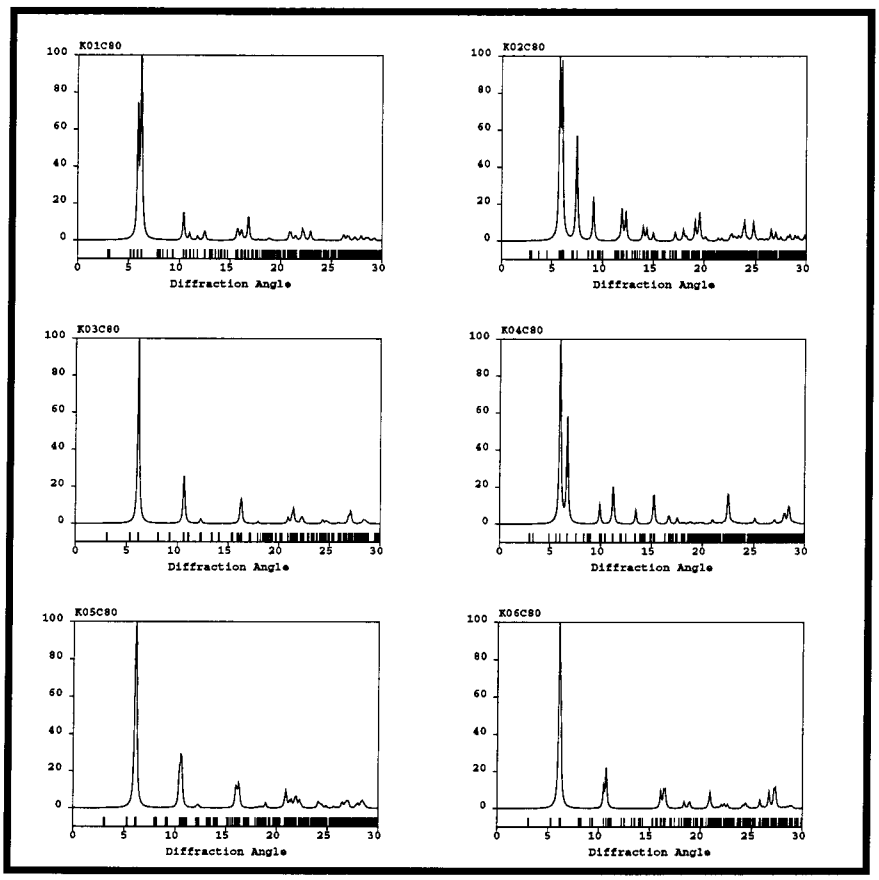

Figure 4.17: X-ray powder diffraction pattern for endo packings

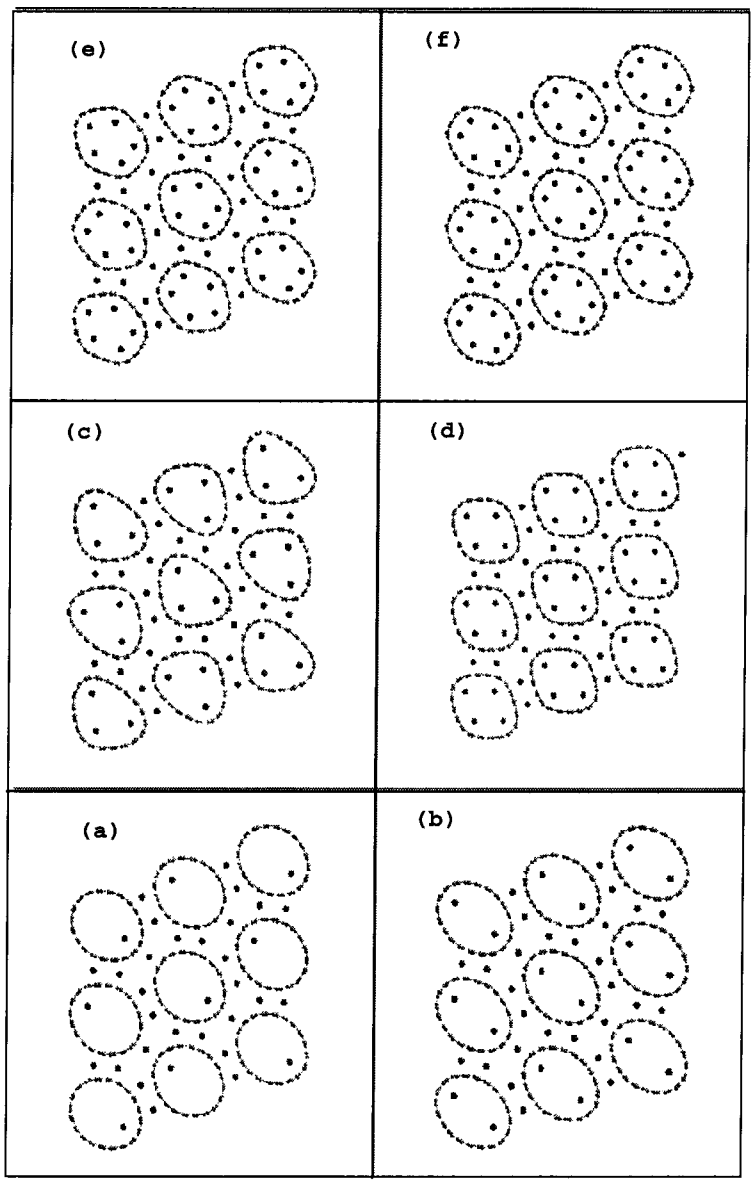

Figure 4.18: Projection of exo-endo packings

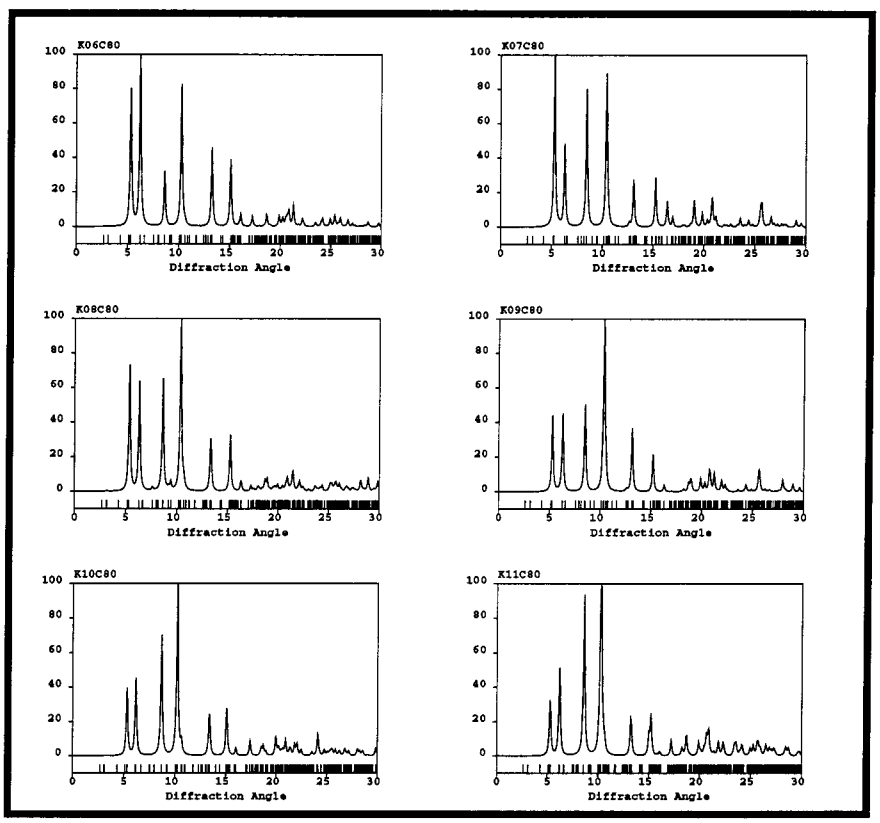

Figure 4.19: X-ray powder diffraction pattern for exo-endo packings

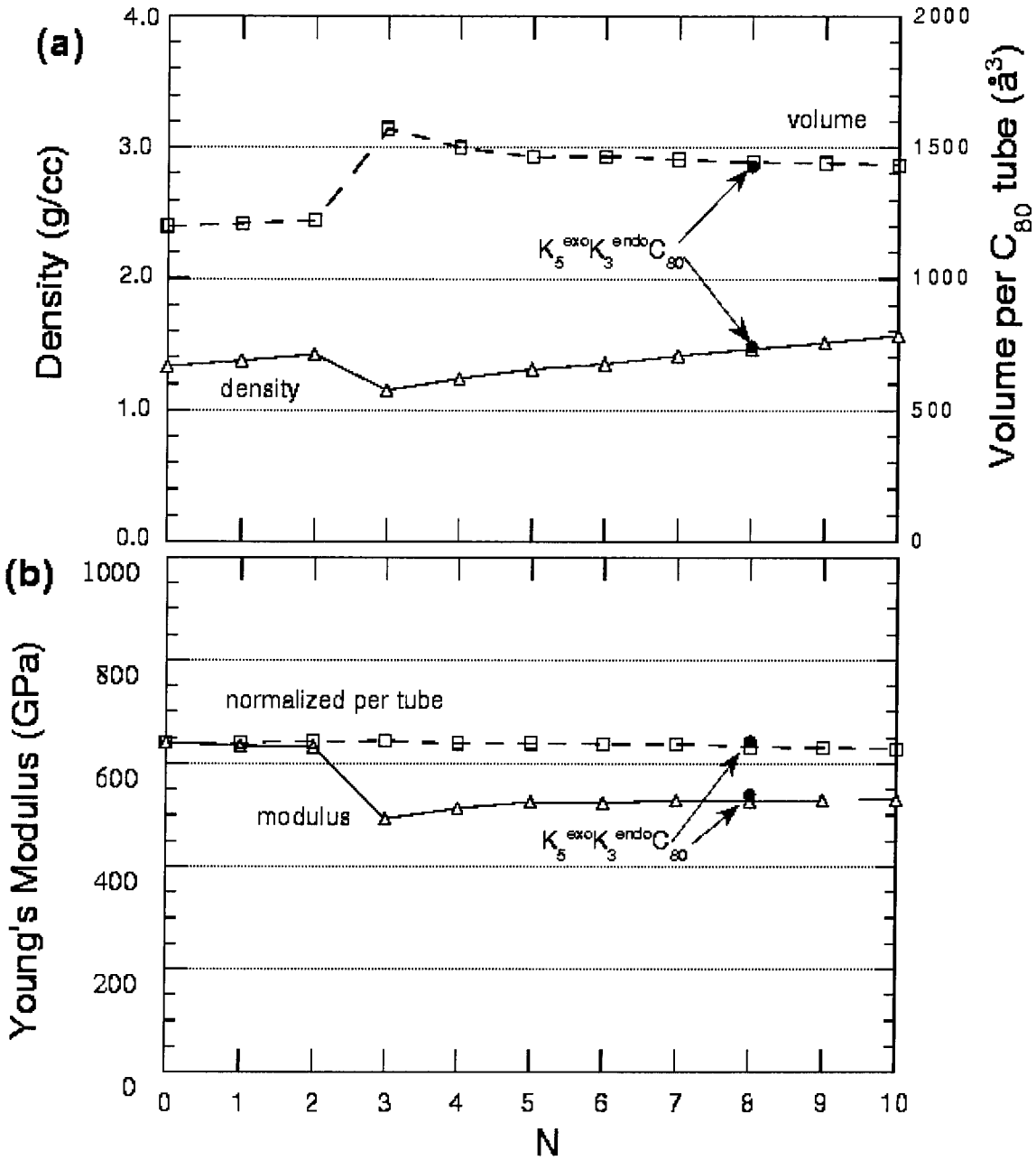

Figure 4.20: Density and Young's Modulus

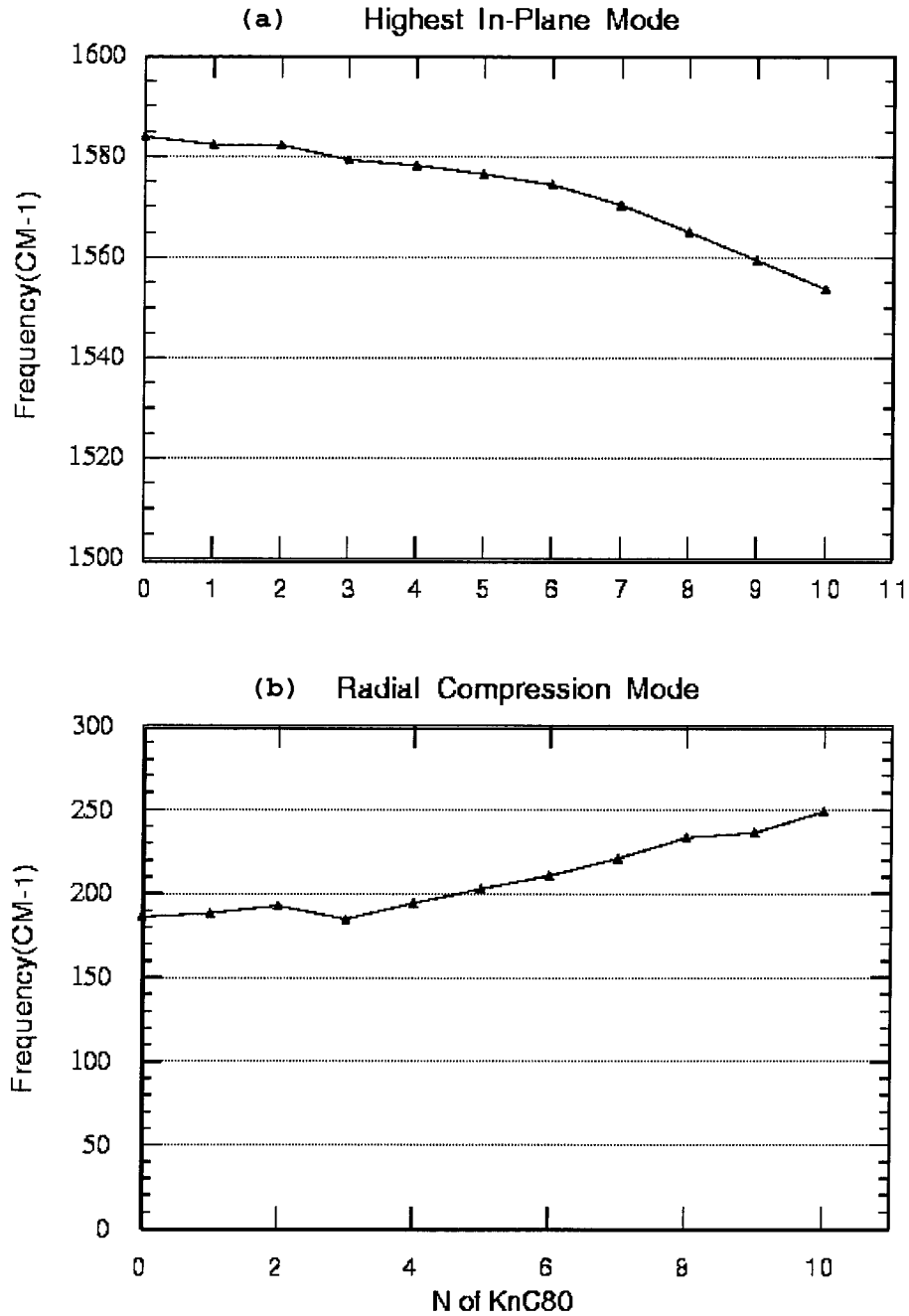

Figure 4.21: Frequencies

4.7 Tables

Table 4.1: Packing Energy (kcal/mol) of K-Doped SWNTs (exo)

N	$FF^{exo}_{triangular}$	$Total^{exo}_{triangular}$	FF^{exo}_{square}	$Total^{exo}_{square}$
1			162.4980	74.1040
2			78.6840	-60.7180
3	43.8708	-109.1736	43.9565	-109.0897
4	-50.7456	-180.0640	-51.2244	-180.5451
5	-150.7528	-219.0146	-120.9504	-189.9083
6	-243.1653	-213.0619	-188.5727	-158.4770
7	-327.9841	-162.2804	-267.5486	-101.8393
8	-398.0421	-59.4983	-341.0815	-2.6208
9	-483.3195	65.1304	-450.9706	97.4543
10	-577.8007	217.6041	-500.5281	294.8269

Table 4.2: Packing Energy of K-Doped SWNTs (exo and exo-endo)

N	FF^{endo}	$Total^{endo}$	N	FF^{endo}_{exo5}	$Total^{endo}_{exo5}$
1	175.0775	86.5928	6	-304.8248	-275.0900
2	122.5152	-16.8919	7	-503.6017	-336.9451
3	78.5685	-73.3507	8	-682.0247	-343.0934
4	46.6587	-82.7348	9	-864.7328	-311.6268
5	36.9011	-31.5333	10	-1009.7575	-212.4807
6	35.1176	64.4412	11	-1150.5749	-67.7510

Table 4.3: Breathing Modes of exo K_nC_{80}

N	L=2	L=3	L=4	L=5	L=6	L=7	L=8	L=9	L=10
0	52.6	48.7	126.8	147.1	201.4	262.4	328.3	375.2	401.9
	53.5	54.7	127.0	147.1	225.9	271.8	330.0	381.3	
1	47.3	49.1	126.2	159.6	201.9	266.4	329.2	376.1	402.1
	47.5	70.3	127.9	160.2	224.4	269.8	329.4	381.9	
2	46.2	49.5	110.0	169.6	203.5	269.8	331.3	377.4	403.5
	48.6	88.2	113.6	170.4	226.2	273.0	332.7	383.2	
3	49.7	43.6	112.0	196.5	205.7	269.1	328.7	375.8	403.4
	50.8	63.1	121.2	200.8	217.2	287.7	330.7	387.1	
4	47.3	35.2	113.0	143.2	217.2	281.3	333.3	378.0	405.4
	54.6	46.0	117.8	156.3	251.1	293.5	335.2	393.3	
5	50.7	47.9	78.9	163.1	215.9	286.3	330.4	379.6	413.7
	65.4	61.7	89.1	168.2	275.1	288.9	350.1	400.8	
6	60.4	41.8	85.8	167.7	224.9	305.7	353.5	394.8	418.0
	64.2	61.5	90.9	179.0	300.5		357.0	397.8	
7	63.1	44.4	86.0	140.8	237.2	295.5	350.0	397.3	422.3
	108.0	101.2	147.8	191.0	290.0	304.4	363.3	411.1	
8	62.2	43.0					349.9	408.5	423.0
	64.7	45.8					369.5	415.7	
9	63.3	39.3	94.1	136.2	273.1	305.5	370.4	426.0	431.6
	71.0	50.5	96.3	138.3	299.6	328.1	372.6	409.	
10	61.5	47.0		139.1	266.5	350.0	386.4	427.1	451.8
	65.8	114.7		142.7			394.7	439.4	

- Frequency in CM^{-1}.

Table 4.4: Cyclop Modes of exo K_nC_{80}

N	L=1	L=2	L=3	L=4	L=5	L=6	L=7
0	242.2	380.6	524.4	671.0	805.1	924.0	1025.7
	243.8	381.0	529.9	671.0	805.2	924.8	1027.2
1	244.2	381.1	526.7	671.4	805.8	924.7	1027.0
	245.3	381.3	528.7	671.6	805.8	925.7	1027.8
2	246.7	381.5	527.1	671.4	805.8	924.4	1027.2
	248.0	381.6	528.5	671.8	805.9	926.0	1027.7
3	248.4	380.1	524.1	671.0	805.2	923.6	1025.2
	257.6	381.7	531.5	671.7	805.3	925.0	1027.4
4	258.5	380.7	526.1	668.2	803.9	923.2	1024.5
	265.6	383.8	529.9	673.9	805.4	923.6	1025.7
5	267.9	379.1	528.7	669.9	801.0	921.1	1022.7
	282.7	390.5	528.9	671.5	805.1	922.4	1023.1
6	232.6	381.2	522.6	669.6	800.2	917.3	1019.9
	244.6	396.0	534.3	670.3	801.1	917.4	1021.6
7	286.8	382.2	524.4	668.7	801.8	916.8	1015.0
	295.1	383.5	529.8	669.9	802.1	922.6	1020.2
8		381.0	520.5	669.0	799.3	915.1	1013.9
		400.8	539.1	671.2	800.9	915.6	1015.7
9	269.2	387.0	511.7	667.2	797.9	911.4	1009.8
	276.3	392.5	544.3	673.9	798.6	912.7	1012.3
10	273.8	381.0	510.2	661.8	792.8	906.7	1005.0
	283.7	403.0	544.8	674.6	796.1	909.4	1007.0

- Frequency in CM^{-1}.

Table 4.5: Shearing Modes of exo K_nC_{80}

N	L=1	L=2	L=3	L=4	L=5	L=6	L=7	L=8	L=9	L=10
0	113.3	222.9	333.2	442.1	548.7	651.8	749.5	838.3	908.5	938.5
	112.0	222.9	333.3	442.1	548.8	651.7	749.6	838.3	908.6	
1	111.1	222.7	332.9	441.8	548.2	651.4	749.2	837.9	908.5	938.5
	112.0	222.9	333.0	441.9	548.4	651.4	749.2	838.0	908.5	
2	111.0	222.5	333.0	441.8	548.2	651.4	749.1	837.9	908.4	938.6
	112.3	223.1	333.0	442.0	548.4	651.4	749.2	838.0	908.5	
3	112.2	223.0	332.7	441.4	547.9	650.7	748.6	837.4	908.2	938.4
	112.8	223.1	333.7	441.5	548.1	651.3	748.8	837.6	908.3	
4	113.1	223.2	332.8	441.2	547.7	650.9	748.4	837.2	908.0	938.5
	113.8	223.6	333.2	442.4	548.3	651.1	748.8	837.5	908.2	
5	114.8	223.9	333.1	443.2	547.0	650.8	748.3	837.1	907.8	
	115.0	224.0	333.1	443.6	549.2	651.3	748.6	837.2	908.1	
6	113.9	222.8	332.3	440.7	547.2	649.6	747.6	836.3	907.3	937.8
	115.1	223.9	333.1	442.5	547.8	651.4	748.0	836.7	907.4	
7	115.6	223.7	331.7	441.4	547.2	650.2	746.5	835.8	906.7	937.9
	116.5	224.4	333.3	442.5	548.6	652.9	748.3	836.3	907.4	
8	115.8	222.5	331.0	432.4	545.9		746.1	834.4	906.1	
	116.5	223.8	332.0	434.8	548.2		746.7	835.6	906.7	
9	112.6	222.4	331.1	431.7	547.5	644.4	744.9	833.2	905.3	
	114.3	222.8	331.5	435.9	547.7	644.8	746.0	834.1	906.1	
10	111.0	221.6	328.7	433.3	547.7	647.7	743.1	832.4	903.9	
	116.8	222.6	329.9	434.8	548.5		744.8	832.9	904.7	

- Frequency in CM^{-1}.

Table 4.6: Uniform Radial Compressing and Stretching Along Tube Axis

N	Radial Compression	Stretching Mode 1	Stretching Mode 2
0	185.7	1127.3	1127.3
1	188.2	1126.2	1126.3
2	192.7	1126.1	1126.3
3	184.6	1124.3	1124.5
4	194.0	1123.6	1124.0
5	202.5	1122.2	1123.5
6	210.6	1121.4	1122.0
7	220.8	1118.8	1119.7
8	233.2	1115.1	1116.1
9	236.2	1110.4	1113.5
10	248.8	1106.4	

- Frequency in CM^{-1}.

Chapter 5 Development of Adiabatic Force Field for Polyvinyl Chloride (PVC) and Chlorinated PVC (CPVC)

5.1 Introduction

Chlorinated polyvinyl chloride has become an important specialty polymer due to its high glass transition temperature, high heat distortion temperature, outstanding mechanical, dielectric, and flame and smoke properties, chemical inertness, and low sensitivity to hydrocarbon costs. However, the mechanism through which the various desired and undesired properties are resulted from is not fully understood. Hopefully, simulation at the atomistic level could lead us to a better understanding of those mechanisms. Currently, direct *ab initio* calculations for polymer systems are not practical. Thus calculations with classical force fields, which are parameterized based on either experimental results or *ab initio* calculations on smaller model systems, are the method of choice. As a first step towards the understanding of CPVC, we developed the adiabatic quantum force field that accurately described the rotational energy surface of the polymer backbone chains.

For amorphous polymers, the distribution of backbone conformations and the rates of conformational transitions have a strong effect on their properties, such as moduli, glass temperature, dielectric constant, and diffusivity of small molecules. It is critical that the FF leads to the correct relative energies of the minima, e.g., *trans* versus *gauche*, and of the barrier heights between them. Thus torsional FF parameters are particularly important for describing amorphous polymers. In many cases, the existence of the molecule in other local minima can be detected, but energies for

these states cannot be reliably obtained from experiments. In addition, the barriers between the local minima can also not be obtained reliably from the experimental data alone.

To circumvent these problems, we use *ab initio* calculations to provide the torsional potential energy surface. With the 6-31G** basis set, the torsional potentials calculated from Hartree-Fock (HF) wavefunctions are adequate. The HF calculations lead to a total torsional potential function $E^{HF}(\phi)$. The classical force field can be fitted to reproduce the quantum energy surface.

$$E^{HF}(\phi) \simeq E^{FF}(\phi) \tag{5.1}$$

In determining $E^{FF}(\phi)$, the usual and simplest approach would be to determine the non-adiabatic surface by fixing all bonds and angles so that only the torsional angle ϕ changes. However, such rigid rotations about backbonds sometimes lead to unfavorable contacts with very short distances between nonbonded atoms. The *ab initio* wavefunction readjusts the molecular orbitals to minimize repulsion, but the functional forms of nonbond interactions in force field representation may not accurately describe the inner repulsive wall and often leads to much higher rotational barriers. In order to accurately describe the rotational energy surface, we calculated adiabatic rotational energy surface of molecules with five backbone carbons. These molecules are used to mimick the corresponding polymer chains. The HF wavefunction was calculated by fixing the dihedrals of interest (in increments of 30^o) and optimizing all other degrees of freedom. These calculations lead to the 2D energy surfaces. Torsional parameters were fitted iteratively so that the force field adiabatic energy surface matchs to *ab initio* adiabatic energy surface.

5.2 The Molecular Simulation Force Field (MSFF)

The force field is taken to be of the form

$$E_{total} = E_{val} + E_{nb}. \tag{5.2}$$

The valence part includes bond interactions, angle interactions, and torsion interactions, as

$$E_{val} = E_{bond} + E_{angle} + E_{torsion}. \tag{5.3}$$

The nonbond part has van der Waals interaction and Coulomb interaction.

$$E_{nb} = E_{vdw} + E_Q \tag{5.4}$$

The torsion terms involve sums of cosine torsional angles such as

$$E_{torsion}(\phi) = \sum_{m=0}^{12} C_m \cos m\phi. \tag{5.5}$$

The nonbond terms have the form of

$$E_Q = \frac{1}{2} \sum_{i \neq j} \frac{q_i q_j}{R_{ij}} \tag{5.6}$$

for electrostatic, and

$$E_{vdw} = \frac{1}{2} \sum_{i \neq j} D_e(\rho_{ij}^{-12} - 2\rho_{ij}^{-6}) \tag{5.7}$$

for van der Waals, where $\rho_{ij} = R_{ij}/R_e$.

Chain conformation and inter-chain interactions are the dominating factors for amorphous polymers. We'll focus on accurate description of charges and torsional potentials. The forms and parameters of E_{bond}, E_{angle}, and E_{vdw} are taken directly

from DREIDING.

The charges and torsional parameters are based on *ab initio* calculations of clusters with five-backbone carbon atoms.

5.2.1 Charges

In order to determine the proper charges, we did *ab initio* calculation for various conformations of clusters with five-backbone carbon atoms:

$$H_3C - CXY - CHH - CXY - CH_3 \tag{5.8}$$

where X and Y are Cl or H, depending on the form of the actual chloro-polymers. For PVC, $X = Cl$ and $Y = H$, and for PVDC, $X = Cl$ and $Y = Cl$. Hartree-Fock (HF) wavefunction with the 6-31G** basis set is used. We considered the following three methods of assigning atomic charges in the chain molecules.

- Potential derived charge (PDQ). The charge density from the HF wave function is used to calculate the potential energy over a numerical grid surrounding the molecule and a set of point charges on the atoms is optimized to fit the potential. We carried out these calculation with PSGVB using a grid of 1000 points outside the van der Waals radii (taken as $R_C = 1.949$ (Å), $R_H = 1.597$ (Å), $R_{Cl} = 1.958$ (Å), and $R_F = 1.739$ (Å)).

- Mulliken charges (Mull). The molecular orbital (MO) coefficients are used to estimate a set of atomic charges where overlap terms are assigned equally to each of the two atoms.

- Charge Equilibration (QEq). The charges of molecules are predicted based on electron affinity (EA) and ionization energy (IE).

Since the atomic charges vary with the change of molecular conformation, the best description of Coulomb interactions in dynamics simulations should be such, that the

atomic charges vary with conformation change. However, for amorphous polymer simulations, which require longer chains, assigning charges at every dynamics integration is simply unrealistic. We have to find a way to best balance various conformations, while compensating the errors made in charge assignment in the torsional force field. We based the charges on PDQ while considering symmetry property of the clusters.

5.2.2 Torsional Potential

We can write

$$E^{hf}(\phi_1, \phi_2) = E^{ff}(\phi_1, \phi_2) + E^{cor}(\phi_1, \phi_2) \tag{5.9}$$

where (ϕ_1, ϕ_2) are the two C–C–C–C backbone torsion angles as in Fig (5.1). $E^{hf}(\phi_1, \phi_2)$ is *ab initio* energy, $E^{ff}(\phi_1, \phi_2)$ is force field energy, and $E^{cor}(\phi_1, \phi_2)$ is the correction with which the old force field should be improved. $E^{ff}(\phi_1, \phi_2)$ is calculated by minimizing the structures while (ϕ_1, ϕ_2) are constraint, so that the adiabatic 2D (ϕ_1, ϕ_2) rotational energy surface of optimized force field can match that of *ab initio* computation well.

In order to get accurate adiabatic potentials, we generated 12×12 2D energy surfaces through quantum computation, i.e., constraint the two torsional angles while full Hartree-Fock optimizations were performed. We also used fully optimized structures of all the local minimums. The 2-D torsional potential surfaces were represented by regular grids which are interpolated from the 12×12 points and all of the local minimum points. The C_m in Eq. 5.5 are least-square-fitted to minimize $E^{cor}(\phi_1, \phi_2)$. Many iterations are performed until the changes of C_m are insignificant.

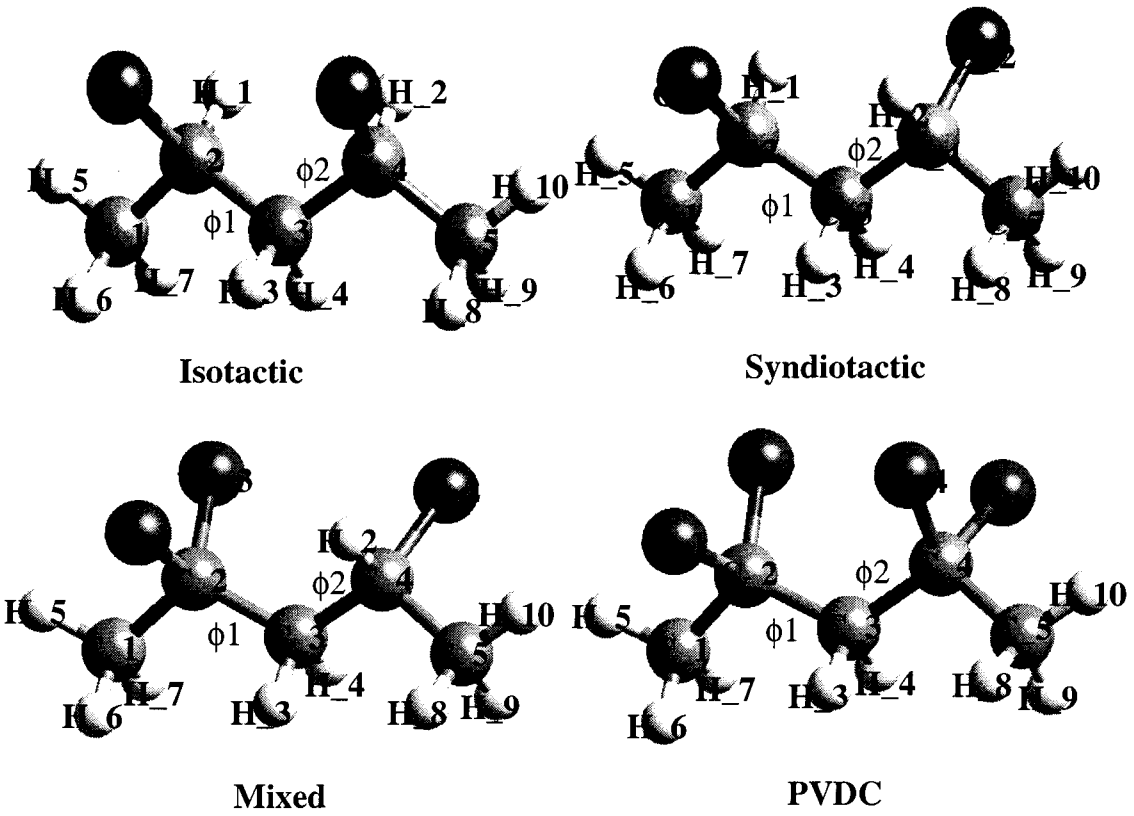

Figure 5.1: Chlorinated clusters used in the calculations

5.3 Quantum Mechanical Adiabatic 2D Rotational Energy Surface and Forece Field Parameters

For PVC, both syndiotactic and isotactic, we use $CH_3CHClCH_2CHClCH_3$ to represent longer chain polymer, as shown in Fig. 5.1a and Fig. 5.1b. For CPVC of -$(CCl_2CH_2CHClCH_2)_n$-, we use $CH_3CCl_2CH_2CHClCH_3$, as in Fig. 5.1c. For PVDC, -(CCl_2CH_2)-, molecule of $CH_3CCl_2CH_2CCl_2CH_3$ is used as in Fig. 5.1d. Figure 5.2 shows the atomic charges assigned to these clusters.

Denote dihedral angle Cl–C_3x–C_3–C_3x as ϕ. For C_3x, if $\phi > 0$, we use atomic type (label) C_3R, while if $\phi < 0$, we use atomic type (label) C_3L. C_32 is used for backbone carbon atoms bonded to two Cl atoms, and C_3 is used for backbone

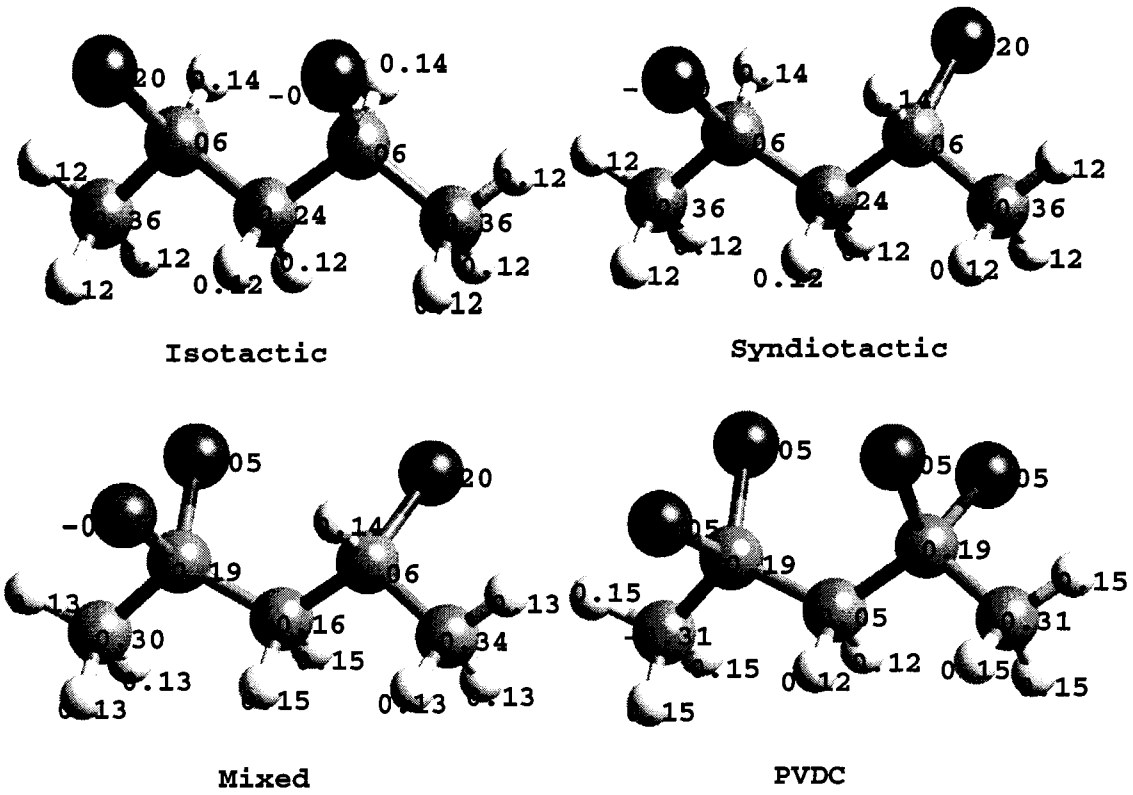

Figure 5.2: Atomic charges of the chlorinated clusters

carbon atoms that are not bonded to any Cl atoms. By doing so, we can use iPVC torsion parameters for C_3–C_3L–C_3–C_3L, or C_3–C_3R–C_3–C_3R, and sPVC torsion parameters for C_3–C_3R–C_3–C_3L. PVDC segments and mixed segments are obvious. All other torsion parameters are default DREIDII parameters ($C_0 = 1.0000$, $C_3 = 1.0000$, and the rest are $C_m = 0$). They are listed in Table 5.1. The optimized torsion parameters are listed in Table 5.2.

Table 5.1: DREIDING Parameters

LJ 12–6 van der Waals			Simple Harmonic Bond		
Atom	R_0[a]	D_0[b]	Bond	K_{bond}[c]	R_0[a]
H	3.1950	0.0152	C–C	699.5920	1.514
C	3.8983	0.0951	C–H	659.7507	1.111
Cl	3.9503	0.2833	C–Cl	510.4743	1.801

Simple Harmonic Cosine Angle					
Angle	K_{angle}[d]	θ_0[e]	Angle	K_{angle}[d]	θ_0[e]
H–C–H	75.2779	109.4710	C–C–C	214.2065	109.4710
H–C–C	117.2321	109.4710	Cl–C–C	197.7159	109.4710
H–C–Cl	99.2533	109.4710	Cl–C–Cl	191.9793	109.4710

[a] $\mathring{A}$; [b] $Kcal/Mol$; [c] $Kcal/Mol/\mathring{A}^2$; [d] $Kcal/Mol/Degree^2$, [e] $degree$.

Table 5.2: Optimized DREIDING Torsion Parameters for PVC

LLL-CCC-CCC-RRR	v_1	v_2	v_3	v_4	v_5	v_6
Isotactic Polyvinyl Chloride (iPVC)						
C_3-C_31-C_3-C_31	-19.021	-8.5939	21.2379	1.9153	-1.3116	3.8905
Cl-C_31-C_3-C_31	-9.3167	-6.6164	-27.937	3.6748	-1.5746	-4.5182
Syndiotactic Polyvinyl Chloride (sPVC)						
C_3-C_31-C_3-C_31	-15.263	-7.8935	-0.8143	1.7958	-5.1511	-0.1850
Cl-C_31-C_3-C_31	-8.9259	-4.5495	-4.4370	5.0627	-5.2440	-1.1746
Polyvinylidene Chloride (PVDC)						
C_3-C_32-C_3-C_32	-166.83	-107.80	-34.733	20.7666	7.9938	-0.7472
Cl-C_32-C_3-C_32	-156.64	-112.12	6.8933	16.2328	19.6499	1.9258
PVC-PVDC						
C_3-C_31-C_3-C_32	-19.193	-12.804	16.4478	-1.9437	-1.0113	-17.410
C_31-C_3-C_32-C_3	0.3342	-162.19	-5.0429	8.4211	25.9489	-9.0685
Cl-C_31-C_3-C_32	-8.0484	-9.8507	-26.899	1.1705	3.9923	19.0126
Cl-C_32-C_3-C_31	7.8963	-167.00	-7.6044	2.5645	37.3312	0.2991

- C_32 is C atom bonded to two Cl atoms, C_31 is C atom bonded to one Cl atom, while C_3 is C atom without Cl atom bonded to. The unit is (kcal/mol).

5.3.1 Isotactic Polyvinyl Chloride

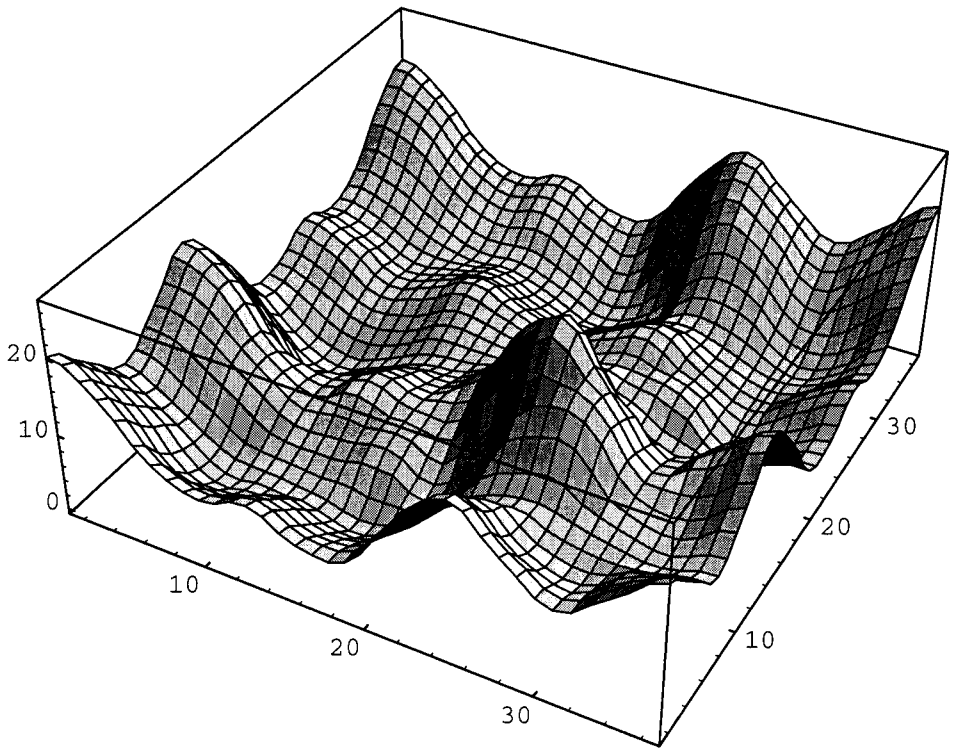

Figure 5.3: 3D plot of the adiabatic 2D-rotation energy surface. The unit of the two torsion angles is in 10^o, while the unit of energy(z-axis) is in kcal/mol

Based on the reflection symmetry of the molecule, we can obtain the whole energy surface by reflecting half of the ϕ_1–ϕ_2 space, as shown in Fig. 5.3. The grid points are generated at interval of 30^o, total of 12×12 grid points. Considering the reflection symmetry and rotational symmetry of two torsion angles, we have 76 independent grid points. For each of the 76 points, as first step approximation, we optimize the structure by using DREIDII force field with the two torsion angles fixed. This gives us a better starting point for quantum optimization that is quite expensive computationally. Then we perform quantum mechanical structural minimization,

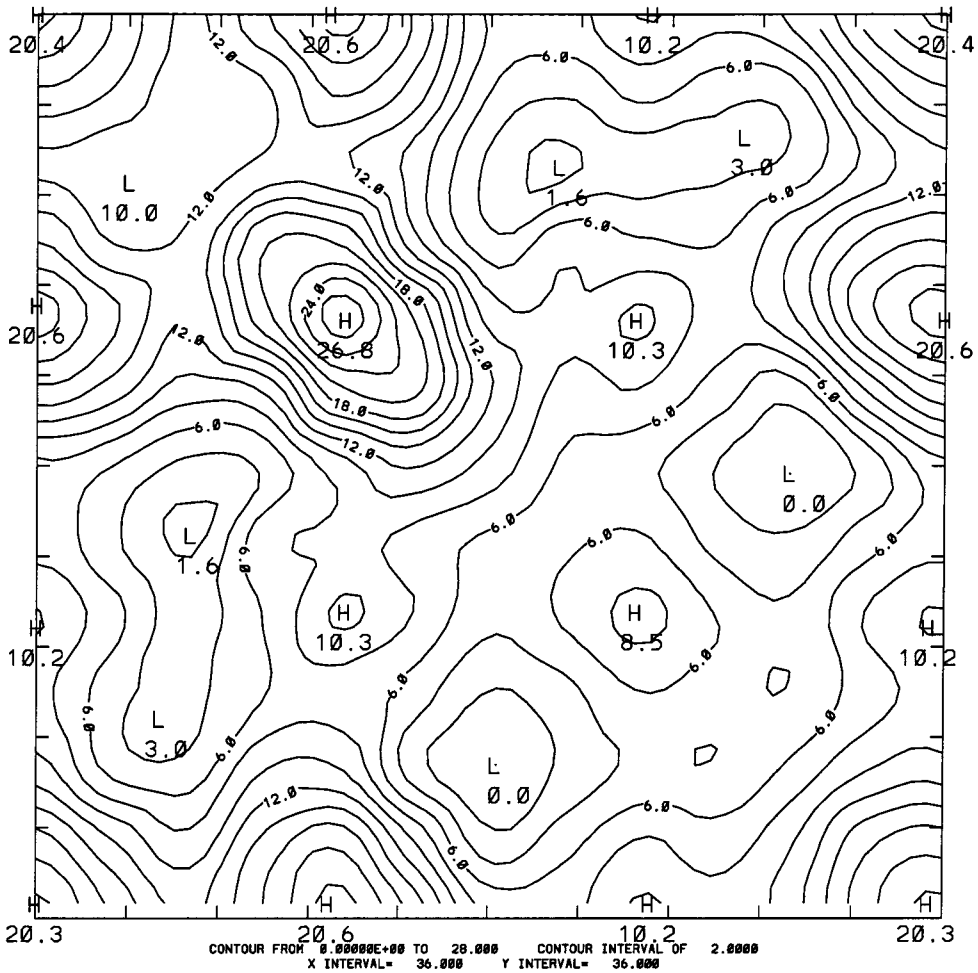

Figure 5.4: Quantum adiabatic 2D rotational surface for iPVC

keeping the two backbone torsions fixed. By plotting the whole energy surface, we can extract 6 local minimum grid poins. Starting from those points, we optimized the whole structures, including the backbone torsion angles. Quantum adiabatic energy surface is interpolated based on 76 grid points and the 6 local minimum points. By doing so, we can capture both the rotational barriers and minimum energies of local minimums. Figure 5.3 is the 3D plot of the energy surface, while Fig. 5.4 is 2D contour plot.

Based on the procedure outlined in Section 2, we calculated the torsional parameters. Figure 5.5 is the contour map of force field adiabatic 2D rotational energy surface. They are in good agreement with the *ab initio* results. The torsion param-

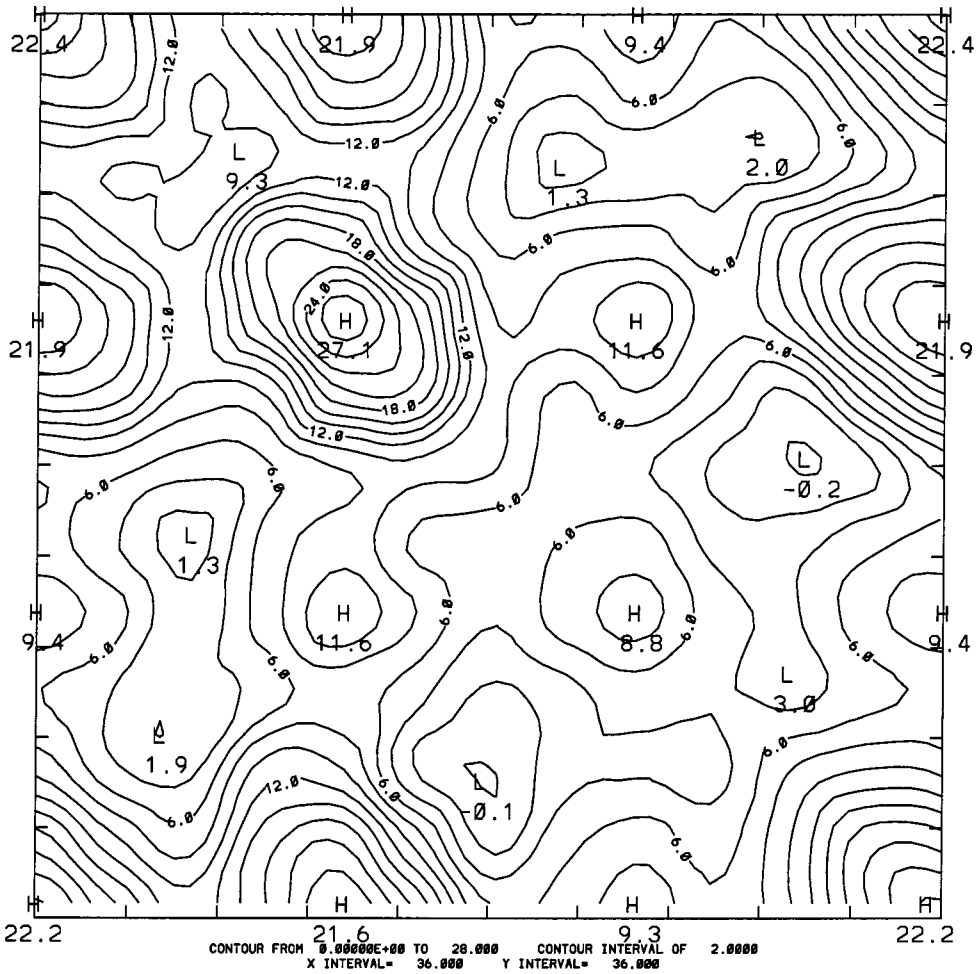

Figure 5.5: Force field adiabatic 2D rotational surface for iPVC

eters are in Table 5.2. The comparisons of quantum and force field energy at each gird point are tabulated in Table 5.3, while comparison of local minimums are in Table 5.4.

Since *ab initio* constraint structure minimization are very expensive, most of researchers calculate quantum energy based on generic force field generated grid points. For 28 grid points(interval of 30^o), we used DREIDII force field minimized the structures while keeping the two backbone torsion angles fixed. For each of those structures, we did one energy quantum calculation. Figure 5.6 is the 2D contour map based on those grid points. The energies are tabulated in Table 5.5 By focusing on the relative energy differences of local minimums and the energy barrieres between

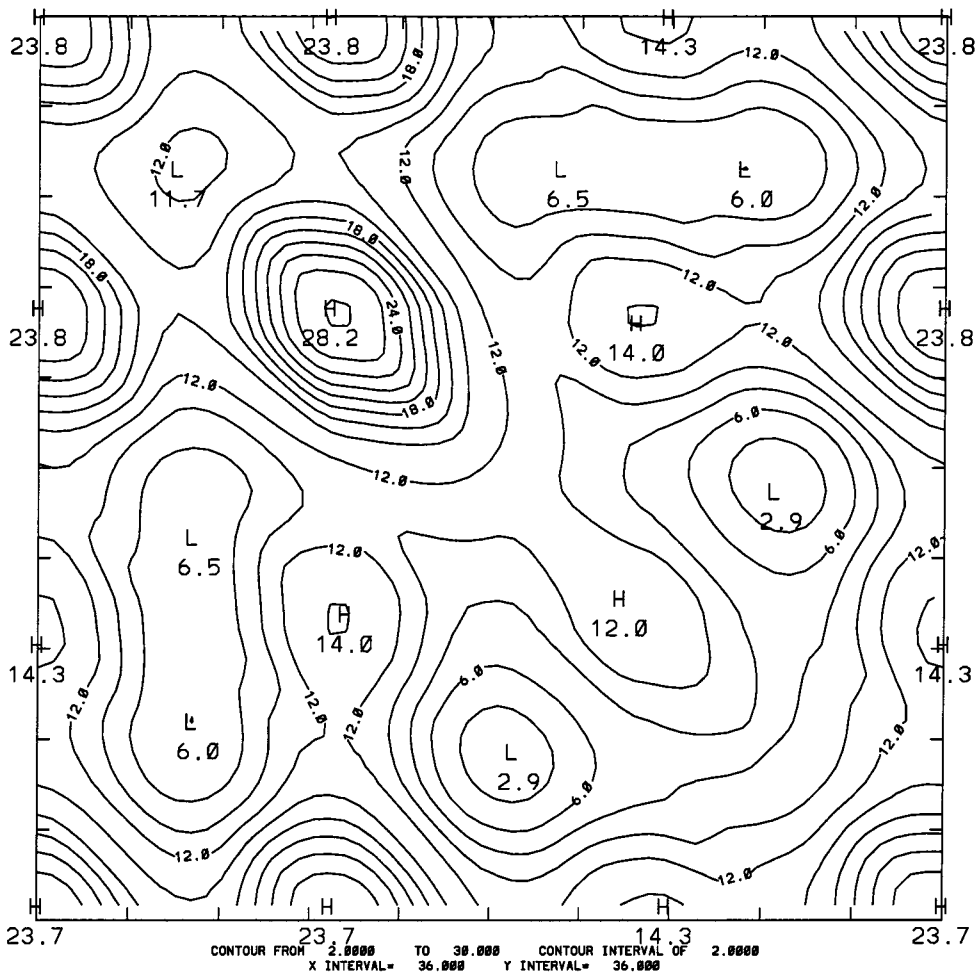

Figure 5.6: One energy quantum calculation of DREIDII adiabatic 2D rotational grids for iPVC

those local minimums, we found the adiabatic quantum rotational energy surface is quite different from the quantum one energy energy surface and the fitted force field energy surface is a very good approximation of the quantum adiabatic energy surface. In molecular dynamics simulations, by using these force fields, we can generate ensembles with the right distribution of thermodynamic density of states and rates of kinetic conformation. These are the general goals of molecular dynamics simulation of amorphous polymer materials.

Table 5.3: Adiabatic QM and FF Energy of iPVC(Kcal/Mol)

Φ_1	Φ_2	QM	FF	Error	Φ_1	Φ_2	QM	FF	Error
30.0	0.0	15.8089	16.9259	-1.1170	120.0	180.0	9.1569	8.2367	0.9202
30.0	30.0	12.2587	10.8467	1.4120	120.0	-150.0	19.5968	19.8119	-0.2151
30.0	60.0	5.3535	4.3767	0.9768	120.0	-120.0	26.8733	27.0582	-0.1849
30.0	90.0	4.8567	3.9588	0.8979	150.0	0.0	15.4643	16.3578	-0.8935
30.0	120.0	6.6466	6.7368	-0.0902	150.0	30.0	10.2474	9.6961	0.5513
30.0	150.0	4.3697	4.2364	0.1333	150.0	60.0	2.9813	2.0368	0.9445
30.0	180.0	5.9952	6.9245	-0.9293	150.0	90.0	5.1055	4.7895	0.3160
30.0	-150.0	12.9656	15.2384	-2.2728	150.0	120.0	7.8812	8.0285	-0.1473
30.0	-120.0	16.3430	17.5058	-1.1628	150.0	150.0	7.3360	5.7343	1.6017
30.0	-90.0	11.7884	12.1166	-0.3282	150.0	180.0	12.1163	9.4241	2.6922
30.0	-60.0	10.2324	10.0156	0.2168	150.0	-150.0	20.3957	19.4888	0.9069
30.0	-30.0	13.8897	16.6105	-2.7208	-180.0	0.0	7.5741	6.6472	0.9269
60.0	0.0	11.7238	11.1711	0.5527	-180.0	30.0	2.8616	1.5604	1.3012
60.0	30.0	8.6727	7.1191	1.5536	180.0	60.0	-0.0022	-0.0358	0.0336
60.0	60.0	4.6264	3.3410	1.2854	-180.0	90.0	1.9730	1.6901	0.2829
60.0	90.0	3.5980	2.9226	0.6754	-180.0	120.0	4.5211	4.1976	0.3235
60.0	120.0	3.0753	2.5728	0.5025	180.0	150.0	5.5894	4.4283	1.1611
60.0	150.0	1.6799	1.2631	0.4168	-180.0	180.0	9.2475	8.2669	0.9806
60.0	180.0	3.5127	4.9334	-1.4207	-150.0	0.0	7.2965	6.5904	0.7061
60.0	-150.0	8.9573	9.6582	-0.7009	-150.0	30.0	5.1871	5.3257	-0.1386
60.0	-120.0	12.2733	11.3416	0.9317	-150.0	60.0	2.3515	3.2187	-0.8672
60.0	-90.0	12.4939	9.8360	2.6579	-150.0	90.0	3.3844	3.2679	0.1165
60.0	-60.0	10.8743	10.0077	0.8666	-150.0	120.0	6.2348	6.8345	-0.5997
90.0	0.0	15.8782	15.6215	0.2567	-150.0	150.0	5.7531	6.1719	-0.4188
90.0	30.0	14.4794	14.9324	-0.4530	-120.0	0.0	10.1112	9.3951	0.7161
90.0	60.0	9.7829	10.6419	-0.8590	-120.0	30.0	8.1835	7.2439	0.9396
90.0	90.0	5.8841	4.8120	1.0721	-120.0	60.0	4.3682	3.8054	0.5628
90.0	120.0	6.1094	6.8685	-0.7591	-120.0	90.0	5.9861	5.0890	0.8971
90.0	150.0	7.1577	6.5007	0.6570	-120.0	120.0	8.5262	8.6714	-0.1452
90.0	180.0	4.5196	5.7023	-1.1827	-90.0	0.0	8.4273	6.0696	2.3577
90.0	-150.0	10.3909	10.4891	-0.0982	-90.0	30.0	6.9850	5.2317	1.7533
90.0	-120.0	19.4740	18.8056	0.6684	-90.0	60.0	4.0977	3.2817	0.8160
90.0	-90.0	19.7082	19.1725	0.5357	-90.0	90.0	4.9734	4.2445	0.7289
120.0	0.0	20.6485	21.8841	-1.2356	-60.0	0.0	10.7522	9.3181	1.4341
120.0	30.0	17.5388	18.0534	-0.5146	-60.0	30.0	9.7813	9.9098	-0.1285
120.0	60.0	9.9411	10.1102	-0.1691	-60.0	60.0	6.3744	7.8857	-1.5113
120.0	90.0	7.2198	6.9026	0.3172	-30.0	0.0	17.0207	17.2469	-0.2262
120.0	120.0	10.1880	11.5163	-1.3283	-30.0	30.0	15.4823	17.1395	-1.6572
120.0	150.0	8.3365	9.0547	-0.7182	0.0	0.0	20.3605	22.4211	-2.0606

Table 5.4: QM and FF Local Minimums of iPVC(Kcal/Mole)

Φ_1	Φ_2	QM	FF	Error	Φ_1	Φ_2	QM	FF	Error
44.9	73.7	3.1331	2.0201	1.1130	56.7	154.1	1.6149	1.3076	0.3073
52.8	-52.8	10.4863	10.8417	-0.3554	-179.5	60.8	0.0000	0.0000	0.0000
-155.9	156.7	5.4815	5.4049	0.0766	-79.2	79.5	4.3209	4.7272	-0.4063

Table 5.5: QM Energy of FF Grids for iPVC(Kcal/Mol)

Φ_1	Φ_2	QM	Φ_1	Φ_2	QM
0.00	0.00	23.8185	120.00	60.00	12.7771
0.00	60.00	13.4073	120.00	120.00	14.0325
0.00	120.00	14.2352	120.00	180.00	11.6897
0.00	180.00	11.8722	120.00	240.00	28.1188
0.00	240.00	23.7898	180.00	0.00	11.8706
0.00	300.00	14.4002	180.00	60.00	3.2899
0.00	360.00	23.8185	180.00	120.00	7.5693
60.00	0.00	14.3980	180.00	180.00	11.8400
60.00	60.00	6.7944	240.00	0.00	14.2382
60.00	120.00	6.6391	240.00	60.00	7.1715
60.00	180.00	7.4092	240.00	120.00	11.8510
60.00	240.00	14.0671	300.00	0.00	13.4102
60.00	300.00	11.7026	300.00	60.00	8.6857
120.00	0.00	23.7916	360.00	0.00	23.8185

5.3.2 Syndiotactic Polyvinyl Chloride

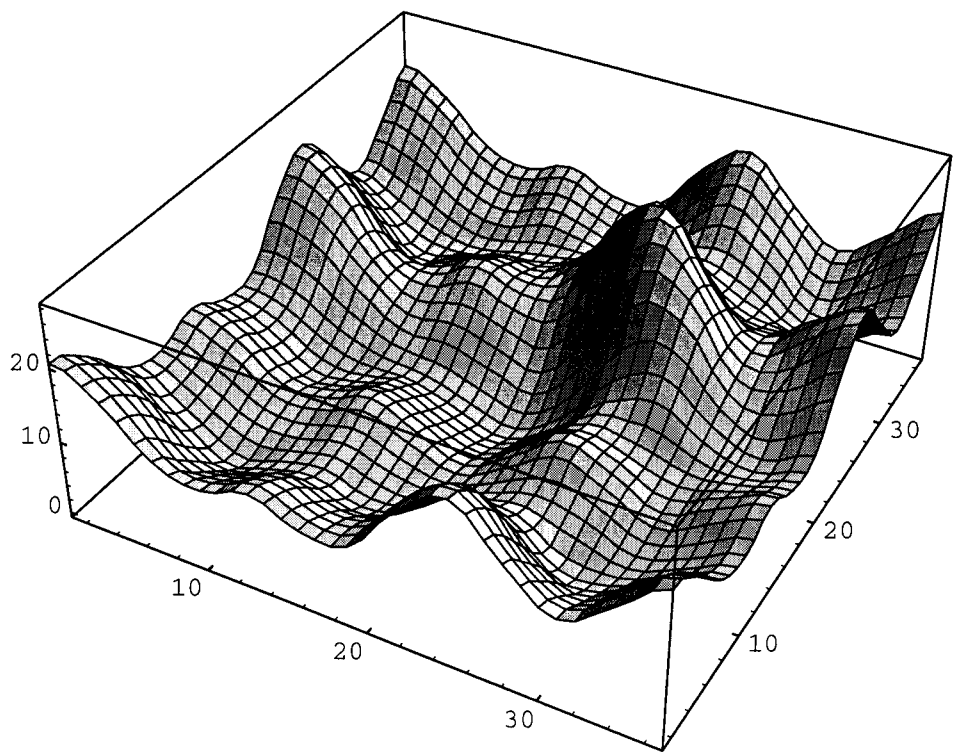

Figure 5.7: 3D plot of adiabatic 2D rotational surface for sPVC, z-axis is the energy with unit kcal/mol. x-axis and y-axis correspond to the two backbone dihedral angles with unit 10^o

Similar to iPVC, there is also a reflection plane on the 2D rotational space for sPVC. The reflection axis is perpendicular to that of iPVC. 76 grid points are required for an angle increment of 30^o. The 3D plot of quantum adiabatic rotational energy surface is in Fig. 5.7, while the 2D contour map is in Fig. 5.8. Figure 5.9 is the 2D contour map of adiabatic rotational energy surface, base on optimized force field. The quantum and force field energies at the grid points are tabulated in Table 5.6, and those of the six local minimums are in Table 5.7. As a comparison, we calculated the quantum one energy on force field generated grids. The 2D contour map is in

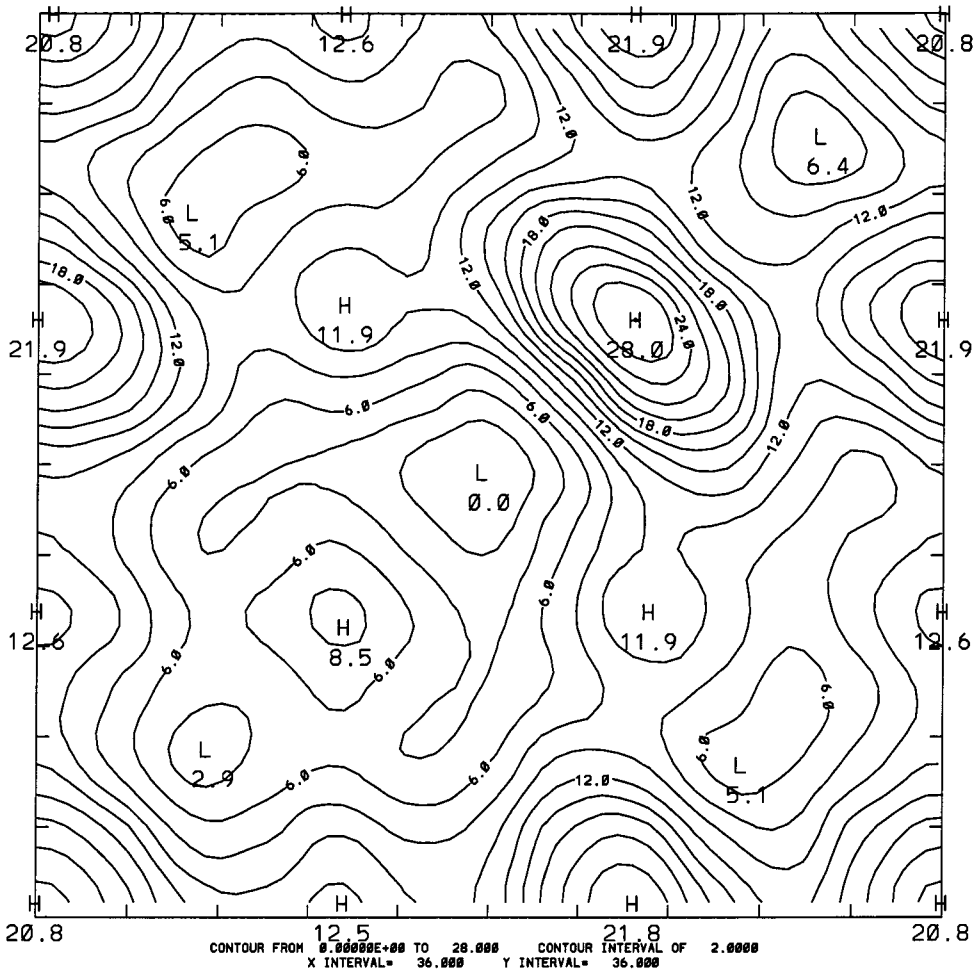

Figure 5.8: Quantum adiabatic 2D rotational surface for sPVC

Fig. 5.10. The energies are tabulated in Table [5.8].

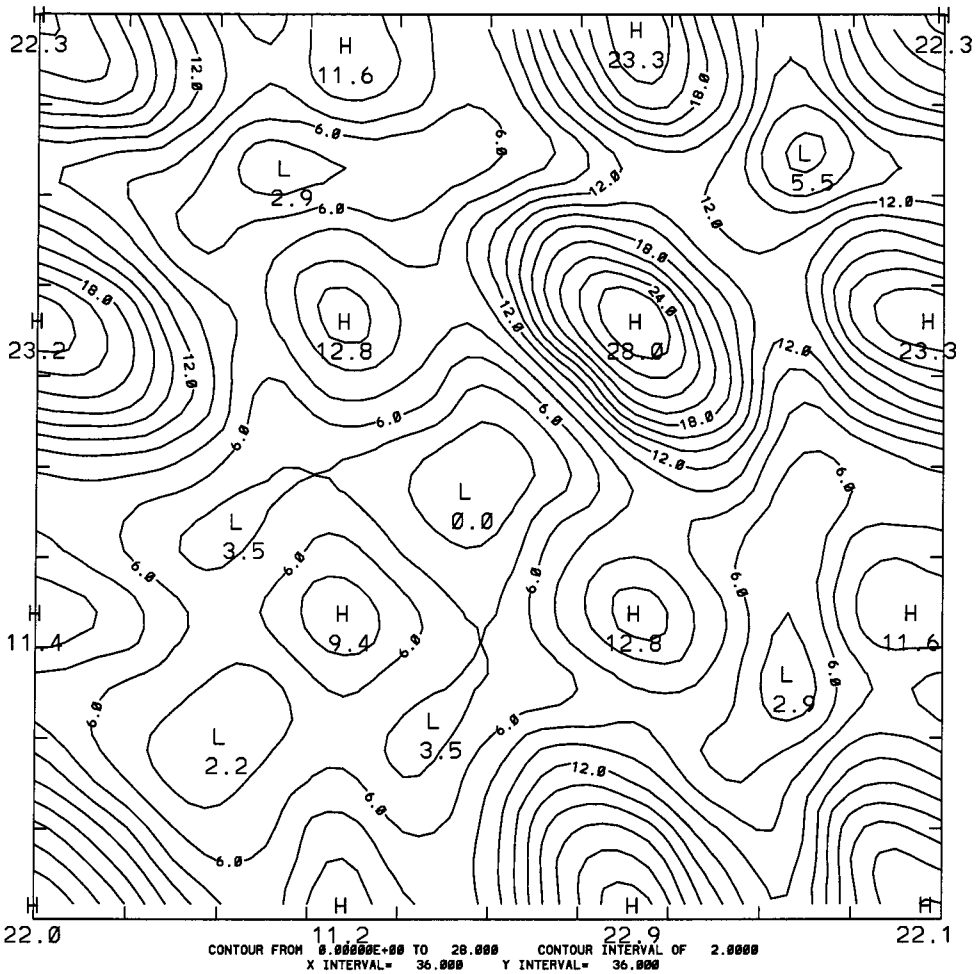

Figure 5.9: Force field adiabatic 2D rotational surface for sPVC

Table 5.6: Adiabatic QM and FF Energy of sPVC(Kcal/Mol)

Φ_1	Φ_2	QM	FF	Error	Φ_1	Φ_2	QM	FF	Error
0.0	0.0	20.7512	22.2526	-1.5014	-120.0	90.0	8.7270	7.8848	0.8422
30.0	0.0	17.7018	17.9686	-0.2668	-120.0	120.0	11.7605	12.7938	-1.0333
30.0	30.0	14.5433	12.7143	1.8290	-120.0	150.0	9.9155	9.4261	0.4894
60.0	0.0	12.1369	11.0654	1.0715	-120.0	180.0	11.6682	9.5211	2.1471
60.0	30.0	7.8451	6.2442	1.6009	-120.0	-150.0	22.8654	21.9387	0.9267
60.0	60.0	3.0885	2.3345	0.7540	-120.0	-120.0	27.8581	27.7586	0.0995
90.0	0.0	10.5627	7.4305	3.1322	-90.0	0.0	16.0561	15.3750	0.6811
90.0	30.0	7.9213	5.8571	2.0642	-90.0	30.0	11.2363	11.2502	-0.0139
90.0	60.0	4.6914	4.1180	0.5734	-90.0	60.0	5.5801	5.9376	-0.3575
90.0	90.0	4.7283	3.2885	1.4398	-90.0	90.0	7.5104	7.1264	0.3840
120.0	0.0	12.5809	11.3823	1.1986	-90.0	120.0	9.6502	8.6833	0.9669
120.0	30.0	10.3198	9.5264	0.7934	-90.0	150.0	9.4032	6.9806	2.4226
120.0	60.0	6.0037	6.0117	-0.0080	-90.0	180.0	14.5115	11.9499	2.5616
120.0	90.0	6.3292	6.0386	0.2906	-90.0	-150.0	20.9291	19.4929	1.4362
120.0	120.0	8.5405	9.4207	-0.8802	-90.0	-120.0	19.2815	17.7766	1.5049
150.0	0.0	10.1142	8.2782	1.8360	-90.0	-90.0	12.2225	12.5022	-0.2797
150.0	30.0	8.0092	6.2557	1.7535	-60.0	0.0	11.4476	10.2491	1.1985
150.0	60.0	4.1812	3.7861	0.3951	-60.0	30.0	8.7952	9.0983	-0.3031
150.0	90.0	4.5879	4.3093	0.2786	-60.0	60.0	5.9185	7.2621	-1.3436
150.0	120.0	5.8998	6.2568	-0.3570	-60.0	90.0	5.1630	2.9834	2.1796
150.0	150.0	3.2461	3.1074	0.1387	-60.0	120.0	6.5757	3.9887	2.5870
180.0	0.0	10.4632	8.3690	2.0942	-60.0	150.0	7.6877	4.5708	3.1169
180.0	30.0	9.5698	8.8535	0.7163	-60.0	180.0	10.0187	5.9194	4.0993
180.0	60.0	6.1067	7.2761	-1.1694	-60.0	-150.0	12.4385	8.7992	3.6393
180.0	90.0	4.1773	4.2475	-0.0702	-60.0	-120.0	13.4105	12.6881	0.7224
180.0	120.0	3.5704	3.9085	-0.3381	-60.0	-90.0	11.0617	12.0989	-1.0372
180.0	150.0	1.6332	2.0600	-0.4268	-60.0	-60.0	7.3634	5.8632	1.5002
180.0	180.0	0.2216	0.3691	-0.1475	-30.0	0.0	15.7345	18.5026	-2.7681
-150.0	0.0	17.7869	18.0511	-0.2642	-30.0	30.0	14.2055	18.9437	-4.7382
-150.0	30.0	16.2873	17.9934	-1.7061	-30.0	60.0	9.3602	12.5579	-3.1977
-150.0	60.0	10.8166	12.3405	-1.5239	-30.0	90.0	7.5116	7.8856	-0.3740
-150.0	90.0	6.5821	5.6859	0.8962	-30.0	120.0	9.6724	10.5458	-0.8734
-150.0	120.0	7.2955	8.4953	-1.1998	-30.0	150.0	8.4496	8.8431	-0.3935
-150.0	150.0	5.7584	7.0988	-1.3404	-30.0	180.0	7.5589	6.5552	1.0037
-150.0	180.0	4.3716	3.7380	0.6336	-30.0	-150.0	12.9275	13.9545	-1.0270
-150.0	-150.0	11.6940	10.0056	1.6884	-30.0	-120.0	17.9070	21.5364	-3.6294
-120.0	0.0	21.8825	23.1340	-1.2515	-30.0	-90.0	14.0468	16.7854	-2.7386
-120.0	30.0	18.1823	18.8285	-0.6462	-30.0	-60.0	8.1658	8.9191	-0.7533
-120.0	60.0	10.3347	10.5278	-0.1931	-30.0	-30.0	11.4063	14.9270	-3.5207

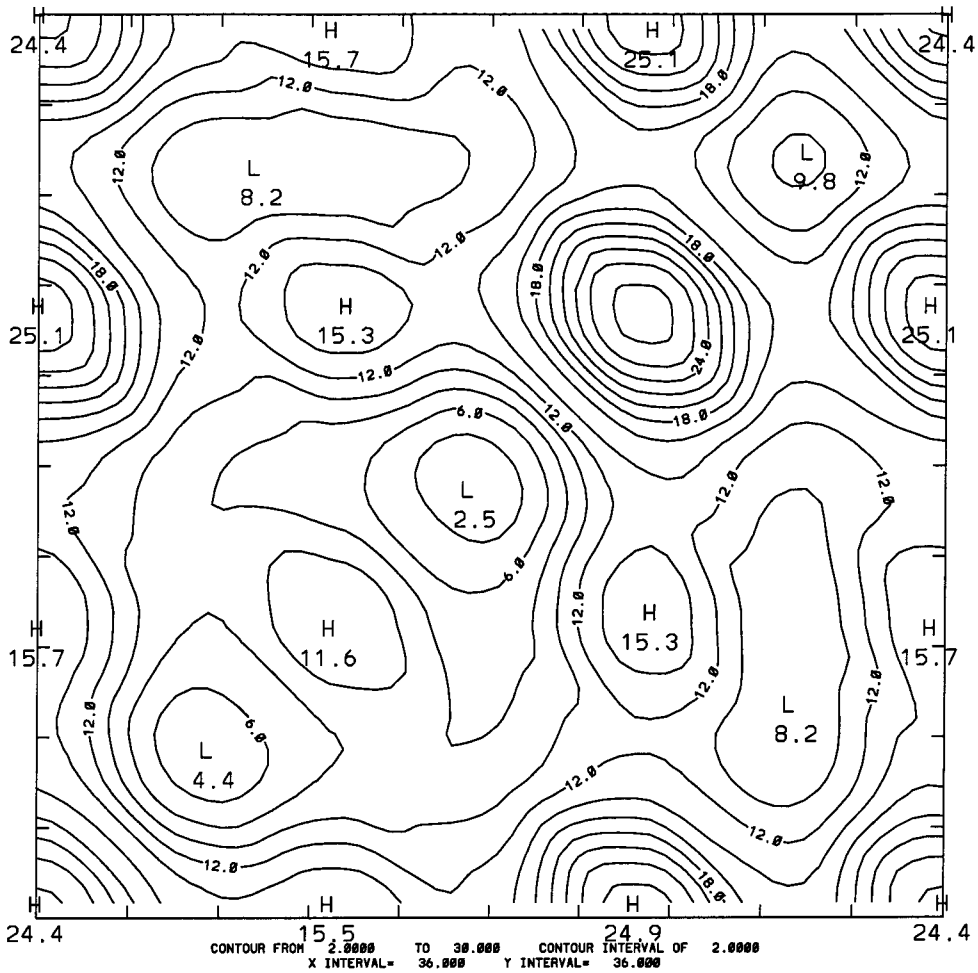

Figure 5.10: Quantum one energy calculation of DREIDII adiabatic 2D rotational grids for sPVC

Table 5.7: Local Minimums for sPVC(Kcal/Mole)

Φ_1	Φ_2	QM	FF	Error	Φ_1	Φ_2	QM	FF	Error
64.2	64.3	2.9916	2.3713	0.6203	160.7	79.1	3.7644	3.5273	0.2371
173.4	173.4	0.0000	0.0000	0.0000	-69.3	71.5	5.1593	5.0076	0.1517
-32.1	171.3	7.2982	6.1663	1.1319	-48.0	-48.0	6.4601	6.1377	0.3224

Table 5.8: QM Energy of FF Grids for sPVC(Kcal/Mole)

Φ_1	Φ_2	QM	Φ_1	Φ_2	QM
360.00	360.00	24.4116	120.00	120.00	28.7529
360.00	300.00	15.2077	360.00	60.00	14.4116
300.00	300.00	5.0835	300.00	60.00	8.8213
360.00	240.00	15.6601	240.00	60.00	8.5839
300.00	240.00	8.0973	180.00	60.00	10.5997
240.00	240.00	11.5547	120.00	60.00	15.4012
360.00	180.00	13.0037	60.00	60.00	9.7703
300.00	180.00	8.7231	360.00	0.00	24.4132
240.00	180.00	6.5478	300.00	0.00	15.1999
180.00	180.00	3.1852	240.00	0.00	15.6611
360.00	120.00	25.0846	180.00	0.00	13.0042
300.00	120.00	12.3637	120.00	0.00	25.0842
240.00	120.00	15.1657	60.00	0.00	14.4159
180.00	120.00	14.1483	0.00	0.00	24.4116

5.3.3 Polyvinylidene Chloride

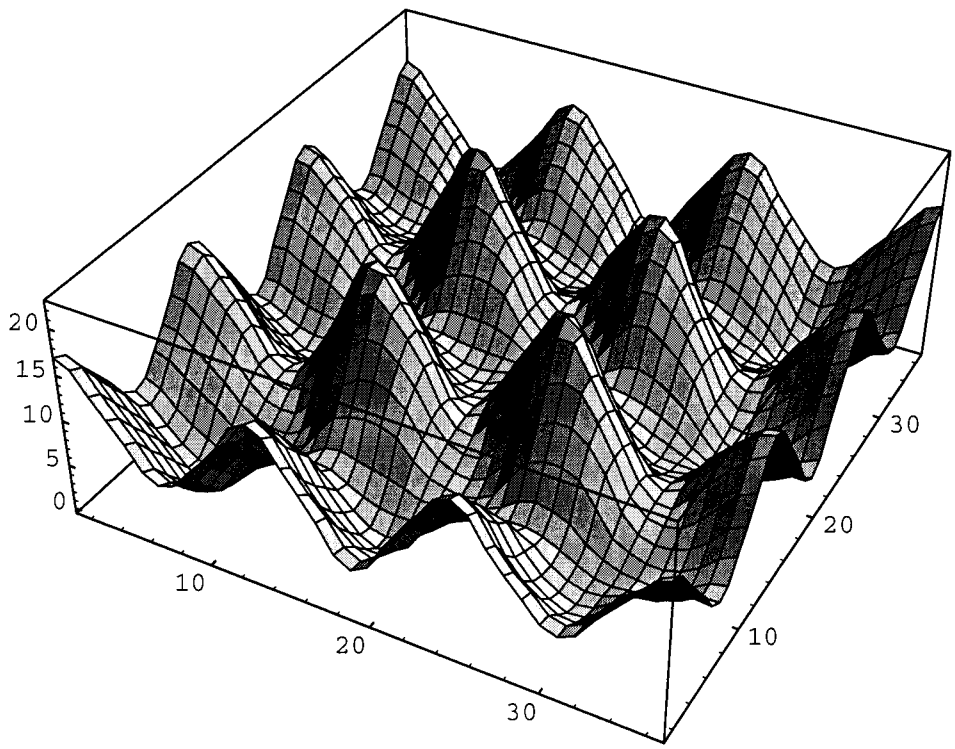

Figure 5.11: 3D plot of adiabatic 2D rotational surface for PVDC (Angle in 10^o)

Polyvinylidene Chloride has higher symmetry than that of iPVC and sPVC. For interval of 30^o, we used 50 grid points that covers one quater of the 2D space, plus four local minimums. Figure 5.11 is the 3D plot of quantum adiabatic energy surface, while the 2D contour map is in Fig. 5.12. The results from optimized force field are plotted in Fig. 5.13. Comparison of energies at each point are tabulated in Table 5.9. We also did quantum one energy calculation on grids generated based on DREIDII force field. The 2D contour map of rotational energy surface is plotted in Fig. 5.14, and tabulated in Table [5.10].

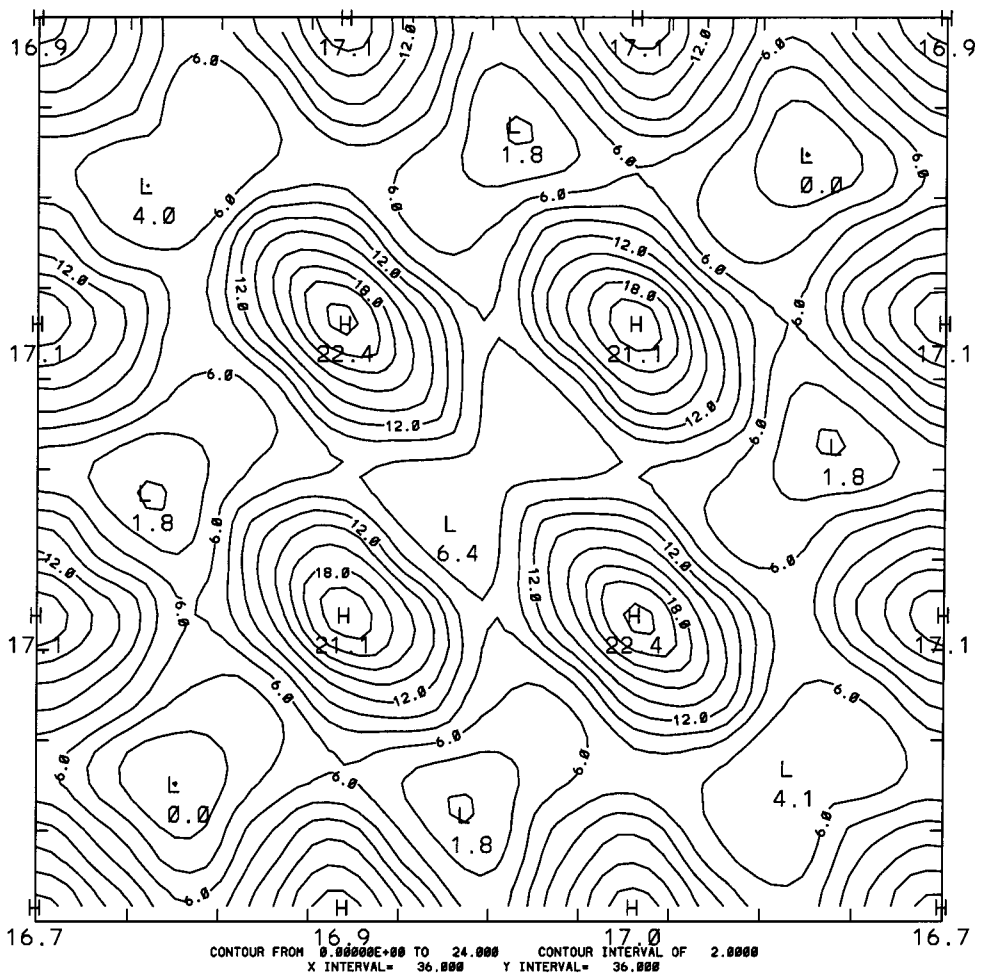

Figure 5.12: Quantum adiabatic 2D rotational surface for PVDC

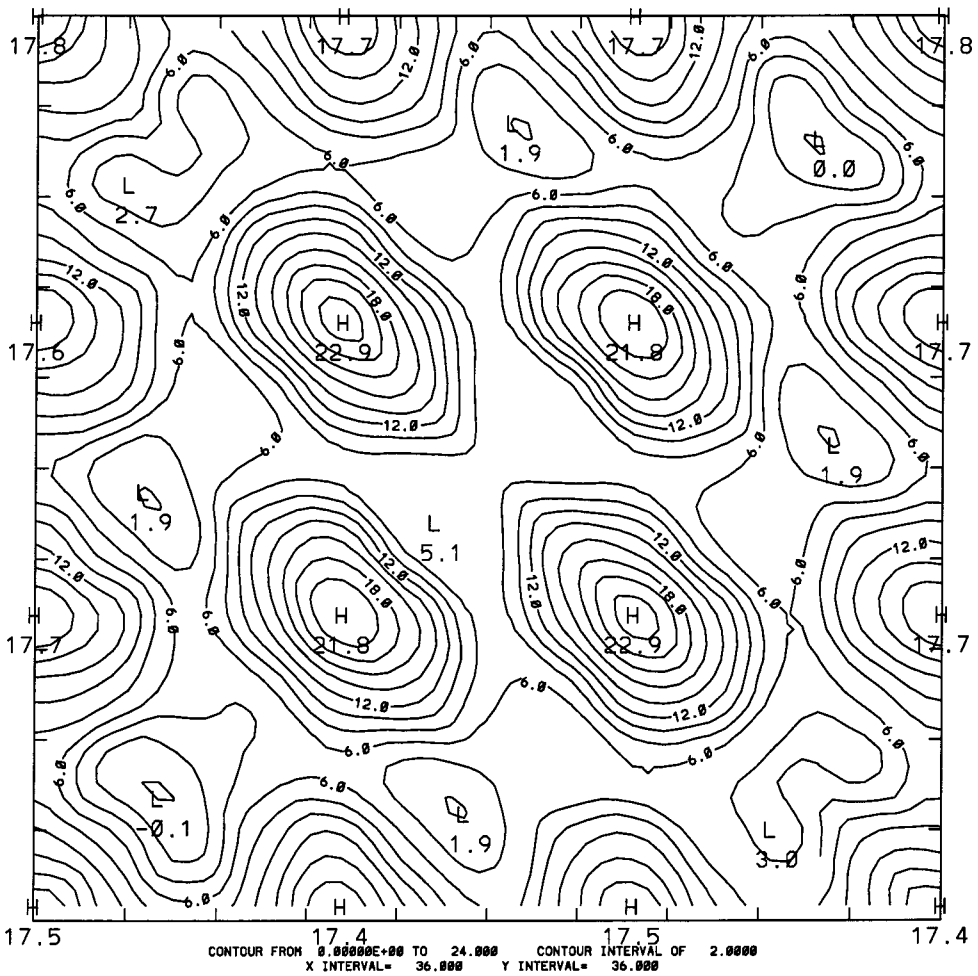

Figure 5.13: Force field adiabatic 2D rotational surface for PVDC

Table 5.9: Adiabatic QM and FF Energy of PVDC (Kcal/Mole)

Φ_1	Φ_2	QM	FF	Error	Φ_1	Φ_2	QM	FF	Error
0.0	0.0	16.9396	17.7674	-0.8278	90.0	-180.0	6.5771	6.6309	-0.0538
0.0	30.0	11.9382	11.3183	0.6199	120.0	-180.0	7.9857	7.2809	0.7048
30.0	30.0	7.0920	7.2073	-0.1153	150.0	180.0	7.4874	6.7613	0.7261
0.0	60.0	6.6058	7.0085	-0.4027	-180.0	-180.0	7.3741	7.4003	-0.0262
30.0	60.0	2.3499	1.0767	1.2732	0.0	-150.0	11.5447	11.9868	-0.4421
60.0	60.0	0.3630	1.6444	-1.2814	30.0	-150.0	9.4859	10.6921	-1.2062
0.0	90.0	11.1026	10.4971	0.6055	60.0	-150.0	5.5174	5.2661	0.2513
30.0	90.0	8.1697	8.6125	-0.4428	90.0	-150.0	6.3921	6.1841	0.2080
60.0	90.0	3.7732	4.7668	-0.9936	120.0	-150.0	14.5706	14.6971	-0.1265
90.0	90.0	4.0411	4.9931	-0.9520	150.0	-150.0	14.8181	15.6382	-0.8201
0.0	120.0	17.1286	17.6353	-0.5067	0.0	-120.0	17.1280	17.6352	-0.5072
30.0	120.0	12.4872	13.1084	-0.6212	30.0	-120.0	12.7333	12.7494	-0.0161
60.0	120.0	5.9531	5.6287	0.3244	60.0	-120.0	7.2256	5.9681	1.2575
90.0	120.0	11.2123	11.9355	-0.7232	90.0	-120.0	14.2035	14.5203	-0.3168
120.0	120.0	20.8974	21.5827	-0.6853	120.0	-120.0	22.4389	22.8679	-0.4290
0.0	150.0	11.5615	11.9933	-0.4318	0.0	-90.0	11.1122	10.4849	0.6273
30.0	150.0	5.9401	6.0794	-0.1393	30.0	-90.0	6.4651	6.7689	-0.3038
60.0	150.0	3.9551	3.2074	0.7477	60.0	-90.0	6.0472	4.9345	1.1127
90.0	150.0	12.3129	12.9045	-0.5916	90.0	-90.0	13.8084	12.7514	1.0570
120.0	150.0	15.8376	16.4206	-0.5830	0.0	-60.0	6.5967	7.0067	-0.4100
150.0	150.0	8.1747	6.7956	1.3791	30.0	-60.0	4.6666	3.4726	1.1940
0.0	-180.0	5.2519	6.1510	-0.8991	60.0	-60.0	4.3747	4.4720	-0.0973
30.0	180.0	3.0201	2.9148	0.1053	0.0	-30.0	11.9398	11.3198	0.6200
60.0	180.0	3.2468	4.2251	-0.9783	30.0	-30.0	9.7730	10.4496	-0.6766
Local Minimums									
52.4	52.4	0.0000	0.0000	0.0000	42.6	167.2	1.8653	1.9294	-0.0641
180.0	179.9	7.3696	7.4012	-0.0316	56.7	-56.5	4.2612	4.3652	-0.1040

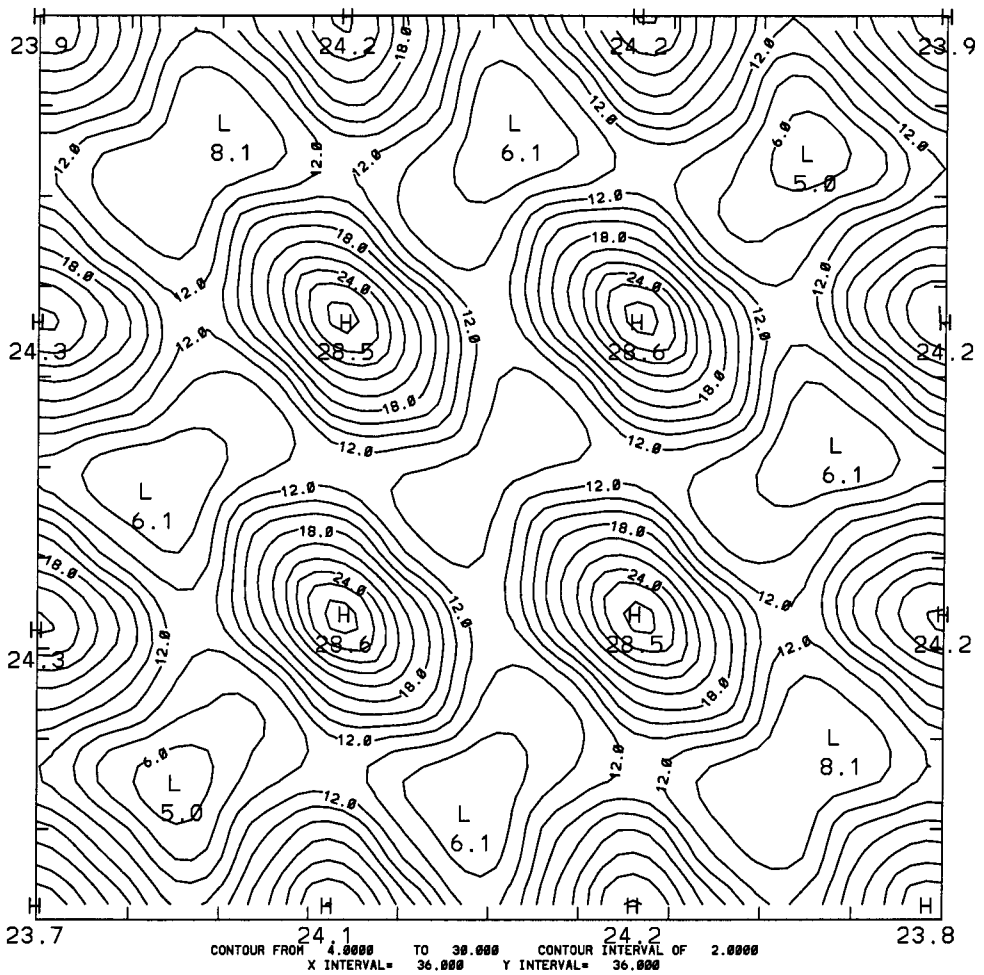

Figure 5.14: Quantum one energy calculation of DREIDII adiabatic 2D rotational grids for PVDC

Table 5.10: QM Energy of FF Grids for PVDC (Kcal/Mole)

Φ_1	Φ_2	QM	Φ_1	Φ_2	QM
360.0	360.0	23.9285	180.0	270.0	9.6934
330.0	360.0	18.1459	180.0	240.0	11.0720
330.0	330.0	12.5615	180.0	210.0	10.1891
300.0	360.0	12.0579	180.0	180.0	9.3368
300.0	330.0	7.0202	150.0	360.0	16.8153
300.0	300.0	5.1921	150.0	330.0	14.7447
270.0	360.0	17.4350	150.0	300.0	9.6692
270.0	330.0	14.3536	150.0	270.0	10.2060
270.0	300.0	8.8495	150.0	240.0	19.7465
270.0	270.0	9.0098	150.0	210.0	18.5852
240.0	360.0	24.2266	120.0	360.0	24.2014
240.0	330.0	18.2955	120.0	330.0	19.2246
240.0	300.0	10.5900	120.0	300.0	12.0979
240.0	270.0	17.9293	120.0	270.0	19.1709
240.0	240.0	28.6327	120.0	240.0	28.5145
210.0	360.0	16.7986	90.0	360.0	17.4333
210.0	330.0	10.0442	90.0	330.0	11.3092
210.0	300.0	8.1266	90.0	300.0	9.7406
210.0	270.0	17.5767	90.0	270.0	18.2809
210.0	240.0	19.2904	60.0	360.0	12.0661
210.0	210.0	10.5292	60.0	330.0	9.0761
180.0	360.0	9.6271	60.0	300.0	8.1909
180.0	330.0	6.9211	30.0	360.0	18.1512
180.0	300.0	6.7819	30.0	330.0	15.7161

5.3.4 Mixture of Polyvinyl Chloride and Polyvinylidene Chloride

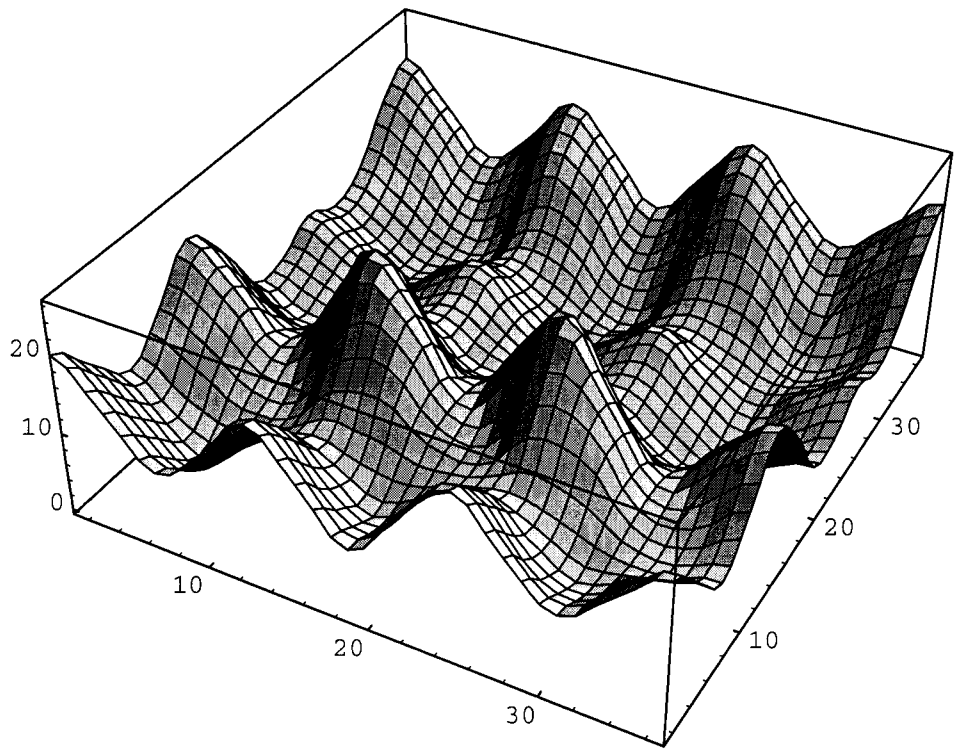

Figure 5.15: 3D plot of adiabatic 2D rotational surface for PVC-PVDC (Angle in 10^o)

In the case of the mixture of Polyvinyl Chloride and Polyvinylidene Chloride, there is no reflection symmetry. For an interval of 30^o, 144 grid points plus 9 local minimums are calculated. The 3D quantum adiabatic energy surface is plotted in Fig. 5.15, while the 2D contour map plot is in Fig. 5.16. Figure 5.17 is the 2D contour map based on optimized force field. The energies at grid points are tabulated in Table 5.11 and Table 5.12. The 9 local minimums are tabulated in Table 5.14.

Figure 5.18 is the 2D contour map of quantum one energy calculations on DREI-

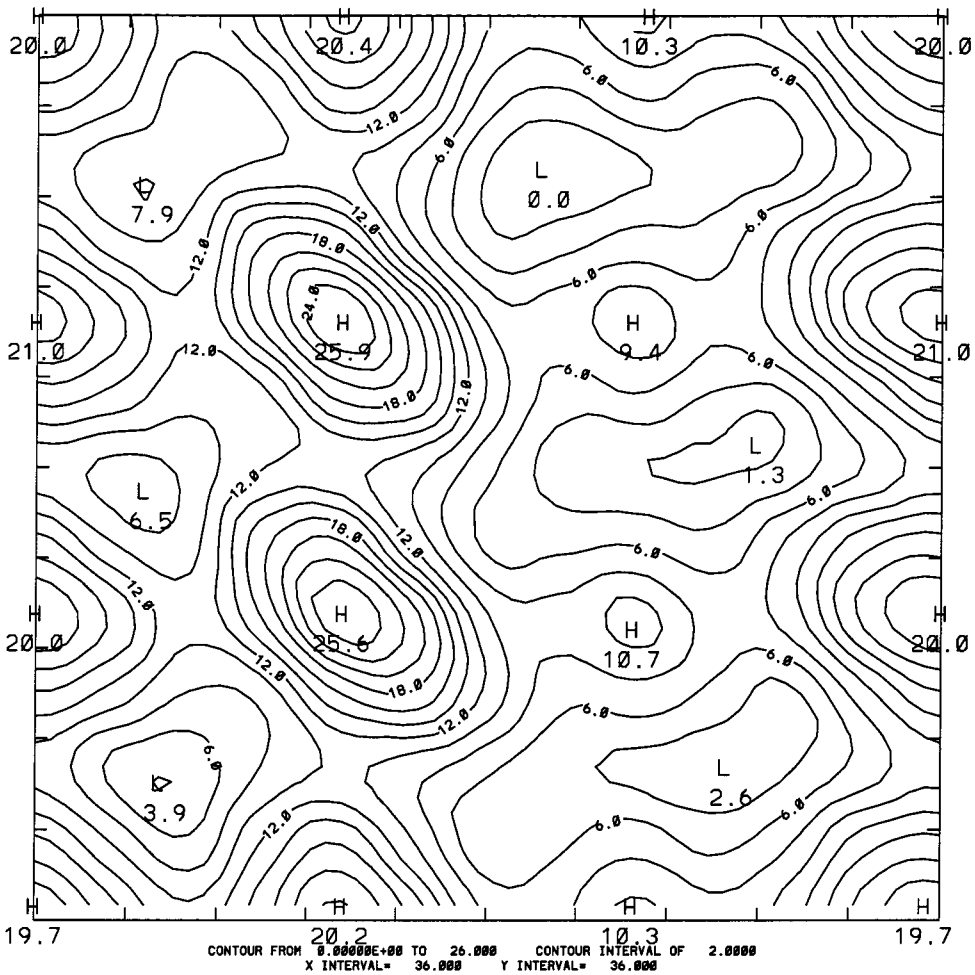

Figure 5.16: Quantum adiabatic 2D rotational surface for PVC-PVDC

IDII force field generated grids. The energies are listed in Table 5.14.

5.4 Summary

The quality of force fields for amorphous polymers are mainly determined by two factors; one is the relative energy difference between the local minimums of torsional conformationsr, which dictates the equilibrium distributions of torsional states thermodynamically; the other factor is the energy barriers between various local optimum conformations, which determines the rate of conformation transitions, i.e., the rigidity of polymer chains. Compared to the usual one-energy quantum potential based on

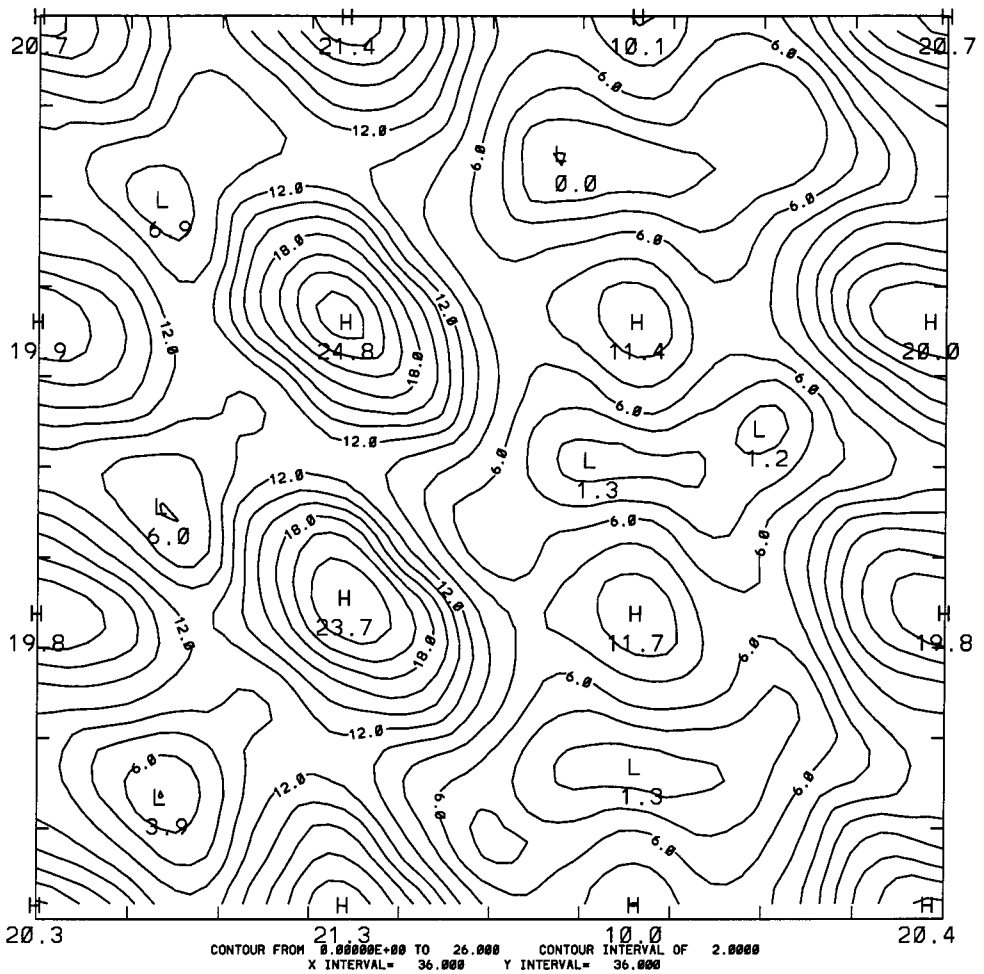

Figure 5.17: Force field adiabatic 2D rotational surface for PVC-PVDC

one torsion angle, adiabatic 2D quantum potential calculations are a big step forward, the new approach included the correlation of adjacent torsion angles.

Adiabatic molecular simulation force field (MSFF) suitable for carrying out molecular dynamics simulations of amorphous polymers (polyvinyl chloride, polyvinylidene chloride) are developed. These force fields can be used in molecular dynamics simulations to study physical properties of amorphous polymers such as glass transition temperature and diffusivity of gas molecules.

The force fields are based on adiabatic 2D (two adjacent backbone torsions) rotational energy surfaces generated by using *ab initio* calculations. Clusters with five-backbone carbon atoms are used to mimmick the polymer chains. These 2D grids

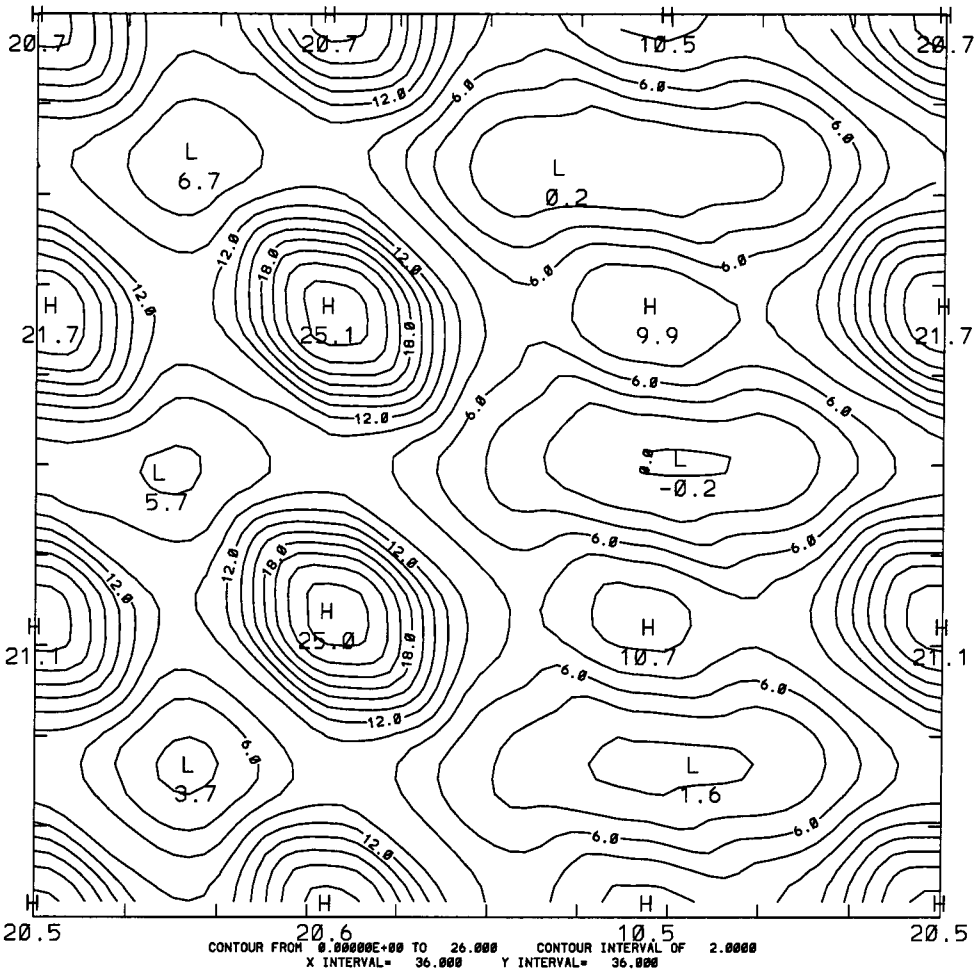

Figure 5.18: Quantum one energy calculation of DREIDII adiabatic 2D rotational grids for PVC-PVDC

are based on rotating two backbone torsions with incement of 30^o. For each conformation (symmetry properties are being used to reduce the number of points), we optimize the whole structure while the two backbone torsions are constrainted. These grid points plus local minimum points (fully optimized) are used to generate the 2-D adiabatic potential energy surfaces. Force fields are fitted so that the adiabatic force field potential energy surfaces match to that of quantum adiabatic potential surface. These force fields will be used in molecular dynamics simulations of glass transition and gas diffusions.

5.5 References

1. R.G. Parker, G.A., Martello, "Chemical Modifications: Chlorinated PVC," *Encyclopedia of PVC*, 1986, 619-654.

2. A.K. Rappe, W.A. Goddard III, "Charge equilibration for molecular-dynamics simulations," *J. Phys. Chem.* **95(8)**, 1991, 3358-3363.

3. S.L. Mayo, B.D. Olafson, W.A. Goddard III, "DREIDING - a generic force-field for molecular simulations," *J. Phys. Chem.* **94(26)**, 1990, 8897-8909.

Table 5.11: Adiabatic QM and FF Energy of PVC-PVDC(I)(Kcal/Mol)

Φ_1	Φ_2	QM	FF	Error	Φ_1	Φ_2	QM	FF	Error
0.0	0.0	19.9762	20.7012	-0.7250	0.0	90.0	13.8179	13.2234	0.5945
30.0	0.0	15.0481	16.5916	-1.5435	30.0	90.0	11.3239	13.1494	-1.8255
60.0	0.0	10.5482	10.9257	-0.3775	60.0	90.0	7.9540	10.9207	-2.9667
90.0	0.0	14.8661	15.6856	-0.8195	90.0	90.0	8.7855	10.2082	-1.4227
120.0	0.0	20.3736	21.3788	-1.0052	120.0	90.0	15.8084	15.0014	0.8070
150.0	0.0	15.6739	16.6426	-0.9687	150.0	90.0	17.7785	16.0937	1.6848
-180.0	0.0	7.8042	8.0675	-0.2633	-180.0	90.0	11.5137	9.3888	2.1249
-150.0	0.0	7.5416	7.2500	0.2916	-150.0	90.0	6.6511	5.0241	1.6270
-120.0	0.0	10.3352	10.1168	0.2184	-120.0	90.0	7.3163	7.0918	0.2245
-90.0	0.0	8.4622	6.5329	1.9293	-90.0	90.0	5.4951	6.2457	-0.7506
-60.0	0.0	10.6236	8.9141	1.7095	-60.0	90.0	3.5514	4.0861	-0.5347
-30.0	0.0	16.7263	16.9315	-0.2052	-30.0	90.0	9.2279	11.0936	-1.8657
0.0	30.0	14.7441	13.5445	1.1996	0.0	120.0	19.9609	19.7939	0.1670
30.0	30.0	10.1531	10.2035	-0.0504	30.0	120.0	15.6855	17.5523	-1.8668
60.0	30.0	6.4123	6.7368	-0.3245	60.0	120.0	10.6193	11.7889	-1.1696
90.0	30.0	12.2198	13.2206	-1.0008	90.0	120.0	16.1165	15.8059	0.3106
120.0	30.0	16.1147	17.2455	-1.1308	120.0	120.0	25.3444	23.2912	2.0532
150.0	30.0	10.3590	9.7034	0.6556	150.0	120.0	20.9443	19.8328	1.1115
-180.0	30.0	4.6262	3.5206	1.1056	-180.0	120.0	10.2243	9.1277	1.0966
-150.0	30.0	5.7643	5.0507	0.7136	-150.0	120.0	8.6180	8.4162	0.2018
-120.0	30.0	7.4031	6.8218	0.5813	-120.0	120.0	10.6005	11.6716	-1.0711
-90.0	30.0	5.5573	4.3182	1.2391	-90.0	120.0	7.4051	7.1531	0.2520
-60.0	30.0	7.8903	7.5299	0.3604	-60.0	120.0	8.9009	7.5315	1.3694
-30.0	30.0	13.2516	14.4476	-1.1960	-30.0	120.0	16.4946	16.1500	0.3446
0.0	60.0	9.3778	10.6221	-1.2443	0.0	150.0	14.7990	14.7035	0.0955
30.0	60.0	5.6312	6.8451	-1.2139	30.0	150.0	10.0124	10.7370	-0.7246
60.0	60.0	4.4995	5.8291	-1.3296	60.0	150.0	9.1348	6.6505	2.4843
90.0	60.0	8.1241	10.9316	-2.8075	90.0	150.0	17.3892	16.4785	0.9107
120.0	60.0	10.1993	11.4540	-1.2547	120.0	150.0	20.3033	20.6689	-0.3656
150.0	60.0	8.8769	7.8059	1.0710	150.0	150.0	11.7127	10.7140	0.9987
-180.0	60.0	6.3909	5.2834	1.1075	180.0	150.0	5.5250	4.4776	1.0474
-150.0	60.0	4.3370	1.7162	2.6208	-150.0	150.0	5.5422	6.5779	-1.0357
-120.0	60.0	3.5902	1.3247	2.2655	-120.0	150.0	5.8219	7.8685	-2.0466
-90.0	60.0	2.6454	1.9353	0.7101	-90.0	150.0	4.6442	4.1449	0.4993
-60.0	60.0	3.8330	4.9469	-1.1139	-60.0	150.0	8.3645	8.4462	-0.0817
-30.0	60.0	6.8525	7.9980	-1.1455	-30.0	150.0	13.3523	14.8192	-1.4669

Table 5.12: Adiabatic QM and FF Energy of PVC-PVDC(II)(Kcal/Mol)

Φ_1	Φ_2	QM	FF	Error	Φ_1	Φ_2	QM	FF	Error
0.0	180.0	9.0038	9.3985	-0.3947	0.0	-90.0	15.3252	13.1480	2.1772
30.0	180.0	7.4941	7.8429	-0.3488	30.0	-90.0	10.7678	11.7926	-1.0248
60.0	180.0	8.5738	7.7518	0.8220	60.0	-90.0	10.9056	8.2794	2.6262
90.0	-180.0	11.9431	11.2798	0.6633	90.0	-90.0	17.9846	16.5977	1.3869
120.0	-180.0	12.4131	11.2679	1.1452	120.0	-90.0	17.5892	18.1186	-0.5294
150.0	180.0	10.7086	9.1172	1.5914	150.0	-90.0	8.3351	9.3409	-1.0058
-180.0	180.0	6.5415	6.3632	0.1783	180.0	-90.0	2.6204	5.7277	-3.1073
-150.0	-180.0	2.8567	1.7441	1.1126	-150.0	-90.0	3.2942	5.7955	-2.5013
-120.0	180.0	2.0276	1.7430	0.2846	-120.0	-90.0	4.8173	6.6368	-1.8195
-90.0	180.0	1.8371	2.2851	-0.4480	-90.0	-90.0	4.9843	4.4986	0.4857
-60.0	-180.0	2.8055	3.9525	-1.1470	-60.0	-90.0	9.2510	8.6804	0.5706
-30.0	-180.0	6.1274	7.0730	-0.9456	-30.0	-90.0	14.1032	13.4640	0.6392
0.0	-150.0	15.2027	15.1317	0.0710	0.0	-60.0	10.7323	11.2059	-0.4736
30.0	-150.0	13.6714	14.9507	-1.2793	30.0	-60.0	8.6991	8.7833	-0.0842
60.0	-150.0	10.6847	10.9255	-0.2408	60.0	-60.0	8.8575	8.2889	0.5686
90.0	-150.0	11.7029	10.6855	1.0174	90.0	-60.0	10.3158	10.2313	0.0845
120.0	-150.0	18.8750	17.4005	1.4745	120.0	-60.0	10.3322	10.3552	-0.0230
150.0	-150.0	18.3598	17.5461	0.8137	150.0	-60.0	7.3471	9.0164	-1.6693
-180.0	-150.0	9.7425	8.4954	1.2471	-180.0	-60.0	1.8799	4.7822	-2.9023
-150.0	-150.0	5.1060	4.8177	0.2883	-150.0	-60.0	0.0747	0.0218	0.0529
-120.0	-150.0	6.0248	7.7307	-1.7059	-120.0	-60.0	1.8095	0.9662	0.8433
-90.0	-150.0	3.9297	4.7020	-0.7723	-90.0	-60.0	2.7045	2.0198	0.6847
-60.0	-150.0	2.7288	2.1862	0.5426	-60.0	-60.0	3.7672	3.2004	0.5668
-30.0	-150.0	9.8623	10.5394	-0.6771	-30.0	-60.0	7.7909	6.9672	0.8237
0.0	-120.0	20.9759	19.8901	1.0858	0.0	-30.0	15.5042	13.9469	1.5573
30.0	-120.0	16.6697	16.3663	0.3034	30.0	-30.0	13.1547	14.5027	-1.3480
60.0	-120.0	12.2783	11.0088	1.2695	60.0	-30.0	8.8985	9.7063	-0.8078
90.0	-120.0	18.9684	18.3175	0.6509	90.0	-30.0	10.3416	10.8283	-0.4867
120.0	-120.0	25.9434	24.8339	1.1095	120.0	-30.0	15.7328	15.2951	0.4377
150.0	-120.0	18.1441	16.9945	1.1496	150.0	-30.0	12.6513	13.8533	-1.2020
-180.0	-120.0	7.5578	7.5011	0.0567	-180.0	-30.0	5.4405	6.5088	-1.0683
-150.0	-120.0	7.1104	8.5841	-1.4737	-150.0	-30.0	3.8506	3.8065	0.0441
-120.0	-120.0	9.3474	11.3717	-2.0243	-120.0	-30.0	6.4863	6.4622	0.0241
-90.0	-120.0	6.5526	6.6365	-0.0839	-90.0	-30.0	4.7655	3.5549	1.2106
-60.0	-120.0	9.6881	9.5182	0.1699	-60.0	-30.0	5.1556	3.2032	1.9524
-30.0	-120.0	17.7739	17.9179	-0.1440	-30.0	-30.0	12.1162	10.3788	1.7374

Table 5.13: Local Minimums for PVC-PVDC(Kcal/Mole)

Structure	Φ_1	Φ_2	QM	FF	Error
1	48.9	52.2	3.9428	3.9824	-0.0396
2	-171.7	37.2	4.2132	4.1230	0.0902
3	-72.8	69.3	2.8813	3.0163	-0.1350
4	38.3	168.0	6.6523	6.6592	-0.0069
5	-101.5	178.2	1.7873	1.6719	0.1154
6	-69.5	-165.9	1.4099	1.3183	0.0916
7	37.5	-71.1	8.0181	7.4327	0.5854
8	-155.2	-60.7	0.0000	0.0000	0.0000
9	-74.4	-48.4	2.5129	2.3245	0.1884

Table 5.14: QM Energy of FF Grids for PVC-PVDC(Kcal/Mole)

Φ_1	Φ_2	QM	Φ_1	Φ_2	QM
0.0	0.0	20.6882	180.0	0.0	7.8939
0.0	60.0	8.7936	180.0	60.0	4.1968
0.0	120.0	21.0308	180.0	120.0	8.7877
0.0	180.0	7.2674	180.0	180.0	3.8761
0.0	240.0	21.6684	180.0	240.0	7.6463
0.0	300.0	9.9833	180.0	300.0	1.2937
60.0	0.0	10.1944	240.0	0.0	10.4056
60.0	60.0	3.6692	240.0	60.0	1.6462
60.0	120.0	9.7714	240.0	120.0	10.6799
60.0	180.0	5.8693	240.0	180.0	0.0000
60.0	240.0	11.2843	240.0	240.0	9.8981
60.0	300.0	6.7427	240.0	300.0	0.4488
120.0	0.0	20.6304	300.0	0.0	10.3548
120.0	60.0	9.0058	300.0	60.0	2.7670
120.0	120.0	25.0148	300.0	120.0	9.1315
120.0	180.0	9.0668	300.0	180.0	1.1101
120.0	240.0	25.0629	300.0	240.0	8.7192
120.0	300.0	8.8143	300.0	300.0	2.3128

5.6 Appendix

Listed in the tables are the geometry of optimized local minimums for iPVC, sPVC, PVDC, and PVC-PVDC.

Table 5.15: Bonds and Angles of iPVC Local Optimums

Structure	1	2	3	4	5	6
Bond Distances (Å)						
C_2—C_1	1.515	1.517	1.519	1.516	1.520	1.517
C_2—C_3	1.526	1.525	1.529	1.524	1.526	1.532
C_3—C_4	1.529	1.524	1.529	1.523	1.526	1.532
C_4—C_5	1.517	1.515	1.519	1.517	1.520	1.517
C_2—Cl_1	1.912	1.913	1.894	1.906	1.893	1.907
C_4—Cl_2	1.908	1.916	1.894	1.908	1.894	1.907
C_2—H_1	1.075	1.075	1.077	1.074	1.077	1.078
C_4—H_2	1.076	1.076	1.077	1.076	1.077	1.078
C_3—H_3	1.085	1.085	1.091	1.082	1.082	1.079
C_3—H_4	1.081	1.084	1.082	1.086	1.088	1.083
C_1—H_5	1.081	1.080	1.081	1.080	1.080	1.080
C_1—H_6	1.081	1.082	1.078	1.083	1.082	1.082
C_1—H_7	1.082	1.085	1.085	1.084	1.085	1.082
C_5—H_8	1.081	1.079	1.078	1.082	1.082	1.082
C_5—H_9	1.085	1.084	1.085	1.085	1.085	1.082
C_5—H_10	1.080	1.081	1.081	1.080	1.080	1.080
Angles (*degree*)						
C_3—C_2—C_1	117.05	113.28	118.79	115.75	112.66	117.38
C_4—C_3—C_2	117.03	117.32	124.49	115.08	117.28	113.88
C_5—C_4—C_3	116.51	117.87	118.79	113.10	112.69	117.40
Cl_1—C_2—H_1	101.59	102.56	100.99	102.53	102.73	102.05
Cl_1—C_2—C_1	107.52	107.24	108.16	107.91	107.26	106.71
Cl_1—C_2—C_3	106.01	109.62	112.01	106.39	111.37	106.65
Cl_2—C_4—H_2	100.86	101.46	106.09	102.28	102.69	102.05
Cl_2—C_4—C_3	111.33	108.22	112.01	109.43	111.35	106.63
Cl_2—C_4—C_5	108.25	108.16	108.16	107.90	107.23	106.73
H_4—C_3—H_3	106.72	106.58	106.10	107.18	106.57	107.10
Backbone Torsion Angles (*degree*)						
C_1–C_2–C_3–C_4	44.9	56.7	52.8	-179.5	-155.9	-79.2
C_2–C_3–C_4–C_5	73.7	154.1	-52.8	60.8	156.7	79.5
Minimium Energy (*Kcal/Mol*)						
Energy	3.1331	1.6149	10.4863	0.0000	5.4815	4.3209

HF (6-31G**) *ab initio* PS-GVB Constraint Minimizations

Table 5.16: Bonds and Angles of sPVC Local Optimums

structure	1	2	3	4	5	6
Bond Distances (Å)						
C_2—C_1	1.517	1.515	1.516	1.516	1.520	1.516
C_3—C_2	1.528	1.527	1.519	1.527	1.522	1.526
C_4—C_3	1.528	1.527	1.519	1.531	1.530	1.526
C_4—C_5	1.517	1.519	1.516	1.518	1.517	1.516
C_2—Cl_1	1.901	1.912	1.911	1.913	1.894	1.917
C_4—Cl_2	1.901	1.907	1.911	1.906	1.898	1.916
C_2—H_1	1.076	1.077	1.075	1.074	1.076	1.076
C_4—H_2	1.076	1.077	1.075	1.077	1.076	1.076
C_3—H_3	1.081	1.084	1.085	1.081	1.081	1.085
C_3—H_4	1.081	1.082	1.085	1.086	1.089	1.085
C_1—H_5	1.080	1.081	1.080	1.080	1.080	1.081
C_1—H_6	1.082	1.081	1.082	1.082	1.082	1.078
C_1—H_7	1.085	1.081	1.085	1.082	1.085	1.083
C_5—H_8	1.085	1.085	1.085	1.085	1.086	1.083
C_5—H_9	1.082	1.082	1.082	1.078	1.080	1.078
C_5—H_10	1.080	1.080	1.080	1.081	1.080	1.081
Angles (*degree*)						
C_1—C_2—C_3	115.54	117.24	113.55	117.57	112.27	118.73
C_2—C_3—C_4	112.61	115.34	116.08	118.25	119.25	121.73
C_3—C_4—C_5	115.54	112.82	113.55	118.71	116.52	118.72
Cl_1—C_2—H_1	102.02	101.86	102.46	102.28	102.55	100.37
Cl_1—C_2—C_1	107.85	107.37	107.88	106.92	107.60	108.41
Cl_1—C_2—C_3	106.89	106.51	108.56	105.57	111.45	110.02
Cl_2—C_4—H_2	102.02	102.34	102.46	101.51	100.83	100.39
Cl_2—C_4—C_3	106.89	111.00	108.56	109.73	111.28	110.02
Cl_2—C_4—C_5	107.85	107.04	107.88	108.30	108.51	108.42
H_3—C_3—H_4	107.30	106.87	107.08	106.80	106.49	106.17
Backbone Torsion Angles (*degree*)						
C_1–C_2–C_3–C_4	64.2	160.7	173.4	-69.3	-32.1	-48.0
C_2–C_3–C_4–C_5	64.3	79.1	173.4	71.5	171.3	-48.0
Minimium Energy ($Kcal/Mol$)						
Energy	2.9916	3.7644	0.0000	5.1593	7.2982	6.4601

HF (6-31G**) *ab initio* PS-GVB Constraint Minimizations

Table 5.17: Bonds and Angles of PVDC Local Optimums

structure	1	2	3	4
Bond Distances (Å)				
C_2—C_1	1.513	1.512	1.523	1.515
C_3—C_2	1.533	1.533	1.531	1.536
C_4—C_3	1.533	1.531	1.531	1.536
C_4—C_5	1.513	1.518	1.523	1.514
C_2—Cl_1	1.880	1.887	1.860	1.888
C_4—Cl_2	1.880	1.879	1.860	1.856
C_2—Cl_3	1.873	1.865	1.860	1.856
C_4—Cl_4	1.873	1.857	1.860	1.888
C_3—H_3	1.080	1.081	1.084	1.079
C_3—H_4	1.080	1.081	1.084	1.083
C_1—H_5	1.079	1.079	1.079	1.079
C_1—H_6	1.080	1.080	1.082	1.082
C_1—H_7	1.079	1.079	1.082	1.078
C_5—H_8	1.079	1.082	1.082	1.082
C_5—H_9	1.080	1.082	1.082	1.078
C_5—H_10	1.079	1.079	1.079	1.079
Angles (*degree*)				
C_1—C_2—C_3	119.05	118.85	109.30	118.52
C_2—C_3—C_4	120.24	122.23	127.97	122.21
C_3—C_4—C_5	119.05	110.61	109.30	118.54
Cl_1—C_2—Cl_3	105.47	105.19	107.55	105.81
Cl_1—C_2—C_1	107.54	107.61	106.74	106.61
Cl_1—C_2—C_3	104.73	104.79	113.06	103.64
Cl_2—C_4—Cl_4	105.47	107.01	107.55	105.81
Cl_2—C_4—C_3	104.72	110.02	113.06	112.57
Cl_2—C_4—C_5	107.54	106.97	106.74	108.63
Cl_3—C_2—C_1	108.62	109.05	106.75	108.63
Cl_3—C_2—C_3	110.50	110.40	113.06	112.59
Cl_4—C_4—C_3	110.51	114.10	113.07	103.64
Cl_4—C_4—C_5	108.62	107.83	106.75	106.62
H_3—C_3—H_4	106.93	106.92	106.99	106.85
Backbone Torsion Angles (*degree*)				
C_1–C_2–C_3–C_4	52.4	42.6	180.0	56.7
C_2–C_3–C_4–C_5	52.4	167.2	179.9	-56.5
Minimium Energy (*Kcal/Mol*)				
Energy	0.0000	1.8653	7.3696	4.2612

HF (6-31G**) *ab initio* PS-GVB Constraint Minimizations

Table 5.18: Bonds and Angles of PVC-PVDC Local Optimums

Property	opt1	opt2	opt3	opt4	opt5	opt6	opt7	opt8	opt9
				Bond Distances (Å)					
C_2—C_1	1.512	1.512	1.514	1.517	1.515	1.516	1.516	1.511	1.513
C_2—C_3	1.520	1.530	1.531	1.527	1.525	1.527	1.530	1.524	1.530
C_3—C_4	1.530	1.525	1.531	1.531	1.532	1.528	1.534	1.526	1.532
C_4—C_5	1.517	1.520	1.517	1.517	1.517	1.515	1.517	1.518	1.516
C_2—Cl_1	1.875	1.859	1.871	1.857	1.872	1.872	1.888	1.875	1.876
C_4—Cl_2	1.910	1.891	1.906	1.904	1.907	1.910	1.898	1.908	1.906
C_2—Cl_3	1.883	1.887	1.877	1.882	1.870	1.871	1.856	1.877	1.871
C_4—H_2	1.076	1.075	1.074	1.077	1.074	1.074	1.077	1.075	1.076
C_3—H_3	1.083	1.080	1.079	1.086	1.080	1.082	1.086	1.082	1.081
C_3—H_4	1.081	1.084	1.083	1.082	1.084	1.083	1.079	1.082	1.080
C_1—H_5	1.079	1.079	1.079	1.079	1.079	1.079	1.079	1.079	1.079
C_1—H_6	1.080	1.083	1.082	1.082	1.082	1.081	1.078	1.080	1.081
C_1—H_7	1.079	1.081	1.078	1.082	1.082	1.082	1.082	1.081	1.083
C_5—H_8	1.079	1.082	1.082	1.078	1.082	1.081	1.080	1.082	1.081
C_5—H_9	1.080	1.080	1.080	1.081	1.080	1.080	1.080	1.080	1.081
C_5—H_{10}	1.083	1.085	1.082	1.083	1.082	1.081	1.085	1.085	1.081
				Angles (*degree*)					
C_3-C_2-C_1	118.26	116.44	118.31	111.51	112.75	112.12	117.11	117.83	116.21
C_4-C_3-C_2	120.91	118.38	117.26	123.12	116.91	118.80	121.81	116.59	116.21
C_5-C_4-C_3	119.74	111.44	117.81	119.46	115.18	117.93	119.69	112.55	117.66
Cl_3-C_2-Cl_1	105.39	105.62	106.62	107.18	106.97	107.22	106.59	106.46	105.74
Cl_1-C_2-C_1	108.78	108.96	108.57	107.88	107.93	107.25	106.26	108.19	107.93
Cl_1-C_2-C_3	110.37	111.35	109.92	113.15	111.16	111.38	104.97	106.36	106.33
Cl_2-C_4-H_2	100.62	102.73	102.42	100.49	102.16	102.17	100.74	102.71	101.77
Cl_2-C_4-C_3	110.25	112.39	105.10	110.11	107.82	104.80	110.78	109.96	105.38
Cl_2-C_4-C_5	108.29	107.50	106.86	108.63	107.08	107.57	108.09	107.35	107.38
Cl_3-C_2-C_1	107.73	107.64	106.96	106.84	108.20	107.95	108.81	108.59	108.64
Cl_3-C_2-C_3	105.49	106.19	105.81	109.99	109.62	110.71	112.35	108.83	111.41
H_4-C_3-H_3	106.58	106.95	107.	106.53	107.18	107.19	106.44	106.97	107.12
				Backbone Torsion Angles (*degree*)					
$C_1C_2C_3C_4$	48.9	-171.7	-72.8	38.3	-101.5	-69.5	37.5	-155.2	-74.4
$C_2C_3C_4C_5$	52.2	37.2	69.3	168.0	178.2	-165.9	-71.1	-60.7	-48.4
				Minimium Energy ($Kcal/Mol$)					
Energy	3.9428	4.2132	2.8813	6.6523	1.7873	1.4099	8.0181	0.0000	2.5129

HF (6-31G**) *ab initio* PS-GVB Constraint Minimizations

Chapter 6 Simulations of Amorphous Polyethylene Glass Transition

6.1 Introduction

Amorphous polymers are widely used in industry. By varying the structural unit of a polymer or even by blending different polymers, a wide range of physical properties, including temperature stability, mechanical property, optical property and processibility can be obtained.[1-2] In order to create a polymer material with a set of desired properties, physics underlying the material behavior must be understood and characterized. Although various macroscopic properties around and below the glass transition temperature have been extensively investigated experimentally, the phenomena of glass transition and relaxation in glasses are not yet fully understood from molecular point of view.

6.2 Survey of Glass Transition Theory

In amorphous polymers, the transition from liquid-like to glass-like behavior is called the glass transition. There are many theories including kinetical, phenomenological and thermo-dynamical models.

In the kinetic regime,[3] the glass transition temperature T_g is defined as the temperature at which large-scale cooperative mobility of the polymer matrix occurs, or alternatively, where the thermal expansion coefficient α changes from the rubbery to the glassy state with its value being dependent on the rate at which data are measured. The secondary or β transition, associated with limited molecular mobility

[4]Based on "Simulations of Amorphous Polyethylene Glass Transition," **G. Gao, Y. Tang, M. Belmares, and W.A., Goddard III, to be published.**

below T_g at a temperature T_β, is a broad relaxational process. This process is related to side chain rotations (such as the wagging of the phenyl unit in polystyrene), the motion of a small number of monomeric units in the main chain, and short chain portions. The relaxations characterized by both T_g and T_β represent a distribution of relaxation times. Among various kinetic models, the free volume theory[4–5] is the most widely accepted one.

The free volume, V_f, is defined as the unoccupied space in a sample, arising from the inefficient packing of disordered chains in the amorphous regions of a polymer sample. It is a measure of the space available for the polymer to undergo rotation and translation. When the polymer is in the liquid or rubberlike state, the amount of free volume will increase with temperature as the molecular motion increases. If the temperature is decreased, this free volume will contract and eventually reach a critical value where there is insufficient free space to allow large scale segmental motion to take place. The temperature at that this critical volume is reached is the glass transition temperature. Below T_g the free volume will remain essentially constant as the temperature decreases further, since the chains have now been immobilized and frozen in position.

The glass transition can then be visualized as the onset of co-ordinated segmental motion, made possible by an increase of the holes in the polymer matrix to a size sufficient to allow this type of motion to occur.

Williams, Lendel and Ferry[6] found an empirical equation (WLF equation). They claimed that the ratio a_T of all mechanical and electrical relaxation times at temperature T to their values at a reference temperature T_s can be expressed, after suitable choice of T_s, by the equation $\log a_T$=-8.86$(T - T_s)/(101.6 + T - T_s)$ over a T range of $T_s \pm 50$ (K). This applies to a wide variety of polymers, polymer solutions, organic glass-forming liquids, and inorganic glasses. As chosen, T_s lies about 50 (K) above the glass transition temperature T_g. If, alternatively, the reference temperature is chosen as T_g, then $\log a_T$=-17.44$(T - T_g)/(51.6 + T - T_g)$.

In the thermodynamic regime, Gibbs and Dimarzio[7] proposed that the glass tran-

sition is a second order phase transition (G-D theory). They consider the fundamental transition to be a true equilibrium. Many experiments imply that the observed T_g would decrease further if a sufficiently long time for measurement was allowed. This aspect is considered in the G-D theory by defining a new transition temperature T_2 at which the configurational entropy of the system is zero. This temperature can be considered in effect to be the limiting value T_g would reach in a hypothetical experiment taking an infinitely long time. The theoretical derivation is based on a lattice treatment. The configurational entropy is found by calculating the number of ways that n_x linear chains each x segments long can be placed on a diamond lattice (coordination number Z=4), with n_0 unoccupied holes. The restrictions imposed on the placing of a chain on the lattice are embodied in the hindered rotation which is expressed as the "flex energy" $\delta\varepsilon$, and ε_h that is the energy of formation of a hole. The flex energy is the energy difference between the potential energy minimum of the located bond and the potential minima of the remaining (z-2) possible orientations that can be used on the lattice. The quantity ε_h is a measure of the cohesive energy. The configurational entropy $S_{conf.}$ is derived from the partition function describing the location of holes and polymer molecules. As the temperature drops to T_2, the number of available configuration states in the system decreases until the system possesses only one degree of freedom. The temperature T_2 is not of course an experimentally measurable quantity but is calculated to lie approximately 50 (K) below the experimental T_g and can be related to T_g on this basis.

An attempt to reunite both the kinetical and dynamical theory were made by Adam and Gibbs[8] (who outlined the molecular kinetic theory). They relate the temperature dependence of the relaxation process to the temperature dependence of the size of a region, which is defined as a volume large enough to allow co-operative rearrangement to take place without affecting a neighbouring region. This "co-operatively rearranging region" is large enough to allow a transition to a new configuration, hence is determined by the chain configuration and by definition will equal the sample size at T_2 where only one conformation is available to each molecule. The polymer sample

is described as an ensemble of co-operative regions, or subsystems, each containing Z monomeric segments. The transition probability of such a co-operative region is then calculated as a function of its size, to be

$$W(T) = Aexp(-Z\Delta\mu/kT)$$

where $\Delta\mu$ is the activation energy for a co-operative rearrangement per monomer segment. This can be approximately expressed in the WLF form.

While these models did a fairly good job in terms of understanding the glass transition process, they are not capable of predicting the glass transition temperature dependence of chain length, side chain, and polarizability, etc. Understanding these dependence are very important in terms of design various exotic polymer materials. In principal, detailed knowledge can be obtained by using numerical simulation techniques.

6.3 Computer Simulations

There are mainly two categories in terms of computer simulation, the Monte Carlo (MC) and molecular dynamics (MD). Of the two methods, MD potentially is the more useful one since it can provide information on the time evolution of a system as well as its time-averaged properties, thus allowing the study of many kinetic aspects of the glassy state. Both MC and MD methods have been applied to the study of glass formation of simple liquid systems. Although some question still remains as to the validity of these studies, mainly because of the very short duration of simulation (10-100 (ps)) in comparison to the laboratory experiments, they have nonetheless found widespread use and provided many useful insights into the nature of the glassy state. Rigby and Roe[9] did a series of molecular dynamics simulations for polymer liquid and glass. Their force field parameters are chosen to mimic polyethylene. Behaviors suggestive of liquid-to-glass transition were exhibited by (i) cessation of trans-gauche

conformational transitions, (ii) changes in the temperature coefficients of the density and internal energy, and (iii) effective vanishing of the segmental self-diffusion coefficient. The duration of these simulation is 100-120 (ps). Inspired by their encouraging work, we hope we can do a better job by using NPT Gibbs dynamics to mimic experimental condition and by using carefully calibrated force field.

6.4 The Force Field

All calculations used the MSXX force field of polyethylene by Karasawa,[10] but including a full torsional potential (based on HF calculations for C_4H_{10}). This force field has the form

$$E = E_{val} + E_{vdw} + E_Q \tag{1}$$

where

$$E_{val} = E_{bond} + E_{angle} + E_{torsion} + E_{cross} \tag{2}$$

Here

- E_Q represents the Coulomb interaction energy (using a charge of +0.144e on each H and balancing charges on each C).
- E_{vdw} uses an exponential-6 function for the nonbond interactions.
- E_{bond} is a harmonic function (same R_e and k_R as for the Morse potential).
- E_{angle} is a cosine harmonic function.
- $E_{torsion}$ describes the rotational barriers for all dihedrals IJKL.
- $E_{cross} = E_{BB1} + E_{BA1} + E_{AA1} + E_{AA2}$, where E_{BB1} and E_{BA1} describe bond-bond and angle-bond cross terms for all bonds sharing a common vertex. E_{AA1} describes one-center angle-angle cross terms, and E_{AA2} describes two-center angle-angle cross terms.

The functional forms and parameters of the force field are summarized in Table [6.1].

Table 6.1: Force Field Parameters for Polyethylene

van der Waals[a]	R_v	D_v	Bond	r_e	k_r	
H	2.9276	0.03350	C–H	1.0758	729.593	
C	3.8050	0.06921	C–C	1.4814	902.669	
Angle	θ_e	k_θ	$k_{r_1\theta}$	$k_{r_2\theta}$	$k_{r_1r_2}$	
H–C–H	119.742	54.065	-22.790	-22.790	4.027	
C–C–H	118.140	64.715	-36.302	-25.208	1.283	
C–C–C	121.518	82.155	-53.249	-53.249	27.286	
Torsion	V_1	V_2	V_3	V_4	V_5	V_6
H–C–C–H			2.313			
C–C–C–H			1.611			
C–C–C–C	-4.505	-0.428	-2.845	0.456	-0.361	-1.260
2c-angang[b]	$k_{\theta_1\theta_2}$					
HCC, CCH	-17.534					
CCC, CCH	-17.996					
CCC, CCC	-23.530					
1c-angang[c]	$k_{\theta_1\theta_2}$					
HCC, CCH	-5.354					
HCH, CCH	-5.785					
HCC, CCC	-8.470					
HCC, CCH	-5.934					

[a] $E_{vdw} = D_v(\rho^{-12} - 2\rho^{-6})$ where $\rho = R/R_v$. The off-diagonal oarameters D_v and R_v are obtained from geometric mean.

[b] $E_{2AA} = k_{\theta_1\theta_2}(\cos\theta_1 - \cos\theta_1^e)(\cos\theta_2 - \cos\theta_2^e)$. This couples I–J–K and J–K–L in the dihedral I–J–K–L.

[c] $E_{1AA} = E_{2AA} = k_{\theta_1\theta_2}(\cos\theta_1 - \cos\theta_1^e)(\cos\theta_2 - \cos\theta_2^e)$. This couples angles I–J–K and I–J–L where J is bonded to atoms I, K and L.

6.5 Dynamics

The properties of amorphous polyethylene were simulated using a single chain of polyethylene with 70 monomer units (including a methyl group at each end) in a triclinic periodic cell. (This leads to $C_{70}H_{142}$ or 212 atoms per cell.) The initial structure of the amorphous system was built by using periodic boundary conditions (PBC) and a random distribution of torsional angles consistent with Monte Carlo exclusions (based on van der Waals radii scaled by 0.3). The final density is 0.85 (g/cc). The starting structure was annealed using molecular dynamics (MD) at various temperatures. The MD simulations used the canonical Gibbs dynamics algorithms based on the work by Nosé,[11] Andersen,[12] Rahman[13] and Parrinello.[14] The Hamiltonian of Gibbs dynamics is

$$H^{gibbs} = H_{part} + H_{nose} + H_{stress} \tag{3}$$

$$H_{part} = \sum_{i=1}^{3N} \frac{1}{2m_i} p_i^2 + V\left(q_1, ..., q_{3N}\right) \tag{4}$$

describes the ordinary Hamiltonian for the N particles,

$$H_{nose} = \frac{1}{2Q} p_s^2 + (3N+1) kT_{bath}\ lns \tag{5}$$

describes the temperature bath, and

$$H_{stress} = \frac{1}{2W} \sum_{i=1}^{6} \dot{h}_i^2 + p\left(\Omega - \Omega_0\right) + \frac{1}{2} \sum_{\alpha\beta\gamma} \Sigma_{\beta\gamma} H_{\alpha\beta} H_{\alpha\gamma} \tag{6}$$

with

$$\Sigma = \Omega_0 H_0^{-1} \left(-S - p\right) \tilde{H}_0^{-1}$$

describes the stress bath. Here the Nosé mass is written as

$$Q = 3NkT_{bath}\tau_s^2 \tag{7}$$

where the Nosé relaxation time τ_s is taken as $\tau_s = 1$ (ps).

The Anderson mass W is written as

$$W = W_{cell} \sum_{i=1}^{N} M_i \tag{8}$$

where M_i is the mass of each particle in the unit cell and $W_{cell} = 1$ is used for measurements while larger variables are used for the initial equilibration (vide infra).

The Coulomb and van der Waals' interactions were calculated using the accuracy bounded convergence acceleration (ABCA) methodology of Karasawa and Goddard.[15] The ABCA accuracies for both Coulomb and van der Waals calculations were set at $0.01 * 212 = 2.12$ (kcal/mol).

6.6 The Annealing and Quenching Procedure

Critical to the prediction of temperature dependent properties, such as glass transition temperatures, is obtaining equilibrated structures at each temperature. Thus we must prevent the dynamics from trapping into local minima for lower temperature simulations.

1. Generate an amorphous structure using a Monte Carlo growth procedure at high temperature, T_{grow}.

2. Anneal the initial structure by high temperature Gibbs dynamics for a time τ_{grow} to obtain an equilibrated amorphous polymer.

3. Decrease the temperature by an amount ΔT and re-equilibrate using Gibbs dynamics for a time τ_{equil} sufficient to re-equilibrate the structure to the new temperature and to measure its properties.

4. Continue step 3 until a sufficiently low temperature T_{final} is reached.

For polyethylene, we grow the amorphous at 450 (K). Set $W_{cell} = 1000$, equilibrate 100 (ps), then decrease W_{cell} to 100 for 20 (ps), to 10 for 20 (ps) and finally reduced

to $W_{cell} = 1$ for 20 (ps). The criterion here is that both atomic kinetic energy and cell temperature do not drift with time. The large initial W_{cell} serves to restrict the cell from expanding too fast due to bad configurations in the initial amorphous structure.

It is essential that the annealing ΔT not be so large as to trap the configuration in metastable configurations. We considered various values for ΔT and τ_{equil} and found that $\Delta T = 50$ (K) with $\tau_{equil} = 100$ (ps) is satisfactory. Figure 6.1 shows the unit cell volume fluctuation during dynamics at various temperatures.

6.7 Results

6.7.1 The Glass Transition Temperature

For the $\Delta T = 50(K), \tau_{equil} = 100$ (ps) runs, by using the equilibrated portion of the dynamics at each temperature (usually the last 75 (ps)), we obtain the average volume as a function of temperature V(T), as shown in Fig. 6.2. A clear kink in the $\bar{V}(T)$ curve occurs at about 235 (K). The volume fluctuation is

$$\langle \delta V^2 \rangle = \langle V^2 - \bar{V}^2 \rangle$$

where

$$\bar{V} = \langle V \rangle. \tag{9a}$$

The average volume fluctuation is related to compressibility $\beta(T)$ by

$$RT\beta(T) = \frac{\langle \delta V^2 \rangle}{\bar{V}} \tag{9b}$$

Figure 6.3 shows a clear kink in the $RT\beta(T)\bar{V}$ curve at about 218 (K). Figure 3 shows the average value, $\bar{R}_{end-end}(T)$, as a function of temperature. There is a clear kink at 225 (K), above which $\bar{R}_{end-end}(T)$ increases rapidly with temperature and below

which it changes slowly. Similarly the fluctuation in end-to-end distances.

$$\delta R_{end-end} = \sqrt{\langle R^2_{end-end} - \bar{R}^2_{end-end} \rangle} \tag{10}$$

shows a slowly increasing value for $T \leq 200$ (K) and a much larger increase above $T > 250$ (K). Figure 6.4a shows the average end-end distance versus dynamics temperature, while Fig. 6.4b is the standard deviation of end-end distance. Thus

a. above 225 (k) polyethylene is a viscous liquid with the conformational structure adapting to the thermodynamics for each temperature.

b. below T_g the conformational is frozen into a glass because the diffusional rates of one polyethylene strand moving amongst the other polyethylene strands becomes too slow.

Based on the above results, we associate the kinks with the glass temperature of PE, obtaining a theoretical value of

$$T_g^{th} = 225 \pm 10(K) \tag{11}$$

Although the literature[16–19] has conflicting experimental T_g values, the calculated value correlates well with the most recent values of 235 to 240 (K) (determined by calorimetry) and 222 to 240 (K) from fitting the WLF equation to values measured for relaxation).

6.7.2 Conformational Transitions

In order to understand the atomistic origins for T_g^{th}, we examined the rate of conformational transformations. Every 0.1 (ps) of dynamics the structure was saved in a trajectory file which was then analyzed to obtain rates as follows. We classify each C-C-C-C dihedral angle in terms of:

i. stable conformations: $T(\phi = 180 \pm 30°)$, $G^+(\phi = 60 \pm 30°)$, $G^-(\phi = 300 \pm 30°)$, and

ii. transitional conformations: $GT^+(120 \pm 30°)$, $GT^-(240 \pm 30°)$, $G^+G^-(0 \pm 30°)$.

[We do not consider rotations of the terminal CH_3 groups, thus there were 67 torsions in the analysis.] A transition is counted for each case where a dihedral changes between two stable configurations, separated only by the corresponding transitional conformation. These rates are plotted in Fig. 6.5. There are no transitions for $T \leq 200$ (K) and an increasing rate of GT transitions for $T \geq 250$ (K). They are also plotted in an Arrhenius form in Fig. 6.6,

$$\kappa_{GT} = A_{GT} exp\left[- \frac{E^{act}_{GT}}{RT} \right]$$

leading to

$$E^{act}_{GT} = 3.45 \ (kcal/mol)$$

$$A_{GT} = 2.39 \times 10^{10} \ (sec^{-1} dih^{-1})$$

There are 67 central dihedrals per polyethylene chain and one chain per unit cell. Thus the frequency factor per dihedral is

$$A_{GT} = 3.52 \times 10^{8} \ (sec^{-1} dih^{-1})$$

For comparison, we carried out similar calculations for an isolated chain with 10 monomers. Here we also find an Arrhenius form, but with

$$E^{act}_{chn} = 3.13 \ (kcal/mol)$$

$$A_{chn} = 3.3 \times 10^{11} \ (sec{-}1)$$

The normalized frequency factor becomes

$$A_{chn} = 3.3 \times 10^{10} \ (sec{-}1dih{-}1)$$

The adiabatic rotational barrier about the central bond of hexane is

$$A_{chn} = 3.0 \ (kcal/mol)$$

The activation energy for GT transition in amorphous polyethylene is about 0.23 (kcal/mol) higher than that of single chain polyethylene. In the condensed phase the effective barrier is increased because of the conformational constraints. These conformational constants decreases the frequency factor by almost two magnitude lower than single chain polyethylene.

The glass transition temperature can be understood as the temperature above which conformational transitions are sufficient fast that the molecule attains conformational equilibrium (a viscous liquid), but below which the inter-diffusion of polymer chains is two slow for the system to equilibrate. The conformational relaxation is directly related to the rate of dihedral angle transitions which in turn depends on both the rotational energy barrier and on how closely the polymer chain is packed in periodic cell.

6.8 Discussion

The simulations performed are quite restricted, the molecular weight is very small and there is only one chain per unit cell. Nevertheless, we believe that the kinkyness observed represent a glass transition with the same atomistic origins as found experimentally for amorphous PE.

Experimental measurements of T_g often involve time scales of sec to msec where the total time for our simulation is about 1 nano second. This raises the question as to whether one should expect a nsec simulation to measure the same phenomena

as observed in a 1 second experiment. We believe that it is plausible that they correspond. The reason is that the use of PBC indicates an infinitely range correlation in the motions. Thus moving an atom in the unit cell simultanously moves atoms that are microns, indeed cm away. Experimentally, the heterogeneity of the system requires time scales sufficiently slow that the entire sample is in thermal and stress equilibrium. For a 1cm sample this may require seconds.

6.9 Conclusion

Using a systematic methodology for molecular dynamics simulations, we obtain clear cut glass transitions at temperature $T_g = 225 \pm 10$ (K). This is close to the most recent experiments which indicates $T_g \approx 235$ (K). We also find that this glass transition correlates quite well with the calculated rates of gauche-trans conformational transitions.

6.10 References

1. P.J. Flory, *Principles of polymer chemistry*, 1953, Ithaca, Cornell University Press.

2. P.J. Flory, *Statistical mechanics of chain molecules*, 1969, New York, Interscience Publishers.

3. K.S. Schweizer, "Microscopic theory of the dynamics of polymeric liquids: general formulation of a mode-mode-coupling approach," *J. Chem. Phys.* **91(9)**, 1989, 5802-21.

4. D. Turnbull, M.H. Cohen, "Free-volume model of the amorphous phase: glass transition," *The Journal of Chemical Physics* **34(1)**, 1961, 120-125.

5. M.H. Cohen, G.S. Grest, "Liquid-glass transition, a free-volume approach," *Physical Review B*, **20(3)**, 1979, 1077-98.

6. M.L. Williams, R.F. Landel and J.D. Ferry, "The temperature dependence of relaxation mechanisms in amorphous polymers and other glass-forming liquids," *J. Am. Chem. Soc.* **77**, 1955, 3701-3707.

7. J.H. Gibbs, E.A. Dimarzio, "Nature of the glass transition and the glassy state," *The Journal of Chemical Physics* **28(3)**, 1958, 373-383.

8. G. Adam and J.H. Gibbs, *J. Chem. Phys.* **43**, 1965, 139.

9. D. Rigby and R. Roe, "Molecular dynamics simulation of polymer liquid and glass. I. Glass transition," *J. Chem. Phys.* **87(12)**, 1987, 7285-92.

10. N. Karasawa, S. Dasgupta, W.A. Goddard III, "Mechanical-properties and force-field parameters for polyethylene crystal," *J. Phys. Chem.*, **95(6)**, 1991, 2260-2272.

11. S. Nose, "Constant temperature molecular-dynamics methods," *Progress of Theoretical Physics Supplement* **103**, 1991, 1-46.

12. H.C. Andersen, *J. Chem. Phys.* **72**, 1980, 2384.

13. J.R. Ray and A. Rahman, *J. Chem. Phys.* **80**, 1984, 4423.

14. M. Parrinello and A. Rahman, *J. Appl. Phys.* **52**, 1981, 7182.

15. N. Karasawa and W.A. Goddard III, "Acceleration of convergence for lattice sums," *J. Phys. Chem.* **93(21)**, 1989, 7320-7327.

16. S.S. Chang., *J. Polym. Sci. Symp.* **43**, 1973, 43.

17. G.T. Davies and R.K. Eby., *Macromolecules* **44**, 1973, 4274.

18. Y.T. Jang, D. Parikh and P.H. Philipps., *J. Polym. Sci.* **23**, 1985, 2483.

19. N. Alberola, J.Y. Cavaille and J. Perez., *Eur. Polym. J.* **28(8)**, 1992, 935-948.

6.11 Figures

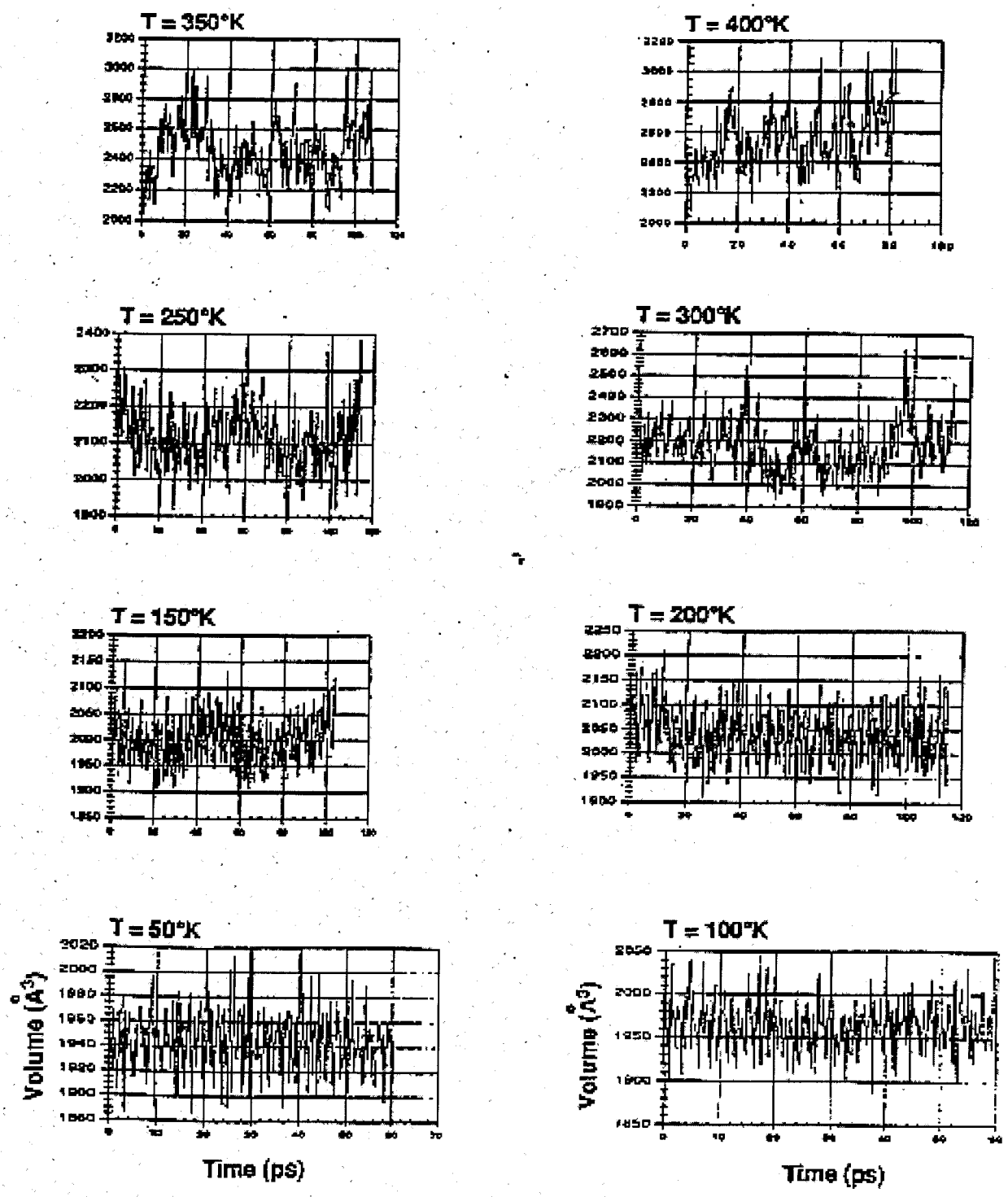

Figure 6.1: Unit Cell Volume Versus Dynamics Time

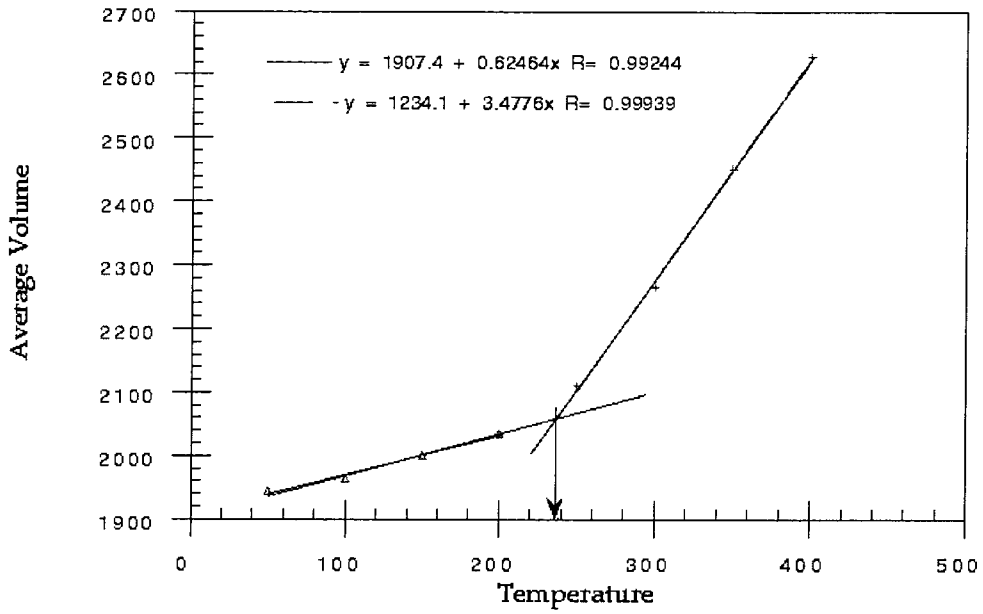

Figure 6.2: Average Unit Cell Volume Versus Dynamics Temperature

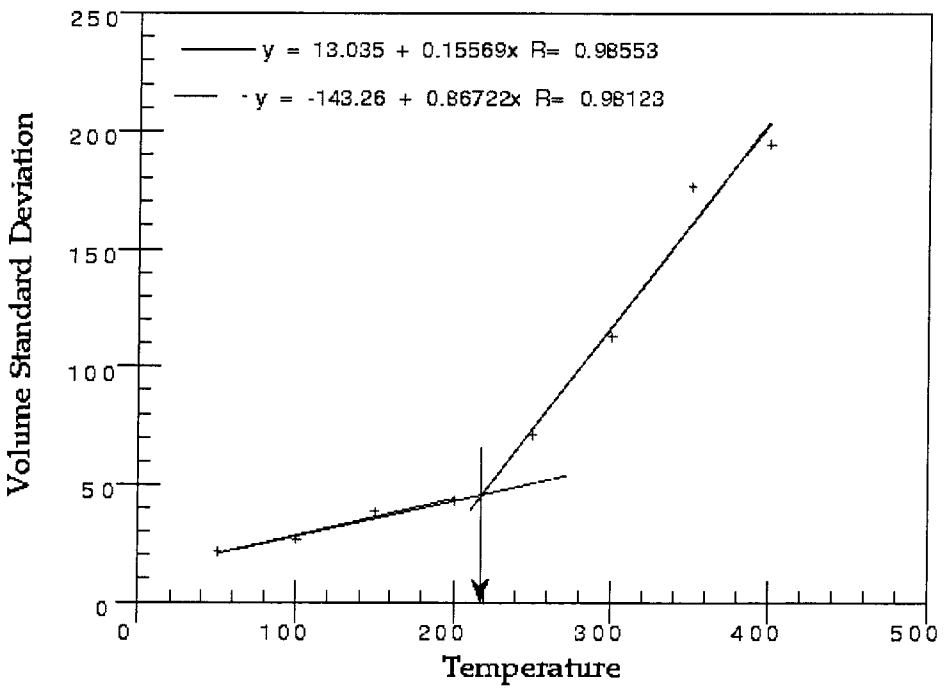

Figure 6.3: Standard Deviation of Unit Cell Volume Versus Dynamics Temperature

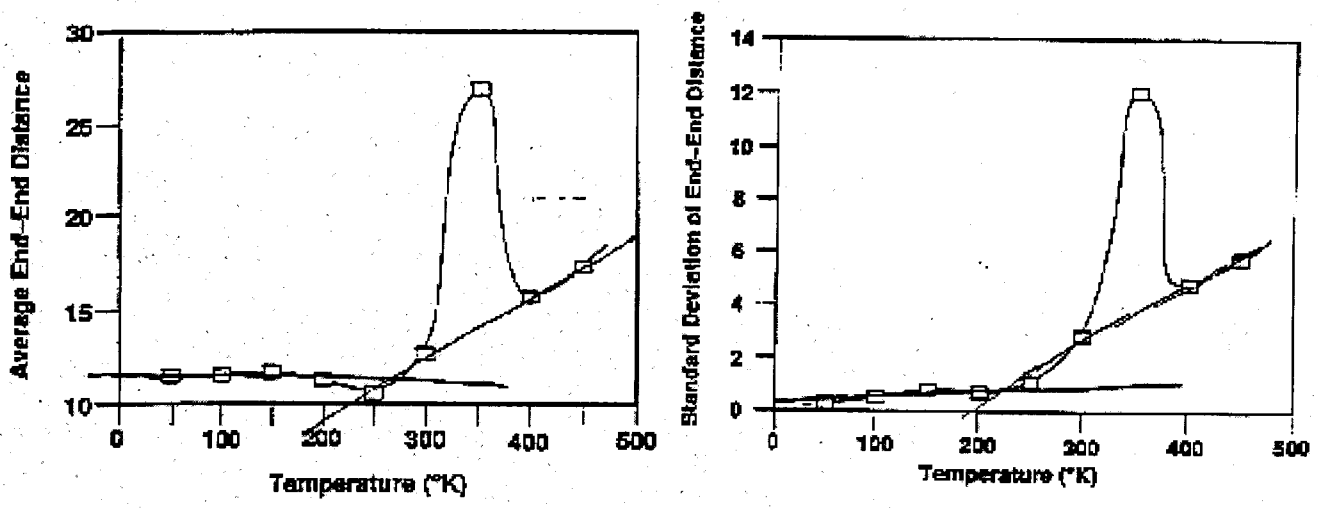

Figure 6.4: End-end Distance Versus Dynamics Temperature

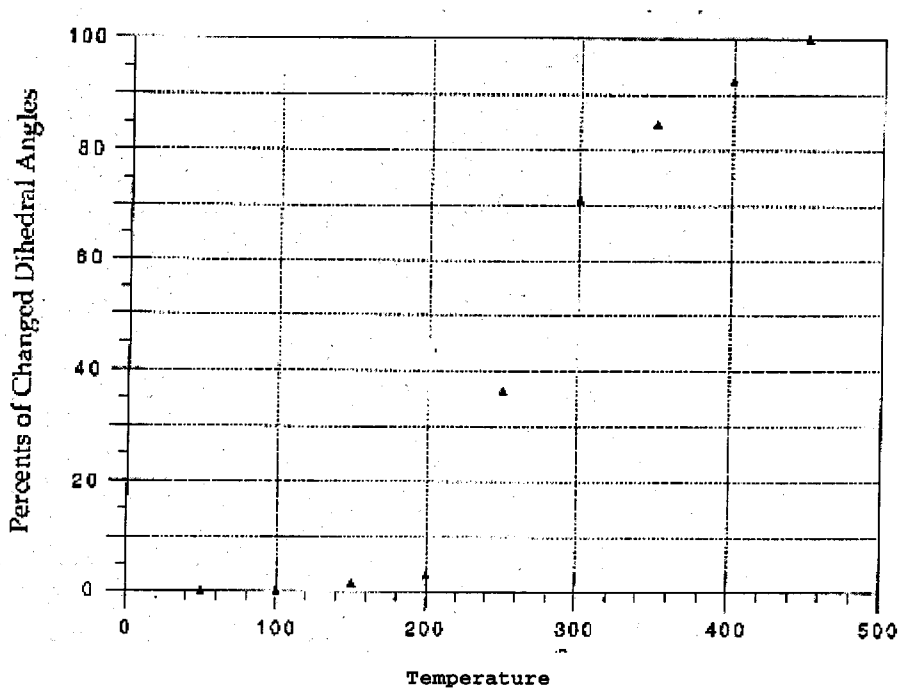

Figure 6.5: Frequency of Torsional Transition Versus Dynamics Temperature

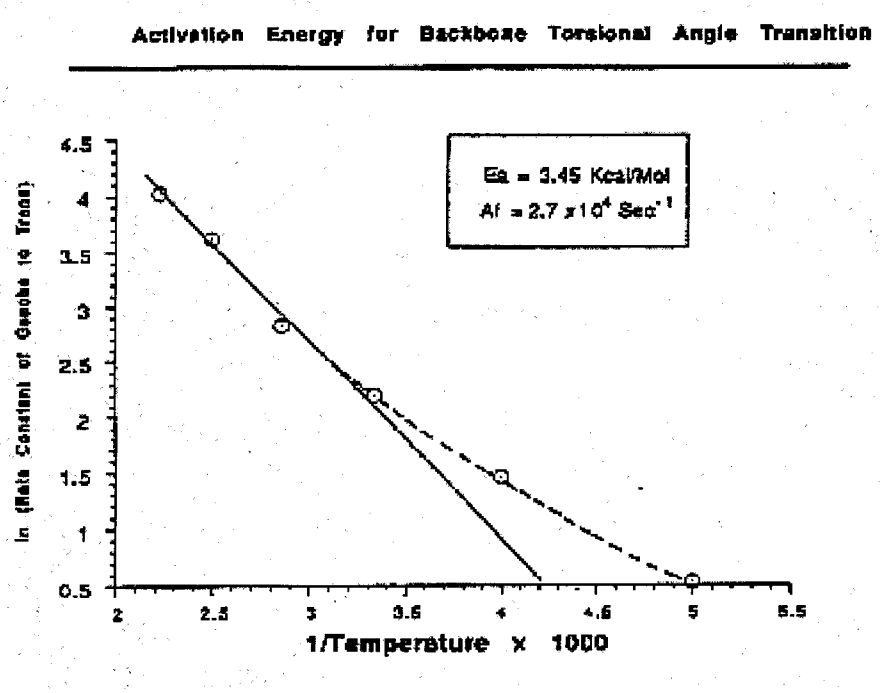

Figure 6.6: Activation Energy of Torsional Rotation

Chapter 7 Molecular Dynamics Simulations of Fluoro Polymers: Prediction of Glass Transition Temperatures Using United Atom Force Fields

7.1 Abstract

We report a new United Atom Force Field (denoted MSUA) for molecular dynamics simulation of the fluoro polymers: Poly(tetrafluoroethylene) (PTFE), Poly(vinylidene fluoride) (PVDF), and Ethylene-tetrafluoroethylene (ETFE). The MSUA was obtained from combining quantum chemistry and experimental results. Using the MSUA and periodic boundary conditions, we carried out molecular dynamics simulations using a Build-Anneal-Quench procedure. For PTFE, PVDF, and ETFE fluoro polymers, these results predict transition temperatures (T_g) in good agreement with the experimental T_g.

7.2 Introduction

Polymer materials containing fluorine atoms have unique properties.[1] Compared to the corresponding hydrocarbon analogues, they have:

i. Very low surface tension and friction coefficient,

[5]Based on "Molecular Dynamics Simulations of Fluoro Polymers: Prediction of Glass Temperatures Using United Atom Force Fields," **H. Murofushi, G. Gao, M.P. Belmares, and W.A. Goddard III**, submitted.

ii. High chemical stability to strongly acidic or basic environments,

iii. High thermal stability,

iv. Piezo- and pyro-electric properties (e.g., PVDF),

v. Low refractive index.

It is important to combine or enhance these basic characteristics of fluoropolymers in order to develop new materials. Thus, an atomistic understanding of the mechanism and origin of these properties is essential.

Fluoro polymers are very useful for many applications,[2] with

$$\text{Poly(tetrafluoroethylene)(PTFE)} : \; -(CF_2 - CF_2)_n- \tag{7.1}$$

$$\text{Poly(vinylidenefluoride)(PVDF)} : \; -(CF_2 - CH_2)_n- \tag{7.2}$$

$$\text{Ethylene} - \text{tetrafluoroethylene(ETFE)} : \; -(CF_2 - CF_2 - CH_2 - CH_2)_n- \tag{7.3}$$

serving as typical and important fluoro polymers. PTFE (DuPont's Teflon^R) is a homopolymer of Tetrafluoroethylene ($CF_2 = CF_2$), PVDF is a homopolymer of Vinylidene fluoride ($CF_2 = CH_2$), and ETFE is a copolymer of Ethylene ($CH_2 = CH_2$) and Tetrafluoroethylene.

These three fluoro polymers provide fundamental structures that might be combined to design and develop novel fluoro polymers. Though often more complicated in practice, we consider here simple models with no branches, with all head-to-tail sequences (PVDF), and with perfectly alternating copolymer structures (ETFE).

The glass transition temperature (T_g) of a polymer is a most important property because it determines the range of temperatures for processing and the range for applications.[3] This temperature is the boundary between a low temperature stiff,

glassy state and a high temperature rubbery state (due to the onset of long-range coordinated motion).[4] The temperature dependence of many properties of amorphous polymers (modulus, specific volume, enthalpy, entropy, specific heat, refractive index, and dielectric constant) changes dramatically at T_g.[5]

The changes in these properties at T_g can be understood as follows.[6] Above T_g, the polymer conformation is in equilibrium; thus the spatial size expands with temperature. To change conformation, the polymer strands must interdiffuse in a matrix of other polymers. Below T_g, this diffusion is too slow, and the conformation does not change. Thus we get a glass. The problem is that there is little understanding of how T_g depends on the atomistic nature of the polymer. Thus to design materials with the proper properties requires numerous experiments, resulting in high cost, long delays, and less optimal performance. In order to determine whether atomistic simulations could provide useful information about the glass temperature, we carried out systematic studies of temperature dependence for several properties of three fluoro polymers, (1)-(3).

7.3 The United Atom Force Field

Normally all atoms are treated explicitly in molecular dynamics simulations. However, for problems in which chain torsions and interchain contacts dominate, use of implicit or United Atoms (UA) may be useful.[19] The concept is that for a polymer such as Fig. 7.1a, each $-CF_2-$ is replaced by a single atom C_F^* and each $-CH_2-$ is replaced by a single atom C_H^*, in such a way that the polymer properties are not changed. The use of UA's can greatly decrease the calculational time. Thus:

- the number of atoms needed in simulation is smaller by a factor of 3,
- the number of nonbond interactions per atom is also reduced by a factor of 3;
- the time steps can be decreased by a factor of 3 (3 fs for UA simulations compared with 1 fs for all atom simulation).

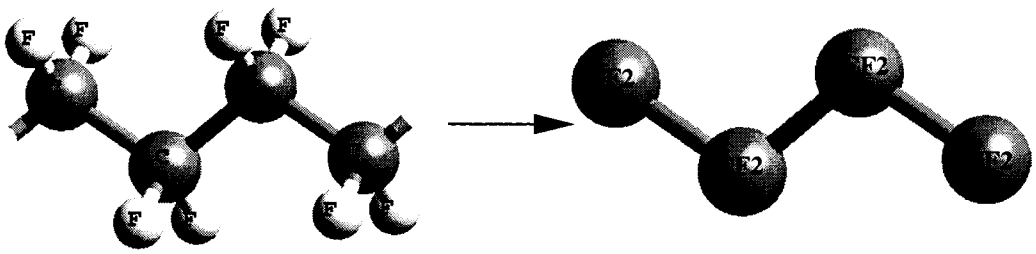

Figure 7.1: Concept of united atoms

This leads to a factor of 27 net savings.

7.3.1 Force Fields

The heart of atomistic simulations is the development of an accurate Force Field (denoted FF) for use in molecular mechanics and molecular dynamics.

The energy expression

$$E_{total} = E_{valence} + E_{nonbond} \tag{7.4}$$

includes valence ($E_{valence}$) terms involving covalent bonds and long-range noncovalent interactions ($E_{nonbond}$) interactions. Here we take the covalent terms

$$E_{valence} = E_{bond} + E_{angle} + E_{torsion} \tag{7.5}$$

to include bond stretch (E_{bond}), angle bend (E_{angle}), and dihedral angle torsion

($E_{torsion}$), while the nonbond terms

$$E_{nonbond} = E_{vdW} + E_{Coulomb} \tag{7.6}$$

consist of van der Waals (E_{vdW}) and electrostatic ($E_{Coulomb}$) terms. We excluded 1-2, 1-3, and 1-4 nonbond interactions.

Valence Interactions

The valence interactions (5) are described using the following expressions:

- Bond Stretch Terms (Harmonic)

$$E_{bond}(R) = \frac{1}{2} K_R (R - R_o)^2 \tag{7.7}$$

  where R is the bond length, R_o is the equilibrium bond length, and K_R is the force constant.

- Angle Bend Terms (Theta Harmonic)

$$E_{angle}(\theta) = \frac{1}{2} K_\theta (\theta - \theta_o)^2 \tag{7.8}$$

  where θ is the angle between two bonds to a common atom, θ_o is the equilibrium length, and K_θ is the force constant.

- Torsion Terms (Cosine Fourier Expansion)

  For a sequence of three bonds IJ, JK, KL along the chain, we define ϕ as the dihedral torsional angle ($\phi = 0$ corresponds to cis) and write the energy as a Fourier expansion

$$E_{torsion}(\phi) = \sum_{n=0}^{12} V_n \, cos(n\phi) \tag{7.9}$$

Nonbond Interactions

The nonbond interactions (6) are described by using the following expressions:

- Electrostatic Terms (Coulomb)

  The electrostatic interactions between two atoms i and j is

$$E_{Coulomb}(R_{ij}) = C_Q \frac{Q_i Q_j}{\epsilon R_{ij}} \tag{7.10}$$

  where Q_i is the charge on center i (electron units), $\epsilon = 1$, and the constant C_Q = 332.0637 gives energies in kcal/mol when R_{ij} is the distance in angstrom.

- van der Waals Terms (Lennard-Jones 12-6)

  The van der Waals interaction between atoms i and j are written as

$$E_{vdW}(R_{ij}) = D_v \left[\left(\frac{R_v}{R_{ij}} \right)^{12} - 2 \left(\frac{R_v}{R_{ij}} \right)^{6} \right] \tag{7.11}$$

  where R_{ij} is the distance between the atoms, R_v is the equilibrium distance, and D_v is the well depth. The geometric mean combination rules is used:

$$R_{vij} = \sqrt{R_{vii} R_{vjj}} \tag{7.12}$$

$$D_{vij} = \sqrt{D_{vii} D_{vjj}} \tag{7.13}$$

  The ABCA Ewald summation method[7] was used to sum the nonbond interactions.[8]

7.3.2 Force Field Parameters

Bond Stretch and Angle Bend Terms

For bond stretch and angle bend parameters, we use the DREIDING FF values.[9] Thus the C-C bond parameters are used for UA C*-C* bonds and C-C-C angle parameters

are used for UA C*-C*-C* angle terms.

Torsional Potentials

The distribution of conformations in a polymer and the rates of conformational transitions have a strong effect on such properties as T_g, and hence it is critical that the FF lead to the correct relative energies of the torsional minima (e.g. trans versus gauche) and barrier heights between them. Thus the torsional FF parameters are particularly important for descrbing amorphous polymers. Consequently, we used *ab initio* calculations on finite model molecules to provide the torsional potential energy parameters for infinite polymer chain.

The Hartree-Fock (HF) calculations lead to a total torsional potential function $E_{HF}(\phi)$ which we want to exactly fit the FF. We determine $E_{HF}(\phi)$ by fixing ϕ and optimizing all other degrees of freedom for each conformation. Thus we write

$$E_{HF}(\phi) \cong E_{FF}(\phi) = E_{bond}(\phi) + E_{angle}(\phi) + E_{torsion}(\phi) + E_{nonbond}(\phi) \tag{7.14}$$

$$= E_{no-torsion}(\phi) + E_{torsion}(\phi) \tag{7.15}$$

[for the C_4 UA model used below, $E_{nonbond}(\phi) = 0$ because 1-2, 1-3, and 1-4 nonbond interactions are excluded]. We define the torsional potential as

$$E_{torsion}(\phi) = E_{HF}(\phi) - E_{no-torsion}(\phi) \tag{7.16}$$

where

$$E_{no-torsion}(\phi) = E_{bond}(\phi) + E_{angle}(\phi) \tag{7.17}$$

Here, $E_{no-torsion} = 0$, because there is no strain in C_4 systems composed of UA's.

Thus,

$$E_{torsion}(\phi) = E_{HF}(\phi) \tag{7.18}$$

Quantum mechanical calculations were at the HF level (using[10] Gaussian 92 and PS-GVB[11]). The D95* basis was used for PTFE model compounds and the 6-31G** basis was used for PVDF and ETFE model compounds. The torsional potentials, Fig. 7.2, are expected to be quite accurate. For PTFE we used $CF_3CF_2 - CF_2CF_3$ as the model. For PVDF we used $CF_3CH_2 - CF_2CH_3$ as the model. For ETFE, we need three kinds of torsional potential because ETFE has three different torsional curves; (1) $-CF_2CF_2 - CH_2CH_2-$, (2) $-CH_2CF_2 - CF_2CH_2-$, and (3) $-CF_2CH_2$-CH_2CF_2-. Thus, we used three model compounds: (1) $CF_3CF_2 - CH_2CH_3$, (2) $CH_3CF_2 - CF_2CH_3$, and (3) $CF_3CH_2CH_2CF_3$, respectively, for these three torsions. Details are as follows:

- PTFE

  This was optimized at five dihedral angles; the global minimum ($\phi = 165.6°$), the gauche minimum ($\phi = 55.28°$), the trans form ($\phi = 180°$), the eclipsed form ($\phi = 120°$), and the cis form ($\phi = 0°$) which were rigidly rotated around the central C-C bond (Table 1).[25] These five points energies were interpolated with cubic splines and the energy calculated at 10° increments (Fig. 7.2a). The Fourier expansion of this torsional potential was used to determine the torsional constants (V_0, V_1, ..., V_{12}) for POLYGRAF.[8]

- PVDF

  This was optimized[26] at seven points; 0°, 30°, 60°, 90°, 120°, 150° and 180° and fitted the same as for PTFE (Fig. 7.2b).

- ETFE

  a. $CF_3CF_2 - CH_2CH_3$: This was optimized at four points; gauche (66.30°), trans (180°), eclipse (120°), and cis (0°).

b. $CH_3CF_2 - CF_2CH_3$: This was optimized at four points; gauche (65.30°), trans (180°), eclipse (120°), and cis (0°).

c. $CF_3CH_2 - CH_2CF_3$: This was optimized at seven points; gauche (73.95°), trans (180°), eclipse (120°), cis (0°), 60°, 100°, and 130°. This torsional potential is strange compared with the other torsional curves. The gauche form seems to be less stable because of repulsion between both terminal CF_3 groups.

These results were fitted with the same procedure for PTFE (Fig. 7.2c, 7.2d, 7.2e).

Charges

The charges for all-atom simulations were obtained (using PS-GVB[11]) from accurate HF calculations (6-31G** basis set) on

$$CF_3 - CH_2 - CF_2 - CH_2 - CF_2 - CH_3 \tag{7.19}$$

for PVDF and on

$$CF_3 - CH_2 - CH_2 - CF_2 - CF_2 - CH_3 \tag{7.20}$$

for ETFE. Using the electron density to calculate electrostatic potentials and fitting to atomic charges leads to the result in Fig. 7.2. For all-atom polymer calculations we used the atomic charges from the central $-CF_2-$ and $-CH_2-$ groups in Fig. 7.3.

For PVDF and ETFE, we estimated the charge of each UA by summing the charges of three atoms.

$$\text{PVDF} : Q_{CF*} = 0.23, Q_{CH*} = -0.23 \tag{7.21}$$

$$\text{ETFE} : Q_{CF*} = -0.06, Q_{CH*} = 0.06 \tag{7.22}$$

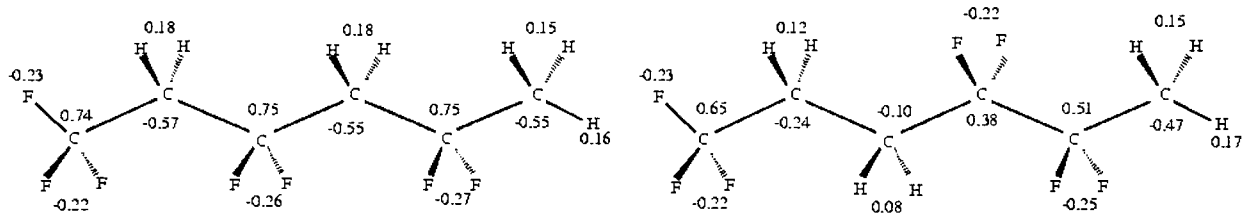

(a) PVDF **(b) ETFE**

Figure 7.2: Atomic charges obtained by fitting electrostatic potential from Hartree-Fock Calculation

van der Waals Parameters

The vdW parameters for C_F* and C_H* were determined from fitting lattice parameters, densities, and compressibilities of PTFE (phase II),[20] PVDF (α and β phases)[21], and ETFE crystal.[22] The results are listed in Table 2. The accuracy in predicting the cell parameters of PTFE, PVDF, and ETFE crystal forms suggest that these vdW parameters are reasonably accurate. For terminal CF_3 and CH_3 groups in amorphous polymers, we used the same vdW parameters as for CF_2 and CH_2.

The C_H* parameters were applied to Polyethylene (PE) crystal,[23] leading to good agreement with experimental (Table 2). Thus, these vdW parameters can be applied to simulation of other hydrocarbon and fluorocarbon polymers.

7.3.3 Summary

The final parameters for the MSUA FF are listed in Table 3.

7.4 Molecular Dynamics Simulations

7.4.1 Simulation Details

The following procedure (denoted as T_g−BAQ) was used in these studies. It has also been used for a number of other polymers (PE,[13], PS,[14] PVC,[15] Cl-PVC[15]) with similar results.

Build an Amorphous Structure

We generated an amorphous structure with random torsions using the RIS Monte Carlo algorithm of POLYGRAF ($R_{cut} = 0.3 * R_{vdW}$) with a temperature of T_{build} = 500 to 600 (K) (chosen well about T_g) at the estimated experimental amorphous density ($\rho_{initial}$). The polymer system consisted of a single chain of 200 UA units in a periodic box.

Anneal the Structure at High Temperature

Gibbs dynamics (NTP)[12] were run at the build temperature until the volume equilibrated. The time step was 3 fs. The Rahman-Parrinello mass,[12b] $W = w * masscell$ (where *masscell* is the total mass per unit cell), was adjusted as follows: a high value (w = 9999) was used initially and was ramped down gradually to w = 0.1 as the system equilibrated. This procedure generally required $\sim$ 200 ps of dynamics.

Quench at Uniform Rate

The temperature was dropped by a fixed amount (ΔT = -50 (K)) and the dynamics started with the structure and velocities from previous temperature. The structure was re-equilibrated for 100 ps. This step was repeated until the final temperature is well below T_g (T_{final} = 50 or 100 (K)).

7.4.2 Results and Discussion

The conformation and properties from $T_g{-}BAQ$ were saved every 0.1 ps (the trajectory file) which was analyzed to obtain the various temperature dependences.

PTFE

For PTFE we used T_{build} = 600 (K), $\rho_{initial}$ = 2.0 (g/cc), $\Delta T = -50$ (K), T_{final} = 50 (K). The simulation results are summarized in Fig. 7.4. The experimental T_g is reported[16] to be about 400 (K).

- Figure 7.4a shows the temperature dependence of the average volume, $\bar{V}(T)$. At lower temperatures (50 to 300 (K)), $\bar{V}(T)$ changes linearly with a small slope, while at higher temperatures (450 to 600 (K)), $V(T)$ is linear with a much larger slope. These two lines intersect, leading to a distinct kink at 396 (K).

- The compressibility, β, is extracted from the dynamics as

$$\beta = \langle (V - \bar{V})^2 \rangle / k_B T \bar{V}$$

  where $\langle (V - \bar{V})^2 \rangle$ is the average volume fluctuation. Figure 7.4b shows the temperature dependence of $\beta(T)$ which also shows a distinct kink at 376 (K).

- Figure 7.4c shows the temperature dependence of the end-to-end distance

$$\bar{R}^2_{end-end}(T) =< R_{end-end}(T)^2 >$$

  This is small and almost constant up to about 400 (K) and increases rapidly for temperatures above 400 (K). Above 400 (K), $\bar{R}^2_{end-end}$ changes nonmonotonically. Thus $\bar{R}^2_{end-end}(T)$ increases from 400 to 550 (K) and decreases above 550 (K).

- Figure 7.4d shows the temperature dependence of the average fluctuation in end-to-end distance

$$\bar{\delta}\bar{R}^2_{end-end}(T) = \langle \left(R^2_{end-end} - \bar{R}^2_{end-end}\right) \rangle$$

  This is also small up to 400 (K) and increases quickly above 400 (K). Above

450 (K), $\bar{\delta}\bar{R}^2_{end-end}$ also decreases. This behavior is similar to $\bar{R}^2_{end-end}(T)$.

These results (i) through (v) are all compatible with a glass temperature of $T_g^{th} = 400$ (K) which is close to the observed glass temperature of PTFE, $T_g^{ex} = 400$ (K). Similar results have been obtained for all other systems examined using the $T_g - BAQ$ procedure. The calculations for PVDF and ETFE are discussed below and those for PE,[13] PS,[14] PVC,[15] and Cl-PVC[15] are discussed elsewhere. Thus we believe that the essence of the glass temperature phenomena has been captured in these calculations. This raises two questions:

- what is the atomistic origin of the glass transition temperature?
- why should atomistic simulations on the small molecular weight (10,000 daltons), short time scale (2 (nsec)) used here be able to calculate a property such as the glass temperature which experimentally seems to require much larger time scales (1 (sec)) and molecular weight?

We shall discuss a here and defer b to the discussion.

To study the atomistic origin of T_g, we examined the rate of gauche-trans transformations (denoted as ν_{GT}) as a function of temperature. The results for PTFE are shown in Fig. 7.4e. We see here a negligible rate for $T < 300$ (K) and a rapidly increasing rate for $T > 450$ (K).

Figure 7.4f shows the Arrhenius plot ν_{GT}, where we see that it exhibits an activation energy of 3.1 (kcal/mol). This is somewhat larger than the backbone conformational barrier, 2.4 (kcal/mol).

In Fig. 7.5 we show the results of similar simulations for an isolated chain of PTFE (also C_{200}). Here we see a kink in $R^2_{end-end}$ at above 250 (K) (corresponding to the coil to globular transition). The activation energy for ν_{GT} is 2.2 (kcal/mol).

These results lead to the following picture: The readjustment of the conformation to remain in equilibrium as the temperature is changed requires gauche-trans transitions. The rate of such transitions is dominated by the rotational barrier and drops

rapidly with temperature. For an isolated polymer strand, there is little difficulty and the end-to-end distance continues to decrease as the temperature decreases (see Fig. 7.6a). However, in a condensed system the polymer strands must interdiffuse for the conformation to change and the rate of this diffusion places a lower bound on the effective rate of conformational changes. When the gauche-trans rate drops below this value, the conformation is frozen, leading to a glass.

As mentioned above, these properties are all consistent with associating the kink at about 400 (K) with the glass temperature, $T_g^{th} = 400$ (K). Indeed for PTFE the $T_g^{ex} = 400$ (K). Thus above T_g the conformation expands with temperature, but below T_g it is frozen into place. This leads to small changes in $< V(T) >$ and $\beta(T)$ below T_g, but large changes above T_g.

PVDF

For PVDF we used $T_{build} = 500$ (K), $\rho_{initial} = 1.7$ (g/cc), $\Delta T = -50$ (K) $T_{final} = 50$ (K). The results of the simulations are shown in Fig. 7.6. The experimental value of T_g is $T_g^{exp} = 233$ (K).[17]

- Figure 7.6a shows the average volume. There is a distinct kink in $\bar{V}(T)$ at about 258 (K).

- The temperature dependence of the compressibility, $\beta(T)$, is plotted in Fig. 7.6b which shows a kink at 339 (K).

- Figure 7.6c shows the average square of the end-to-end distance, $\bar{R}^2_{end-end}$, which is almost constant up to about 250 (K). Dramatic changes occur above 250 (K).

- Figure 7.6d shows the average fluctuation $\bar{\delta}\bar{R}^2_{end-end}$, which is also constant up to 250 (K) and increases quickly above 250 (K).

- The transition frequencies, ν_{GT}, of PVDF are shown in Fig. 7.6e. There is a negligible rate for $T \leq 200$ (K) and a rapidly increasing rate for $T \geq 300$ (K) with $T_g = 275$ (K). Figure 7.6f shows the Arrhenius plot ν_{GT}. Here we see

an activation energy (2.5 (kcal/mol)) similar to the backbone conformational barrier, 2.8 (kcal/mol).

- Results for simulations on isolated chains are shown in Fig. 7.7.

Although less consistent than for PTFE, we take the theoretical value to be $T_g^{th} =$ 250 (K) which is in rough agreement with experiment.

ETFE

For ETFE we used $T_{build} = 600$ (K), $\rho_{initial} = 1.7$ (g/cc), $\Delta T = -50$ (K), and $T_{final} = 50$ (K). The simulation results are shown in Fig. 7.8.

- Figure. 7.8a shows that the average volume, $\bar{V}(T)$, has a distinct kink at 376 (K).

- The compressibility, $\beta(T)$, is plotted in Fig. 7.8b, which shows a kink at about 363K, similer to the average volume results.

- Figure 7.8c shows that $\bar{R}^2_{end-end}$ is constant up to 200 (K), changes a small amount up to 400 (K), increases rapidly at 400 (K), and decreases rapidly for temperatures above 450 (K). This behavior is similar to the results for PTFE except that the tendency is a decrease with temperature (except 450 (K)).

- Figure 7.8d shows the average fluctuations $\bar{\delta}\bar{R}^2_{end-end}$. The change is also small up to 400 (K) and increases quickly above 400 (K). This is similar to the results for PTFE and ETFE. The temperature dependence of the fluctuations is different than $\bar{R}^2_{end-end}$. However, the temperature at which big changes occur is the same.

- The transition frequencies, ν_{GT}, for ETFE are shown in Fig. 7.8e. We see here a negligible rate for T <300 (K) and a rapidly increasing rate for $T >$ 400 (K). From this, we predict $T_g = 393$ (K) for ETFE. Figure 7.8f shows the Arrhenius plot of this rate, where we see that it exhibits an activation energy

(3.3 (kcal/mol)), somewhat larger than the backbone conformational barrier, 2.8 (kcal/mol) (the smallest barrier of the three kinds of torsion curves).

- Calculations on isolated chains are in Fig. 7.9.

An experimental T_g for perfectly alternating copolymer ETFE does not exist because of the difficulty of making the perfect alternate copolymer. Thus we estimated the $T_g^{exp} = 420$ (K) of amorphous ETFE, by extrapolation.[18] The predicted value $T_g^{th} =$ 385 (K) which is in rough agreement with the estimate (420 (K)) from experiment.

7.4.3 Discussion

The effective T_g from various simulations are compared in Table 4. Here we see that there is reasonable consistency between the theoretical numbers and reasonable agreement with experiment. Thus we believe that the results discussed above indicate that the calculation have captured the essence of what is experimentally characterized as the T_g.

As discussed above and shown in Table 4, we find an excellent correlation of T_g with the onset of gauche-trans transformation, ν_{GT}. Thus our atomistic interpretation of the T_g is that it is the temperature above which gauche-trans transformations can compete with diffusion to change the conformation states. The Arrhenius parameters are summarized in Table 5. Here we see that the observed E_{act} correlates reasonably well with the rotation barriers of the isolated polymer chain and that all three cases have similar pre-exponential factors, A.

We turn to the question as to why we were able to calculate T_g. General experience with measuring T_g is that the experiments must be on a fairly slow time scale, say (msec) to (sec), whereas the time scale for our simulations is $\sim$2 (nsec). General experience is that a 2 (nsec) experiment would lead to a T_g much too high. We believe that the explanation of why the calculated T_g correlates well with experiment has to do with the way the calculations are done. The calculations use periodic boundary

conditions (PBC). Thus starting at a location $(x, y, z = 0, 0, 0)$ the polymer is built with no constraints except that:

- we simultaneously grow equivalent polymers starting at $m\mathbf{a}$, $n\mathbf{b}$, $p\mathbf{c}$ where m, n, p are all possible integers,
- the lattice vectors **a**, **b**, **c** are chosen so that the volume per chain leads to the proper density, and
- each polymer chain is in equilibrium with itself and all other polymer chains.

This means that locally the polymer has a random configuration but it also has long-range order. That is, the same random configuration occurs in every region of the infinite polymer. Thus although *heterogeneous* on the scale of the unit cell lengths (say 30 (Å)), the material is *homogeneous* over the scale of microns or meters. This contrasts with the experimental materials which are heterogeneous over the entire sample (say 3 (cm)); that is, the local conformation is different in every region of the system. Thus to observe a phase transition for the experimental system, the time scale must be slow enough that energy information can be transferred throughout the material. For a 3 (cm) sample, a velocity of 100 (m/sec) would require $3 * 10^{-4}$ (sec) for the energy information to propagate through the system. However, for the simulated material the long-range homogeneity requires only 30 ps for the energy information to be transferred throughout the 30 (Å) of the unit cell. Thus because of the long-range order, a 30 ps calculation using PBC is equivalent to a 0.3 (msec) experiment on a 3 (cm) heterogeneous system.

A second difference between the simulations and experiment is that the simulated polymer is monodisperse. That is, it has exactly the same MW throughout the whole polymer. In contrast, the experimental polymer has a distribution of MW, causing additional heterogeneities in the experimental system.

These results are most exciting. First, the $T_g{-}BAQ$ strategy for mimicking the T_g of such materials should be most valuable in predicting the T_g for new materials

(of course we need to test this strategy for copolymers, blends, higher MV system, etc.).

Second, the association of T_g with conformational rates provides an atomistic interpretation that should be valuable in developing new polymer materials with T_g, moduli, and other properties adjusted to match specific requirements.

Third, the association of T_g with conformation barrier suggests that we might be able to correlate T_g with other indicators of conformation barrier. This might allow very fast calculations to predict the T_g of new materials (involving ps of dynamics rather than ns).

7.5 Conclusion

Using a systematic annealing methodology for molecular dynamics simulations, we obtain well defined glass transitions that correlate well with the calculated rates of gauche-trans conformational transitions above T_g.

The use of united atom potentials allows more rapid calculation of these quantitites. The good agreement between T_g^{ex} and T_g^{th} with the use of MSUA suggests that the main chain dominates the T_g phenomenon.

We cannot assume yet that these same results will obtain for more realistic simulations on polymers involving say, a million atoms per cell. However, the good correlation between the calculated T_g and the experimental T_g for similar calculations on several polymers encourages us to believe that the same trends will be found for copolymers and blends. If so, the correlation of T_g with atomistic quantities (e.g., internal conformation barrier, vide infra) could allow atomistic reasoning to be used in the design of new polymers with modified T_g and modulus. In addition, it could allow much faster calculation of T_g. Thus reliable rates for gauche-trans transitions can be calculated with much less computational effort than the lengthy simulations required to fully equilibrate and measure volume and compressibility.

7.6 Acknowledgements

We thank Asahi Glass (Dr. K. Sato) for supporting the research. Additional support came from the National Science Foundation (CHE 91-100289). The facilities of the MSC are also supported by grant from DOE-AICD, NSF-ACR, Allied-Signal Corp., Asahi Chemical, BP America, Chevron, BF Goodrich, Xerox, and Beckman Institute. Some of the calculations were carried out on the Pittsburgh NSF supercomputer and some on the JPL Cray.

7.7 References

1. J. Brandup and E.H. Immergut, *Polymer Handbook*, Wiley, 1989.

2. C.A. Sperati and H.W. Starkweather, Jr., *Adv. Polym. Sci.* **2**, 1961, 465.

3. P. Meares, *Polymers: Structure and Bulk Properties*, B. Van Nostrand Company, 1965.

4. N.G. McCrum, B.E. Read, and G. Williams, *Anelastic and Dielectric Effects in Polymeric Solids*, John Wiley and Sons, 1967.

5. F. Bueche, *Physical Properties of Polymers*, Interscience Publishers, 1962.

6. L.H. Sperling, *Introduction to Physical Polymer Science*, John Wiley and Sons, 1986.

7. N. Karasawa and W.A. Goddard III, *J. Phys. Chem.* **93**, 1989, 7320.

8. All calculations used POLYGRAF (V 4.0) from Molecular Simulation Inc., Burlington, Mass.

9. S.L. Mayo, B.D. Olafson, and W.A. Goddard III, *J. Phys. Chem.* **94**, 1990, 8897.

10. The *ab initio* Calculations used Gaussian 92, Revision B, M.J. Frisch, G.W. Trucks, M. Head-Gordon, P.M.W. Gill, M.W. Wong, J.B. Foresman, B.G. Johnson, H.B. Schlegel, M.A. Robb, E.S. Replogle, R. Gomperts, J.L. Andres, K. Raghavachari, J.S. Binkley, C. Gonzalez, R.L. Martin, D.J. Fox, D.J. Defrees, J. Baker, J.J.P. Stewart, and J.A. Pople, Gaussian, Inc., Pittsburgh, PA, 1992.

11. M.N. Ringnalda, J-M. Langlois, B.H. Greeley, T.V. Russo, R.P. Muller, B. Marten, Y. Won, R.E. Donnelly, Jr., W.T. Pollard, G.H. Miller, W.A. Goddard III, and R.A. Freisner, PS-GVB v1.0, Schrödinger, Inc., Pasadena, California, 1994.

12. S. Nosè, *J. Chem. Phys.* **81**, 1984, 511. W.G. Hoover, *Phys. Rev.* **31**, 1985, 1695. M. Parrinello and A. Rahman, *J. Appl. Phys.* **52**, 1981, 7182. S. Nosè and M. L. Klein, *Mol. Phys.* **50**, 1983, 1055. H. C. Andersen, *J. Chem. Phys.* **72**, 1980, 2384. T. Cagin, N. Karasawa, S. Dasgupta, and W.A. Goddard, III, *Mat. Res. Soc. Symp. Proc.* **278**, 1992, 61. T. Cagin, W.A. Goddard, III, and M.L. Ary, *J. Computational Polymer Physics* **I**, 1991, 241.

13. Y. Tang, G. Gao, M. Belmares, and W. A. Goddard III, "The Glass Temperature of Amorphous Polyethylene from Molecular Dynamics Simulations," to be published.

14. M. Belmares, G. Gao, R. Wissenger, P. Adriani, and W.A. Goddard III, "Force Field and Molecular Dynamics Simulations of PVC and CPVC," to be published.

15. G. Gao, M. Belmares, Y. Tang, and W.A. Goddard, "Force Field and Molecular Dynamics Simulations of Polystyrene," to be published.

16. Y. Araki, *J. Appl. Polym. Sci.* **9**, 1965, 421.

17. P. Bonardelli, G. Moggi, and A. Turturro, *Polymer* **27**, 1986, 905.

18. The estimated T_g for ETFE was based on Terpolymers (tetrafluoroethylene, ethylene, vinylmonomers) having various composition ratios. H. Murofushi, private communication.

19. P.V.K. Pant, J. Han, G.D. Smith, and R.H. Boyd, *J. Chem. Phys.* **99**, 1993, 597.

20. J.J. Weeks, E.S. Clark and R.K. Eby, *Polymer* **22**, 1981, 1480.

21. R. Hasegawa, M. Kobayashi, and H. Tadokoro, *Polym. J.* **3**, 1972, 591.

22. F.C. Wilson and H.W. Starkweather, JR., *J. Polym. Sci., Polym. Phys. Ed.* **11**, 1973, 919.

23. G. Avitabile, R. Napolitano, B. Pirozzi, K.D. Rouse, M.W. Thomas, and B.T.M. Willis, *J. Polym. Sci., Polym. Lett. Ed.* **13**, 1975, 351.

24. T. Ito, *Polymer* **23**, 1982, 1412.

25. T. Miyajima and W.A. Goddard III, "The Off-Trans Torsional Distortion for C_4F_{10} and C_4C_{10}, Implications for the Crystalline Phases," *J. Phys. Chem.*, to be published.

26. N. Karasawa and W.A. Goddard III, *Macromolecules* **25**, 1992, 7268.

7.8 Tables

Table 7.1: Total energies for Hartree-Fock calculations. The total energy of the trans form is in Hartree, the relative energy for each configuration is in (kcal/mol).

Torsion Angle	CF_3CF_2- -CF_2CF_3	CF_3CH_2- -CF_2CH_3	CF_3CF_2- -CH_2CH_3	CH_3CF_2- -CF_2CH_3	CF_3CH_2- -CH_2CF_3
0^o, cis	8.251	5.828	6.377	10.874	9.922
30^o		3.061			
60^o		0.615			
gauche[a]	1.081		1.078	2.905	2.557
90^o		1.297			
100^o					2.653
120^o, eclipsed	2.348	2.784	3.721	6.181	2.757
130^o					2.490
150^o		1.740			
165.6^o	0.000				
180^o, trans	0.137	0.000	0.000	0.000	0.000
Total Energy, trans	-1146.17855	-651.61444	-651.60683	-552.75101	-750.48619

- [a] Dihedral torsional angles are 55.28^o for $CF_3CF_2CF_2CF_3$, 66.30^o for $CF_3CF_2CH_2CH_3$, 65.30^o for $CH_3CF_2CF_2CH_3$, and 73.95^o for $CF_3CH_2CH_2CF_3$.

Table 7.2: Properties of polymer crystals using the MSUA. Experimental values (in paranthesis) are at room temperature unless otherwise noted. In all polymers the c axis corresponds to the chain direction.

	PTFE[a]	PVDF-I[b]	PVDF-II[c]	ETFE[d]	PE[e]
A (Å)	5.61(5.65)	8.37(8.58)	4.78(4.96)	9.98(9.60)	7.37(7.12)
B (Å)	11.13(11.18)	4.88(4.91)	9.59(9.64)	9.02(9.25)	4.71(4.85)
C (Å)	70.04(70.20)	2.56(2.56)	4.61(4.62)	5.13(5.00)	2.56(2.55)
ρ^f	2.38(2.34)	2.04(1.97)	2.01(1.92)	1.84(1.90)	1.05(1.06)
β^g	0.188(0.189)	0.104(0.110)	0.121(0.126)	0.157	0.099(0.095)
CED[h]	1.8	2.6	2.2	1.9	2.2

- [a] PTFE phase II. This contains a left- and right-handed 54/25 helix pair in the unit cell (at 275 (K)).
- [b] PVDF form I (β form) has a planar-zigzag conformation (all trans; TTTT), with two chains in the unit cell. These chains are aligned in the direction parallel to b axis, leading to a polar crystal.
- [c] PVDF form II (α form) has the TG^+TG^- conformation with two chains in the unit cell. These chains are aligned antiparallel (nonpolar) in the a direction perpendicular to the chains.
- [d] ETFE crystal has the extended zigzag conformation with four chains in the unit cell. Each chain monomer has four nearest neighbors with the CH_2 groups of one chain adjacent to the CF_2 groups of the next.
- [e] Polyethylene unit cell has a planar-zigzag type of conformation (all trans) with two chains in the unit cell. The cell parameters were measured at 4 (K).
- [f] Density in units of $(g/cm)^3$.
- [g] Compressibility in units of (1/GPa). [24]
- [h] Cohesive energy density per one carbon atom in units of (kcal/mol).

Table 7.3: Force field parameters for the MSUA (FF). Here C_F represents -CF_2- or -CF_3, C_H represents -CH_2- or -CH_3

Bond	C_FC_F	C_FC_H	C_HC_H		
K_R[a]	700.0	700.0	700.0		
R_o (Å)	1.590	1.520	1.520		
Angle	$C_FC_FC_F$	$C_FC_HC_F$	$C_FC_FC_H$	$C_HC_FC_H$	$C_FC_HC_H$
K_θ[b]	100.0	100.0	100.0	100.0	100.0
θ_o(degrees)	110.0	114.5	114.5	114.5	112.0
Torsion[c]	$C_FC_FC_FC_F$	$C_FC_HC_FC_H$	$C_FC_FC_HC_H$	$C_HC_FC_FC_H$	$C_FC_HC_HC_F$
V_0	2.3844	2.0685	2.7072	4.9025	3.5542
V_1	2.2043	0.9915	1.3039	2.5875	3.2813
V_2	0.8916	0.7711	0.4978	0.4920	1.2005
V_3	1.7947	1.6703	1.8730	2.8102	1.5713
V_4	0.7312	0.0348	-0.0200	0.0462	0.2132
V_5	0.1592	0.1797	-0.0202	-0.0015	0.1200
V_6	0.1366	0.0354	-0.0009	-0.0100	-0.0234
V_7	-0.0848	0.0473	0.0070	-0.0006	-0.0530
V_8	-0.0073	0.0021	0.0062	0.0061	0.0148
V_9	-0.0216	0.0214	0.0239	0.0393	0.0395
V_{10}	0.0336	0.0014	-0.0024	0.0013	0.0023
V_{11}	0.0104	0.0005	-0.0019	-0.0019	0.0014
V_{12}	0.0235	0.0001	0.0002	-0.0020	-0.0027
van der Waals	C_F	C_H			
R_ν(Å)	5.650	4.500			
D_ν(kcal/mol)	0.080	0.120			
Charge[d]	C_F	C_H			
PTFE	0	-			
PVDF	0.23	-0.23			
ETFE	-0.06	0.06			

- [a] (kcal/mol)/Å^2.
- [b] (kcal/mol)/rad^2.
- [c] (kcal/mol).
- [d] Electron units.

Table 7.4: Predicted glass temperatures (K) from molecular dynamics simulations of fluoro polymers.

Polymer	Experiment	Theory				
		Selected	V	β	$\overline{R}_{end-end}$	ν_{GT}
PTFE[a]	400 ± 10	400	396(360)	376(389)	400(400)	399
PVDF	233 ± 10	260	258	339	250	275
ETFE	420 ± 20	390	376	363	400	393

[a] Values shown in parentheses are from the heating cycle rather than cooling.

Table 7.5: Arrhenius relation, $\nu_{GT} = Aexp(-E_{act}/RT)$ from the transition frequencies

Polymer	Condensed System		Isolated Chain		Model System
	E_{act} (kcal/mol)	A (sec^{-1})	E_{act} (kcal/mol)	A (sec^{-1})	E_{bar} (kcal/mol)
PTFE	3.05	3.25×10^{14}	2.15	3.11×10^{14}	2.4
PVDF	2.53	3.36×10^{14}	2.51	4.51×10^{14}	2.8
ETFE	3.25	3.57×10^{14}	2.92	4.10×10^{14}	2.8

7.9 Figures

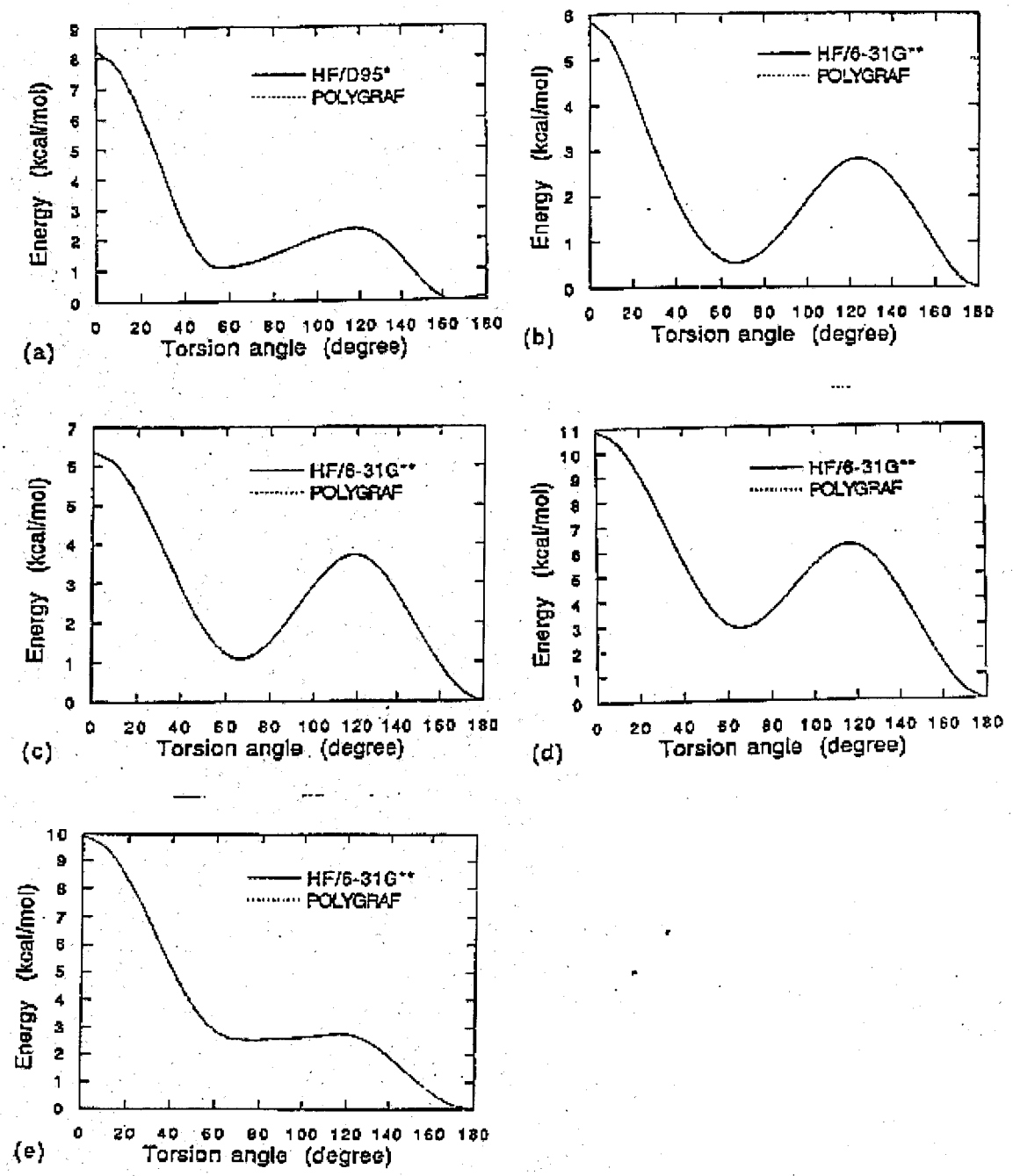

Figure 7.3: Torsional potential curves of C_4 compounds obtained for Hartree-Fock calculations and from the force field (POLYGRAF). (a) $CF_3CF_2CF_2CF_3$, (b)$CF_3CH_2CF_2CH_3$, (c)$CF_3CF_2CH_2CH_3$, (d)$CH_3CF_2CF_2CH_3$, and (e) $CF_3CH_2CH_2CF_3$. The *cisi* conformation has $\phi = 0^o$.

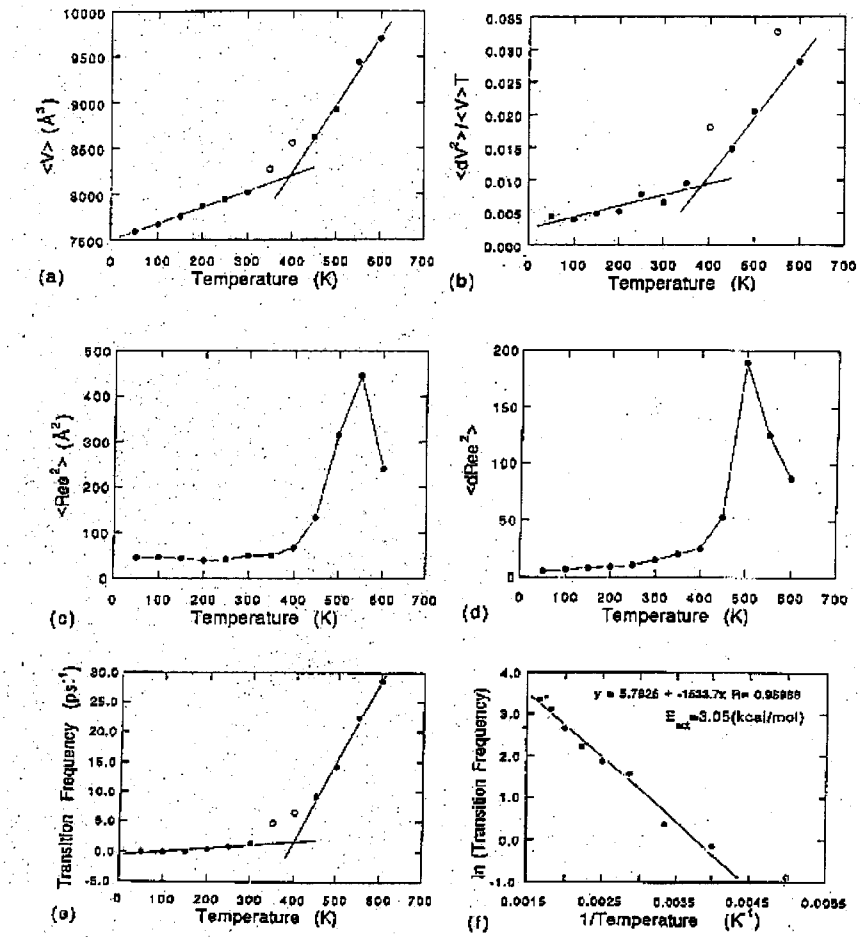

Figure 7.4: Molecular dynamics simulations on PTFE, using $T_g - BAQ$. The temperature dependence of

a. the average volume, $\overline{V}(T)$,

b. compressibility, $\beta(T)$,

c. average square of end-to-end distance, $\overline{R}^2_{end-end}$,

d. standard deviation of square of end-to-end distance, $\overline{\delta R}^2_{end-to-end}$,

e. transition frequency. ν_{GT},

f. Arrhenuim plot of transition frequency.

The filled circles were used for linear fits while the open circles were excluded.

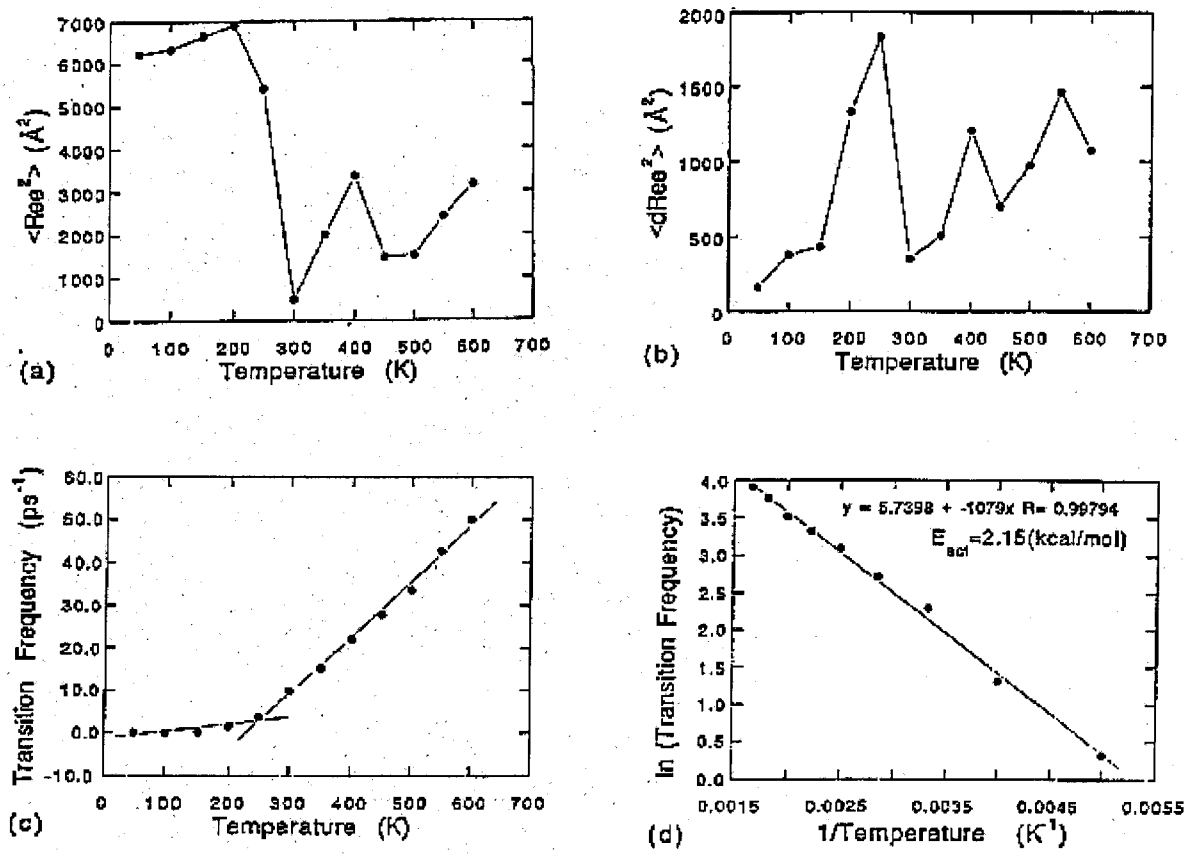

Figure 7.5: Dynamics on isolated chains of PTFE

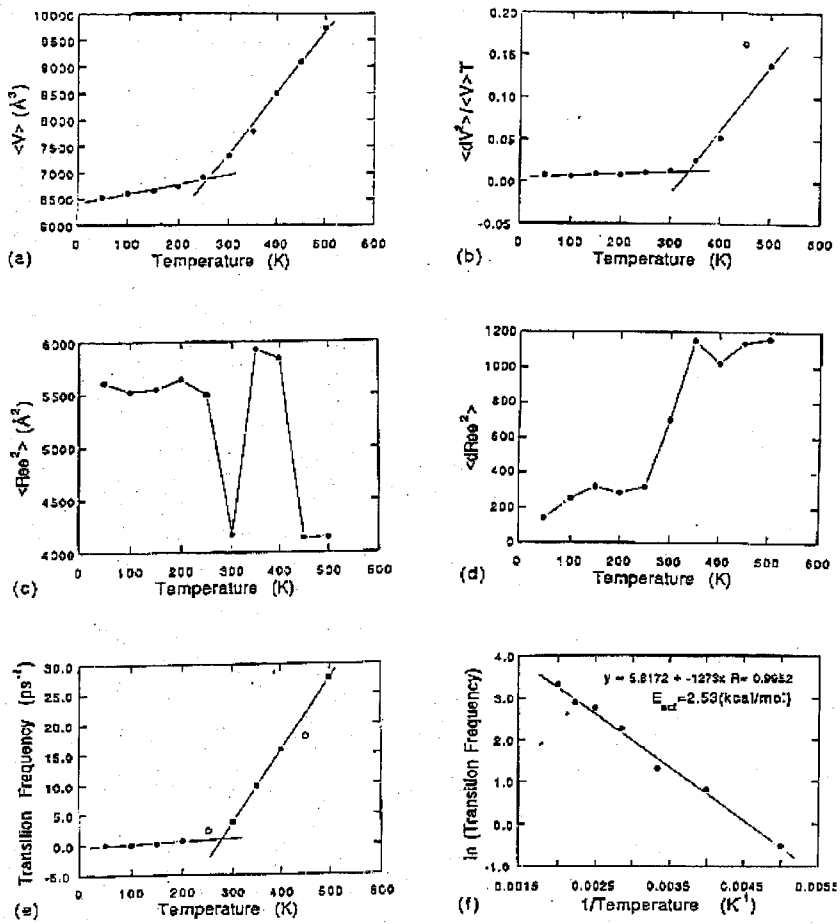

Figure 7.6: Molecular dynamics simulation on PVDF, using $T_g - BAQ$. The temperature dependence of

a. the average volume, $\overline{V}(T)$,

b. compressibility, $\beta(T)$,

c. average square of end-to-end distance, $\overline{R}^2_{end-end}$,

d. standard deviation of square of end-to-end distance, $\overline{\delta R}^2_{end-to-end}$,

e. transition frequency. ν_{GT},

f. Arrhenuim plot of transition frequency.

The filled circles were used for linear fits while the open circles were excluded.

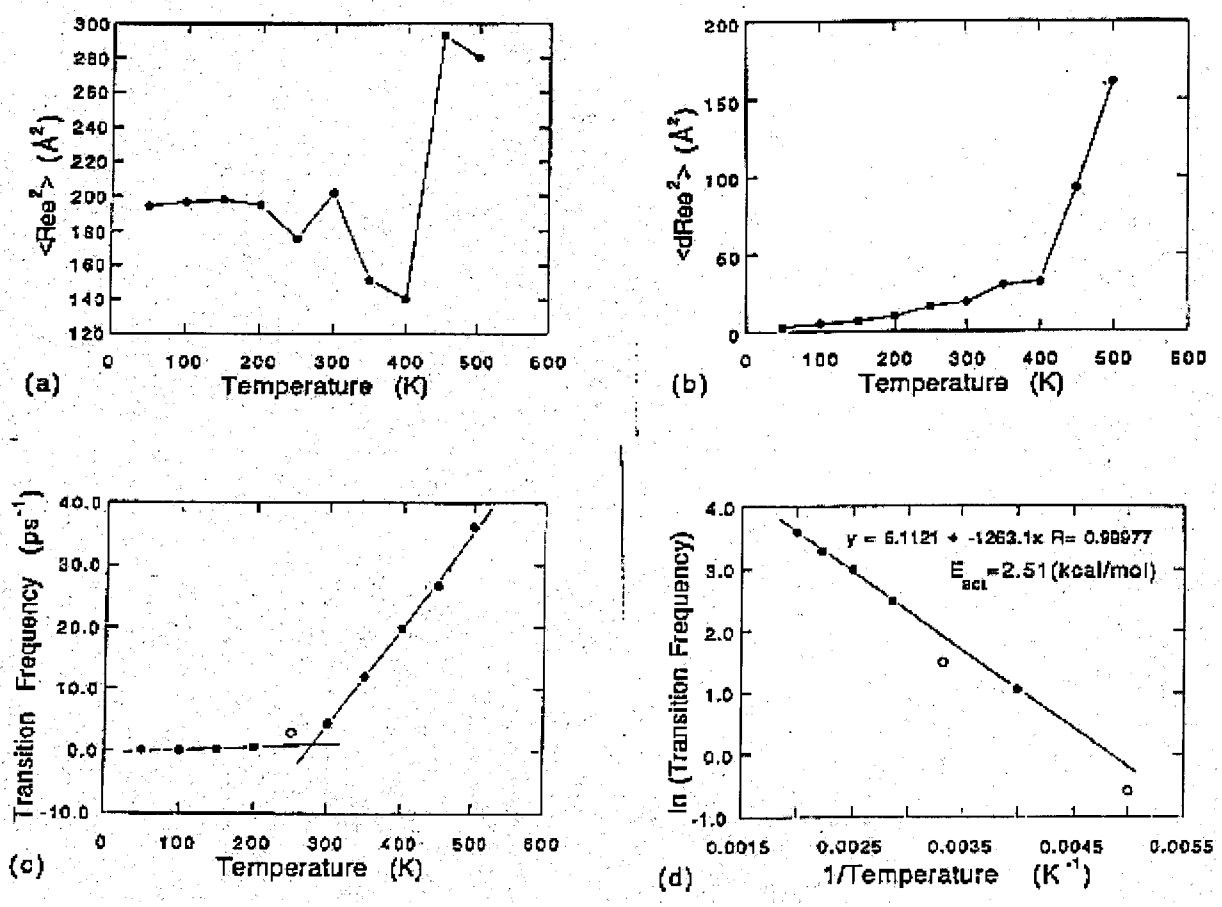

Figure 7.7: Dynamics on isolated chains of PVDF

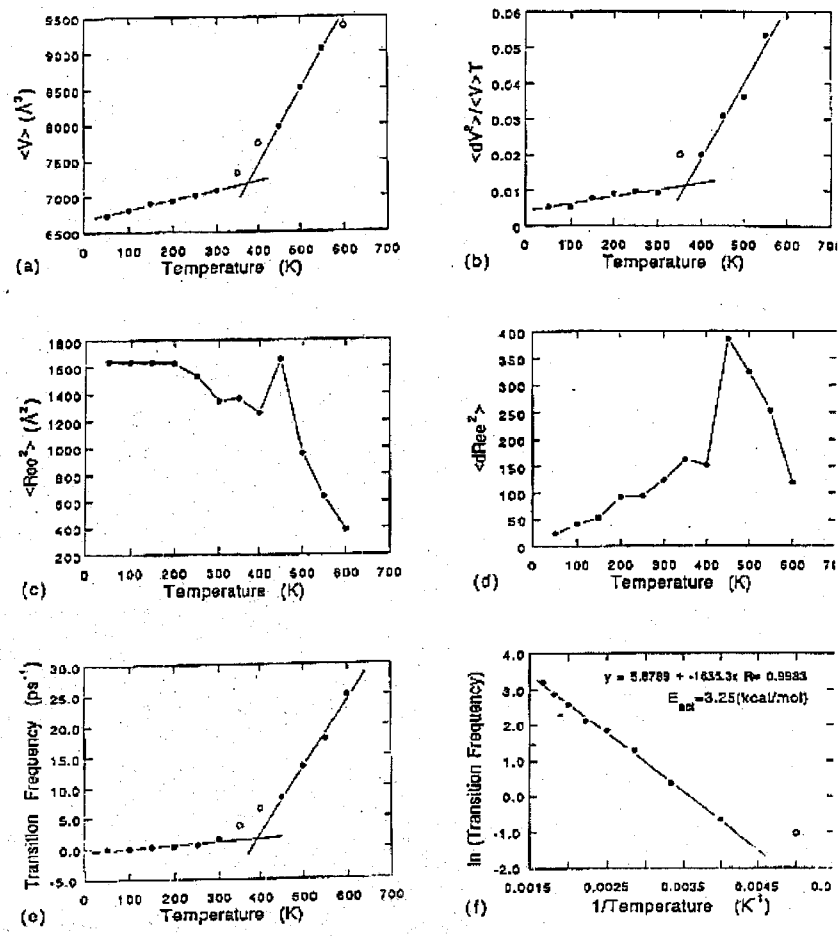

Figure 7.8: Molecular dynamics simulation on ETFE, using $T_g - BAQ$. The temperature dependence of

a. the average volume, $\overline{V}(T)$,

b. compressibility, $\beta(T)$,

c. average square of end-to-end distance, $\overline{R}^2_{end-end}$,

d. standard deviation of square of end-to-end distance, $\overline{\delta R}^2_{end-to-end}$,

e. transition frequency. ν_{GT},

f. Arrhenuim plot of transition frequency.

The filled circles were used for linear fits while the open circles were excluded.

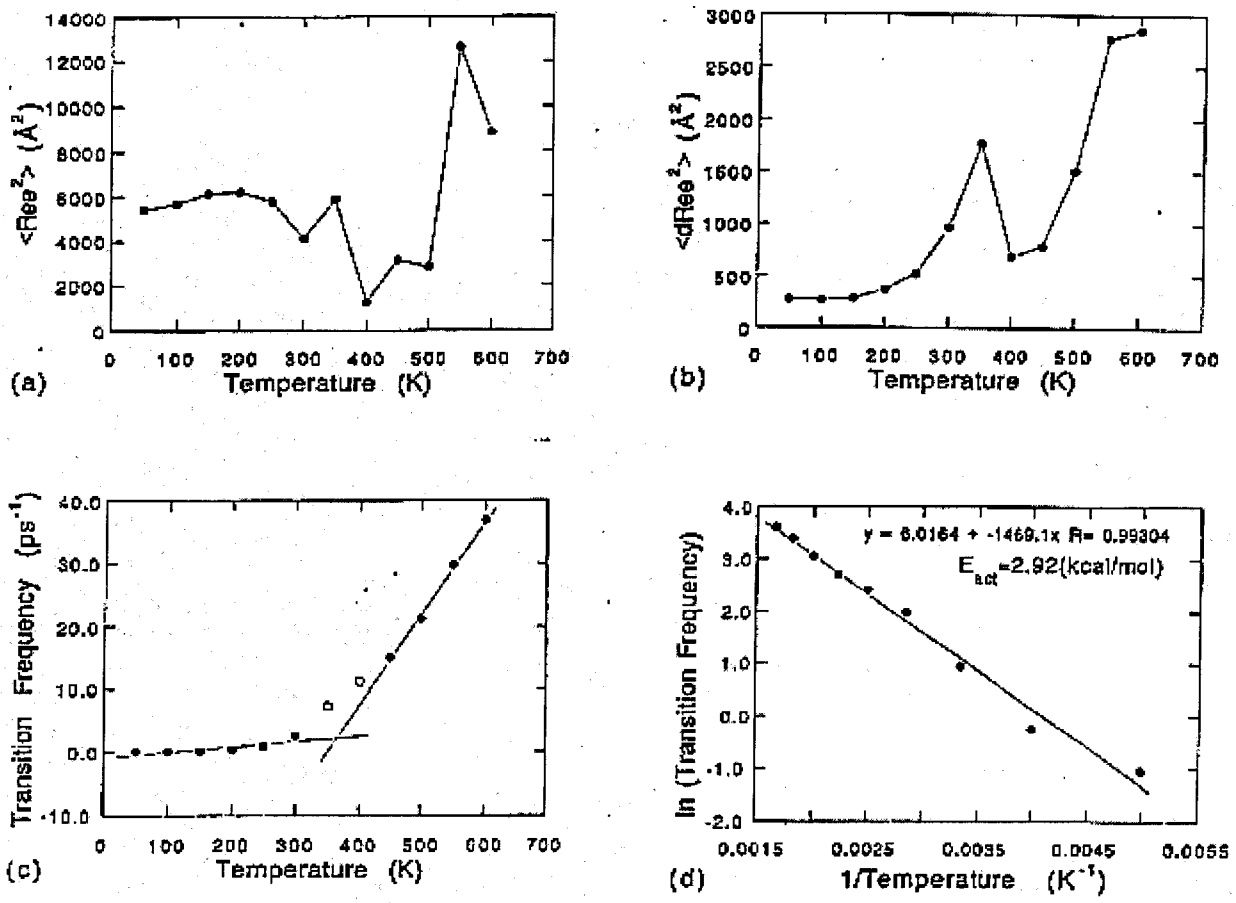

Figure 7.9: Dynamics on isolated chains of ETFE

Massively Parallel Simulation Program (MPSim)

Appendix A Valence Force Fields

A.1 Introduction

Valence force fields are used to describe intra-molecular interactions in terms of 2-body, 3-body, and 4-body (and higher) interactions. We implemented many popular functional forms in our program.

A.2 Bond

Bond interactions are included for any two atoms which are "connected." No special sequence is assumed. Two types of bond parameters are currently implemented; they are Harmonic (Type=1) and Morse (Type=2).

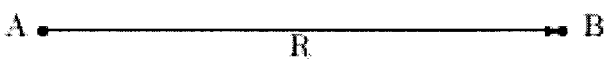

Figure A.1: Bond interaction

A.2.1 Harmonic Bond

The simplest energy expression is the harmonic interaction

$$E = \frac{1}{2}K_e(R - R_e)^2 \tag{A.1}$$

where the equilibrium bond distance R_e is in Ångstroms (Å) and the force constant K_e is in (kcal/mol)/Å^2.

The α component of the force on atom B can be derived as:

$$\begin{aligned} F_\alpha^B &= -\frac{\partial E}{\partial R_\alpha} \\ &= -K_e(R - R_e)\frac{R_\alpha}{R} \end{aligned} \tag{A.2}$$

where we have used

$$2R\frac{\partial R}{\partial R_\alpha} = \frac{\partial (R_\gamma R_\gamma)}{\partial R_\alpha} = 2R_\alpha \tag{A.3}$$

The second derivative:

$$\begin{aligned} \frac{\partial^2 E}{\partial R_\alpha \partial R_\beta} &= K_e \frac{\partial}{\partial R_\beta}\Big[(R - R_e)\frac{R_\alpha}{R}\Big] \\ &= K_e\Big[(1 - \frac{R_e}{R})\delta_{\alpha\beta} + \frac{R_e}{R^3}R_\alpha R_\beta\Big] \end{aligned} \tag{A.4}$$

A.2.2 Morse Bond

The simplest energy expression capable of describing bond disruption is the Morse interaction

$$E = D_e(\chi - 1)^2 \tag{A.5}$$

with

$$\chi = e^{-\gamma(R - R_e)} \tag{A.6}$$

Here R_e is the equilibrium bond distance (Å), D_e is the bond energy (kcal/mol), and γ is a parameter related to K_e (the curvature or force constant at R_e). The zero energy is defined so that $E = 0$ at R_e. The parameter γ is related to K_e and D_e as

in Equation A.7:

$$\gamma = \sqrt{\frac{K_e}{2D_e}} \tag{A.7}$$

The α component of the force on atom B:

$$\begin{aligned} F_\alpha^B &= -\frac{\partial E}{\partial R_\alpha} \\ &= -2D_e(\chi - 1)\frac{\partial \chi}{\partial R_\alpha} \\ &= 2\gamma D_e(\chi - 1)\chi\frac{R_\alpha}{R} \end{aligned} \tag{A.8}$$

Here we have used:

$$\begin{aligned} \frac{\partial \chi}{\partial R_\alpha} &= -\gamma e^{-\gamma(R-R_e)}\frac{R_\alpha}{R} \\ &= -\gamma\chi\frac{R_\alpha}{R} \end{aligned} \tag{A.9}$$

The second derivatives:

$$\begin{aligned} \frac{\partial^2 E}{\partial R_\alpha \partial R_\beta} &= -2\gamma D_e\frac{\partial}{\partial R_\beta}\left[\chi(\chi - 1)\frac{R_\alpha}{R}\right] \\ &= -2\gamma D_e\left[-(2\chi - 1)\gamma\chi\frac{R_\beta}{R}\frac{R_\alpha}{R} + \chi(\chi - 1)\frac{\delta_{\alpha\beta}}{R} - \chi(\chi - 1)\frac{R_\alpha}{R^2}\frac{R_\beta}{R}\right] \\ &= 2\gamma D_e\left[\gamma\chi(2\chi - 1)\frac{R_\alpha R_\beta}{R^2} + \chi(\chi - 1)\frac{R_\alpha R_\beta}{R^3} - \chi(\chi - 1)\frac{\delta_{\alpha\beta}}{R}\right] \end{aligned} \tag{A.10}$$

A.3 Angle

Angle interactions are included for any two atoms that are bonded to a common atom. Currently four types of angle functionals are implemented; they are Harmonic Cosine (Type=1), Harmonic Cosine with Stretching (Type=11), Harmonic (Type=21), and Harmonic with Stretching (Type=31). As in Fig. A.2, we have

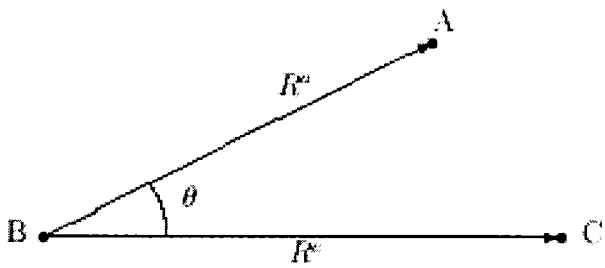

Figure A.2: Angle interaction

$$\cos\theta = \frac{\mathbf{R^A} \cdot \mathbf{R^C}}{R^A R^C} \tag{A.11}$$

Before we get into computation of forces and second derivatives, we'll derive two useful entities.

$$\frac{\partial \cos\theta}{\partial R^A_\alpha} = \frac{R^C_\alpha}{R^A R^C} - \cos\theta \frac{R^A_\alpha}{(R^A)^2} \tag{A.12}$$

and

$$\begin{aligned} \frac{\partial^2 \cos\theta}{\partial R^A_\alpha \partial R^A_\beta} &= \frac{\partial}{\partial R^A_\beta}\Big[\frac{R^C_\alpha}{R^A R^C} - \cos\theta \frac{R^A_\alpha}{(R^A)^2}\Big] \\ &= -\frac{R^C_\alpha R^A_\beta}{R^C (R^A)^3} + 2\cos\theta \frac{R^A_\alpha R^A_\beta}{(R^A)^4} - \cos\theta \frac{\delta_{\alpha\beta}}{(R^A)^2} \\ &\quad -\Big[\frac{R^C_\beta}{R^A R^C} - \cos\theta \frac{R^A_\beta}{(R^A)^2}\Big] \frac{R^A_\alpha}{(R^A)^2} \end{aligned} \tag{A.13}$$

A.3.1 Harmonic Cosine Angle

General Case

The cosine harmonic potential has the following form:

$$E = \frac{1}{2} C (\cos\theta - \cos\theta_e)^2 \tag{A.14}$$

where θ_e is the equilibrium angle and C is a parameter related to the force constant. Differentiate Equation A.14 with respect to $\cos\theta$, and we obtain

$$E' = \frac{\partial E}{\partial \cos\theta} = C(\cos\theta - \cos\theta_e) \tag{A.15}$$

$$E'' = \frac{\partial^2 E}{\partial^2 \cos\theta} = C \tag{A.16}$$

Thus the θ energy derivatives are

$$\frac{\partial E}{\partial \theta} = -E' \sin\theta \tag{A.17}$$

$$\begin{aligned} \frac{\partial^2 E}{\partial^2 \theta} &= -E' \cos\theta - E'' \sin\theta \frac{\partial \cos\theta}{\partial \theta} \\ &= E'' \sin^2\theta - E' \cos\theta \end{aligned} \tag{A.18}$$

Then the force constant K_e becomes

$$K_e = \frac{\partial^2 E}{\partial^2 \theta}\Big|_{\theta_e} = C \sin^2\theta_e \tag{A.19}$$

leading to

$$C = \frac{K_e}{\sin^2\theta_e} \tag{A.20}$$

The zero of energy is defined so that $E(\theta_e) = 0$, hence the barrier toward linearization is

$$E_{barrier} = E(180^o) = \frac{1}{2} C(1 + \cos\theta_e)^2 \tag{A.21}$$

In general, the parameters in force field definition are in terms of θ_e (degree) and K_e ((kcal/mol)/rad^2).

The α component of the force on atom A is:

$$\begin{aligned} F_\alpha^A &= -\frac{\partial E}{\partial R_\alpha^A} \\ &= -C(\cos\theta - \cos\theta_e)\frac{\partial \cos\theta}{\partial R_\alpha^A} \\ &= -C(\cos\theta - \cos\theta_e)\Big[\frac{R_\alpha^C}{R^A R^C} - \cos\theta\frac{R_\alpha^A}{(R^A)^2}\Big] \end{aligned} \tag{A.22}$$

The second derivative on atom A is:

$$\begin{aligned} \frac{\partial^2 E}{\partial R_\alpha^A \partial R_\beta^A} &= C\frac{\partial}{\partial R_\beta^A}\Big[(\cos\theta - \cos\theta_e)\frac{\partial \cos\theta}{\partial R_\alpha}\Big] \\ &= C\frac{\partial \cos\theta}{\partial R_\beta^A}\frac{\partial \cos\theta}{\partial R_\alpha^A} + C(\cos\theta - \cos\theta_e)\frac{\partial^2 \cos\theta}{\partial R_\alpha \partial R_\beta} \\ &= C\Big[\frac{R_\alpha^C}{R^A R^C} - \cos\theta\frac{R_\alpha^A}{(R^A)^2}\Big]\Big[\frac{R_\beta^C}{R^A R^C} - \cos\theta\frac{R_\beta^A}{(R^A)^2}\Big] \\ &\quad -C(\cos\theta - \cos\theta_e)\Big[\frac{R_\alpha^C R_\beta^A}{R^C (R^A)^3} + \cos\theta(\frac{\delta_{\alpha\beta}}{(R^A)^2} - 2\frac{R_\alpha^A R_\beta^A}{(R^A)^4})\Big] \\ &\quad -C(\cos\theta - \cos\theta_e)\Big[\frac{R_\beta^C}{R^A R^C} - \cos\theta\frac{R_\beta^A}{(R^A)^2}\Big]\frac{R_\alpha^A}{(R^A)^2} \end{aligned} \tag{A.23}$$

Similarly, the force on atom C

$$F_\alpha^C = -C(\cos\theta - \cos\theta_e)\Big[\frac{R_\alpha^A}{R^A R^C} - \cos\theta\frac{R_\alpha^C}{(R^C)^2}\Big] \tag{A.24}$$

and the second derivative on atom C

$$\begin{aligned} \frac{\partial^2 E}{\partial R_\alpha^C R_\beta^C} &= C\Big[\frac{R_\alpha^A}{R^C R^A} - \cos\theta\frac{R_\alpha^C}{(R^C)^2}\Big]\Big[\frac{R_\beta^A}{R^C R^A} - \cos\theta\frac{R_\beta^C}{(R^C)^2}\Big] \\ &\quad -C(\cos\theta - \cos\theta_e)\Big[\frac{R_\alpha^A R_\beta^C}{R^A (R^C)^3} + \cos\theta(\frac{\delta_{\alpha\beta}}{(R^C)^2} - 2\frac{R_\alpha^C R_\beta^C}{(R^C)^4})\Big] \\ &\quad -C(\cos\theta - \cos\theta_e)\Big[\frac{R_\beta^A}{R^C R^A} - \cos\theta\frac{R_\beta^C}{(R^C)^2}\Big]\frac{R_\alpha^C}{(R^C)^2} \end{aligned} \tag{A.25}$$

The force on atom B

$$F_\alpha^B = -F_\alpha^A - F_\alpha^C \tag{A.26}$$

and the second derivative on atom B

$$\frac{\partial^2 E}{\partial R_\alpha^B \partial R_\beta^B} = -\frac{\partial^2 E}{\partial R_\alpha^A R_\beta^A} - \frac{\partial^2 E}{\partial R_\alpha^C R_\beta^C} \tag{A.27}$$

Linear Case

As $\theta \to \pi$, $\sin\theta \to 0$, and C in Equation A.20 goes to infinity. Consequently, for the linear geometry the Equation A.14 is replaced by

$$E = C(1 + \cos\theta) \tag{A.28}$$

For angles close to linear, $\theta \simeq \pi - \epsilon$,

$$\cos\theta \simeq -1 + \frac{1}{2}\epsilon^2 \tag{A.29}$$

leading to

$$E = \frac{1}{2}C\epsilon^2 \tag{A.30}$$

Thus C is now the force constant of the linear molecule.

The α component of the force on atom A is:

$$\begin{aligned} F_\alpha^A &= -\frac{\partial E}{\partial R_\alpha^A} = -C\frac{\partial \cos\theta}{\partial R_\alpha^A} \\ &= C\Big[\frac{R_\alpha^C}{R^A R^C} - \cos\theta \frac{R_\alpha^A}{(R^A)^2}\Big] \end{aligned} \tag{A.31}$$

The second derivative on atom A is:

$$\begin{aligned}\frac{\partial^2 E}{\partial R^A_\alpha \partial R^A_\beta} &= C\frac{\partial}{\partial R^A_\beta}\Big[\frac{R^C_\alpha}{R^A R^C} - \cos\theta\frac{R^A_\alpha}{(R^A)^2}\Big] \\ &= -C\frac{1}{(R^A)^2}\frac{R^A_\beta}{R^A}\frac{R^C_\alpha}{R^C} - C\Big[\frac{R^C_\beta}{R^A R^C} - \cos\theta\frac{R^A_\beta}{(R^A)^2}\Big]\frac{R^A_\alpha}{(R^A)^2} \\ &\quad +2C\cos\theta\frac{R^A_\alpha R^A_\beta}{(R^A)^4} - C\cos\theta\frac{\delta_{\alpha\beta}}{(R^A)^2} \\ &= C\Big[-\frac{R^C_\alpha R^A_\beta + R^A_\alpha R^C_\beta}{(R^A)^3 R^C} + 3\cos\theta\frac{R^A_\alpha R^A_\beta}{(R^A)^4} - \cos\theta\frac{\delta_{\alpha\beta}}{(R^A)^2}\Big] \qquad \text{(A.32)}\end{aligned}$$

Similarly, the force on atom C is:

$$F^C_\alpha = C\Big[\frac{R^A_\alpha}{R^C R^A} - \cos\theta\frac{R^C_\alpha}{(R^C)^2}\Big] \qquad \text{(A.33)}$$

The second derivative on atom C is:

$$\frac{\partial^2 E}{\partial R^C_\alpha \partial R^C_\beta} = C\Big[-\frac{R^A_\alpha R^C_\beta + R^C_\alpha R^A_\beta}{(R^C)^3 R^A} + 3\cos\theta\frac{R^C_\alpha R^C_\beta}{(R^C)^4} - \cos\theta\frac{\delta_{\alpha\beta}}{(R^C)^2}\Big] \qquad \text{(A.34)}$$

Again for atom B,

$$F^B_\alpha = -F^A_\alpha - F^C_\alpha, \qquad \text{(A.35)}$$

and

$$\frac{\partial^2 E}{\partial R^B_\alpha \partial R^B_\beta} = -\frac{\partial^2 E}{\partial R^A_\alpha R^A_\beta} - \frac{\partial^2 E}{\partial R^C_\alpha R^C_\beta}. \qquad \text{(A.36)}$$

A.3.2 Harmonic Cosine Angle Coupled with Bond Stretch

General Case

For good description of vibrational frequencies, it is necessary to use an angle term that depends on bond distance. The simplest such potential having the proper sym-

metry, $E(\theta - \pi) = E(\theta + \pi)$, is

$$E(\theta, R^A, R^C) = \frac{1}{2}C(\cos\theta - \cos\theta_e)^2 + D(R^A - R_e^A)(\cos\theta - \cos\theta_e) + E(R^C - R_e^C)(\cos\theta - \cos\theta_e) + F(R^A - R_e^A)(R^C - R_e^C) \quad \text{(A.37)}$$

The α component of the force on atom A for this energy expression is:

$$\begin{aligned}
F_\alpha^A &= -\frac{\partial E}{\partial R_\alpha^A} \\
&= -C(\cos\theta - \cos\theta_e)\frac{\partial \cos\theta}{R_\theta^A} \\
&\quad - D(R^A - R_e^A)\frac{\partial \cos\theta}{R_\theta^A} - D(\cos\theta - \cos\theta_e)\frac{R_\alpha^A}{R^A} \\
&\quad - E(R^C - R_e^C)\frac{\partial \cos\theta}{R_\theta^A} - F(R^C - R_e^C)\frac{R_\alpha^A}{R^A} \\
&= -\Big[C(\cos\theta - \cos\theta_e) + D(R^A - R_e^A) + E(R^C - R_e^C)\Big]\frac{\partial \cos\theta}{R_\theta^A} \\
&\quad - D(\cos\theta - \cos\theta_e)\frac{R_\alpha^A}{R^A} - F(R^C - R_e^C)\frac{R_\alpha^A}{R^A} \\
&= -\Big[C(\cos\theta - \cos\theta_e) + D(R^A - R_e^A) + E(R^C - R_e^C)\Big]\Big(\frac{R_\alpha^C}{R^A R^C} - \cos\theta\frac{R_\alpha^A}{(R^A)^2}\Big) \\
&\quad - D(\cos\theta - \cos\theta_e)\frac{R_\alpha^A}{R^A} - F(R^C - R_e^C)\frac{R_\alpha^A}{R^A}
\end{aligned} \quad \text{(A.38)}$$

The second derivative at atom A:

$$\begin{aligned}
\frac{\partial^2 E}{\partial R_\alpha^A R_\beta^A} &= \frac{\partial^2 \cos\theta}{\partial R_\alpha^A R_\beta^A}\Big[C(\cos\theta - \cos\theta_e) + D(R^A - R_e^A) + E(R^C - R_e^C)\Big] \\
&\quad + \frac{\partial \cos\theta}{\partial R_\alpha^A}\Big[C\frac{\partial \cos\theta}{\partial R_\beta^A} + D\frac{R_\beta^A}{R^A}\Big] + \qquad + D\frac{\partial \cos\theta}{\partial R_\beta^A}\frac{R_\alpha^A}{R^A} + D(\cos\theta - \\
&\quad + F\frac{\delta_{\alpha\beta}}{R^A}(R^C - R_e^C) - F\frac{R_\alpha^A R_\beta^A}{(R^A)^3}(R^C - R_e^C)
\end{aligned} \quad \text{(A.39)}$$

where $\partial^2 \cos\theta / \partial R_\alpha^A R_\beta^A$ and $\partial \cos\theta / \partial R_\alpha^A$ have been derived in previous sections.

Linear Case

For linear molecules ($\theta = \pi$) we use the following

$$\begin{aligned} E = &(1+\cos\theta)\Big[C + D(R^A - R_e^A) + E(R^C - R_e^C)\Big] \\ &+ F(R^A - R_e^A)(R^C - R_e^C) \end{aligned} \tag{A.40}$$

The force on atom A is:

$$\begin{aligned} F_\alpha^A =& -\frac{\partial E}{\partial R_\alpha^A} \\ =& -\frac{\partial \cos\theta}{\partial R_\alpha^A}\Big[C + D(R^A - R_e^A) + E(R^C - R_e^C)\Big] \\ &+ (\cos\theta + 1)D\frac{R_\alpha^A}{R^A} + F(R^C - R_e^C)\frac{R_\alpha^A}{R^A} \\ =& -\Big[\frac{R_\alpha^C}{R^A R^C} - \cos\theta\frac{R_\alpha^A}{(R^A)^2}\Big]\Big[C + D(R^A - R_e^A) + E(R^C - R_e^C)\Big] \\ &+ \Big[D(\cos\theta + 1) + F(R^C - R_e^C)\Big]\frac{R_\alpha^A}{R^A} \end{aligned} \tag{A.41}$$

The second derivative on atom A:

$$\begin{aligned} \frac{\partial^2 E}{\partial R_\alpha^A R_\beta^A} =& \frac{\partial^2 \cos\theta}{\partial R_\alpha^A R_\beta^A}\Big[C + D(R^A - R_e^A) + E(R^C - R_e^C)\Big] + D\frac{\partial \cos\theta}{\partial R_\beta^A}\frac{R_\alpha^A}{R^A} \\ &+ \Big[\frac{\delta_{\alpha\beta}}{R^A} - \frac{R_\alpha^A R_\beta^A}{(R^A)^3}\Big]\Big[D(\cos\theta + 1) + F(R^C - R_e^C)\Big] \end{aligned} \tag{A.42}$$

The computations of forces and second derivatives on atom C are similar to that of atom A; forces and second derivatives on atom B follow that of previous sections.

A.3.3 Simple Harmonic Angle

General Case

$$E(\theta) = \frac{1}{2}K_\theta(\theta - \theta_e)^2 \tag{A.43}$$

For the simple harmonic potential Equation A.43, θ_e (degree) is the equilibrium angle while K_θ ((kcal/mol)/rad^2) is the force constant. Since

$$\frac{\partial\theta}{\partial R_\alpha^A} = \frac{\partial\theta}{\partial\cos\theta}\frac{\partial\cos\theta}{\partial R_\alpha^A} = -\frac{1}{\sin\theta}\frac{\partial\cos\theta}{\partial R_\alpha^A} \tag{A.44}$$

The force on atom A is:

$$F_\alpha^A = K(\theta-\theta_e)\sin^{-1}\theta\frac{\partial\cos\theta}{\partial R_\alpha^A} \tag{A.45}$$

The second derivative on atom A

$$\begin{aligned}\frac{\partial^2 E}{\partial R_\alpha^A \partial R_\beta^A} =& -K\frac{\partial}{\partial R_\beta^A}\left[(\theta-\theta_e)\sin^{-1}\theta\frac{\partial\cos\theta}{\partial R_\alpha^A}\right] \\ =& -K(\theta-\theta_e)\sin^{-1}\theta\frac{\partial^2\cos\theta}{\partial R_\alpha^A\partial R_\beta^A} \\ &+K\left[\sin^{-2}\theta-(\theta-\theta_e)\frac{\cos\theta}{\sin^3\theta}\right]\frac{\partial\cos\theta}{\partial R_\alpha^A}\frac{\partial\cos\theta}{\partial R_\beta^A}\end{aligned} \tag{A.46}$$

where we have used

$$\frac{\partial\sin\theta}{\partial R_\alpha^A} = \frac{\partial\sin\theta}{\partial\theta}\frac{\partial\theta}{\partial\cos\theta}\frac{\partial\cos\theta}{\partial R_\alpha^A} = -\frac{\cos\theta}{\sin\theta}\frac{\partial\cos\theta}{\partial R_\alpha^A} \tag{A.47}$$

Linear Case

Assuming $\theta = \pi - \epsilon$, we have

$$E = \frac{1}{2}K(\epsilon)^2 \tag{A.48}$$

Since

$$\cos(\pi-\delta) = -1+\frac{1}{2}\epsilon^2+O(\epsilon^3) \tag{A.49}$$

the force on atom A to second-order is:

$$\begin{aligned} F_\alpha^A &= -\frac{1}{2}K\frac{\partial\delta^2}{\partial\cos\theta}\frac{\partial\cos\theta}{\partial R_\alpha^A} \\ &= -\frac{1}{2}K\frac{\partial\delta^2}{\partial(\frac{1}{2}\delta^2)}\frac{\partial\cos\theta}{\partial R_\alpha^A} \\ &= -K\frac{\partial\cos\theta}{\partial R_\alpha^A} \end{aligned} \tag{A.50}$$

The second derivative on atom A is:

$$\frac{\partial^2 E}{\partial R_\alpha^A \partial R_\beta^A} = K\frac{\partial^2\cos\theta}{\partial R_\alpha^A \partial R_\beta^A} \tag{A.51}$$

A.3.4 Harmonic Angle Coupled with Bond Stretch

General Case

The general expression which couples a harmonic angle with bond stretch is:

$$\begin{aligned} E = &\frac{1}{2}K(\theta-\theta_e)^2 + D(R^A - R_e^A)(\theta-\theta_e) \\ &+ E(R^C - R_e^C)(\theta-\theta_e) + F(R^A - R_e^A)(R^C - R_e^C) \end{aligned} \tag{A.52}$$

The force on atom A is:

$$\begin{aligned} F_\alpha^A = &-\frac{\partial E}{\partial R_\alpha^A} \\ = &-K(\theta-\theta_e)\frac{\partial\theta}{\partial\cos\theta}\frac{\partial\cos\theta}{\partial R_\alpha^A} \\ &-\frac{\partial\theta}{\partial\cos\theta}\frac{\partial\cos\theta}{\partial R_\alpha^A}\Big[D(R^A - R_e^A) + E(R^C - R_e^C)\Big] \\ &-\Big[D(\theta-\theta_e) + F(R^C - R_e^C)\Big]\frac{R_\alpha^A}{R^A} \end{aligned}$$

$$
\begin{aligned}
=&K(\theta-\theta_e)\sin^{-1}\theta\frac{\partial\cos\theta}{\partial R_\alpha^A} \\
&+\Big[D(R^A-R_e^A)+E(R^C-R_e^C)\Big]\sin^{-1}\theta\frac{\partial\cos\theta}{\partial R_\alpha^A} \\
&-\Big[D(\theta-\theta_e)+F(R^C-R_e^C)\Big]\frac{R_\alpha^A}{R^A}
\end{aligned}
\tag{A.53}
$$

The second derivative at atom A is:

$$
\begin{aligned}
\frac{\partial^2 E}{\partial R_\alpha^A \partial R_\beta^A} =&-\Big[K(\theta-\theta_e)+D(R^A-R_e^A)+E(R^C-R_e^C)\Big]\sin^{-1}\theta\frac{\partial^2\cos\theta}{\partial R_\alpha^A\partial R_\beta^A} \\
&-\Big[K(\theta-\theta_e)+D(R^A-R_e^A)+E(R^C-R_e^C)\Big]\frac{\cos\theta}{\sin^3\theta}\frac{\partial\cos\theta}{\partial R_\alpha^A}\frac{\partial\cos\theta}{\partial R_\beta^A} \\
&-\Big[-K\sin^{-1}\theta\frac{\partial\cos\theta}{\partial R_\beta^A}+D\frac{R_\beta^A}{R^A}\Big]\sin^{-1}\theta\frac{\partial\cos\theta}{\partial R_\alpha^A} \\
&+\Big[D(\theta-\theta_e)+F(R^C-R_e^C)\Big]\Big(\frac{\delta_{\alpha\beta}}{R^A}-\frac{R_\alpha^A R_\beta^A}{(R^A)^3}\Big) \\
&-D\sin^{-1}\theta\frac{\partial\cos\theta}{\partial R_\beta^A}\frac{R_\alpha^A}{R^A}
\end{aligned}
\tag{A.54}
$$

Linear Case

There is no definition for linear case.

A.4 Torsion

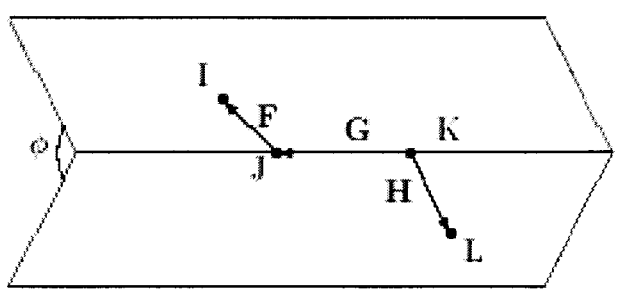

Figure A.3: Torsion interaction

A torsion interaction is defined with respect to four atoms I, J, K, L as in Fig. A.3.

The bonds are I–J, J–K, and K–L. Define: Let's define

$$\begin{aligned}\mathbf{F} =& \mathbf{R^I} - \mathbf{R^J} \\ \mathbf{G} =& \mathbf{R^J} - \mathbf{R^K} \\ \mathbf{H} =& \mathbf{R^L} - \mathbf{R^K},\end{aligned} \tag{A.55}$$

and

$$\begin{aligned}\mathbf{A} =& \mathbf{F} \times \mathbf{G} \\ \mathbf{B} =& \mathbf{H} \times \mathbf{G}.\end{aligned} \tag{A.56}$$

Then

$$\cos\phi = \frac{\mathbf{A}}{A} \cdot \frac{\mathbf{B}}{B} \tag{A.57}$$

The torsion energy is a function of either the dihedral angle ϕ, or $\cos\phi$. For $x = I,\ J,\ K$, or L, we'll derive the entities used in computing of forces and second derivatives.

$$\begin{aligned}\frac{\partial \cos\phi}{\partial R_\alpha^x} =& \Big[\frac{\partial}{\partial R_\alpha^x}(\frac{\mathbf{A}}{A})\Big] \cdot \frac{\mathbf{B}}{B} + \frac{\mathbf{A}}{A} \cdot \Big[\frac{\partial}{\partial R_\alpha^x}(\frac{\mathbf{B}}{B})\Big] \\ =& \Big[\frac{1}{A}\frac{\partial \mathbf{A}}{\partial R_\alpha^x} - \frac{\partial A}{\partial R_\alpha^x}\frac{\mathbf{A}}{A^2}\Big] \cdot \frac{\mathbf{B}}{B} + \frac{\mathbf{A}}{A} \cdot \Big[\frac{1}{B}\frac{\partial \mathbf{B}}{\partial R_\alpha^x} - \frac{\partial B}{\partial R_\alpha^x}\frac{\mathbf{B}}{B^2}\Big] \\ =& \Big[\frac{1}{A}\frac{\partial \mathbf{A}}{\partial R_\alpha^x} - (\mathbf{A} \cdot \frac{\partial \mathbf{A}}{\partial R_\alpha^x})\frac{\mathbf{A}}{A^3}\Big] \cdot \frac{\mathbf{B}}{B} + \frac{\mathbf{A}}{A} \cdot \Big[\frac{1}{B}\frac{\partial \mathbf{B}}{\partial R_\alpha^x} - (\mathbf{B} \cdot \frac{\partial \mathbf{B}}{\partial R_\alpha^x})\frac{\mathbf{B}}{B^3}\Big] \\ =& \frac{1}{AB}(\mathbf{B} \cdot \frac{\partial \mathbf{A}}{\partial R_\alpha^x}) - (\mathbf{A} \cdot \frac{\partial \mathbf{A}}{\partial R_\alpha^x})\frac{\mathbf{A} \cdot \mathbf{B}}{A^3 B} \\ &+ \frac{1}{AB}(\mathbf{A} \cdot \frac{\partial \mathbf{B}}{\partial R_\alpha^x}) - (\mathbf{B} \cdot \frac{\partial \mathbf{A}}{\partial R_\alpha^x})\frac{\mathbf{B} \cdot \mathbf{A}}{B^3 A}\end{aligned} \tag{A.58}$$

and

$$\frac{\partial^2 \cos\phi}{\partial R_\alpha^x \partial R_\beta^x} = \Big[\frac{1}{A}\frac{\partial \mathbf{A}}{\partial R_\alpha^x} - (\mathbf{A} \cdot \frac{\partial \mathbf{A}}{\partial R_\alpha^x})\frac{\mathbf{A}}{A^3}\Big] \cdot \Big[\frac{1}{B}\frac{\partial \mathbf{B}}{\partial R_\beta^x} - (\mathbf{B} \cdot \frac{\partial \mathbf{B}}{\partial R_\beta^x})\frac{\mathbf{B}}{B^3}\Big] +$$

$$
\begin{aligned}
&+\Big[\frac{1}{A}\frac{\partial \mathbf{A}}{\partial R^x_\beta}-(\mathbf{A}\cdot\frac{\partial \mathbf{A}}{\partial R^x_\beta})\frac{\mathbf{A}}{A^3}\Big]\cdot\Big[\frac{1}{B}\frac{\partial \mathbf{B}}{\partial R^x_\alpha}-(\mathbf{B}\cdot\frac{\partial \mathbf{B}}{\partial R^x_\alpha})\frac{\mathbf{B}}{B^3}\Big]\\
&+\frac{\partial}{\partial R^x_\beta}\Big[\frac{1}{A}\frac{\partial \mathbf{A}}{\partial R^x_\alpha}-(\mathbf{A}\cdot\frac{\partial \mathbf{A}}{\partial R^x_\alpha})\frac{\mathbf{A}}{A^3}\Big]\cdot\frac{\mathbf{B}}{B}\\
&+\frac{\mathbf{A}}{A}\cdot\frac{\partial}{\partial R^x_\beta}\Big[\frac{1}{B}\frac{\partial \mathbf{B}}{\partial R^x_\alpha}-(\mathbf{B}\cdot\frac{\partial \mathbf{B}}{\partial R^x_\alpha})\frac{\mathbf{B}}{B^3}\Big].
\end{aligned}
\tag{A.59}
$$

Further expanding, we have:

$$
\frac{\partial}{\partial R^x_\beta}(\frac{1}{A}\frac{\partial \mathbf{A}}{\partial R^x_\alpha})=-\frac{1}{A^3}\Big(\mathbf{A}\cdot\frac{\partial \mathbf{A}}{\partial R^x_\beta}\Big)\frac{\partial \mathbf{A}}{\partial R^x_\alpha}+\frac{1}{A}\frac{\partial^2 \mathbf{A}}{\partial R^x_\alpha \partial R^x_\beta} \tag{A.60}
$$

$$
\frac{\partial}{\partial R^x_\beta}(\frac{1}{B}\frac{\partial \mathbf{B}}{\partial R^x_\alpha})=-\frac{1}{B^3}\Big(\mathbf{B}\cdot\frac{\partial \mathbf{B}}{\partial R^x_\beta}\Big)\frac{\partial \mathbf{B}}{\partial R^x_\alpha}+\frac{1}{B}\frac{\partial^2 \mathbf{B}}{\partial R^x_\alpha \partial R^x_\beta} \tag{A.61}
$$

$$
\begin{aligned}
\frac{\partial}{\partial R^x_\beta}\Big[(\mathbf{A}\cdot\frac{\partial \mathbf{A}}{\partial R^x_\alpha})\frac{\mathbf{A}}{A^3}\Big]=&\Big(\frac{\partial \mathbf{A}}{\partial R^x_\beta}\cdot\frac{\partial \mathbf{A}}{\partial R^x_\alpha}\Big)\frac{\mathbf{A}}{A^3}+\Big(\mathbf{A}\cdot\frac{\partial^2 \mathbf{A}}{\partial R^x_\alpha \partial R^x_\beta}\Big)\frac{\mathbf{A}}{A^3}\\
&+\Big(\mathbf{A}\cdot\frac{\partial \mathbf{A}}{\partial R^x_\alpha}\Big)\Big[\frac{1}{A^3}\frac{\partial \mathbf{A}}{\partial R^x_\beta}-3\frac{\mathbf{A}}{A^5}(\mathbf{A}\cdot\frac{\partial \mathbf{A}}{\partial R^x_\beta})\Big]
\end{aligned}
\tag{A.62}
$$

$$
\begin{aligned}
\frac{\partial}{\partial R^x_\beta}\Big[(\mathbf{B}\cdot\frac{\partial \mathbf{B}}{\partial R^x_\alpha})\frac{\mathbf{B}}{B^3}\Big]=&\Big(\frac{\partial \mathbf{B}}{\partial R^x_\beta}\cdot\frac{\partial \mathbf{B}}{\partial R^x_\alpha}\Big)\frac{\mathbf{B}}{B^3}+\Big(\mathbf{B}\cdot\frac{\partial^2 \mathbf{B}}{\partial R^x_\alpha \partial R^x_\beta}\Big)\frac{\mathbf{B}}{B^3}\\
&+\Big(\mathbf{B}\cdot\frac{\partial \mathbf{B}}{\partial R^x_\alpha}\Big)\Big[\frac{1}{B^3}\frac{\partial \mathbf{B}}{\partial R^x_\beta}-3\frac{\mathbf{B}}{B^5}(\mathbf{B}\cdot\frac{\partial \mathbf{B}}{\partial R^x_\beta})\Big]
\end{aligned}
\tag{A.63}
$$

where we have used

$$
\frac{\partial A}{\partial R^x_\alpha}=\frac{1}{2A}\frac{\partial(\mathbf{A}\cdot\mathbf{A})}{\partial R^x_\alpha}=\frac{\mathbf{A}}{A}\cdot\frac{\partial \mathbf{A}}{\partial R^x_\alpha} \tag{A.64}
$$

$$
\frac{\partial B}{\partial R^x_\alpha}=\frac{\mathbf{B}}{B}\cdot\frac{\partial \mathbf{B}}{\partial R^x_\alpha} \tag{A.65}
$$

Now let's compute the individual terms

$$
\begin{aligned}
\frac{\partial A_\beta}{\partial R^x_\alpha}=&\frac{\partial}{\partial R^x_\alpha}(\mathbf{F}\times\mathbf{G})_\beta=\frac{\partial}{\partial R^x_\alpha}(\epsilon_{\beta\mu\nu}F_\mu G_\nu)\\
=&\epsilon_{\beta\mu\nu}\frac{\partial F_\mu}{\partial R^x_\alpha}G_\nu+\epsilon_{\beta\mu\nu}F_\mu\frac{\partial G_\nu}{\partial R^x_\alpha}
\end{aligned}
\tag{A.66}
$$

where $\epsilon_{\alpha\beta\gamma}$ is the Levi-Civita vector. Similarly

$$\frac{\partial B_\beta}{\partial R_\alpha^x} = \epsilon_{\beta\mu\nu}\frac{\partial H_\mu}{\partial R_\alpha^x}G_\nu + \epsilon_{\beta\mu\nu}H_\mu\frac{\partial G_\nu}{\partial R_\alpha^x} \tag{A.67}$$

For $x = I$, which is atom I, we have

$$\mathbf{A}\cdot\frac{\partial \mathbf{A}}{\partial R_\alpha^I} = A_\beta\frac{\partial A_\beta}{\partial R_\alpha^I} = A_\beta\epsilon_{\beta\mu\nu}\delta_{\alpha\mu}G_\nu = -\epsilon_{\alpha\beta\nu}A_\beta G_\nu = -(\mathbf{A}\times\mathbf{G})_\alpha \tag{A.68}$$

Similarly

$$\mathbf{B}\cdot\frac{\partial \mathbf{A}}{\partial R_\alpha^I} = -(\mathbf{B}\times\mathbf{G})_\alpha \tag{A.69}$$

$$\mathbf{A}\cdot\frac{\partial \mathbf{B}}{\partial R_\alpha^I} = 0 \tag{A.70}$$

$$\mathbf{B}\cdot\frac{\partial \mathbf{B}}{\partial R_\alpha^I} = 0 \tag{A.71}$$

For $x = J$, which is atom J, we have

$$\mathbf{A}\cdot\frac{\partial \mathbf{A}}{\partial R_\alpha^J} = (\mathbf{A}\times\mathbf{G})_\alpha - (\mathbf{F}\times\mathbf{A}) \tag{A.72}$$

$$\mathbf{B}\cdot\frac{\partial \mathbf{A}}{\partial R_\alpha^J} = (\mathbf{B}\times\mathbf{G})_\alpha - (\mathbf{F}\times\mathbf{B}) \tag{A.73}$$

$$\mathbf{A}\cdot\frac{\partial \mathbf{B}}{\partial R_\alpha^J} = -(\mathbf{H}\times\mathbf{A})_\alpha \tag{A.74}$$

$$\mathbf{B}\cdot\frac{\partial \mathbf{B}}{\partial R_\alpha^J} = -(\mathbf{H}\times\mathbf{B})_\alpha \tag{A.75}$$

For $x = K$, which is atom K, we have

$$\mathbf{A}\cdot\frac{\partial \mathbf{A}}{\partial R_\alpha^K} = -(\mathbf{A}\times\mathbf{F})_\alpha \tag{A.76}$$

$$\mathbf{B}\cdot\frac{\partial \mathbf{A}}{\partial R_\alpha^K} = -(\mathbf{B}\times\mathbf{F})_\alpha \tag{A.77}$$

$$\mathbf{A}\cdot\frac{\partial \mathbf{B}}{\partial R_\alpha^K} = (\mathbf{A}\times\mathbf{G})_\alpha + (\mathbf{H}\times\mathbf{A})_\alpha \tag{A.78}$$

$$\mathbf{B} \cdot \frac{\partial \mathbf{B}}{\partial R_\alpha^K} = (\mathbf{B} \times \mathbf{G})_\alpha + (\mathbf{H} \times \mathbf{B})_\alpha \tag{A.79}$$

And for $x = L$, which is atom L, we have

$$\mathbf{A} \cdot \frac{\partial \mathbf{A}}{\partial R_\alpha^L} = 0 \tag{A.80}$$

$$\mathbf{B} \cdot \frac{\partial \mathbf{A}}{\partial R_\alpha^L} = 0 \tag{A.81}$$

$$\mathbf{A} \cdot \frac{\partial \mathbf{B}}{\partial R_\alpha^L} = -(\mathbf{A} \times \mathbf{G})_\alpha \tag{A.82}$$

$$\mathbf{B} \cdot \frac{\partial \mathbf{B}}{\partial R_\alpha^L} = -(\mathbf{B} \times \mathbf{G})_\alpha \tag{A.83}$$

Terms used in second derivatives

$$\begin{aligned} \frac{\partial^2 A_\gamma}{\partial R_\alpha^x \partial R_\beta^x} &= \frac{\partial^2}{\partial R_\alpha^x \partial R_\beta^x}(\epsilon_{\gamma\mu\nu} F_\mu G_\nu) \\ &= \epsilon_{\gamma\mu\nu}\left[\frac{\partial F_\mu}{\partial R_\alpha^x}\frac{\partial G_\nu}{\partial R_\beta^x} + \frac{\partial F_\mu}{\partial R_\beta^x}\frac{\partial G_\nu}{\partial R_\alpha^x}\right] \end{aligned} \tag{A.84}$$

$$\frac{\partial^2 A_\gamma}{\partial R_\alpha^I \partial R_\beta^I} = 0 \tag{A.85}$$

$$\begin{aligned} \frac{\partial^2 A_\gamma}{\partial R_\alpha^J \partial R_\beta^J} &= \epsilon_{\gamma\mu\nu}(-\delta_{\mu\beta}\delta_{\nu\alpha} - \delta_{\mu\alpha}\delta_{\nu\beta}) \\ &= -\epsilon_{\gamma\beta\alpha} - \epsilon_{\gamma\alpha\beta} = 0 \end{aligned} \tag{A.86}$$

$$\frac{\partial^2 A_\gamma}{\partial R_\alpha^K \partial R_\beta^K} = 0 \tag{A.87}$$

$$\frac{\partial^2 A_\gamma}{\partial R_\alpha^L \partial R_\beta^L} = 0 \tag{A.88}$$

Similarly

$$\frac{\partial^2 B_\gamma}{\partial R_\alpha^x \partial R_\beta^x} = \epsilon_{\gamma\mu\nu}\left[\frac{\partial H_\mu}{\partial R_\alpha^x}\frac{\partial G_\nu}{\partial R_\beta^x} + \frac{\partial H_\mu}{\partial R_\beta^x}\frac{\partial G_\nu}{\partial R_\alpha^x}\right] \tag{A.89}$$

$$\frac{\partial^2 B_\gamma}{\partial R_\alpha^I \partial R_\beta^I} = 0 \tag{A.90}$$

$$\frac{\partial^2 B_\gamma}{\partial R_\alpha^J \partial R_\beta^J} = 0 \tag{A.91}$$

$$\begin{aligned}
\frac{\partial^2 B_\gamma}{\partial R_\alpha^K \partial R_\beta^K} &= \epsilon_{\gamma\mu\nu}(\delta_{\mu\beta}\delta_{\nu\alpha} + \delta_{\mu\alpha}\delta_{\nu\beta}) \\
&= \epsilon_{\gamma\beta\alpha} + \epsilon_{\gamma\alpha\beta} = 0 \qquad \text{(A.92)} \\
\frac{\partial^2 B_\gamma}{\partial R_\alpha^L \partial R_\beta^L} &= 0 \qquad \text{(A.93)}
\end{aligned}$$

For $x = I$

$$\begin{aligned}
\frac{\partial \mathbf{A}}{\partial R_\alpha^I} \cdot \frac{\partial \mathbf{A}}{\partial R_\beta^I} &= \epsilon_{\gamma\mu\nu} \frac{\partial}{\partial R_\alpha^I}(F_\mu G_\nu)\epsilon_{\gamma\kappa\lambda} \frac{\partial}{\partial R_\beta^I}(F_\kappa G_\lambda) \\
&= \epsilon_{\gamma\mu\nu}\epsilon_{\gamma\kappa\lambda}\delta_{\mu\alpha}\delta_{\kappa\beta}G_\nu G_\lambda \\
&= \epsilon_{\gamma\alpha\nu}\epsilon_{\gamma\beta\lambda}G_\nu G_\lambda \\
&= (\delta_{\alpha\beta}\delta_{\nu\lambda} - \delta_{\alpha\lambda}\delta_{\nu\beta})G_\nu G_\lambda \\
&= \delta_{\alpha\beta}(\mathbf{G}\cdot\mathbf{G}) - G_\alpha G_\beta \qquad \text{(A.94)} \\
\frac{\partial \mathbf{A}}{\partial R_\alpha^I} \cdot \frac{\partial \mathbf{B}}{\partial R_\beta^I} &= 0 \qquad \text{(A.95)} \\
\frac{\partial \mathbf{B}}{\partial R_\alpha^I} \cdot \frac{\partial \mathbf{B}}{\partial R_\beta^I} &= 0 \qquad \text{(A.96)}
\end{aligned}$$

For $x = J$

$$\begin{aligned}
\frac{\partial \mathbf{A}}{\partial R_\alpha^J} \cdot \frac{\partial \mathbf{A}}{\partial R_\beta^J} &= \epsilon_{\gamma\mu\nu}(-\delta_{\mu\alpha}G_\nu + \delta_{\nu\alpha}F_\mu)\epsilon_{\gamma\kappa\lambda}(-\delta_{\kappa\beta}G_\lambda + \delta_{\lambda\beta}F_\kappa) \\
&= \epsilon_{\gamma\alpha\nu}\epsilon_{\gamma\beta\lambda}G_\nu G_\lambda - \epsilon_{\gamma\alpha\nu}\epsilon_{\gamma\kappa\beta}G_\nu F_\kappa \\
&\quad -\epsilon_{\gamma\mu\alpha}\epsilon_{\gamma\beta\lambda}F_\nu G_\lambda + \epsilon_{\gamma\mu\alpha}\epsilon_{\gamma\kappa\beta}F_\nu F_\kappa \\
&= \delta_{\alpha\beta}(\mathbf{G}\cdot\mathbf{G}) - G_\alpha G_\beta + \delta_{\alpha\beta}(\mathbf{F}\cdot\mathbf{F}) - F_\alpha F_\beta \\
&\quad +\delta_{\alpha\beta}(\mathbf{G}\cdot\mathbf{F}) - G_\beta F_\alpha + \delta_{\alpha\beta}(\mathbf{F}\cdot\mathbf{G}) - F_\beta G_\alpha \qquad \text{(A.97)} \\
\frac{\partial \mathbf{A}}{\partial R_\alpha^J} \cdot \frac{\partial \mathbf{B}}{\partial R_\beta^J} &= \epsilon_{\gamma\mu\nu}(-\delta_{\mu\alpha}G_\nu + \delta_{\nu\alpha}F_\mu)\epsilon_{\gamma\kappa\lambda}\delta_{\lambda\beta}H_\kappa \\
&= -\epsilon_{\gamma\alpha\nu}\epsilon_{\gamma\kappa\beta}G_\nu H_\kappa + \epsilon_{\gamma\mu\alpha}\epsilon_{\gamma\kappa\beta}F_\mu H_\kappa \\
&= -G_\beta H_\alpha + \delta_{\alpha\beta}(\mathbf{G}\cdot\mathbf{H}) + \delta_{\alpha\beta}(\mathbf{F}\cdot\mathbf{H}) - F_\beta H_\alpha \qquad \text{(A.98)} \\
\frac{\partial \mathbf{B}}{\partial R_\alpha^J} \cdot \frac{\partial \mathbf{B}}{\partial R_\beta^J} &= \epsilon_{\gamma\mu\nu}H_\mu\delta_{\nu\alpha}\epsilon_{\gamma\kappa\lambda}H_\kappa\delta_{\lambda\beta} \\
&= (\mathbf{H}\cdot\mathbf{H})\delta_{\alpha\beta} - H_\beta H_\alpha \qquad \text{(A.99)}
\end{aligned}$$

For $x = K$

$$\begin{aligned}
\frac{\partial \mathbf{A}}{\partial R^K_\alpha} \cdot \frac{\partial \mathbf{A}}{\partial R^K_\beta} &= \epsilon_{\gamma\mu\nu} F_\mu \delta_{\nu\alpha} \epsilon_{\gamma\kappa\lambda} F_\kappa \delta_{\lambda\beta} \\
&= \epsilon_{\gamma\mu\alpha} \epsilon_{\gamma\kappa\beta} F_\mu F_\kappa \\
&= (\mathbf{F}\cdot\mathbf{F})\delta_{\alpha\beta} - F_\beta F_\alpha \qquad \text{(A.100)} \\
\frac{\partial \mathbf{A}}{\partial R^K_\alpha} \cdot \frac{\partial \mathbf{B}}{\partial R^K_\beta} &= \epsilon_{\gamma\mu\nu}(-F_\mu \delta_{\nu\alpha}) \epsilon_{\gamma\kappa\lambda}(-\delta_{\kappa\beta} G_\lambda - H_\kappa \delta_{\lambda\beta}) \\
&= \epsilon_{\gamma\mu\alpha} \epsilon_{\gamma\beta\lambda} F_\mu G_\lambda + \epsilon_{\gamma\mu\alpha} \epsilon_{\gamma\kappa\beta} F_\mu H_\kappa \\
&= F_\beta G_\alpha - \delta_{\alpha\beta}(\mathbf{F}\cdot\mathbf{G}) + \delta_{\alpha\beta}(\mathbf{F}\cdot\mathbf{H}) - H_\alpha F_\beta \qquad \text{(A.101)} \\
\frac{\partial \mathbf{B}}{\partial R^K_\alpha} \cdot \frac{\partial \mathbf{B}}{\partial R^K_\beta} &= \epsilon_{\gamma\mu\nu}(-\delta_{\mu\alpha} G_\nu - \delta_{\nu\alpha} H_\mu) \epsilon_{\gamma\kappa\lambda}(-\delta_{\kappa\beta} G_\lambda - \delta_{\lambda\beta} H_\kappa) \\
&= \epsilon_{\gamma\alpha\nu} \epsilon_{\gamma\beta\lambda} G_\nu G_\lambda + \epsilon_{\gamma\mu\alpha} \epsilon_{\gamma\beta\lambda} H_\mu G_\lambda + \epsilon_{\gamma\alpha\nu} \epsilon_{\gamma\kappa\beta} G_\nu H_\kappa + \epsilon_{\gamma\mu\alpha} \epsilon_{\gamma\kappa\beta} H_\mu H_\kappa \\
&= \delta_{\alpha\beta}(\mathbf{G}\cdot\mathbf{G}) - G_\alpha G_\beta - \delta_{\alpha\beta}(\mathbf{H}\cdot\mathbf{G}) + G_\alpha H_\beta \\
&\quad -\delta_{\alpha\beta}(\mathbf{G}\cdot\mathbf{H}) + H_\alpha G_\beta + \delta_{\alpha\beta}(\mathbf{H}\cdot\mathbf{H}) + H_\alpha H_\beta \qquad \text{(A.102)}
\end{aligned}$$

For $x = L$

$$\begin{aligned}
\frac{\partial \mathbf{A}}{\partial R^L_\alpha} \cdot \frac{\partial \mathbf{A}}{\partial R^L_\beta} &= 0 \qquad \text{(A.103)} \\
\frac{\partial \mathbf{A}}{\partial R^L_\alpha} \cdot \frac{\partial \mathbf{B}}{\partial R^L_\beta} &= 0 \qquad \text{(A.104)} \\
\frac{\partial \mathbf{B}}{\partial R^L_\alpha} \cdot \frac{\partial \mathbf{B}}{\partial R^L_\beta} &= \epsilon_{\gamma\mu\nu} \delta_{\mu\alpha} G_\nu \epsilon_{\gamma\kappa\lambda} \delta_{\kappa\beta} G_\lambda \\
&= \epsilon_{\gamma\alpha\nu} \epsilon_{\gamma\beta\lambda} G_\nu G_\lambda \\
&= \delta_{\alpha\beta}(\mathbf{G}\cdot\mathbf{G}) - G_\alpha G_\beta \qquad \text{(A.105)}
\end{aligned}$$

A.4.1 Pure Torsion

The general energy is defined by:

$$E(\phi) = \sum_{i=0}^{n} C_i \cos(i\phi) \qquad \text{(A.106)}$$

where ϕ is the angle between plane IJK and JKL. The sum can include up to $n = 12$. Typically, all of the C_i are zero, except C_0 and C_3. Knowing $\cos\phi$, $\cos(n\phi)$ can be computed by the recursive formula

$$\cos(n\phi) = \cos[(n-1)\phi]\cos\phi - \cos[(n-2)\phi] \tag{A.107}$$

In order to compute the forces and second derivatives, we need

$$\begin{aligned} \frac{\partial \cos(n\phi)}{\partial \cos\phi} &= \frac{\partial \cos(n\phi)}{\partial\phi}\frac{\partial\phi}{\partial\cos\phi} \\ &= n\frac{\sin(n\phi)}{\sin\phi} \end{aligned} \tag{A.108}$$

and

$$\begin{aligned} \frac{\partial^2 \cos(n\phi)}{\partial^2 \cos\phi} &= n\frac{\partial}{\partial\phi}\left[\frac{\sin(n\phi)}{\sin\phi}\right]\frac{\partial\phi}{\partial\cos\phi} \\ &= n\frac{\sin(n\phi)\cos\phi - n\cos(n\phi)\sin\phi}{\sin^3\phi} \end{aligned} \tag{A.109}$$

where the sines can be computed from the cosines. When $\phi \longrightarrow 0$,

$$\frac{\partial \cos(n\phi)}{\partial \cos\phi} = n\lim_{\phi\longrightarrow 0}\frac{n\phi}{\phi} = n^2 \tag{A.110}$$

and

$$\begin{aligned} \frac{\partial^2 \cos(n\phi)}{\partial^2 \cos\phi} &= n\lim_{\phi\longrightarrow 0^o}\frac{n\phi(1-\frac{1}{2}\phi^2) - n(1-\frac{1}{2}n^2\phi^2)\phi}{\phi^3} \\ &= \frac{1}{2}n^2(n^2-1) \end{aligned} \tag{A.111}$$

Having the above entities and formulas in the previous section, we can compute the force of atom x, with $x = I,\ J,\ K,$ or L as:

$$F_\alpha^x = -\frac{\partial \cos(n\phi)}{\partial R_\alpha^x} = -\frac{\partial \cos(n\phi)}{\partial \cos\phi}\frac{\partial \cos\phi}{\partial R_\alpha^x} \tag{A.112}$$

and the second derivative as

$$\frac{\partial^2 \cos(n\phi)}{\partial R_\alpha^x \partial R_\beta^x} = \frac{\partial \cos(n\phi)}{\partial \cos\phi} \frac{\partial^2 \cos\phi}{\partial R_\alpha^x \partial R_\beta^x} + \frac{\partial^2 \cos(n\phi)}{\partial^2 \cos\phi} \frac{\partial \cos\phi}{\partial R_\alpha^x} \frac{\partial \cos\phi}{\partial R_\beta^x} \tag{A.113}$$

A.4.2 Cross Coupling

For chain molecules, an accurate description of their rotational vibration frequencies often requires the introduction of cross coupling terms. Three types of cross couplings are implemented, bond cross coupling, cosine angle cross couping, and angle cross coupling.

Bond Cross Coupling

In addition to the pure torsion terms, the coupling energy of the two outer bonds (IJ and KL) is introduced as

$$E = K_{bb}(R^{IJ} - R_e^{IJ})(R^{LK} - R_e^{LK}) \tag{A.114}$$

with additional forces on the four atoms as

$$F_\alpha^I = -K_{bb}(R^{LK} - R_e^{LK}) \frac{R_\alpha^{IJ}}{R^{IJ}} \tag{A.115}$$

$$F_\alpha^J = K_{bb}(R^{LK} - R_e^{LK}) \frac{R_\alpha^{IJ}}{R^{IJ}} \tag{A.116}$$

$$F_\alpha^K = -K_{bb}(R^{IJ} - R_e^{IJ}) \frac{R_\alpha^{LK}}{R^{LK}} \tag{A.117}$$

$$F_\alpha^L = K_{bb}(R^{IJ} - R_e^{IJ}) \frac{R_\alpha^{LK}}{R^{LK}} \tag{A.118}$$

and additional second derivatives as

$$\frac{\partial^2 E}{\partial R_\alpha^I \partial R_\beta^I} = K_{bb}(R^{LK} - R_e^{LK}) \left(\frac{\delta_{\alpha\beta}}{R^{IJ}} - \frac{R_\alpha^{IJ} R_\beta^{IJ}}{(R^{IJ})^3} \right) \tag{A.119}$$

$$\frac{\partial^2 E}{\partial R_\alpha^J \partial R_\beta^J} = K_{bb}(R^{LK} - R_e^{LK}) \left(\frac{\delta_{\alpha\beta}}{R^{IJ}} - \frac{R_\alpha^{IJ} R_\beta^{IJ}}{(R^{IJ})^3} \right) \tag{A.120}$$

$$\frac{\partial^2 E}{\partial R_\alpha^K \partial R_\beta^K} = K_{bb}(R^{IJ} - R_e^{IJ})\Big(\frac{\delta_{\alpha\beta}}{R^{LK}} - \frac{R_\alpha^{LK} R_\beta^{LK}}{(R^{LK})^3}\Big) \tag{A.121}$$

$$\frac{\partial^2 E}{\partial R_\alpha^L \partial R_\beta^L} = K_{bb}(R^{IJ} - R_e^{IJ})\Big(\frac{\delta_{\alpha\beta}}{R^{LK}} - \frac{R_\alpha^{LK} R_\beta^{LK}}{(R^{LK})^3}\Big) \tag{A.122}$$

Cosine Angle Cross Coupling

Similar to bond cross coupling, this is also an additional term. The energy which couples cosines of the two angles (θ^{IJK} or θ^{JKL}) with the torsion angle ϕ is given as

$$E = K_{aa}(\cos\theta^{IJK} - \cos\theta_e^{IJK})(\cos\theta^{JKL} - \cos\theta_e^{JKL})\cos\phi \tag{A.123}$$

For $x = I,\ J,\ K$, and L, the additional force is given by:

$$\begin{aligned} F_\alpha^x &= -\frac{\partial E}{\partial R_\alpha^x} \\ &= -K_{aa}\cos\phi\Big[\frac{\partial\cos\theta^{IJK}}{\partial R_\alpha^x}(\cos\theta^{JKL} - \cos\theta_e^{JKL}) + (\cos\theta^{IJK} - \cos\theta_e^{IJK})\frac{\partial\cos\theta^{JKL}}{\partial R_\alpha^x}\Big] \\ &\quad -K_{aa}(\cos\theta^{IJK} - \cos\theta_e^{IJK})(\cos\theta^{JKL} - \cos\theta_e^{JKL})\frac{\partial\cos\phi}{\partial R_\alpha^x} \end{aligned} \tag{A.124}$$

and the additional terms in the second derivative are:

$$\begin{aligned} \frac{\partial^2 E}{\partial R_\alpha^x \partial R_\beta^x} &= K_{aa}\frac{\partial\cos\phi}{\partial R_\beta^x}\Big[\frac{\partial\cos\theta^{IJK}}{\partial R_\alpha^x}(\cos\theta^{JKL} - \cos\theta_e^{JKL}) + (\cos\theta^{IJK} - \cos\theta_e^{IJK})\frac{\partial\cos\theta^{JKL}}{\partial R_\alpha^x}\Big] \\ &\quad +K_{aa}\cos\phi\Big[\frac{\partial\cos\theta^{IJK}}{\partial R_\alpha^x}\frac{\partial\cos\theta^{JKL}}{\partial R_\beta^x} + \frac{\partial\cos\theta^{IJK}}{\partial R_\beta^x}\frac{\partial\cos\theta^{JKL}}{\partial R_\alpha^x}\Big] \\ &\quad +K_{aa}\cos\phi\frac{\partial^2\cos\theta^{IJK}}{\partial R_\alpha^x \partial R_\beta^x}(\cos\theta^{JKL} - \cos\theta_e^{JKL}) \\ &\quad +K_{aa}\cos\phi(\cos\theta^{IJK} - \cos\theta_e^{IJK})\frac{\partial^2\cos\theta^{JKL}}{\partial R_\alpha^x \partial R_\beta^x} \\ &\quad +K_{aa}\frac{\partial\cos\phi}{\partial R_\alpha^x}\Big[\frac{\partial\cos\theta^{IJK}}{\partial R_\beta^x}(\cos\theta^{JKL} - \cos\theta_e^{JKL}) + (\cos\theta^{IJK} - \cos\theta_e^{IJK})\frac{\partial\cos\theta^{JKL}}{\partial R_\beta^x}\Big] \\ &\quad +K_{aa}(\cos\theta^{IJK} - \cos\theta_e^{IJK})(\cos\theta^{JKL} - \cos\theta_e^{JKL})\frac{\partial^2\cos\phi}{\partial R_\alpha^x \partial R_\beta^x} \end{aligned} \tag{A.125}$$

Angle Cross Coupling

Similar to cosine angle cross coupling, here the two angles (θ^{IJK} and θ^{JKL}) are coupled with the torsion angle ϕ to give an energy:

$$E = K_{aa}(\theta^{IJK} - \theta_e^{IJK})(\theta^{JKL} - \theta_e^{JKL})\cos\phi \tag{A.126}$$

The additional forces are given by

$$\begin{aligned} F_\alpha^x &= -\frac{\partial E}{\partial R_\alpha^x} \\ &= K_{aa}\frac{\theta^{JKL} - \theta_e^{JKL}}{\sin\theta^{IJK}}\frac{\partial\cos\theta^{IJK}}{\partial R_\alpha^x}\cos\phi \\ &\quad + K_{aa}\frac{\theta^{IJK} - \theta_e^{IJK}}{\sin\theta^{JKL}}\frac{\partial\cos\theta^{JKL}}{\partial R_\alpha^x}\cos\phi \\ &\quad - K_{aa}(\theta^{IJK} - \theta_e^{IJK})(\theta^{JKL} - \theta_e^{JKL})\frac{\partial\cos\phi}{\partial R_\alpha^x} \end{aligned} \tag{A.127}$$

and addtional terms for second derivatives are given by

$$\begin{aligned} \frac{\partial^2 E}{\partial R_\alpha^x \partial R_\beta^x} &= -K_{aa}\left[\frac{\theta^{JKL} - \theta_e^{JKL}}{\sin\theta^{IJK}}\frac{\partial\cos\theta^{IJK}}{\partial R_\alpha^x} + \frac{\theta^{IJK} - \theta_e^{IJK}}{\sin\theta^{JKL}}\frac{\partial\cos\theta^{JKL}}{\partial R_\alpha^x}\right]\frac{\partial\cos\phi}{\partial R_\beta^x} \\ &\quad -K_{aa}\left[\frac{\theta^{JKL} - \theta_e^{JKL}}{\sin\theta^{IJK}}\frac{\partial^2\cos\theta^{IJK}}{\partial R_\alpha^x \partial R_\beta^x} + \frac{\theta^{IJK} - \theta_e^{IJK}}{\sin\theta^{JKL}}\frac{\partial^2\cos\theta^{JKL}}{\partial R_\alpha^x \partial R_\beta^x}\right]\cos\phi \\ &\quad +K_{aa}\cos\phi\frac{1}{\sin\theta^{IJK}}\frac{1}{\sin\theta^{JKL}}\left[\frac{\partial\cos\theta^{IJK}}{\partial R_\alpha^x}\frac{\partial\cos\theta^{JKL}}{\partial R_\beta^x} + \frac{\partial\cos\theta^{IJK}}{\partial R_\beta^x}\frac{\partial\cos\theta^{JKL}}{\partial R_\alpha^x}\right] \\ &\quad +K_{aa}\cos\phi\frac{(\theta^{JKL} - \theta_e^{JKL})\cos\theta^{IJK}}{\sin^3\theta^{IJK}}\frac{\partial\cos\theta^{IJK}}{\partial R_\alpha^x}\frac{\partial\cos\theta^{IJK}}{\partial R_\beta^x} \\ &\quad +K_{aa}\cos\phi\frac{(\theta^{IJK} - \theta_e^{IJK})\cos\theta^{JKL}}{\sin^3\theta^{JKL}}\frac{\partial\cos\theta^{JKL}}{\partial R_\alpha^x}\frac{\partial\cos\theta^{JKL}}{\partial R_\beta^x} \\ &\quad +K_{aa}(\theta^{IJK} - \theta_e^{IJK})(\theta^{JKL} - \theta_e^{JKL})\frac{\partial^2\cos\phi}{\partial R_\alpha^x \partial R_\beta^x} \end{aligned} \tag{A.128}$$

where x can be I, J, K, or L and similar derivation of $\partial\cos\phi/\partial R_\alpha^x$, $\partial\cos\theta^{IJK}/\partial R_\alpha^x$, $\partial\cos\theta^{JKL}/\partial R_\alpha^x$, $\partial^2\cos\theta^{IJK}/\partial R_\alpha^x\partial R_\alpha^x$, $\partial^2\cos\theta^{JKL}/\partial R_\alpha^x\partial R_\alpha^x$, and $\partial^2\cos\phi/\partial R_\alpha^x\partial R_\alpha^x$ can be found in previous sections.

A.5 Inversion

Consider a case in which three (and only three) atoms, J, K, and L are bonded to a central atom I. The umbrella motion in which the angle ϕ of IL with respect to the plane IJK changes from plus to minus sometimes requires a special interaction term; this is the inversion term. Two types of inversion terms are implemented. They are Amber improper torsion and spectroscopic inversion.

A.5.1 Amber Improper Torsion

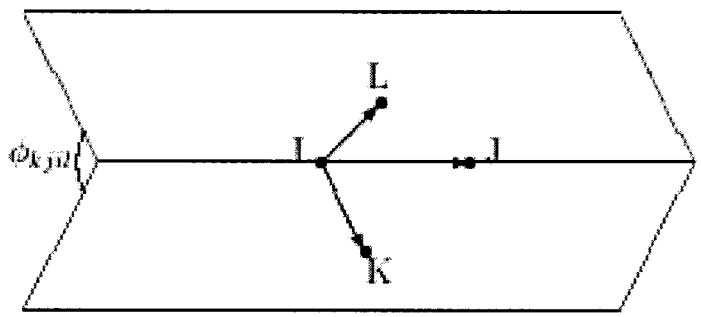

Figure A.4: Amber improper torsion

For atom J, K, and L bonded to atom I, we have three dihedral angles. The energy is the average of the three "torsion terms." For angle ϕ_{kjil}, defined as the angle between the LIJ and KIJ planes, the energy is taken as

$$E^{LIJ-KIJ} = \frac{1}{2}C\cos(N\phi_{kjil}) \tag{A.129}$$

So

$$E_{inv} = \frac{1}{6}C\Big[\cos(N\phi_{jkil}) + \cos(N\phi_{kjil}) + \cos(N\phi_{klij})\Big] \tag{A.130}$$

where $N = 2$ for planar and $N = 3$ for tetrahedral. With $N = 2$, the potential has a minimum for planar ($\phi_e = 180^o$) and the maxima at $\phi = 90, 270^o$. There is also a minimum at $\phi = 0^o$. With $N = 3$, the potential has a maximum at 180^o and minimua

at 120^o and 240^o, followed by maxima at 60^o and 300^o. Energy, forces and second derivatives can be calculated as torsion interaction.

A.5.2 Spectroscopic Inversion

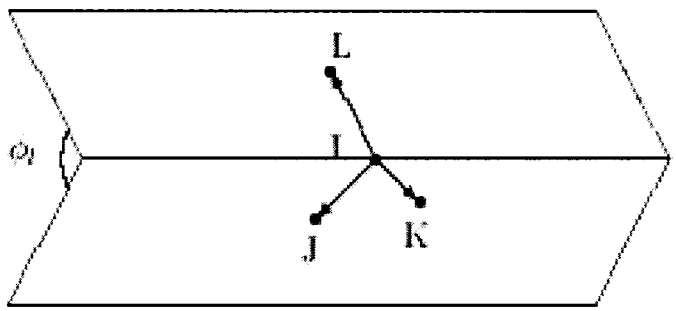

Figure A.5: Spectroscopic inversion

The spectroscopic inversion energy is defined by

$$E_{inv} = \frac{1}{6}C\Big[(\cos\phi_j - \cos\phi_e)^2 + (\cos\phi_k - \cos\phi_e)^2 + (\cos\phi_\ell) - \cos\phi_e)^2\Big] \quad \text{(A.131)}$$

with angle ϕ_l as the angle between line IL and plane IJK, ϕ_k as the angle between line IK and plane IJL, and ϕ_j as the angle between line IK and plane IKL. We'll only consider term $\cos\phi_l$; the other two terms can be calculated accordingly. Defining $\mathbf{A} = \mathbf{R}^{IJ} \times \mathbf{R}^{IK}$, we have:

$$\sin\phi_l = \left|\frac{\mathbf{R}^{IL}\cdot\mathbf{A}}{R^{IL}A}\right| \quad \text{(A.132)}$$

$$\cos\phi_l = \sqrt{1-\sin^2\phi_\ell}. \quad \text{(A.133)}$$

Let:

$$E_\ell = \frac{1}{6}C(\cos\phi_\ell - \cos\phi_e)^2 \quad \text{(A.134)}$$

For $x = I,\ J,\ K$, or L, we have

$$F_\alpha^x = \frac{\partial E_l}{\partial R_\alpha^x}$$

$$\begin{aligned} &= \frac{1}{3}C(\cos\phi_l - \cos\phi_e)\frac{\partial\cos\phi_l}{\partial\sin\phi_l}\frac{\partial\sin\phi_l}{\partial R_\alpha^x} \\ &= -\frac{1}{3}C(\cos\phi_l - \cos\phi_e)\frac{\sin\phi_l}{\cos\phi_l}\frac{\partial\sin\phi_l}{\partial R_\alpha^x} \end{aligned} \tag{A.135}$$

and

$$\begin{aligned} \frac{\partial^2 E_l}{\partial R_\alpha^x \partial R_\beta^x} &= \frac{1}{3}C(\frac{\sin\phi_l}{\cos\phi_l})^2\frac{\partial\sin\phi_l}{\partial R_\alpha^x}\frac{\partial\sin\phi_l}{\partial R_\beta^x} - \frac{1}{3}C(\cos\phi_l - \cos\phi_e)\frac{\sin\phi_l}{\cos\phi_l}\frac{\partial^2\sin\phi_l}{\partial R_\alpha^x \partial R_\beta^x} \\ &\quad -\frac{1}{3}C(\cos\phi_l - \cos\phi_e)\cos^{-3}\phi_l\frac{\partial\sin\phi_l}{\partial R_\alpha^x}\frac{\partial\sin\phi_l}{\partial R_\beta^x} \end{aligned} \tag{A.136}$$

Further

$$\begin{aligned} \frac{\partial\sin\phi_l}{\partial R_\alpha^x} &= \frac{1}{R^{IL}}(\frac{\partial\mathbf{R}^{IL}}{\partial R_\alpha^x}\cdot\frac{\mathbf{A}}{A}) - (\mathbf{R}^{IL}\cdot\frac{\partial\mathbf{R}^{IL}}{\partial R_\alpha^x})(\frac{\mathbf{R}^{IL}}{(R^{IL})^3}\cdot\frac{\mathbf{A}}{A}) \\ &\quad +\frac{\mathbf{R}^{IL}}{R^{IL}}\cdot\frac{\partial\mathbf{A}}{\partial R_\alpha^x}\frac{1}{A} - (\frac{\mathbf{R}^{IL}}{R^{IL}}\cdot\frac{\mathbf{A}}{A^3})(\mathbf{A}\cdot\frac{\partial\mathbf{A}}{\partial R_\alpha^x}) \end{aligned} \tag{A.137}$$

and

$$\begin{aligned} \frac{\partial^2\sin\phi_l}{\partial R_\alpha^x \partial R_\beta^x} &= \Big[\frac{1}{R^{IL}}\frac{\partial\mathbf{R}^{IL}}{\partial R_\alpha^x} - (\mathbf{R}^{IL}\cdot\frac{\partial\mathbf{R}^{IL}}{\partial R_\alpha^x})\frac{\mathbf{R}^{IL}}{(R^{IL})^3}\Big]\cdot\Big[\frac{1}{A}\frac{\partial\mathbf{A}}{\partial R_\beta^x} - (\mathbf{A}\cdot\frac{\partial\mathbf{A}}{\partial R_\beta^x})\frac{\mathbf{A}}{A^3}\Big] \\ &\quad +\Big[\frac{1}{R^{IL}}\frac{\partial\mathbf{R}^{IL}}{\partial R_\beta^x} - (\mathbf{R}^{IL}\cdot\frac{\partial\mathbf{R}^{IL}}{\partial R_\beta^x})\frac{\mathbf{R}^{IL}}{(R^{IL})^3}\Big]\cdot\Big[\frac{1}{A}\frac{\partial\mathbf{A}}{\partial R_\alpha^x} - (\mathbf{A}\cdot\frac{\partial\mathbf{A}}{\partial R_\alpha^x})\frac{\mathbf{A}}{A^3}\Big] \\ &\quad +\frac{\partial}{\partial R_\beta^x}\Big[\frac{1}{R^{IL}}\frac{\partial\mathbf{R}^{IL}}{\partial R_\alpha^x} - (\mathbf{R}^{IL}\cdot\frac{\partial\mathbf{R}^{IL}}{\partial R_\alpha^x})\frac{\mathbf{R}^{IL}}{(R^{IL})^3}\Big]\cdot\frac{\mathbf{A}}{A} \\ &\quad +\frac{\mathbf{R}^{IL}}{R^{IL}}\cdot\frac{\partial}{\partial R_\beta^x}\Big[\frac{1}{A}\frac{\partial\mathbf{A}}{\partial R_\alpha^x} - (\mathbf{A}\cdot\frac{\partial\mathbf{A}}{\partial R_\alpha^x})\frac{\mathbf{A}}{A^3}\Big] \end{aligned} \tag{A.138}$$

Further expand this to give:

$$\frac{\partial}{\partial R_\beta^x}\left(\frac{1}{R^{IL}}\frac{\partial \mathbf{R}^{IL}}{\partial R_\alpha^x}\right) = -\frac{1}{(R^{IL})^3}\left(\mathbf{R}^{IL}\cdot\frac{\partial \mathbf{R}^{IL}}{\partial R_\beta^x}\right)\frac{\partial \mathbf{R}^{IL}}{\partial R_\alpha^x} + \frac{1}{R^{IL}}\frac{\partial^2 \mathbf{R}^{IL}}{\partial R_\alpha^x \partial R_\beta^x} \quad \text{(A.139)}$$

$$\frac{\partial}{\partial R_\beta^x}\left(\frac{1}{A}\frac{\partial \mathbf{A}}{\partial R_\alpha^x}\right) = -\frac{1}{A^3}\left(\mathbf{A}\cdot\frac{\partial \mathbf{A}}{\partial R_\beta^x}\right)\frac{\partial \mathbf{A}}{\partial R_\alpha^x} + \frac{1}{A}\frac{\partial^2 \mathbf{A}}{\partial R_\alpha^x \partial R_\beta^x} \quad \text{(A.140)}$$

$$\begin{aligned}\frac{\partial}{\partial R_\beta^x}\left[(\mathbf{R}^{IL}\cdot\frac{\partial \mathbf{R}^{IL}}{\partial R_\alpha^x})\frac{\mathbf{R}^{IL}}{(R^{IL})^3}\right] = \\ \left(\frac{\partial \mathbf{R}^{IL}}{\partial R_\beta^x}\cdot\frac{\partial \mathbf{R}^{IL}}{\partial R_\alpha^x}\right)\frac{\mathbf{R}^{IL}}{(R^{IL})^3} + \left(\mathbf{R}^{IL}\cdot\frac{\partial^2 \mathbf{R}^{IL}}{\partial R_\alpha^x \partial R_\beta^x}\right)\frac{\mathbf{R}^{IL}}{(R^{IL})^3} \\ +\left(\mathbf{R}^{IL}\cdot\frac{\partial \mathbf{R}^{IL}}{\partial R_\alpha^x}\right)\left[\frac{1}{(R^{IL})^3}\frac{\partial \mathbf{R}^{IL}}{\partial R_\beta^x} - 3\frac{\mathbf{R}^{IL}}{(R^{IL})^5}(\mathbf{R}^{IL}\cdot\frac{\partial \mathbf{R}^{IL}}{\partial R_\beta^x})\right]\end{aligned} \quad \text{(A.141)}$$

$$\begin{aligned}\frac{\partial}{\partial R_\beta^x}\left[(\mathbf{A}\cdot\frac{\partial \mathbf{A}}{\partial R_\alpha^x})\frac{\mathbf{A}}{A^3}\right] &= \left(\frac{\partial \mathbf{A}}{\partial R_\beta^x}\cdot\frac{\partial \mathbf{A}}{\partial R_\alpha^x}\right)\frac{\mathbf{A}}{A^3} + \left(\mathbf{A}\cdot\frac{\partial^2 \mathbf{A}}{\partial R_\alpha^x \partial R_\beta^x}\right)\frac{\mathbf{A}}{A^3} \\ &\quad +\left(\mathbf{A}\cdot\frac{\partial \mathbf{A}}{\partial R_\alpha^x}\right)\left[\frac{1}{A^3}\frac{\partial \mathbf{A}}{\partial R_\beta^x} - 3\frac{\mathbf{A}}{A^5}(\mathbf{A}\cdot\frac{\partial \mathbf{A}}{\partial R_\beta^x})\right]\end{aligned} \quad \text{(A.142)}$$

Replace the individual terms in the above equations by the following for atom I:

$$\frac{\partial R_\gamma^{IL}}{\partial R_\alpha^I} = -\delta_{\alpha\gamma} \quad \text{(A.143)}$$

$$\frac{\partial A_\gamma}{\partial R_\alpha^I} = -\epsilon_{\gamma\alpha\nu}R_\nu^{IK} - \epsilon_{\gamma\mu\beta}R_\mu^{IJ} \quad \text{(A.144)}$$

$$\frac{\partial^2 A_\gamma}{\partial R_\alpha^I} = \epsilon_{\gamma\alpha\beta} + \epsilon_{\gamma\beta\alpha} = 0 \quad \text{(A.145)}$$

and for atom J:

$$\frac{\partial R_\gamma^{IL}}{\partial R_\alpha^J} = 0 \tag{A.146}$$

$$\frac{\partial A_\gamma}{\partial R_\alpha^J} = \epsilon_{\gamma\alpha\nu} R_\nu^{IK} \tag{A.147}$$

$$\frac{\partial^2 A_\gamma}{\partial R_\alpha^J \partial R_\beta^J} = 0 \tag{A.148}$$

and for atom K:

$$\frac{\partial R_\gamma^{IL}}{\partial R_\alpha^K} = 0 \tag{A.149}$$

$$\frac{\partial A_\gamma}{\partial R_\alpha^K} = \epsilon_{\gamma\alpha\nu} R_\nu^{IJ} \tag{A.150}$$

$$\frac{\partial^2 A_\gamma}{\partial R_\alpha^K \partial R_\beta^K} = 0 \tag{A.151}$$

Finally, for atom L

$$\frac{\partial R_\gamma^{IL}}{\partial R_\alpha^L} = \delta_{\gamma\alpha} \tag{A.152}$$

$$\frac{\partial^2 R_\gamma^{IL}}{\partial R_\alpha^L \partial R_\beta^L} = 0 \tag{A.153}$$

$$\frac{\partial A_\gamma}{\partial R_\alpha^L} = 0 \tag{A.154}$$

Using these, we can complete the terms of forces and second derivatives originated from E_l. Terms of E_j and E_k can be computed accordingly.

A.6 Stress Contributions

Since the valence force fields only depend on atomic positions, energy conservation applies. Thus if Ω is the unit cell volume and $\Pi_{\alpha\beta}$ the stress, we can write the valence

stress contribution as

$$\Omega\Pi_{\alpha\beta} = \sum_{i=1}^{N} F_{\alpha}^{i} R_{\beta}^{i} \tag{A.155}$$

where N is the number of atoms in the unit cell, $\mathbf{F}^i$ is the force of atom i, while $\mathbf{R}^i$ is the coordinates of atom i.

Appendix B Non-bonded Force Fields

B.1 Introduction

Non-bond force fields are used to describe two-body (electrostatic and van der Waals) and three-body (DREIDING hydrogen-bond) interactions. Usually non-bond interactions are excluded for 1-2 (two atoms bonded) and 1-3 (two atoms are bonded to a common atom) because these pairs are modeled by bond and angle terms. Sometimes the 1-4 (two atoms at the ends of a torsion configuration) interactions are also excluded, or scaled by 0.5 (AMBER). We implemented most of the generally used functional forms in our program.

B.2 Electrostatic

Figure B.1: Electrostatic interaction

Electrostatic interactions play a critical role in determining the structure and packing of molecules, both organic and inorganic. The Coulombic energy can be written as

$$E = C_0 \frac{Q_i Q_j}{\varepsilon R} \tag{B.1}$$

where Q_i and Q_j are the atomic charges in electron units ($Q = +1$ for a proton), R is the distance in Å, ε is the dielectric constant, and the conversion factor $C_0 = 332.0637$ takes care of the units transformation, so that E is given in kcal/mol. In vancuum, ε equals 1. For biological systems in which solvent molecules are not included explicitly

in the simulation, it is common to use $\varepsilon = R$. A shielded Coulomb interaction implicitly includes the solvent electric effect. The energy takes the form of

$$E = C_0 \frac{Q_i Q_j}{R^2} \tag{B.2}$$

Assume $E = C_0 Q_i Q_j / R^p$ with $p = 1$ for regular Coulomb while $p = 2$ for shielded Coulomb. For atom j, α component of force is given by

$$F_\alpha^j = -\frac{\partial E}{\partial R_\alpha^j} = C_0 p \frac{R_\alpha}{R^{p+2}} \tag{B.3}$$

and the second derivative is given by

$$\frac{\partial^2 E}{\partial R_\alpha^j \partial R_\beta^j} = -C_0 p \Big[\frac{\delta_{\alpha\beta}}{R^{p+2}} - (p+2) \frac{R_\alpha R_\beta}{R^{p+4}} \Big] \tag{B.4}$$

B.3 Van der Waals Interaction

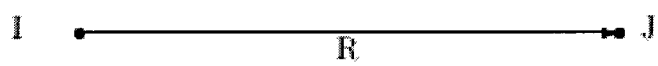

Figure B.2: Van der Waals interaction

All atoms exhibit a long range attraction which is proportional to R^{-6}. This is generally referred to as van der Waals (vdW) attraction since the van der Waals equation of state postulated such a universal attraction. At sufficiently short distances the interactions of all atoms are repulsive. We implemented three types; they are Lennard-Jones 12-6, Exponential-6, and Morse. In each case the interaction is specified with up to three parameters, R_0 (equilibrium distance), D_0 (equilibrium energy, or well-depth), and γ (scale parameter). These nonbonded interactions are of two-body type requiring $N(N+1)/2$ sets of parameters for a system with N different

atoms. However, the following combination rules,

$$R_{0,ij} = \frac{1}{2}(R_{0,ii} + R_{0,jj}) \tag{B.5}$$

$$D_{0,ij} = \sqrt{D_{0,ii} D_{0,jj}} \tag{B.6}$$

$$\gamma_{ij} = \frac{1}{2}(\gamma_{ii}\gamma_{jj}) \tag{B.7}$$

are often adequate for relating the parameters of different atoms (i with j) to the corresponding homo nuclear parameters (i–i and j–j). Sometimes for LJ 12-6 potentials, the arithmetic average is replaced by the geometric mean.

$$R_{0,ij} = \sqrt{R_{0,ii} R_{0,jj}} \tag{B.8}$$

$$D_{0,ij} = \sqrt{D_{0,ii} D_{0,jj}} \tag{B.9}$$

B.3.1 Lennard-Jones 12-6

For Lennard-Jones 12-6, the energy is given by

$$E = \frac{A}{R^{12}} - \frac{B}{R^6} = D_0\left[(\frac{R_0}{R})^{12} - (\frac{R_0}{R})^6\right] \tag{B.10}$$

where D_0 is the equilibrium energy in kcal/mol and R_0 is the equilibrium distance in Å. The α component of force on atom J is given by

$$F_\alpha^J = -\frac{\partial E}{\partial R_\alpha^J} = 12A\frac{R_\alpha}{R^{14}} - 6B\frac{R_\alpha}{R^8} \tag{B.11}$$

and its second derivative is:

$$\frac{\partial^2 E}{\partial R_\alpha^J \partial R_\beta^J} = -12A\frac{\delta_{\alpha\beta}}{R^{14}} + 168A\frac{R_\alpha R_\beta}{R^{16}} - 6A\frac{\delta_{\alpha\beta}}{R^8} + 48B\frac{R_\alpha R_\beta}{R^{10}} \tag{B.12}$$

B.3.2 Exponential-6

For Exponential-6, the energy is given by

$$E = Ae^{CR} - \frac{B}{R^6} = D_0\Big[\frac{6}{\zeta - 6}\exp\big(\zeta(1 - \frac{R}{R_0})\big) - \frac{\zeta}{\zeta - 6}\big(\frac{R_0}{R}\big)^6\Big] \tag{B.13}$$

where again D_0 is the equilibrium energy in kcal/mol and R_0 is the equilibrium distance in Å; ζ is the scaling factor. The default value for ζ is 12, which approximates the Lennard-Jones 12-6 potential at long distances.

The α component of force on atom J is given by

$$F_\alpha^J = -\frac{\partial E}{\partial R_\alpha^J} = -ACe^{CR}\frac{R_\alpha}{R} - 6B\frac{R_\alpha}{R^8} \tag{B.14}$$

The second derivative is given by

$$\frac{\partial^2 E}{\partial R_\alpha^J \partial R_\beta^J} = \Big(AC\frac{e^{CR}}{R} + \frac{6B}{R^8}\Big)\delta_{\alpha\beta} + \Big(AC^2\frac{e^{CR}}{R^2} - AC\frac{e^{CR}}{R^3} - 48\frac{B}{R^{10}}\Big)R_\alpha R_\beta \tag{B.15}$$

B.3.3 Morse Potential

The Morse potential is given by:

$$E = D_0[\chi^2 - 2\chi] \tag{B.16}$$

where

$$\chi = e^{-\alpha(R-R_0)} = \exp\big(-\frac{\gamma}{2}(\frac{R}{R_0} - 1)\big) \tag{B.17}$$

where again D_0 is the equilibrium energy in kcal/mol and R_0 is the equilibrium distance in Å, and γ is the scaling factor. The force and second derivative of atom J

are given by

$$\frac{\partial E}{\partial R_\alpha^J} = 2D_0(\chi - 1)\frac{\partial \chi}{\partial R_\alpha^J}, \tag{B.18}$$

and

$$\frac{\partial^2 E}{\partial R_\alpha^J \partial R_\beta^J} = 2D_0\frac{\partial \chi}{\partial R_\alpha^J}\frac{\partial \chi}{\partial R_\beta^J} + 2D_0(\chi - 1)\frac{\partial^2 \chi}{\partial R_\alpha^J \partial R_\beta^J}, \tag{B.19}$$

where

$$\frac{\partial \chi}{\partial R_\alpha^J} = -\alpha\chi\frac{R_\alpha}{R} \tag{B.20}$$

$$\frac{\partial^2 \chi}{\partial R_\alpha^J \partial R_\beta^J} = \alpha^2\chi\frac{R_\alpha R_\beta}{R^2} - \alpha\chi\frac{\delta_{\alpha\beta}}{R} + \alpha\chi\frac{R_\alpha R_\beta}{R^3}. \tag{B.21}$$

B.4 Hydrogen Bonding

In molecules having hydrogen atoms bonded to very electronegative (donor) atoms (F, O, Cl, N, S), the electrostatic interactions between this H and a neighboring electronegative (acceptor) atom may not be well described just with standard atom-centered charges. Thus a special type of non bonded interaction is allowed to account for such terms. We implemented two strategies, as used in the AMBER and CHARMM force fields.

B.4.1 AMBER

In AMBER, the charges assigned to the H (Hydrogen) and A (Acceptor) are used to account for the bulk of the attractive interactions. This is supplemented by a weak 12-10 potential designed to help adjust the resulting H-A distance. The normal 12-6 interaction between H and A is ignored. The energy takes the form of

$$E = \frac{A}{R^{12}} - \frac{B}{R^{10}} = D_0\Big[5(\frac{R_0}{R})^{12} - 6(\frac{R_0}{R})^6\Big] \tag{B.22}$$

and the α component of force on atom J is

$$\frac{\partial E}{\partial R_\alpha^J} = -12A\frac{R_\alpha}{R^{14}} + 10B\frac{R_\alpha}{R^{12}} \tag{B.23}$$

while the second derivative is

$$\frac{\partial^2 E}{\partial R_\alpha^J \partial R_\beta^J} = -12A\frac{\delta_{\alpha\beta}}{R^{14}} + 168A\frac{R_\alpha R_\beta}{R^{16}} + 10A\frac{\delta_{\alpha\beta}}{R^8} - 120B\frac{R_\alpha R_\beta}{R^{10}} \tag{B.24}$$

B.4.2 CHARMM

The normal van der Waals and electrostatic interactions of the H with all other atoms is ignored and replaced with a special H-Bond potential involving the D–A distance and the D–H–A angle. Let R_{AD} be the radial distance between the donor (D) and

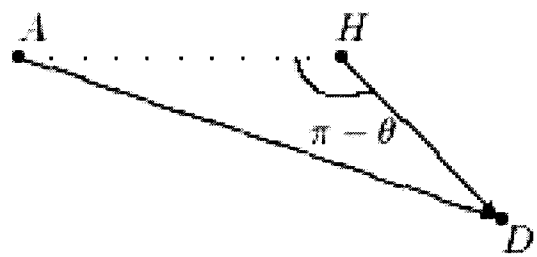

Figure B.3: Hydrogen bond interaction

acceptor (A) atoms and θ be the bond angle between the acceptor (A), the hydrogen (H), and the donor (D) atoms as in the Fig. B.3. The potential has the general form

$$E = E^{hb}(R_{AD})\, S(R_{AD}^2, R_{on}^2, R_{off}^2)\, S(\cos^2\theta, \cos^2\theta_{on}, \cos^2\theta_{off}) \cos^4\theta \tag{B.25}$$

where S is the cubic spline switching function which smoothly cuts off the interaction,

$$S(x, x_{on}, x_{off}) = \begin{cases} 1 & \text{if } x \le x_{on} \\ \frac{(x_{off}-x)^2(x_{off}+2x-3x_{on})}{(x_{off}-x_{on})^3} & \text{if } x_{on} < x < x_{off} \\ 0 & \text{if } x \ge x_{off} \end{cases} \tag{B.26}$$

with $R_{on} = 4.0$Å, $R_{off} = 4.5$Å, $\theta_{on} = 65^o$, $\theta_{off} = 75^o$, and E^{hb} is the Morse potential.

$$E^{hb} = D_0(\chi^2 - 2\chi) \tag{B.27}$$

with

$$\chi = e^{-\alpha(R-R_0)} = e^{-\frac{\gamma}{2}(\frac{R}{R_0}-1)} \tag{B.28}$$

Let

$$E_r = E^{hb}(R_{AD})\, S(R_{AD}^2, R_{on}^2, R_{off}^2) \tag{B.29}$$

and

$$E_\theta = S(\cos^2\theta, \cos^2\theta_{on}, \cos^2\theta_{off}) \cos^4\theta \tag{B.30}$$

The α component of force on atom x, with $x = H,\ A$, and D, is given by

$$F_\alpha^x = -\frac{\partial E}{\partial R_\alpha^x} = -\frac{\partial E_r}{\partial R_{AD}} \frac{\partial R_{AD}}{\partial R_\alpha^x} E_\theta - E_r \frac{\partial E_\theta}{\partial \cos\theta} \frac{\partial \cos\theta}{\partial R_\alpha^x} \tag{B.31}$$

and the second derivative given by

$$\begin{aligned} \frac{\partial^2 E}{\partial R_\alpha^x \partial R_\beta^x} &= \frac{\partial E_r}{\partial R_{AD}} \frac{\partial E_\theta}{\partial \cos\theta} \left[\frac{\partial R_{AD}}{\partial R_\alpha^x} \frac{\partial \cos\theta}{\partial R_\beta^x} + \frac{\partial R_{AD}}{\partial R_\beta^x} \frac{\partial \cos\theta}{\partial R_\alpha^x} \right] \\ &+ \frac{\partial^2 E_r}{\partial^2 R_{AD}} E_\theta \frac{\partial R_{AD}}{\partial R_\alpha^x} \frac{\partial R_{AD}}{\partial R_\beta^x} + E_r \frac{\partial^2 E_\theta}{\partial^2 \cos\theta} \frac{\partial \cos\theta}{\partial R_\alpha^x} \frac{\partial \cos\theta}{\partial R_\beta^x} \\ &+ \frac{\partial E_r}{\partial R_{AD}} \frac{\partial^2 R_{AD}}{\partial R_\alpha^x \partial R_\beta^x} E_\theta + E_r \frac{\partial E_\theta}{\partial \cos\theta} \frac{\partial^2 \cos\theta}{\partial R_\alpha^x \partial R_\beta^x} \end{aligned} \tag{B.32}$$

where, for the distance related terms, we have

$$\frac{\partial E_r}{\partial R_{AD}} = \frac{\partial E^{hb}}{\partial R_{AD}} S(R_{AD}^2, R_{on}^2, R_{off}^2) + E^{hb} S'(R_{AD}^2, R_{on}^2, R_{off}^2) 2R_{AD} \tag{B.33}$$

$$\frac{\partial^2 E_r}{\partial^2 R_{AD}} = \frac{\partial^2 E^{hb}}{\partial^2 R_{AD}} S(R^2_{AD}, R^2_{on}, R^2_{off}) + E^{hb} S''(R^2_{AD}, R^2_{on}, R^2_{off}) 4R^2_{AD} + \frac{\partial E^{hb}}{\partial R_{AD}} S'(R^2_{AD}, R^2_{on}, R^2_{off}) 4R_{AD} + 2E^{hb} S'(R^2_{AD}, R^2_{on}, R^2_{off}) \quad \text{(B.34)}$$

and, for the angle related terms, we have

$$\frac{\partial E_\theta}{\partial \cos\theta} = 4\cos^3\theta\, S(\cos^2\theta, \cos^2\theta_{on}, \cos^2\theta_{off}) + 2\cos^5\theta\, S'(\cos^2\theta, \cos^2\theta_{on}, \cos^2\theta_{off}) \quad \text{(B.35)}$$

$$\frac{\partial^2 E_\theta}{\partial^2 \cos\theta} = 12\cos^2\theta S(\cos^2\theta, \cos^2\theta_{on}, \cos^2\theta_{off}) + 18\cos^4\theta S'(\cos^2\theta, \cos^2\theta_{on}, \cos^2\theta_{off}) + 4\cos^6\theta S''(\cos^2\theta, \cos^2\theta_{on}, \cos^2\theta_{off}) \quad \text{(B.36)}$$

The cubic spline functions S are defined as

$$S'(x, x_{on}, x_{off}) = \begin{cases} 6\frac{(x_{off}-x)(x_{on}-x))}{(x_{off}-x_{on})^3} & \text{if } x_{on} < x < x_{off} \\ 0 & \text{else} \end{cases} \quad \text{(B.37)}$$

For distance cutoff, $x = R^2$, $x_{on} = R^2_{on}$ and $x_{off} = R^2_{off}$. While for angle cutoff, $x = \cos^2\theta$, $x_{on} = \cos^2\theta_{on}$, and $x_{off} = \cos^2\theta_{off}$. Using the following entities

$$\frac{\partial \chi}{\partial R_{AD}} = -2\alpha D_0(\chi - 1)\chi \quad \text{(B.38)}$$

$$\frac{\partial^2 \chi}{\partial^2 R_{AD}} = 2\alpha^2 D_0(2\chi - 1)\chi \quad \text{(B.39)}$$

$$\frac{\partial R_{AD}}{\partial R^A_\alpha} = -\frac{R_{AD\alpha}}{R_{AD}} \quad \text{(B.40)}$$

$$\frac{\partial \cos\theta}{\partial R^A_\alpha} = \frac{R_{DH\alpha}}{R_{DH}R_{AH}} - \cos\theta\frac{R_{AH\alpha}}{R^2_{AH}} \quad \text{(B.41)}$$

$$\frac{\partial^2 \cos\theta}{\partial R^A_\alpha \partial R^A_\beta} = \frac{R_{AH\alpha}R_{DH\beta} + R_{AH\beta}R_{DH\alpha}}{R^3_{AH}R_{DH}} - \cos\theta\Big[\frac{\delta_{\alpha\beta}}{R^2_{AH}} + 3\frac{R_{AH\alpha}R_{AH\beta}}{R^4_{AH}}\Big] \tag{B.42}$$

$$\frac{\partial R_{AD}}{\partial R^D_\alpha} = \frac{R_{AD\alpha}}{R_{AD}} \tag{B.43}$$

$$\frac{\partial \cos\theta}{\partial R^D_\alpha} = \frac{R_{AH\alpha}}{R_{AH}R_{DH}} - \cos\theta\frac{R_{DH\alpha}}{R^2_{DH}} \tag{B.44}$$

$$\frac{\partial^2 \cos\theta}{\partial R^D_\alpha \partial R^D_\beta} = \frac{R_{DH\alpha}R_{AH\beta} + R_{DH\beta}R_{AH\alpha}}{R^3_{DH}R_{AH}} - \cos\theta\Big[\frac{\delta_{\alpha\beta}}{R^2_{DH}} + 3\frac{R_{DH\alpha}R_{DH\beta}}{R^4_{DH}}\Big] \tag{B.45}$$

we can calculate the forces and second derivatives at atom A, D, and H.

B.5 Convergence of Non-bond Summations

For isolated systems with million atoms, or systems with periodic boundary conditions, the computation of non-bond energy becomes impossible, with the simple pair-wise summation. For such systems, three methods are implemented to reduce the inhabitive computing cost with certain accuracy. They are Cubic-Spline cutoff, cell multipole method (CMM), and Ewald summation. We'll discuss the CMM and Ewald methods in future chapters.

B.5.1 Spline Cutoff

For each pair of nonbond interaction (Coulomb and van der Waals), the energy is multiplied by switching function $S(R^2, R^2_{on}, R^2_{off})$, giving the energy as

$$E_{spline} = E_{nb}S(R^2, R^2_{on}, R^2_{off}) \tag{B.46}$$

Where R is the distance between two atoms, typically we have $R_{on} = 8.0\text{Å}$ and $R_{off} = 8.5\text{Å}$. The cutoff function is defined as Eq. (B.37). The computation of forces and second derivatives are similar to that of the distance related energy term in DREIDII Hydrogen-Bond interaction.

Appendix C Cell Multipole Method

C.1 Introduction

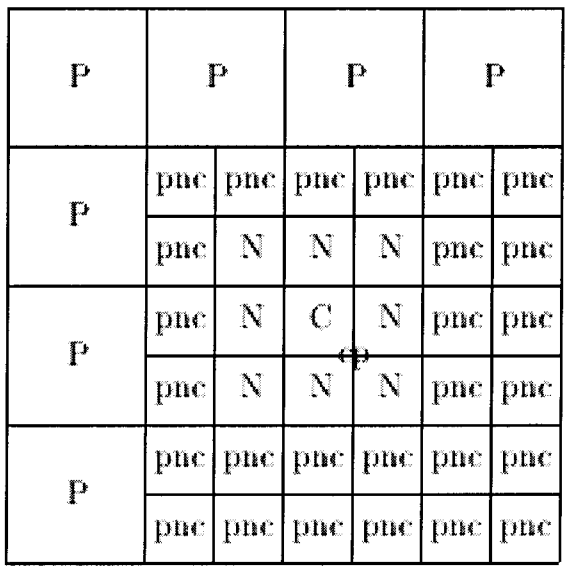

Figure C.1: Cell hierarchy

In the molecular dynamics of a system of N particles for which there is no finite range cut-off, direct evaluation of the forces takes a computation time per time step which grows as N^2. For biological systems and amorphous polymer systems, hundreds of thousands of atoms are needed to approximate those systems. Obviously direct evaluation method cannot handle such systems, even with today's fast computers. Besides optimized Ewald method (which scales as $N^{\frac{3}{2}}$), cell multipole method (CMM)[1–5] is developed to handle such systems. CMM is fast; it scales linearly with N (the CMM setup scales as $N \log N$) and requires modest memory.

CMM method is a typical divide and conquer algorithm. The simulation cell is recursively sub-divided into octants. At the finest level (leaf level), the influence of

the particles within a cell onto sufficiently separated cells is subsumed into a multipole series expansion. These multipole expansions are combined in the upper levels, until the root (simulation cell) of the oct-tree contains a multipole expansion. For atoms within the 27 nearest neighbor leaf cells, direct pair-wise summation is used to compute the energy, stress, and forces. Contribution from atoms outside the 27 nearest neighbor leaf cells are calculated through field expansion, i.e., through the Taylor expansion of the far field with respect to the center of leaf cells, which is the contribution from the far cells.

Figure C.1 shows the first three levels of division. We'll look at the force and energy of atoms in cell C, the level-3 cell. We start with cell C's parent cell (cp). Taylor expansion coeffiecients with respect to the center of cell cp are calculated by summing up the contribution from cp's next nearest neighbor cells, the P cells. Taylor expansion coefficients with respect to the center of cell C have two terms. One is the contribution from C's next nearest neighbor cells, the pnc cells, while the rest is from the P cells, which are computed through translating cp cell's Taylor expansion coefficients from center of cp cell to the center of C cell. This process continues to the lowest level, leaf cells.

C.2 Multipole Representation of Field

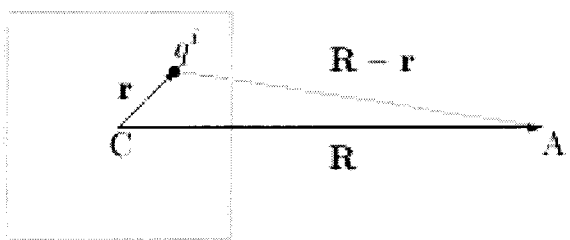

Figure C.2: Multipole representation

As in Fig. C.2, C is the cell within which there are many point "charges." We'll compute the field at A due to "charges" in cell C. We assume $|\mathbf{R}| \gg |\mathbf{r}|$ applies for

all of the "charges" within cell C.

First, let's look at the potential at $\mathbf{R}$ due to point "charge" q^i

$$V^i(\mathbf{R}) = \frac{q^i}{(\mathbf{R}\cdot\mathbf{R} - 2\mathbf{R}\cdot\mathbf{r} + \mathbf{r}\cdot\mathbf{r})^{p/2}} \tag{C.1}$$

For $p = 1$ is the Coulomb interaction, $p = 2$ is the shielded Coulomb interaction, while $p = 6$ is the van der Waals attraction, or London dispersion. In the rest of derivation, we'll use Einstein convention, where double appearance of a subscribe means summation over that index.

Since $r/R \ll 1$, we can expand the formula at $r = 0$

$$\begin{aligned}
\frac{\partial V^i}{\partial r_\alpha} &= -\frac{p}{2}q^i\frac{-2R_\gamma\delta_{\alpha\gamma} + 2r_\gamma\delta_{\alpha\gamma}}{(R_\gamma R_\gamma - 2R_\gamma r_\gamma + r_\gamma r_\gamma)^{\frac{p+2}{2}}} \\
&= pq^i\frac{R_\alpha - r_\alpha}{(R_\gamma R_\gamma - 2R_\gamma r_\gamma + r_\gamma r_\gamma)^{\frac{p+2}{2}}} \qquad \text{(C.2)} \\
\frac{\partial^2 V^i}{\partial r_\alpha \partial r_\beta} &= pq^i\frac{-\delta_{\alpha\beta}}{(R_\gamma R_\gamma - 2R_\gamma r_\gamma + r_\gamma r_\gamma)^{\frac{p+2}{2}}} - p\frac{p+2}{2}q^i\frac{-2(R_\alpha - r_\alpha)(R_\beta - r_\beta)}{(R_\gamma R_\gamma - 2R_\gamma r_\gamma + r_\gamma r_\gamma)^{\frac{p+4}{2}}} \\
&= p(p+2)q^i\frac{(R_\alpha - r_\alpha)(R_\beta - r_\beta)}{(R_\gamma R_\gamma - 2R_\gamma r_\gamma + r_\gamma r_\gamma)^{\frac{p+4}{2}}} - pq^i\frac{\delta_{\alpha\beta}}{(R_\gamma R_\gamma - 2R_\gamma r_\gamma + r_\gamma r_\gamma)^{\frac{p+2}{2}}} \qquad \text{(C.3)}
\end{aligned}$$

$$\begin{aligned}
\frac{\partial^3 V^i}{\partial R_\alpha \partial R_\beta \partial R_\gamma} &= p(p+2)(p+4)q^i\frac{(R_\alpha - r_\alpha)(R_\beta - r_\beta)(R_\gamma - r_\gamma)}{(R_\lambda R_\lambda - 2R_\lambda r_\lambda + r_\lambda r_\lambda)^{\frac{p+6}{2}}} \\
&\quad -p(p+2)q^i\frac{\delta_{\alpha\beta}(R_\gamma - r_\gamma) + \delta_{\beta\gamma}(R_\alpha - r_\alpha) + \delta_{\gamma\alpha}(R_\beta - r_\beta)}{(R_\lambda R_\lambda - 2R_\lambda r_\lambda + r_\lambda r_\lambda)^{\frac{p+4}{2}}} \qquad \text{(C.4)}
\end{aligned}$$

Thus

$$\left.\frac{\partial V^i}{\partial r_\alpha}\right|_{r=0} = pq^i\frac{R_\alpha}{R^{p+2}} \tag{C.5}$$

$$\left.\frac{\partial^2 V^i}{\partial r_\alpha \partial r_\beta}\right|_{r=0} = p(p+2)q^i\frac{R_\alpha R_\beta}{R^{p+4}} - pq^i\frac{\delta_{\alpha\beta}}{R^{p+2}} \tag{C.6}$$

$$\begin{aligned}\left.\frac{\partial^3 V^i}{\partial r_\alpha \partial r_\beta \partial r_\gamma}\right|_{r=0} &= p(p+2)(p+4)q^i\frac{R_\alpha R_\beta R_\gamma}{R^{p+6}} \\ &\quad -p(p+2)q^i\frac{\delta_{\alpha\beta}R_\gamma + \delta_{\beta\gamma}R_\alpha + \delta_{\gamma\alpha}R_\beta}{R^{p+4}}\end{aligned} \tag{C.7}$$

The potential at point R due to "charges" within the cell is

$$\begin{aligned}V(R) &= \sum_i V^i(R) \\ &= \sum_i V^i(R)\Big|_{r=0} + \sum_i r_\alpha \left.\frac{\partial V}{\partial r_\alpha}\right|_{r=0} + \sum_i \frac{1}{2}r_\alpha r_\beta \left.\frac{\partial^2 V}{\partial r_\alpha \partial r_\beta}\right|_{r=0} \\ &\quad + \sum_i \frac{1}{6}r_\alpha r_\beta r_\gamma \left.\frac{\partial^3 V^i}{\partial r_\alpha \partial r_\beta \partial r_\gamma}\right|_{r=0} + \dots \\ &= \frac{\sum_i q^i}{R^p} + \frac{R_\alpha \sum_i pq^i r_\alpha}{R^{p+2}} + \frac{R_\alpha R_\beta \sum_i \frac{1}{2}q^i\left[p(p+2)r_\alpha r_\beta - pr^2\delta_{\alpha\beta}\right]}{R^{p+4}} \\ &\quad + \frac{R_\alpha R_\beta R_\gamma}{R^{p+6}}\sum_i \frac{p(p+2)(p+4)}{6}q^i r_\alpha r_\beta r_\gamma \\ &\quad + \frac{R_\alpha R_\beta R_\gamma}{R^{p+6}}\sum_i \frac{p(p+2)}{6}q^i(r^2\delta_{\alpha\beta}r_\gamma + r^2\delta_{\beta\gamma}r_\alpha + r^2\delta_{\gamma\alpha}r_\beta) + \dots\end{aligned} \tag{C.8}$$

where we have used

$$\begin{aligned}R^2\delta_{\alpha\beta}r_\alpha r_\beta &= R^2 r^2 \\ R_\alpha R_\beta \delta_{\alpha\beta} r^2 &= R^2 r^2\end{aligned} \tag{C.9}$$

if we define

$$Z = \sum_i q^i \tag{C.10}$$

$$\mu_\alpha = \sum_i p q^i r_\alpha \tag{C.11}$$

$$Q_{\alpha\beta} = \sum_i \frac{1}{2} q^i \Big[p(p+2) r_\alpha r_\beta - p r^2 \delta_{\alpha\beta} \Big] \tag{C.12}$$

$$O_{\alpha\beta\gamma} = \sum_i \frac{1}{6} p(p+2) q^i \big[(p+4) r_\alpha r_\beta r_\gamma - (\delta_{\alpha\beta} r_\gamma + \delta_{\beta\gamma} r_\alpha + \delta_{\gamma\alpha} r_\beta) r^2 \big] \tag{C.13}$$

we have

$$V(R) = \frac{Z}{R^p} + \frac{\mu_\alpha R_\alpha}{R^{p+2}} + \frac{R_\alpha R_\beta Q_{\alpha\beta}}{R^{p+4}} + \frac{O_{\alpha\beta\gamma} R_\alpha R_\beta R_\gamma}{R^{p+6}} + \ldots \tag{C.14}$$

Alternatively, we can also define

$$Z = \sum_i q^i \tag{C.15}$$

$$F_\alpha = \sum_i q^i r_\alpha \tag{C.16}$$

$$S_{\alpha\beta} = \sum_i q^i r_\alpha r_\beta \tag{C.17}$$

$$T_{\alpha\beta\gamma} = \sum_i q^i r_\alpha r_\beta r_\gamma \tag{C.18}$$

(F, S, T) can be transformed into (μ, Q, O) by using the following equations.

$$\mu_\alpha = p F_\alpha \tag{C.19}$$

$$Q_{\alpha\beta} = \frac{1}{2} p \big[(p+2) S_{\alpha\beta} - Trace(S) \delta_{\alpha\beta} \big] \tag{C.20}$$

$$O_{\alpha\beta\gamma} = \frac{1}{6} p(p+2) \big[(p+4) T_{\alpha\beta\gamma} - (\delta_{\alpha\beta} T_{\lambda\lambda\gamma} + \delta_{\beta\gamma} T_{\lambda\lambda\alpha} + \delta_{\gamma\alpha} T_{\lambda\lambda\beta}) \big] \tag{C.21}$$

C.3 Upward Pass

Given the multipole moments of level l cells, the multipole moments of level $l-1$ cells are calculated as the following

$$
\begin{aligned}
Z^{l-1} &= \sum_{i\in C_{l-1}} q^i = \sum_l \sum_{i\in C_l} q^i = \sum_l Z^l && \text{(C.22)}\\
\mu_\alpha^{l-1} &= \sum_{i\in C_{l-1}} pq^i r_\alpha^{l-1} = \sum_l \sum_{i\in C_l} pq^i (R_\alpha^l + r_\alpha^l)\\
&= \sum_l R_\alpha^l p \sum_{i\in C_l} q^i + \sum_l \sum_{i\in C_l} pq^i r_\alpha^l\\
&= p\sum_l Z^l R_\alpha^l + \sum_l \mu_\alpha^l && \text{(C.23)}\\
Q_{\alpha\beta}^{l-1} &= \sum_{i\in C_{l-1}} \frac{1}{2} q^i \Big[p(p+2) r_\alpha^{l-1} r_\beta^{l-1} - p(r^{l-1})^2 \delta_{\alpha\beta}\Big]\\
&= \sum_{i\in C_{l-1}} \frac{1}{2} q^i \Big[p(p+2)(R_\alpha^l + r_\alpha^l)(R_\beta^l + r_\beta^l) - p(R_\gamma^l + r_\gamma^l)(R_\gamma^l + r_\gamma^l)\delta_{\alpha\beta}\Big]
\end{aligned}
$$

$$
\begin{aligned}
&= \sum_{i\in C_{l-1}} \frac{1}{2} q^i \Big[p(p+2) R_\alpha^l R_\beta^l - p R_\gamma^l R_\gamma^l \delta_{\alpha\beta}\Big]\\
&\quad + \sum_{i\in C_{l-1}} \frac{1}{2} q^i \Big[p(p+2) r_\alpha^l r_\beta^l - p r_\gamma^l r_\gamma^l \delta_{\alpha\beta}\Big]\\
&\quad - \sum_{i\in C_{l-1}} \frac{1}{2} q^i \Big[p(p+2)(R_\alpha^l r_\beta^l + r_\alpha^l R_\beta^l) - 2p R_\gamma^l r_\gamma^l\Big]\\
&= \sum_l \frac{1}{2} Z^l \Big[p(p+2) R_\alpha^l R_\beta^l - p R_\gamma^l R_\gamma^l \delta_{\alpha\beta}\Big]\\
&\quad + \sum_l \sum_{i\in C_l} \frac{1}{2} q^i \Big[p(p+2) r_\alpha^l r_\beta^l - p r_\gamma^l r_\gamma^l \delta_{\alpha\beta}\Big]\\
&\quad - \sum_l \frac{1}{2} \Big[(p+2)(R_\alpha^l \sum_{i\in C_l} pq^i r_\beta^l + R_\beta^l \sum_{i\in C_l} pq^i r_\alpha^l) - 2(R_\gamma^l \sum_{i\in C_l} pq^i r_\gamma^l)\delta_{\alpha\beta}\Big]\\
&= \frac{1}{2} p \sum_l Z^l \Big[(p+2) R_\alpha^l R_\beta^l - R^{l^2}\delta_{\alpha\beta}\Big] + \sum_l Q_{\alpha\beta}^l\\
&\quad + \frac{1}{2} \sum_l \Big[(p+2)(\mu_\alpha^l R_\beta^l + \mu_\beta^l R_\alpha^l) - 2(\vec{\mu}\cdot\vec{R}^l)\delta_{\alpha\beta}\Big] && \text{(C.24)}
\end{aligned}
$$

$$
\begin{aligned}
O^{l-1}_{\alpha\beta\gamma} &= \sum_i \frac{1}{6}p(p+2)q^i\Big[(p+4)r^{l-1}_\alpha r^{l-1}_\beta r^{l-1}_\gamma - (\delta_{\alpha\beta}r^{l-1}_\gamma + \delta_{\beta\gamma}r^{l-1}_\alpha + \delta_{\gamma\alpha}r^{l-1}_\beta)(r^{l-1})^2\Big] \\
&= \sum_i \frac{1}{6}p(p+2)(p+4)q^i(R^l_\alpha + r^l_\alpha)(R^l_\beta + r^l_\beta)(R^l_\gamma + r^l_\gamma) \\
&\quad - \sum_i \frac{1}{6}p(p+2)q^i\Big[\delta_{\alpha\beta}(R^l_\gamma + r^l_\gamma) + \delta_{\beta\gamma}(R^l_\alpha + r^l_\alpha) + \delta_{\gamma\alpha}(R^l_\alpha + r^l_\alpha)\Big]\Big|\vec{R}^l + \vec{r}^l\Big|^2 \\
&= \sum_i \frac{1}{6}p(p+2)(p+4)q^iA_i - \sum_i \frac{1}{6}p(p+2)q^iB_i \qquad \text{(C.25)}
\end{aligned}
$$

where we write

$$
\begin{aligned}
A_i &= (R^l_\alpha + r^l_\alpha)(R^l_\beta + r^l_\beta)(R^l_\gamma + r^l_\gamma) \\
&= R^l_\alpha R^l_\beta R^l_\gamma + R^l_\alpha R^l_\beta r^l_\gamma + R^l_\alpha r^l_\beta R^l_\gamma + r^l_\alpha R^l_\beta R^l_\gamma \\
&\quad + R^l_\alpha r^l_\beta r^l_\gamma + r^l_\alpha R^l_\beta r^l_\gamma + r^l_\alpha r^l_\beta R^l_\gamma + r^l_\alpha r^l_\beta r^l_\gamma \qquad \text{(C.26)} \\
B_i &= \Big[\delta_{\alpha\beta}(R^l_\gamma + r^l_\gamma) + \delta_{\beta\gamma}(R^l_\alpha + r^l_\alpha) + \delta_{\gamma\alpha}(R^l_\alpha + r^l_\alpha)\Big]\Big|\vec{R}^l + \vec{r}^l\Big|^2
\end{aligned}
$$

$$
\begin{aligned}
&= (\delta_{\alpha\beta}R^l_\gamma + \delta_{\beta\gamma}R^l_\alpha + \delta_{\gamma\alpha}R^l_\beta)R^l_mR^l_m + (\delta_{\alpha\beta}r^l_\gamma + \delta_{\beta\gamma}r^l_\alpha + \delta_{\gamma\alpha}r^l_\beta)R^l_mR^l_m \\
&\quad + (\delta_{\alpha\beta}R^l_\gamma + \delta_{\beta\gamma}R^l_\alpha + \delta_{\gamma\alpha}R^l_\beta)2R^l_mr^l_m + (\delta_{\alpha\beta}r^l_\gamma + \delta_{\beta\gamma}r^l_\alpha + \delta_{\gamma\alpha}r^l_\beta)2R^l_mr^l_m \\
&\quad + (\delta_{\alpha\beta}R^l_\gamma + \delta_{\beta\gamma}R^l_\alpha + \delta_{\gamma\alpha}R^l_\beta)r^l_mr^l_m + (\delta_{\alpha\beta}r^l_\gamma + \delta_{\beta\gamma}r^l_\alpha + \delta_{\gamma\alpha}r^l_\beta)r^l_mr^l_m \qquad \text{(C.27)}
\end{aligned}
$$

sum over contributions at level-l cells, we have following entities.

$$\sum_i \frac{1}{6}p(p+2)q^i\Big[(p+4)r^l_\alpha r^l_\beta r^l_\gamma - (\delta_{\alpha\beta}r^l_\gamma + \delta_{\beta\gamma}r^l_\alpha + \delta_{\gamma\alpha}r^l_\beta)(r^l)^2\Big] = \sum_l O^l_{\alpha\beta\gamma} \tag{C.28}$$

$$\sum_i \frac{1}{6}p(p+2)q^i\Big[(p+4)R^l_\alpha R^l_\beta R^l_\gamma - (\delta_{\alpha\beta}R^l_\gamma + \delta_{\beta\gamma}R^l_\alpha + \delta_{\gamma\alpha}R^l_\beta)(R^l)^2\Big]$$
$$= \sum_l \frac{1}{6}p(p+2)Z^l\Big[(p+4)R^l_\alpha R^l_\beta R^l_\gamma - (\delta_{\alpha\beta}R^l_\gamma + \delta_{\beta\gamma}R^l_\alpha + \delta_{\gamma\alpha}R^l_\beta)(R^l)^2\Big] \tag{C.29}$$

$$\sum_i \frac{1}{6}p(p+2)(p+4)q^i(r^l_\alpha r^l_\beta R^l_\gamma + r^l_\alpha R^l_\beta r^l_\gamma + R^l_\alpha r^l_\beta r^l_\gamma) = \sum_l \frac{1}{3}(p+4)(Q^l_{\alpha\beta}R^l_\gamma + Q^l_{\beta\gamma}R^l_\alpha + Q^l_{\gamma\alpha}R^l_\beta)$$
$$+ \sum_i \frac{1}{6}p(p+4)(\delta_{\alpha\beta}R^l_\gamma + \delta_{\beta\gamma}R^l_\alpha + \delta_{\gamma\alpha}R^l_\beta)(r^l)^2 \tag{C.30}$$

$$\sum_i \frac{1}{6}p(p+2)(p+4)q^i(R^l_\alpha R^l_\beta r^l_\gamma + R^l_\alpha r^l_\beta R^l_\gamma + r^l_\alpha R^l_\beta R^l_\gamma)$$
$$= \sum_l \frac{1}{6}(p+2)(p+4)(R^l_\alpha R_\beta \mu_\gamma + R^l_\alpha \mu_\beta R^l_\gamma + \mu_\alpha R_\beta R^l_\gamma) \tag{C.31}$$

$$\sum_i \frac{1}{6}p(p+2)q^i(\delta_{\alpha\beta}r^l_\gamma + \delta_{\beta\gamma}r^l_\alpha + \delta_{\gamma\alpha}r^l_\beta)(R^l)^2$$
$$= \sum_l \frac{1}{6}p(p+2)(\delta_{\alpha\beta}\mu_\gamma + \delta_{\beta\gamma}\mu_\alpha + \delta_{\gamma\alpha}\mu_\beta)(R^l)^2 \tag{C.32}$$

$$\sum_i \frac{1}{6}p(p+2)q^i(\delta_{\alpha\beta}R^l_\gamma + \delta_{\beta\gamma}R^l_\alpha + \delta_{\gamma\alpha}R^l_\beta)2\mathbf{R}^l \cdot \mathbf{r}^l$$
$$= \sum_l \frac{1}{6}p(p+2)(\delta_{\alpha\beta}R^l_\gamma + \delta_{\beta\gamma}R^l_\alpha + \delta_{\gamma\alpha}R^l_\beta)2\mathbf{R}^l \cdot \mu^l \tag{C.33}$$

$$\sum_i \frac{1}{6}p(p+2)q^i(\delta_{\alpha\beta}r^l_\gamma + \delta_{\beta\gamma}r^l_\alpha + \delta_{\gamma\alpha}r^l_\beta)2R^l_m r^l_m$$
$$= \sum_l \frac{2}{3}(\delta_{\alpha\beta}Q^l_{\gamma m}R^l_m + \delta_{\beta\gamma}Q^l_{\alpha m}R^l_m + \delta_{\gamma\alpha}Q^l_{\beta m}R^l_m)$$
$$+ \sum_i \frac{1}{3}pq^i(\delta_{\alpha\beta}R^l_\gamma + \delta_{\beta\gamma}R^l_\alpha + \delta_{\gamma\alpha}R^l_\beta)(r^l)^2 \tag{C.34}$$

Collecting the above equations together, we have

$$\begin{aligned} O^{l-1}_{\alpha\beta\gamma} &= \sum_l \frac{1}{6}p(p+2)Z^l\Big[(p+4)R^l_\alpha R^l_\beta R^l_\gamma - (\delta_{\alpha\beta}R^l_\gamma + \delta_{\beta\gamma}R^l_\alpha + \delta_{\gamma\alpha}R^l_\beta)(R^l)^2\Big] \\ &+ \sum_l \frac{1}{6}(p+2)(p+4)(\mu^l_\alpha R^l_\beta R^l_\gamma + R^l_\alpha \mu^l_\beta R^l_\gamma + R^l_\alpha R^l_\beta \mu^l_\gamma) \\ &- \sum_l \frac{1}{3}(p+2)(\vec{\mu^l}\cdot\vec{R^l})(\delta_{\alpha\beta}R^l_\gamma + \delta_{\beta\gamma}R^l_\alpha + \delta_{\gamma\alpha}R^l_\beta) \\ &- \sum_l \frac{1}{6}(p+2)(R^l)^2(\delta_{\alpha\beta}\mu^l_\gamma + \delta_{\beta\gamma}\mu^l_\alpha + \delta_{\gamma\alpha}\mu^l_\beta) \\ &- \sum_l \frac{2}{3}(\delta_{\alpha\beta}Q^l_{\gamma\lambda}R^l_\lambda + \delta_{\beta\gamma}Q^l_{\alpha\lambda}R^l_\lambda + \delta_{\gamma\alpha}Q^l_{\beta\lambda}R^l_\lambda) \\ &+ \sum_l O^l_{\alpha\beta\gamma} \end{aligned} \tag{C.35}$$

If we use $(\mathbf{F}, \mathbf{S}, \mathbf{T})$, instead of $(\mu, \mathbf{Q}, \mathbf{O})$, we have

$$Z^{l-1} = \sum_l Z^l \tag{C.36}$$

$$F^{l-1}_\alpha = \sum_l F^l_\alpha + \sum_l Z^l r^l_\alpha \tag{C.37}$$

$$S^{l-1}_{\alpha\beta} = \sum_l S^l_{\alpha\beta} + \sum_l (F^l_\alpha R^l_\beta + F^l_\beta R^l_\alpha) + \sum_l Z^l R^l_\alpha R^l_\beta \tag{C.38}$$

$$\begin{aligned} T^{l-1}_{\alpha\beta\gamma} &= \sum_l T^l_{\alpha\beta\gamma} + \sum_l (S^l_{\alpha\beta}R^l_\gamma + S^l_{\beta\gamma}R^l_\alpha + S^l_{\gamma\alpha}R^l_\beta) \\ &+ \sum_l (F^l_\alpha R^l_\beta R^l_\gamma + F^l_\beta R^l_\gamma R^l_\alpha + F^l_\gamma R^l_\alpha R^l_\beta) + \sum_l Z^l R^l_\alpha R^l_\beta R^l_\gamma \end{aligned} \tag{C.39}$$

First Eq. (C.15–C.21) are used to compute multipoles of the leaf cells. Then Eq. (C.22–C.24, C.35) are used to combine multipoles of leaf level cells into multipoles of next level cells. This process continues recursively to the root cell.

C.4 Downward Pass

C.4.1 Contribution from Parent's Neighbor's Children

In CMM, all far field terms are approximated by Taylor series expansions around the central position of the cell containing $\mathbf{r}$ as the following

$$V(\mathbf{r}) = V^{(0)} + V_{\alpha}^{(1)} r_{\alpha} + V_{\alpha\beta}^{(2)} r_{\alpha} r_{\beta} + V_{\alpha\beta\gamma}^{(3)} r_{\alpha} r_{\beta} r_{\gamma} + \ldots \tag{C.40}$$

where

$$V_{\alpha}^{(1)} = \left. \frac{\partial V}{\partial r_{\alpha}} \right|_{r=0} \tag{C.41}$$

$$V_{\alpha\beta}^{(2)} = \left. \frac{1}{2} \frac{\partial^2 V}{\partial r_{\alpha} \partial r_{\beta}} \right|_{r=0} \tag{C.42}$$

$$V_{\alpha\beta\gamma}^{(3)} = \left. \frac{1}{6} \frac{\partial^3 V}{\partial r_{\alpha} \partial r_{\beta} \partial r_{\gamma}} \right|_{r=0} \tag{C.43}$$

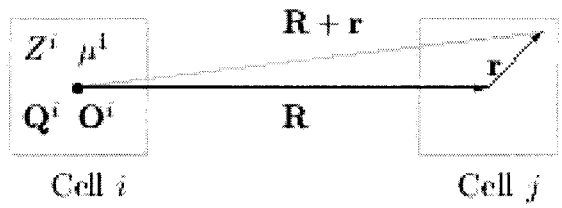

Figure C.3: Multipole field expansion

Assuming $\mathbf{R}$ is the vector between center of two cells, we'll calculate Taylor expansion coefficients of the field at the center of cell j due to multipole moments of cell i. Coefficients $V^{(0)}$, $V^{(1)}$, and $V^{(2)}$ are obtained by summing expansion coefficients of charge, dipole, and quadrupole terms as

$$V^{(0)} = V_Z^{(0)} + V_{\mu}^{(0)} + V_Q^{(0)} + V_O^{(0)} \tag{C.44}$$

$$V_{\alpha}^{(1)} = V_{Z\alpha}^{(1)} + V_{\mu\alpha}^{(1)} + V_{Q\alpha}^{(1)} + V_{O\alpha}^{(1)} \tag{C.45}$$

$$V^{(2)}_{\alpha\beta} = V^{(2)}_{Z\alpha\beta} + V^{(2)}_{\mu\alpha\beta} + V^{(2)}_{Q\alpha\beta} + V^{(2)}_{O\alpha\beta} \tag{C.46}$$

$$V^{(3)}_{\alpha\beta\gamma} = V^{(3)}_{Z\alpha\beta\gamma} + V^{(3)}_{\mu\alpha\beta\gamma} + V^{(3)}_{Q\alpha\beta\gamma} + V^{(3)}_{O\alpha\beta\gamma} \tag{C.47}$$

The "charge" terms $V^{(i)}_Z$ are obtained by the expansion

$$\frac{Z}{|\mathbf{R}+\mathbf{r}|^p} = V^{(0)}_Z + V^{(1)}_{Z\alpha} r_\alpha + V^{(2)}_{Z\alpha\beta} r_\alpha r_\beta + V^{(3)}_{Z\alpha\beta\gamma} r_\alpha r_\beta r_\gamma + \ldots \tag{C.48}$$

where

$$V^{(0)}_Z = \frac{Z}{R^p} \tag{C.49}$$

$$V^{(1)}_{Z\alpha} = -\frac{pZR_\alpha}{R^{p+2}} \tag{C.50}$$

$$V^{(2)}_{Z\alpha\beta} = \frac{pZ}{2R^{p+4}}\Big[(p+2)R_\alpha R_\beta - \delta_{\alpha\beta}R^2\Big] \tag{C.51}$$

$$V^{(3)}_{Z\alpha\beta\gamma} = -\frac{p(p+2)Z}{R^{p+6}}\Big[(p+4)R_\alpha R_\beta R_\gamma - (\delta_{\alpha\beta}R_\gamma + \delta_{\beta\gamma}R_\alpha + \delta_{\gamma\alpha}R_\beta)R^2\Big] \tag{C.52}$$

The dipole terms $V^{(i)}_\mu$ are obtained by the expansion

$$\frac{\mu\cdot(\mathbf{R}+\mathbf{r})}{|\mathbf{R}+\mathbf{r}|^{p+2}} = V^{(0)}_\mu + V^{(1)}_{\mu\alpha} r_\alpha + V^{(2)}_{\mu\alpha\beta} r_\alpha r_\beta + V^{(3)}_{\mu\alpha\beta} r_\alpha r_\beta r_\gamma + \ldots \tag{C.53}$$

where

$$V^{(0)}_\mu = \frac{\mu\cdot\mathbf{R}}{R^{p+2}} \tag{C.54}$$

$$V^{(1)}_{\mu\alpha} = \frac{\mu_\alpha}{R^{p+2}} - (p+2)\frac{(\mu\cdot\mathbf{R})R_\alpha}{R^{p+4}} \tag{C.55}$$

$$V^{(2)}_{\mu\alpha\beta} = -\frac{p+2}{2R^{p+4}}\Big[(\mu_\alpha R_\beta + \mu_\beta R_\alpha) + (\mu\cdot\mathbf{R})(\delta_{\alpha\beta} - \frac{p+4}{R^2}R_\alpha R_\beta)\Big] \tag{C.56}$$

$$\begin{aligned} V^{(3)}_{\mu\alpha\beta\gamma} = {} & -\frac{p+2}{6}\,\frac{\mu_\alpha\delta_{\beta\gamma} + \mu_\beta\delta_{\gamma\alpha} + \mu_\gamma\delta_{\alpha\beta}}{R^{p+4}} \\ & + \frac{(p+2)(p+4)}{6}\,\frac{\mu_\alpha R_\beta R_\gamma + \mu_\beta R_\gamma R_\alpha + \mu_\gamma R_\alpha R_\beta}{R^{p+6}} \\ & + \frac{(p+2)(p+4)}{6}\,\frac{(\mu\cdot\mathbf{R})(\delta_{\alpha\beta}R_\gamma + \delta_{\beta\gamma}R_\alpha + \delta_{\gamma\alpha}R_\beta)}{R^{p+6}} \\ & - \frac{(p+2)(p+4)(p+6)}{6}\,\frac{(\mu\cdot\mathbf{R})R_\alpha R_\beta R_\gamma}{R^{p+8}} \end{aligned} \tag{C.57}$$

The quadrupole terms $V_Q^{(i)}$ are obtained by the expansion

$$\frac{Q_{\mu\nu}(R_\mu + r_\mu)(R_\nu + r_\nu)}{\left|\mathbf{R} + \mathbf{r}\right|^{p+4}} = V_Q^{(0)} + V_{Q\alpha}^{(1)} r_\alpha + V_{Q\alpha\beta}^{(2)} r_\alpha r_\beta + V_{Q\alpha\beta\gamma}^{(3)} r_\alpha r_\beta r_\gamma + \dots \tag{C.58}$$

where

$$V_Q^{(0)} = \frac{Q_{\mu\nu} R_\mu R_\nu}{R^{p+4}} \tag{C.59}$$

$$V_{Q\alpha}^{(1)} = \frac{Q_{\alpha\nu} R_\nu + Q_{\mu\alpha} R_\mu}{R^{p+4}} - (p+4)\frac{Q_{\mu\nu} R_\mu R_\nu}{R^{p+6}} R_\alpha \tag{C.60}$$

$$\begin{aligned} V_{Q\alpha\beta}^{(2)} = {} & -\frac{p+4}{2R^{p+6}}\left[Q_{\mu\nu} R_\mu R_\nu \delta_{\alpha\beta} + (Q_{\mu\alpha} R_\mu R_\beta + Q_{\alpha\nu} R_\nu R_\beta + Q_{\mu\beta} R_\mu R_\alpha + Q_{\beta\nu} R_\nu R_\alpha)\right] \\ & + \frac{Q_{\alpha\beta}}{R^{p+4}} + \frac{(p+4)(p+6)}{2}\frac{Q_{\mu\nu} R_\mu R_\nu}{R^{p+8}} R_\alpha R_\beta \end{aligned} \tag{C.61}$$

$$\begin{aligned} V_{Q\alpha\beta\gamma}^{(3)} = {} & -\frac{p+4}{3}\frac{Q_{\alpha\beta} R_\gamma + Q_{\beta\gamma} R_\alpha + Q_{\gamma\alpha} R_\beta}{R^{p+6}} \\ & - \frac{p+4}{3}\frac{Q_{\alpha\lambda} R_\lambda \delta_{\beta\gamma} + Q_{\beta\lambda} R_\lambda \delta_{\gamma\alpha} + Q_{\gamma\lambda} R_\lambda \delta_{\alpha\beta}}{R^{p+6}} \\ & + \frac{(p+4)(p+6)}{3}\frac{Q_{\alpha\lambda} R_\lambda R_\beta R_\gamma + Q_{\beta\lambda} R_\lambda R_\gamma R_\alpha + Q_{\gamma\lambda} R_\lambda R_\alpha R_\beta}{R^{p+8}} \\ & + \frac{(p+4)(p+6)}{3}\frac{Q_{\mu\nu} R_\mu R_\nu (\delta_{\alpha\beta} R_\gamma + \delta_{\beta\gamma} R_\alpha + \delta_{\gamma\alpha} R_\beta)}{R^{p+8}} \\ & - \frac{(p+4)(p+6)(p+8)}{}\frac{Q_{\mu\nu} R_\mu R_\nu R_\alpha R_\beta R_\gamma}{R^{p+10}} \end{aligned} \tag{C.62}$$

The octopole terms $V_O^{(i)}$ are obtained by the expansion

$$\frac{O_{\alpha\beta\gamma}(R_\alpha + r_\alpha)(R_\beta + r_\beta)(R_\gamma + r_\gamma)}{\left|\mathbf{R} + \mathbf{r}\right|^{p+6}} = V_O^{(0)} + V_{O\alpha}^{(1)} r_\alpha + V_{O\alpha\beta}^{(2)} r_\alpha r_\beta + V_{O\alpha\beta\gamma}^{(3)} r_\alpha r_\beta r_\gamma + \dots \tag{C.63}$$

where, by considering the symmetry property of $O_{\alpha\beta\gamma}$

$$V_O^{(0)} = \frac{O_{\mu\nu\lambda} R_\mu R_\nu R_\lambda}{R^{p+6}} \tag{C.64}$$

$$V_{O\alpha}^{(1)} = \frac{3O_{\mu\nu\alpha} R_\mu R_\nu}{R^{p+6}} - (p+6)\frac{O_{\mu\nu\lambda} R_\mu R_\nu R_\lambda R_\alpha}{R^{p+8}} \tag{C.65}$$

$$
\begin{aligned}
V^{(2)}_{O\alpha\beta} &= 3\frac{O_{\mu\alpha\beta}R_\mu}{R^{p+6}} - \frac{p+6}{2}\frac{3(O_{\mu\nu\alpha}R_\mu R_\nu R_\beta + O_{\mu\nu\beta}R_\mu R_\nu R_\alpha)}{R^{p+8}} \\
&\quad + \frac{p+6}{2}\frac{O_{\mu\nu\lambda}R_\mu R_\nu R_\lambda}{R^{p+10}}[(p+8)R_\alpha R_\beta - \delta_{\alpha\beta}R^2] \qquad \text{(C.66)} \\
V^{(3)}_{O\alpha\beta\gamma} &= \frac{O_{\alpha\beta\gamma}}{R^{p+6}} - (p+6)\frac{R_\mu(O_{\mu\alpha\beta}R_\gamma + O_{\mu\beta\gamma}R_\alpha + O_{\mu\gamma\alpha}R_\beta)}{R^{p+8}} \\
&\quad - \frac{p+6}{2}\frac{R_\mu R_\nu(O_{\mu\nu\alpha}\delta_{\beta\gamma} + O_{\mu\nu\beta}\delta_{\gamma\alpha} + O_{\mu\nu\gamma}\delta_{\alpha\beta})}{R^{p+8}} \\
&\quad + \frac{(p+6)(p+8)}{2}\frac{R_\mu R_\nu(O_{\mu\nu\alpha}R_\beta R_\gamma + O_{\mu\nu\beta}R_\gamma R_\alpha + O_{\mu\nu\gamma}R_\alpha R_\beta)}{R^{p+10}} \\
&\quad + \frac{(p+6)(p+8)}{6}\frac{R_\mu R_\nu R_\lambda O_{\mu\nu\lambda}(\delta_{\alpha\beta}R_\gamma + \delta_{\beta\gamma}R_\alpha + \delta_{\gamma\alpha}R_\beta)}{R^{p+10}} \\
&\quad - \frac{(p+6)(p+8)(p+10)}{6}\frac{R_\mu R_\nu R_\lambda O_{\mu\nu\lambda}R_\alpha R_\beta R_\gamma}{R^{p+12}} \qquad \text{(C.67)}
\end{aligned}
$$

When we store $(\mathbf{F}, \mathbf{S}, \mathbf{T})$ instead of $(\mu, \mathbf{Q}, \mathbf{O})$, then we can convert $(\mathbf{F}, \mathbf{S}, \mathbf{T})$ into $(\mu, \mathbf{Q}, \mathbf{O})$ by using Eq. (C.19–C.21), then use the above same equations to compute Taylor expansion coefficients.

C.4.2 Contribution from Parent Cell

Contribution outside parent cell's 27 nearest neigbor cells is represented by parent cell's Taylor expansion coefficients. We have to translate those coefficients with respect to center of parent cell to the center of that cell. The field at $\mathbf{r}$

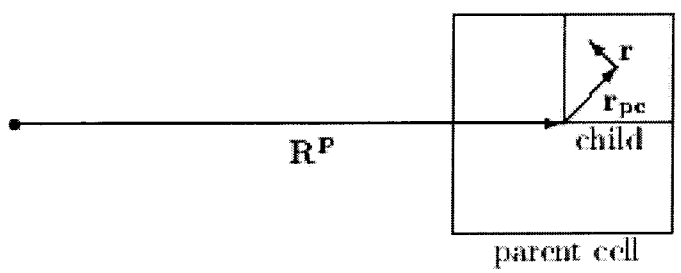

Figure C.4: Combine Taylor coefficients of parent cell with that of its child cell

$$
\begin{aligned}
V_r &= V^{(0)}_P + V^{(1)}_{P\alpha}(r_{pc\alpha} + r_\alpha) + V^{(2)}_{P\alpha\beta}(r_{pc\alpha} + r_\alpha)(r_{pc\beta} + r_\beta) \\
&\quad + V^{(3)}_{P\alpha\beta\gamma}(r_{pc\alpha} + r_\alpha)(r_{pc\beta} + r_\beta)(r_{pc\gamma} + r_\gamma)
\end{aligned}
$$

$$
\begin{aligned}
= \; & V_P^{(0)} + V_{P\alpha}^{(1)} r_{pc\alpha} + V_{P\alpha\beta}^{(2)} r_{pc\alpha} r_{pc\beta} + V_{P\alpha}^{(1)} r_\alpha + V_{P\alpha\beta}^{(2)} r_{pc\alpha} r_\beta + V_{P\alpha\beta}^{(2)} r_{pc\beta} r_\alpha + V_{P\alpha\beta}^{(2)} r_\alpha r_\beta \\
& + V_{P\alpha\beta\gamma}^{(3)} r_{pc\alpha} r_{pc\beta} r_{pc\gamma} + V_{P\alpha\beta\gamma}^{(3)} (r_{pc\alpha} r_{pc\beta} r_\gamma + r_{pc\beta} r_{pc\gamma} r_\alpha + r_{pc\gamma\alpha} r_{pc\alpha} r_\beta) \\
& + V_{P\alpha\beta\gamma}^{(3)} (r_{pc\alpha} r_\beta r_\gamma + r_{pc\beta} r_\gamma r_\alpha + r_{pc\gamma\alpha} r_\alpha r_\beta) + V_{P\alpha\beta\gamma}^{(3)} r_\alpha r_\beta r_\gamma \qquad \text{(C.68)}
\end{aligned}
$$

By using the symmetry properties of $V_{P\alpha\beta}^{(2)}$ and $V_{P\alpha\beta\gamma}^{(3)}$ we have

$$
\begin{aligned}
V_C^{(0)} &= V_P^{(0)} + V_{P\alpha}^{(1)} r_{pc\alpha} + V_{P\alpha\beta}^{(2)} r_{pc\alpha} r_{pc\beta} + V_{P\alpha\beta\gamma}^{(3)} r_{pc\alpha} r_{pc\beta} r_{pc\gamma} && \text{(C.69)} \\
V_{C\alpha}^{(1)} &= V_{P\alpha}^{(1)} + 2V_{P\alpha\beta}^{(2)} r_{pc\beta} + 3V_{P\alpha\beta\gamma}^{(3)} r_{pc\beta} r_{pc\gamma} && \text{(C.70)} \\
V_{C\alpha\beta}^{(2)} &= V_{P\alpha\beta}^{(2)} + 3V_{P\alpha\beta\gamma}^{(3)} r_{pc\gamma} && \text{(C.71)} \\
V_{C\alpha\beta\gamma}^{(3)} &= V_{P\alpha\beta\gamma}^{(3)} && \text{(C.72)}
\end{aligned}
$$

C.5 Energy and Force Evaluation

In addition to explicit interactions with atoms in the nearest neighbor cells, the contribution from far cells are

$$
\begin{aligned}
E(\vec{r^i}) &= V_{cell}^{(0)} + V_{cell,\alpha}^{(1)} r_\alpha^i + V_{cell,\alpha\beta}^{(2)} r_\alpha^i r_\beta^i + V_{cell,\alpha\beta\gamma}^{(3)} r_\alpha^i r_\beta^i r_\gamma^i && \text{(C.73)} \\
\frac{\partial E(\vec{r^i})}{\partial r_\alpha^i} &= V_{cell,\alpha}^{(1)} + 2V_{cell,\alpha\beta}^{(2)} r_\beta^i + 3V_{cell,\alpha\beta\gamma}^{(3)} r_\beta^i r_\gamma^i && \text{(C.74)}
\end{aligned}
$$

C.6 Stress Calculation

For periodic systems we need to calculate the stress, $\Pi_{\alpha\beta}$ with $\alpha\beta = xx,\ yy,\ zz,\ yz,\ zx,\ xy$. At the leaf cell level, the stress components $\Pi_{\alpha\beta}$ from the nearest neighbor contributions are calculated as

$$
\Omega \Pi_{\alpha\beta} = -\frac{p}{2} \sum_{i,j} \frac{q^i q^j}{\left| \vec{r_i} - \vec{r_j} \right|^{p+2}} (\vec{r_i} - \vec{r_j})_\alpha (\vec{r_i} - \vec{r_j})_\beta \qquad \text{(C.75)}
$$

where Ω is the volume of the unit cell and the sum is over atoms in the 27 nearest neighbor leaf cells.

The long range components of the stress are calculated during downward pass as contributions from interactions of the multipole moments between the cells. Since it's a periodic system, we start from level-1. While we compute Taylor expansion coefficients of one level-1 cell by combining the contribution from its pnc's, we also add the stress contributions from the pnc cells, which is the stress of interacting multipoles between the level-1 cell being considered and that of its pnc cells. This process continues down to the leaf-level, then we have the total stress contribution from interacting far cells.

C.6.1 Interactions Between $(Z^i, F^i_\alpha, S^i_{\alpha\beta}, T^i_{\alpha\beta\gamma})$ and $(Z^j, F^j_\alpha, S^j_{\alpha\beta}, T^j_{\alpha\beta\gamma})$

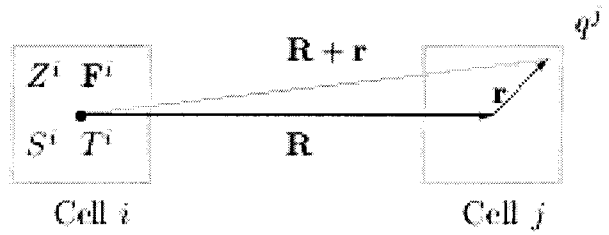

Figure C.5: Alternative multipole moments interaction

Figure C.5 shows interactions between "charges" of cell j and the multipoles in cell i. We'll examine the monopole, dipole, quadrupole, and octopole separately. Considering $R \ll r$, we can again expand the potential around $r = 0$, and approximate the contribution from all of the "charges" in cell j by multipoles of cell j. By doing so, we can approximate the interactions between atoms in two far cells as interaction between their multipoles.

Energy of Z^i with Cell j

The energy between Z^i and q^j

$$E_{Z^iq^j} = \frac{Z^iq^j}{|\mathbf{R}+\mathbf{r}|^p} \tag{C.76}$$

$$\frac{\partial E_{Z^iq^j}}{\partial r_\alpha} = -p\frac{Z^iq^j(R_\alpha+r_\alpha)}{|\mathbf{R}+\mathbf{r}|^{p+2}} \tag{C.77}$$

$$\frac{\partial^2 E_{Z^iq^j}}{\partial r_\alpha \partial r_\beta} = p(p+2)\frac{Z^iq^j(R_\alpha+r_\alpha)(R_\beta+r_\beta)}{|\mathbf{R}+\mathbf{r}|^{p+4}} - p\frac{Z^iq^j\delta_{\alpha\beta}}{|\mathbf{R}+\mathbf{r}|^{p+2}} \tag{C.78}$$

$$\begin{aligned}\frac{\partial^3 E_{Z^iq^j}}{\partial r_\alpha \partial r_\beta \partial r_\gamma} &= p(p+2)\frac{Z^iq^j\left[(R_\alpha+r_\alpha)\delta_{\beta\gamma}+(R_\beta+r_\beta)\delta_{\gamma\alpha}+(R_\gamma+r_\gamma)\delta_{\beta\gamma}\right]}{|\mathbf{R}+\mathbf{r}|^{p+4}} \\ &\quad - p(p+2)(p+4)\frac{Z^iq^j(R_\alpha+r_\alpha)(R_\beta+r_\beta)(R_\gamma+r_\gamma)}{|\mathbf{R}+\mathbf{r}|^{p+6}}\end{aligned} \tag{C.79}$$

Sum over q^j, we have the energy between Z^i and cell j as

$$\begin{aligned}E_{Z^i,j} &= \frac{Z^iZ^j}{R^p} - p\frac{Z^iF^j_\alpha R_\alpha}{R^{p+2}} + \frac{p(p+2)}{2}\frac{Z^iS^j_{\alpha\beta}R_\alpha R_\beta}{R^{p+4}} - \frac{p}{2}\frac{Z^iTrace(S^j)}{R^{p+2}} \\ &\quad - \frac{p(p+2)(p+4)}{6}\frac{Z^iT^j_{\alpha\beta\gamma}R_\alpha R_\beta R_\gamma}{R^{p+6}} + \frac{p(p+2)}{2}\frac{Z^iT^j_{\lambda\lambda\alpha}R_\alpha}{R^{p+4}} + \ldots\end{aligned} \tag{C.80}$$

Energy of F^i with Cell j

The energy between F^i and q^j

$$E_{F^iq^j} = p\frac{q^jF^i_\mu(R_\mu+r_\mu)}{|\mathbf{R}+\mathbf{r}|^{p+2}} \tag{C.81}$$

$$\frac{\partial E_{F^iq^j}}{\partial r_\alpha} = p\frac{F^i_\alpha q^j}{|\mathbf{R}+\mathbf{r}|^{p+2}} - p(p+2)\frac{q^jF^i_\mu(R_\mu+r_\mu)(R_\alpha+r_\alpha)}{|\mathbf{R}+\mathbf{r}|^{p+4}} \tag{C.82}$$

$$\begin{aligned}\frac{\partial^2 E_{F^iq^j}}{\partial r_\alpha \partial r_\beta} &= -p(p+2)\frac{q^j\left[F^i_\alpha(R_\beta+r_\beta)+F^i_\beta(R_\alpha+r_\alpha)\right]}{|\mathbf{R}+\mathbf{r}|^{p+4}} \\ &\quad + p(p+2)(p+4)\frac{q^jF^i_\mu(R_\mu+r_\mu)(R_\alpha+r_\alpha)(R_\beta+r_\beta)}{|\mathbf{R}+\mathbf{r}|^{p+6}} \\ &\quad - p(p+2)\frac{q^jF^i_\mu(R_\mu+r_\mu)\delta_{\alpha\beta}}{|\mathbf{R}+\mathbf{r}|^{p+4}}\end{aligned} \tag{C.83}$$

$$\frac{\partial^3 E_{F^i q^j}}{\partial r_\alpha \partial r_\beta \partial r_\gamma} = -p(p+2)\frac{q^j(F^i_\alpha \delta_{\beta\gamma} + F^i_\beta \delta_{\gamma\alpha} + F^i_\gamma \delta_{\alpha\beta})}{|\mathbf{R}+\mathbf{r}|^{p+4}}$$
$$+ p(p+2)(p+4)\Big\{\frac{q^j F^i_\mu (R_\mu + r_\mu)\big[(R_\alpha + r_\alpha)\delta_{\beta\gamma} + (R_\beta + r_\beta)\delta_{\gamma\alpha} + (R_\gamma + r_\gamma)\delta_{\alpha\beta}\big]}{|\mathbf{R}+\mathbf{r}|^{p+6}}$$
$$+ \frac{q^j\big[F^i_\alpha (R_\beta + r_\beta)(R_\gamma + r_\gamma) + F^i_\beta (R_\gamma + r_\gamma)(R_\alpha + r_\alpha) + F^i_\gamma (R_\alpha + r_\alpha)(R_\beta + r_\beta)\big]}{|\mathbf{R}+\mathbf{r}|^{p+6}}\Big\}$$
$$- p(p+2)(p+4)(p+6)\frac{q^j F^i_\mu (R_\mu + r_\mu)(R_\alpha + r_\alpha)(R_\beta + r_\beta)(R_\gamma + r_\gamma)}{|\mathbf{R}+\mathbf{r}|^{p+8}} \qquad \text{(C.84)}$$

Sum over q^j, we have the energy between F^i and cell j as

$$\begin{aligned} E_{F^i,j} &= p\frac{Z^j F^i_\alpha R_\alpha}{R^{p+2}} + p\frac{F^i_\alpha F^j_\alpha}{R^{p+2}} - p(p+2)\frac{F^i_\alpha R_\alpha F^j_\beta R_\beta}{R^{p+4}} \\ &\quad -p(p+2)\frac{F^i_\alpha S^j_{\alpha\beta} R_\beta}{R^{p+4}} + \frac{p(p+2)(p+4)}{2}\frac{F^i_\gamma R_\gamma S^j_{\alpha\beta} R_\alpha R_\beta}{R^{p+6}} \\ &\quad -\frac{p(p+2)}{2}\frac{F^i_\alpha R_\alpha Trace(S^j)}{R^{p+4}} \\ &\quad -\frac{p(p+2)}{2}\frac{F^i_\alpha T^j_{\alpha\beta\beta}}{R^{p+4}} + \frac{p(p+2)(p+4)}{2}\frac{F^i_\alpha R_\alpha T^j_{\beta\beta\gamma} R_\gamma}{R^{p+6}} \\ &\quad +\frac{p(p+2)(p+4)}{2}\frac{F^i_\alpha T^j_{\alpha\beta\gamma} R_\beta R_\gamma}{R^{p+6}} \\ &\quad -\frac{p(p+2)(p+4)(p+6)}{6}\frac{F^i_\lambda R_\lambda T^j_{\alpha\beta\gamma} R_\alpha R_\beta R_\gamma}{R^{p+8}} + \ldots \end{aligned} \qquad \text{(C.85)}$$

Energy of S^i with Cell j

The energy between $\mathbf{S}^i$ and q^j

$$E_{S^i q^j} = \frac{p(p+2)}{2}\frac{q^j S^i_{\mu\nu}(R_\mu + r_\mu)(R_\nu + r_\nu)}{|\mathbf{R}+\mathbf{r}|^{p+4}} - \frac{p}{2}\frac{q^j Trace(S^i)}{|\mathbf{R}+\mathbf{r}|^{p+2}} \qquad \text{(C.86)}$$

$$\frac{\partial E_{S^i q^j}}{\partial r_\alpha} = \frac{p(p+2)}{2}\frac{2q^j S^i_{\alpha\mu}(R_\mu + r_\mu)}{|\mathbf{R}+\mathbf{r}|^{p+4}} - \frac{p(p+2)(p+4)}{2}\frac{q^j S^i_{\mu\nu}(R_\mu + r_\mu)(R_\nu + r_\nu)(R_\alpha + r_\alpha)}{|\mathbf{R}+\mathbf{r}|^{p+6}}$$
$$+\frac{p(p+2)}{2}\frac{q^j Trace(S^i)(R_\alpha + r_\alpha)}{|\mathbf{R}+\mathbf{r}|^{p+4}} \qquad \text{(C.87)}$$

$$\begin{aligned}
\frac{\partial^2 E_{S^i q^j}}{\partial r_\alpha \partial r_\beta} &= p(p+2)\frac{q^j S^i_{\alpha\beta}}{\left|\mathbf{R}+\mathbf{r}\right|^{p+4}} \\
&-p(p+2)(p+4)\frac{q^j(R_\mu+r_\mu)\left[S^i_{\mu\alpha}(R_\beta+r_\beta)+S^i_{\mu\beta}(R_\alpha+r_\alpha)\right]}{\left|\mathbf{R}+\mathbf{r}\right|^{p+6}} \\
&+\frac{p(p+2)(p+4)(p+6)}{2}\frac{q^j S^i_{\mu\nu}(R_\mu+r_\mu)(R_\nu+r_\nu)(R_\alpha+r_\alpha)(R_\beta+r_\beta)}{\left|\mathbf{R}+\mathbf{r}\right|^{p+8}} \\
&-\frac{p(p+2)(p+4)}{2}\frac{q^j S^i_{\mu\nu}(R_\mu+r_\mu)(R_\nu+r_\nu)\delta_{\alpha\beta}}{\left|\mathbf{R}+\mathbf{r}\right|^{p+6}} \\
&-\frac{p(p+2)(p+4)}{2}\frac{q^j Trace(S^i)(R_\alpha+r_\alpha)(R_\beta+r_\beta)}{\left|\mathbf{R}+\mathbf{r}\right|^{p+6}} \\
&+\frac{p(p+2)}{2}\frac{q^j Trace(S^i)\delta_{\alpha\beta}}{\left|\mathbf{R}+\mathbf{r}\right|^{p+4}}
\end{aligned} \tag{C.88}$$

$$\begin{aligned}
\frac{\partial^3 E_{S^i q^j}}{\partial r_\alpha \partial r_\beta \partial r_\gamma} &= p(p+2)(p+4)q^j\Big\{-\frac{S^i_{\alpha\beta}(R_\gamma+r_\gamma)+S^i_{\beta\gamma}(R_\alpha+r_\alpha)+S^i_{\gamma\alpha}(R_\beta+r_\beta)}{\left|\mathbf{R}+\mathbf{r}\right|^{p+6}} \\
&-\frac{(R_\mu+r_\mu)(S^i_{\mu\alpha}\delta_{\beta\gamma}+S^i_{\mu\beta}\delta_{\gamma\alpha}+S^i_{\mu\gamma}\delta_{\alpha\beta})}{\left|\mathbf{R}+\mathbf{r}\right|^{p+6}} \\
&+(p+6)(R_\mu+r_\mu)\Big[\frac{R_\nu+r_\nu}{2}\frac{S^i_{\mu\nu}\left[\delta_{\alpha\beta}(R_\gamma+r_\gamma)+\delta_{\beta\gamma}(R_\alpha+r_\alpha)+\delta_{\gamma\alpha}(R_\beta+r_\beta)\right]}{\left|\mathbf{R}+\mathbf{r}\right|^{p+8}} \\
&+\frac{\left[S^i_{\mu\alpha}(R_\beta+r_\beta)(R_\gamma+r_\gamma)+S^i_{\mu\beta}(R_\gamma+r_\gamma)(R_\alpha+r_\alpha)+S^i_{\mu\gamma}(R_\alpha+r_\alpha)(R_\beta+r_\beta)\right]}{\left|\mathbf{R}+\mathbf{r}\right|^{p+8}}\Big] \\
&-\frac{(p+6)(p+8)}{2}\frac{S^i_{\mu\nu}(R_\mu+r_\mu)(R_\nu+r_\nu)(R_\alpha+r_\alpha)(R_\beta+r_\beta)(R_\gamma+r_\gamma)}{\left|\mathbf{R}+\mathbf{r}\right|^{p+10}}\Big\} \\
&-\frac{p(p+2)(p+4)}{2}\frac{q^j Trace(S^i)\left[\delta_{\alpha\beta}(R_\gamma+r_\gamma)+\delta_{\beta\gamma}(R_\alpha+r_\alpha)+\delta_{\gamma\alpha}(R_\beta+r_\beta)\right]}{\left|\mathbf{R}+\mathbf{r}\right|^{p+6}} \\
&+\frac{p(p+2)(p+4)(p+6)}{2}\frac{q^j Trace(S^i)(R_\alpha+r_\alpha)(R_\beta+r_\beta)(R_\gamma+r_\gamma)}{\left|\mathbf{R}+\mathbf{r}\right|^{p+8}}
\end{aligned} \tag{C.89}$$

Sum over q^j, we have the energy between $\mathbf{S}^i$ and cell j as

$$\begin{aligned}
E_{S^i,j} &= \frac{p(p+2)}{2}\frac{S^i_{\alpha\beta}R_\alpha R_\beta Z^j}{R^{p+4}}-\frac{p}{2}\frac{Trace(S^i)Z^j}{R^{p+2}}+p(p+2)\frac{R_\alpha S^i_{\alpha\beta}F^j_\beta}{R^{p+4}} \\
&-\frac{p(p+2)(p+4)}{2}\frac{S^i_{\alpha\beta}R_\alpha R_\beta F^j_\gamma R_\gamma}{R^{p+6}}+\frac{p(p+2)}{2}\frac{Trace(S^i)F^j_\alpha R_\alpha}{R^{p+4}}
\end{aligned}$$

$$
\begin{aligned}
&+\frac{p(p+2)}{2}\frac{S^i_{\alpha\beta}S^j_{\alpha\beta}}{R^{p+4}} - p(p+2)(p+4)\frac{R_\alpha S^i_{\alpha\beta}S^j_{\beta\gamma}R_\gamma}{R^{p+6}} \\
&+\frac{p(p+2)(p+4)}{4}\left[(p+6)\frac{S^i_{\alpha\beta}R_\alpha R_\beta S^j_{\mu\nu}R_\mu R_\nu}{R^{p+8}} - \frac{S^i_{\alpha\beta}R_\alpha R_\beta Trace(S^j)}{R^{p+6}}\right] \\
&-\frac{p(p+2)(p+4)}{4}\frac{Trace(S^i)S^j_{\alpha\beta}R_\alpha R_\beta}{R^{p+6}} + \frac{p(p+2)}{4}\frac{Trace(S^i)Trace(S^j)}{R^{p+4}} \\
&-\frac{p(p+2)(p+4)}{2}\left[\frac{S^i_{\alpha\beta}T^j_{\alpha\beta\gamma}R_\gamma}{R^{p+6}} + \frac{R_\alpha S^i_{\alpha\beta}T^j_{\beta\gamma\gamma}}{R^{p+6}}\right] \\
&+\frac{p(p+2)(p+4)(p+6)}{2}\left[\frac{S^i_{\alpha\beta}R_\alpha R_\beta T^j_{\lambda\lambda\gamma}R_\gamma}{2R^{p+8}} + \frac{R_\mu S^i_{\mu\alpha}T^j_{\alpha\beta\gamma}R_\beta R_\gamma}{R^{p+8}}\right] \\
&-\frac{p(p+2)(p+4)(p+6)(p+8)}{12}\frac{S^i_{\mu\nu}R_\mu R_\nu T^j_{\alpha\beta\gamma}R_\alpha R_\beta R_\gamma}{R^{p+10}} \\
&-\frac{p(p+2)(p+4)}{4}\frac{Trace(S^i)T^j_{\alpha\alpha\beta}R_\beta}{R^{p+6}} \\
&+\frac{p(p+2)(p+4)(p+6)}{12}\frac{Trace(S^i)T^j_{\alpha\beta\gamma}R_\alpha R_\beta R_\gamma}{R^{p+8}} + \ldots
\end{aligned}
\tag{C.90}
$$

Energy of T^i with Cell j

The energy between T^i and q^j

$$
E_{T^iq^j} = \frac{p(p+2)(p+4)}{6}E_{1,T^iq^j} - \frac{p(p+2)}{2}E_{2,T^iq^j} \tag{C.91}
$$

where

$$
E_{1,T^iq^j} = \frac{q^jT^i_{\mu\nu\lambda}(R_\mu+r_\mu)(R_\nu+r_\nu)(R_\lambda+r_\lambda)}{\left|\mathbf{R}+\mathbf{r}\right|^{p+6}} \tag{C.92}
$$

$$
\begin{aligned}
\frac{\partial E_{1,T^iq^j}}{\partial r_\alpha} &= 3\frac{q^jT^i_{\mu\nu\alpha}(R_\mu+r_\mu)(R_\nu+r_\nu)}{\left|\mathbf{R}+\mathbf{r}\right|^{p+6}} \\
&\quad -(p+6)\frac{q^jT^i_{\mu\nu\lambda}(R_\mu+r_\mu)(R_\nu+r_\nu)(R_\lambda+r_\lambda)(R_\alpha+r_\alpha)}{\left|\mathbf{R}+\mathbf{r}\right|^{p+8}}
\end{aligned}
\tag{C.93}
$$

$$
\begin{aligned}
\frac{\partial^2 E_{1,T^iq^j}}{\partial r_\alpha \partial r_\beta} &= 6\frac{q^jT^i_{\mu\alpha\beta}(R_\mu+r_\mu)}{\left|\mathbf{R}+\mathbf{r}\right|^{p+6}} \\
&\quad -3(p+6)\frac{q^j(R_\mu+r_\mu)(R_\nu+r_\nu)\left[T^i_{\mu\nu\alpha}(R_\beta+r_\beta)+T^i_{\mu\nu\beta}(R_\alpha+r_\alpha)\right]}{\left|\mathbf{R}+\mathbf{r}\right|^{p+8}}
\end{aligned}
$$

$$+(p+6)(p+8)\frac{q^j T^i_{\mu\nu\lambda}(R_\mu+r_\mu)(R_\nu+r_\nu)(R_\lambda+r_\lambda)(R_\alpha+r_\alpha)(R_\beta+r_\beta)}{\left|\mathbf{R}+\mathbf{r}\right|^{p+10}}$$

$$-(p+6)\frac{q^j T^i_{\mu\nu\lambda}(R_\mu+r_\mu)(R_\nu+r_\nu)(R_\lambda+r_\lambda)\delta_{\alpha\beta}}{\left|\mathbf{R}+\mathbf{r}\right|^{p+8}} \tag{C.94}$$

$$\frac{\partial^3 E_{1,T^iq^j}}{\partial r_\alpha \partial r_\beta \partial r_\gamma} = 6\frac{q^j T^i_{\alpha\beta\gamma}}{\left|\mathbf{R}+\mathbf{r}\right|^{p+6}}$$

$$-6(p+6)\frac{q^j(R_\mu+r_\mu)\left[T^i_{\mu\alpha\beta}(R_\gamma+r_\gamma)+T^i_{\mu\beta\gamma}(R_\alpha+r_\alpha)+T^i_{\mu\gamma\alpha}(R_\beta+r_\beta)\right]}{\left|\mathbf{R}+\mathbf{r}\right|^{p+8}}$$

$$+(p+6)q^j(R_\mu+r_\mu)(R_\nu+r_\nu)\Bigg\{-3\frac{(T^j_{\mu\nu\alpha}\delta_{\beta\gamma}+T^j_{\mu\nu\beta}\delta_{\gamma\alpha}+T^j_{\mu\nu\gamma}\delta_{\alpha\beta})}{\left|\mathbf{R}+\mathbf{r}\right|^{p+8}}$$

$$+(p+8)\Bigg[\frac{T^i_{\mu\nu\lambda}(R_\lambda+r_\lambda)\left[\delta_{\alpha\beta}(R_\gamma+r_\gamma)+\delta_{\beta\gamma}(R_\beta+r_\beta)+\delta_{\gamma\beta}(R_\beta+r_\beta)\right]}{\left|\mathbf{R}+\mathbf{r}\right|^{p+10}}$$

$$+3\frac{\left[T^i_{\mu\nu\alpha}(R_\beta+r_\beta)(R_\gamma+r_\gamma)+T^i_{\mu\nu\beta}(R_\gamma+r_\gamma)(R_\alpha+r_\alpha)+T^i_{\mu\nu\gamma}(R_\alpha+r_\alpha)(R_\beta+r_\beta)\right]}{\left|\mathbf{R}+\mathbf{r}\right|^{p+10}}\Bigg]$$

$$-(p+8)(p+10)\frac{(R_\lambda+r_\lambda)T^i_{\mu\nu\lambda}(R_\alpha+r_\alpha)(R_\beta+r_\beta)(R_\gamma+r_\gamma)}{\left|\mathbf{R}+\mathbf{r}\right|^{p+12}}\Bigg\} \tag{C.95}$$

and

$$E_{2,T^iq^j} = \frac{q^j T^i_{\lambda\lambda\mu}(R_\mu+r_\mu)}{\left|\mathbf{R}+\mathbf{r}\right|^{p+4}} \tag{C.96}$$

$$\frac{\partial E_{2,T^iq^j}}{\partial r_\alpha} = \frac{q^j T^i_{\lambda\lambda\alpha}}{\left|\mathbf{R}+\mathbf{r}\right|^{p+4}} - (p+4)\frac{q^j T^i_{\lambda\lambda\mu}(R_\mu+r_\mu)(R_\alpha+r_\alpha)}{\left|\mathbf{R}+\mathbf{r}\right|^{p+6}} \tag{C.97}$$

$$\frac{\partial^2 E_{2,T^iq^j}}{\partial r_\alpha \partial r_\beta} = -(p+4)\frac{q^j\left[T^i_{\lambda\lambda\alpha}(R_\beta+r_\beta)+T^i_{\lambda\lambda\beta}(R_\alpha+r_\alpha)\right]}{\left|\mathbf{R}+\mathbf{r}\right|^{p+6}} - (p+4)\frac{T^i_{\lambda\lambda\mu}(R_\mu+r_\mu)\delta_{\alpha\beta}}{\left|\mathbf{R}+\mathbf{r}\right|^{p+6}}$$

$$+(p+4)(p+6)\frac{q^j T^i_{\lambda\lambda\mu}(R_\mu+r_\mu)(R_\alpha+r_\alpha)(R_\beta+r_\beta)}{\left|\mathbf{R}+\mathbf{r}\right|^{p+8}} \tag{C.98}$$

$$\frac{\partial^3 E_{2,T^iq^j}}{\partial r_\alpha \partial r_\beta \partial r_\gamma} = -(p+4)\frac{q^j(T^i_{\lambda\lambda\alpha}\delta_{\beta\gamma}+T^i_{\lambda\lambda\beta}\delta_{\gamma\alpha}+T^i_{\lambda\lambda\gamma}\delta_{\alpha\beta})}{\left|\mathbf{R}+\mathbf{r}\right|^{p+6}}$$

$$+(p+4)(p+6)\frac{q^i\left[T^i_{\lambda\lambda\alpha}(R_\beta+r_\beta)(R_\gamma+r_\gamma)+T^i_{\lambda\lambda\beta}(R_\gamma+r_\gamma)(R_\alpha+r_\alpha)+T^i_{\lambda\lambda\gamma}(R_\alpha+r_\alpha)(R_\beta+r_\beta)\right]}{\left|\mathbf{R}+\mathbf{r}\right|^{p+8}}$$

$$+(p+4)(p+6)\frac{q^i T^i_{\lambda\lambda\mu}(R_\mu+r_\mu)\left[(R_\alpha+r_\alpha)\delta_{\beta\gamma}+(R_\beta+r_\beta)\delta_{\gamma\alpha}+(R_\gamma+r_\gamma)\delta_{\alpha\beta}\right]}{\left|\mathbf{R}+\mathbf{r}\right|^{p+8}}$$

$$- (p+4)(p+6)(p+8)\frac{q^i T^i_{\lambda\lambda\mu}(R_\mu + r_\mu)(R_\alpha + r_\alpha)(R_\beta + r_\beta)(R_\gamma + r_\gamma)}{|\mathbf{R}+\mathbf{r}|^{p+10}} \tag{C.99}$$

Sum over q^j, we have the energy between T^i and cell j as

$$\begin{aligned}
E_{T^i,j} = {} & \frac{p(p+2)(p+4)}{6}\Bigg\{\frac{T^i_{\alpha\beta\gamma}R_\alpha R_\beta R_\gamma Z^j}{R^{p+6}} + 3\frac{T^i_{\alpha\beta\gamma}R_\alpha R_\beta F^j_\gamma}{R^{p+6}} - (p+6)\frac{T^i_{\alpha\beta\gamma}R_\alpha R_\beta R_\gamma F^j_\mu R_\mu}{R^{p+8}} \\
& + 3\frac{R_\alpha T^i_{\alpha\beta\gamma}S^j_{\beta\gamma}}{R^{p+8}} - 3(p+6)\frac{R_\mu R_\nu T^i_{\mu\nu\alpha}R_\beta S^j_{\alpha\beta}}{R^{p+8}} + \frac{(p+6)(p+8)}{2}\frac{T^i_{\mu\nu\lambda}R_\mu R_\nu R_\lambda S^j_{\alpha\beta}R_\alpha R_\beta}{R^{p+10}} \\
& - \frac{p+2}{2}\frac{T^i_{\mu\nu\lambda}R_\mu R_\nu R_\lambda Trace(S^j)}{R^{p+8}} \\
& + \frac{T^i_{\alpha\beta\gamma}T^j_{\alpha\beta\gamma}}{R^{p+6}} - 3(p+6)\frac{R_\mu T^i_{\mu\alpha\beta}R_\gamma T^j_{\alpha\beta\gamma}}{R^{p+8}} - \frac{3(p+6)}{2}\frac{R_\alpha R_\beta T^i_{\alpha\beta\gamma}T^j_{\gamma\lambda\lambda}}{R^{p+8}} \\
& + \frac{3(p+6)(p+8)}{2}\Big[\frac{R_\alpha R_\beta T^i_{\alpha\beta\gamma}R_\gamma T^j_{\lambda\lambda\mu}R_\mu}{R^{p+10}} + \frac{R_\alpha R_\beta T^i_{\alpha\beta\gamma}T^j_{\gamma\mu\nu}R_\mu R_\nu}{R^{p+10}}\Big] \\
& - \frac{(p+6)(p+8)(p+10)}{6}\frac{T^i_{\alpha\beta\gamma}R_\alpha R_\beta R_\gamma T^j_{\mu\nu\lambda}R_\mu R_\nu R_\lambda}{R^{p+12}}\Bigg\} \\
& - \frac{p(p+2)}{2}\Bigg\{\frac{T^i_{\alpha\alpha\beta}R_\beta Z^j}{R^{p+4}} + \frac{T^i_{\alpha\alpha\beta}F^j_\beta}{R^{p+4}} - (p+4)\frac{T^i_{\alpha\alpha\beta}R_\beta F^j_\gamma R_\gamma}{R^{p+6}} \\
& - (p+4)\frac{T^i_{\alpha\alpha\beta}S^j_{\beta\gamma}R_\gamma}{R^{p+6}} - \frac{p+4}{2}\frac{T^i_{\alpha\alpha\beta}R_\beta Trace(S^j)}{R^{p+6}} + \frac{(p+4)(p+6)}{2}\frac{T^i_{\alpha\alpha\beta}R_\beta S^j_{\mu\nu}R_\mu R_\nu}{R^{p+8}} \\
& - \frac{p+4}{2}\frac{T^i_{\alpha\alpha\beta}T^j_{\beta\gamma\gamma}}{R^{p+6}} + \frac{(p+4)(p+6)}{2}\Big[\frac{T^i_{\mu\mu\alpha}T^j_{\alpha\beta\gamma}R_\beta R_\gamma}{R^{p+8}} + \frac{T^i_{\mu\mu\nu}R_\nu T^j_{\alpha\alpha\beta}R_\beta}{R^{p+8}}\Big] \\
& - \frac{(p+4)(p+6)(p+8)}{6}\frac{T^i_{\mu\mu\nu}R_\mu T^j_{\alpha\beta\gamma}R_\alpha R_\beta R_\gamma}{R^{p+10}}\Bigg\}
\end{aligned} \tag{C.100}$$

C.6.2 Approximations at Different Level

We consider three levels of approximation. They are the first (F), second (S) and third (T). Before we compute stress, let's first look at the quantities upon which the derivatives with respect to strain tensor $\epsilon_{\alpha\beta}$ have to be calculated.

Derivatives with Respect to Strain Tensor

The strain tensor is defined by

$$\epsilon_{\kappa\lambda} = \frac{1}{2}(\tilde{H}^{-1}_{0\kappa\mu} G_{\mu\nu} H^{-1}_{0\nu\lambda} - 1) \tag{C.101}$$

where $H = [\mathbf{a}, \mathbf{b}, \mathbf{c}]$, and $\mathbf{a}, \mathbf{b}, \mathbf{c}$ are the unit cell vectors, and $G_{\mu\nu} = \tilde{H}_{\mu\gamma} H_{\gamma\mu}$

$$G_{\mu\nu} = 2\tilde{H}_{0\mu\kappa}\epsilon_{\kappa\lambda} H_{0\lambda\nu} + \tilde{H}_{0\mu\gamma} H_{0\gamma\nu} \tag{C.102}$$

$$\begin{aligned}\frac{\partial G_{\mu\nu}}{\partial \epsilon_{\alpha\beta}} =& 2\tilde{H}_{0\mu\kappa}\frac{\partial \epsilon_{\kappa\lambda}}{\partial \epsilon_{\alpha\beta}} H_{0\lambda\nu} \\ =& \tilde{H}_{0\mu\kappa}(\delta_{\kappa\alpha}\delta_{\lambda\beta} + \delta_{\kappa\beta}\delta_{\lambda\alpha}) H_{0\lambda\nu} \\ =& \tilde{H}_{0\mu\alpha} H_{0\beta\nu} + \tilde{H}_{0\mu\beta} H_{0\alpha\nu}\end{aligned} \tag{C.103}$$

Following are the terms used in stress calculation

$$\begin{aligned}\frac{\partial(\mathbf{R}\cdot\mathbf{R})}{\partial \epsilon_{\alpha\beta}} =& \frac{\partial(\rho_\mu G_{\mu\nu}\rho_\nu)}{\partial \epsilon_{\alpha\beta}} \\ =& \rho_\mu(\tilde{H}_{0\mu\alpha} H_{0\beta\nu} + \tilde{H}_{0\mu\beta} H_{0\alpha\nu})\rho_\nu \\ =& 2R_\alpha R_\beta\end{aligned} \tag{C.104}$$

$$\frac{\partial(\mathbf{F}\cdot\mathbf{R})}{\partial \epsilon_{\alpha\beta}} = R_\alpha F_\beta + R_\beta F_\alpha \tag{C.105}$$

$$\frac{\partial(\mathbf{F}^i\cdot\mathbf{F}^j)}{\partial \epsilon_{\alpha\beta}} = F^i_\alpha F^j_\beta + F^i_\beta F^j_\alpha \tag{C.106}$$

$$\frac{\partial(\mathbf{R}\cdot S\cdot\mathbf{R})}{\partial \epsilon_{\alpha\beta}} = 2(R_\alpha S_{\beta\gamma} + R_\beta S_{\alpha\gamma})R_\gamma \tag{C.107}$$

$$\frac{\partial(\mathbf{F}^i\cdot S^j\cdot\mathbf{R})}{\partial \epsilon_{\alpha\beta}} = F^i_\gamma(S^j_{\gamma\alpha}R_\beta + S^j_{\gamma\beta}R_\alpha) + (F^i_\alpha S^j_{\beta\gamma} + F^i_\beta S^j_{\alpha\gamma})R_\gamma \tag{C.108}$$

$$\frac{\partial S^i_{\mu\nu} S^j_{\mu\nu}}{\partial \epsilon_{\alpha\beta}} = 2(S^i_{\alpha\gamma} S^j_{\gamma\beta} + S^i_{\beta\gamma} S^j_{\gamma\alpha}) \tag{C.109}$$

$$\begin{aligned}\frac{\partial(R_\mu S^i_{\mu\gamma} S^j_{\gamma\nu} R_\nu)}{\partial \epsilon_{\alpha\beta}} =& (R_\alpha S^i_{\beta\gamma} + R_\beta S^i_{\alpha\gamma}) S^j_{\gamma\nu} R_\nu + R_\mu S^i_{\mu\gamma}(S^j_{\gamma\alpha}R_\beta + S^j_{\gamma\beta}R_\alpha) \\ &+ R_\mu(S^i_{\mu\alpha} S^j_{\beta\nu} + S^i_{\mu\beta} S^j_{\alpha\nu})R_\nu\end{aligned} \tag{C.110}$$

$$\begin{aligned}\frac{\partial Trace(S)}{\partial\epsilon_{\alpha\beta}} &= \frac{\partial}{\partial\epsilon_{\alpha\beta}}(\sum_i q^i r^2) = \frac{\partial}{\partial\epsilon_{\alpha\beta}}(\sum_i q^i \rho^i_\mu G_{\mu\nu}\rho^i_\nu) \\ &= \sum_i q^i \rho^i_\mu (\tilde{H}_{0\mu\alpha}H_{0\beta\nu} + \tilde{H}_{0\mu\beta}H_{0\alpha\nu})\rho^i_\nu \\ &= 2\,S_{\alpha\beta} \end{aligned} \tag{C.111}$$

Similarly we have the following for T related terms

$$\frac{\partial(T_{\mu\nu\kappa}R_\mu R_\nu R_\kappa)}{\partial\epsilon_{\alpha\beta}} = 3(R_\alpha T_{\beta\mu\nu} + R_\beta T_{\alpha\mu\nu})R_\mu R_\nu \tag{C.112}$$

$$\frac{\partial(T_{\lambda\lambda\gamma}R_\gamma)}{\partial\epsilon_{\alpha\beta}} = 2T_{\alpha\beta\gamma}R_\gamma + T_{\lambda\lambda\alpha}R_\beta + T_{\lambda\lambda\beta}R_\alpha \tag{C.113}$$

$$\frac{\partial(T^i_{\lambda\lambda\gamma}F^j_\gamma)}{\partial\epsilon_{\alpha\beta}} = 2T^i_{\alpha\beta\gamma}F^j_\gamma + T^i_{\lambda\lambda\alpha}F^j_\beta + T^i_{\lambda\lambda\beta}F^j_\alpha \tag{C.114}$$

$$\frac{\partial(F^i_\lambda T^j_{\lambda\mu\nu}R_\mu R_\nu)}{\partial\epsilon_{\alpha\beta}} = (F^i_\alpha T^j_{\beta\mu\nu} + F^i_\beta T^j_{\alpha\mu\nu})R_\mu R_\nu + 2F^i_\lambda(T^j_{\lambda\alpha\gamma}R_\beta + T^j_{\lambda\beta\gamma}R_\alpha)R_\gamma \tag{C.115}$$

$$\frac{\partial(S^i_{\mu\nu}T^j_{\mu\nu\lambda}R_\lambda)}{\partial\epsilon_{\alpha\beta}} = 2\,(S^i_{\alpha\gamma}T^j_{\gamma\beta\lambda} + S^i_{\beta\gamma}T^j_{\gamma\alpha\lambda})R_\lambda + S^i_{\mu\nu}(T^j_{\mu\nu\alpha}R_\beta + T^j_{\mu\nu\beta}R_\alpha) \tag{C.116}$$

$$\frac{\partial(T^i_{\mu\nu\lambda}T^j_{\mu\nu\lambda})}{\partial\epsilon_{\alpha\beta}} = 3\,(T^i_{\alpha\mu\nu}T^j_{\mu\nu\beta} + T^i_{\beta\mu\nu}T^j_{\mu\nu\alpha}) \tag{C.117}$$

$$\begin{aligned}\frac{\partial(R_\mu T^i_{\mu\kappa\lambda}T^j_{\kappa\lambda\nu}R_\nu)}{\partial\epsilon_{\alpha\beta}} &= (R_\alpha T^i_{\beta\kappa\lambda} + R_\beta T^i_{\alpha\kappa\lambda})T^j_{\kappa\lambda\nu}R_\nu + R_\mu T^i_{\mu\kappa\lambda}(T^j_{\kappa\lambda\alpha}R_\beta + T^j_{\kappa\lambda\beta}R_\alpha) \\ &\quad + R_\mu T^i_{\mu\alpha\lambda}T^j_{\lambda\beta\nu}R_\nu + R_\mu T^i_{\mu\beta\lambda}T^j_{\lambda\alpha\nu}R_\nu \end{aligned} \tag{C.118}$$

$$\begin{aligned}\frac{\partial(R_\mu R_\nu T^i_{\mu\nu\gamma}T^j_{\lambda\lambda\gamma})}{\partial\epsilon_{\alpha\beta}} &= 2R_\mu R_\nu T^i_{\mu\nu\gamma}T^j_{\alpha\beta\gamma} + 2R_\mu(R_\alpha T^i_{\beta\mu\gamma} + R_\beta T^i_{\alpha\mu\gamma})T^j_{\lambda\lambda\gamma} \\ &\quad + R_\mu R_\nu(T^i_{\mu\nu\alpha}T^j_{\lambda\lambda\beta} + T^i_{\mu\nu\beta}T^j_{\lambda\lambda\alpha}) \end{aligned} \tag{C.119}$$

$$\begin{aligned}\frac{\partial(R_\mu R_\nu T^i_{\mu\nu\gamma}T^j_{\gamma\kappa\lambda}R_\kappa R_\lambda)}{\partial\epsilon_{\alpha\beta}} &= 2R_\mu(R_\alpha T^i_{\mu\beta\gamma} + R_\beta T^i_{\mu\alpha\gamma})T^j_{\gamma\kappa\lambda}R_\kappa R_\lambda \\ &\quad + R_\mu R_\nu T^i_{\mu\nu\gamma}(T^j_{\gamma\alpha\lambda}R_\beta + T^j_{\gamma\beta\lambda}R_\alpha)R_\lambda \\ &\quad + R_\mu R_\nu(T^i_{\mu\nu\alpha}T^j_{\beta\kappa\lambda} + T^i_{\mu\nu\beta}T^j_{\alpha\kappa\lambda})R_\kappa R_\lambda \end{aligned} \tag{C.120}$$

Up to F^i and F^j

Collecting the energy terms up to F^i and F^j, we have

$$E_{F^i,F^j} = \frac{Z^i Z^j}{R^p} - p\,\frac{Z^i(\mathbf{F}^j\cdot\mathbf{R}) - Z^j(\mathbf{F}^i\cdot\mathbf{R})}{R^{p+2}} + p\,\frac{\mathbf{F}^i\cdot\mathbf{F}^j}{R^{p+2}} - p(p+2)\,\frac{(\mathbf{F}^i\cdot\mathbf{R})(\mathbf{F}^j\cdot\mathbf{R})}{R^{p+4}} \tag{C.121}$$

Stress contribution

$$\begin{aligned}
\Omega\Pi_{\alpha\beta} &= -\frac{\partial E_{F^i,F^j}}{\partial \epsilon_{\alpha\beta}} \\
&= p\,\frac{Z^i\,Z^j}{R^{p+2}}\,R_\alpha R_\beta - p(p+2)\,\frac{Z^i(\mathbf{F}^j\cdot\mathbf{R}) - Z^j(\mathbf{F}^i\cdot\mathbf{R})}{R^{p+4}}\,R_\alpha R_\beta \\
&+ p\,\frac{Z^i(R_\alpha F^j_\beta + R_\beta F^j_\alpha) - Z^j(R_\alpha F^i_\beta + R_\beta F^i_\alpha)}{R^{p+2}} \\
&- p\,\frac{F^i_\alpha F^j_\beta + F^j_\alpha F^i_\beta}{R^{p+2}} + p(p+2)\,\frac{\mathbf{F}^i\cdot\mathbf{F}^j}{R^{p+4}}\,R_\alpha R_\beta \\
&+ p(p+2)\,\frac{(F^i_\alpha R_\beta + F^i_\beta R_\alpha)(\mathbf{F}^j\cdot\mathbf{R}) + (\mathbf{F}^i\cdot\mathbf{R})(F^j_\alpha R_\beta + F^j_\beta R_\alpha)}{R^{p+4}} \\
&- p(p+2)(p+4)\,\frac{(\mathbf{F}^i\cdot\mathbf{R})(\mathbf{F}^j\cdot\mathbf{R})}{R^{p+6}}\,R_\alpha R_\beta
\end{aligned} \tag{C.122}$$

Up to S^i and S^j

In addition to terms in E_{F^i,F^j}, we have

$$\begin{aligned}
E_{S^i,S^j} &= \frac{p(p+2)}{2}\,\frac{Z^i S^j_{\alpha\beta} R_\alpha R_\beta + Z^j S^i_{\alpha\beta} R_\alpha R_\beta}{R^{p+4}} - \frac{p}{2}\,\frac{Z^i Trace(S^j) + Z^j Trace(S^i)}{R^{p+2}} \\
&- p(p+2)\,\frac{F^i_\alpha S^j_{\alpha\beta} R_\beta - F^j_\alpha S^i_{\alpha\beta} R_\beta}{R^{p+4}} \\
&+ \frac{p(p+2)(p+4)}{2}\,\frac{F^i_\gamma R_\gamma S^j_{\alpha\beta} R_\alpha R_\beta - F^j_\gamma R_\gamma S^i_{\alpha\beta} R_\alpha R_\beta}{R^{p+6}} \\
&- \frac{p(p+2)}{2}\,\frac{F^i_\alpha R_\alpha Trace(S^j) - F^j_\alpha R_\alpha Trace(S^i)}{R^{p+4}} \\
&+ \frac{p(p+2)}{2}\,\frac{S^i_{\alpha\beta} S^j_{\alpha\beta}}{R^{p+4}} - p(p+2)(p+4)\,\frac{R_\alpha S^i_{\alpha\beta} S^j_{\beta\gamma} R_\gamma}{R^{p+6}}
\end{aligned}$$

$$- \frac{p(p+2)(p+4)}{4} \frac{S^i_{\alpha\beta} R_\alpha R_\beta Trace(S^j) + S^j_{\alpha\beta} R_\alpha R_\beta Trace(S^i)}{R^{p+6}}$$
$$+ \frac{p(p+2)}{4} \frac{Trace(S^i) Trace(S^j)}{R^{p+4}} + \frac{p(p+2)(p+4)(p+6)}{4} \frac{S^i_{\alpha\beta} R_\alpha R_\beta S^j_{\mu\nu} R_\mu R_\nu}{R^{p+8}} \tag{C.123}$$

Stress contribution

$$\begin{aligned}
\Omega \Pi_{\alpha\beta} &= -\frac{\partial E_{S^i,S^j}}{\partial \epsilon_{\alpha\beta}} \\
&= -p(p+2) \frac{Z^i (R_\alpha S^j_{\beta\gamma} + R_\beta S^j_{\alpha\gamma}) R_\gamma + Z^j (R_\alpha S^i_{\beta\gamma} + R_\beta S^i_{\alpha\gamma} R_\gamma}{R^{p+4}} \\
&+ \frac{p(p+2)(p+4)}{2} \frac{Z^i S^j_{\mu\nu} R_\mu R_\nu + Z^j S^i_{\mu\nu} R_\mu R_\nu}{R^{p+6}} R_\alpha R_\beta \\
&+ p \frac{Z^i S^j_{\alpha\beta} + Z^j S^i_{\alpha\beta}}{R^{p+2}} - \frac{p(p+2)}{2} \frac{Z^i Trace(S^j) + Z^j Trace(S^i)}{R^{p+4}} R_\alpha R_\beta \\
&+ p(p+2) \frac{F^i_\gamma (S^j_{\gamma\alpha} R_\beta + S^j_{\gamma\beta} R_\alpha) + (F^i_\alpha S^j_{\beta\gamma} + F^i_\beta S^j_{\alpha\gamma}) R_\gamma}{R^{p+4}} \\
&- p(p+2) \frac{F^j_\gamma (S^i_{\gamma\alpha} R_\beta + S^i_{\gamma\beta} R_\alpha) + (F^j_\alpha S^i_{\beta\gamma} + F^j_\beta S^i_{\alpha\gamma}) R_\gamma}{R^{p+4}} \\
&- p(p+2)(p+4) \frac{F^i_\mu S^j_{\mu\nu} R_\nu - F^j_\mu S^i_{\mu\nu} R_\nu}{R^{p+6}} R_\alpha R_\beta \\
&- \frac{p(p+2)(p+4)}{2} \frac{(F^i_\alpha R_\beta + F^i_\beta R_\alpha) S^j_{\mu\nu} R_\mu R_\nu - F^j_\alpha R_\beta + F^j_\beta R_\alpha) S^i_{\mu\nu} R_\mu R_\nu}{R^{p+6}} \\
&+ p(p+2)(p+4) \frac{(\mathbf{F}^i \cdot \mathbf{R})(R_\alpha S^j_{\beta\gamma} + R_\beta S^j_{\alpha\gamma}) R_\gamma - (\mathbf{F}^j \cdot \mathbf{R})(R_\alpha S^i_{\beta\gamma} + R_\beta S^i_{\alpha\gamma}) R_\gamma}{R^{p+6}} \\
&+ \frac{p(p+2)}{2} \frac{(F^i_\alpha R_\beta + F^i_\beta R_\alpha) Trace(S^j) - (F^j_\alpha R_\beta + F^j_\beta R_\alpha) Trace(S^i)}{R^{p+4}} \\
&+ p(p+2) \frac{(\mathbf{F}^i \cdot \mathbf{R}) S^j_{\alpha\beta} - (\mathbf{F}^j \cdot \mathbf{R}) S^i_{\alpha\beta}}{R^{p+4}} \\
&- \frac{p(p+2)(p+4)}{2} \frac{(\mathbf{F}^i \cdot \mathbf{R}) Trace(S^j) - (\mathbf{F}^j \cdot \mathbf{R}) Trace(S^i)}{R^{p+6}} R_\alpha R_\beta \\
&- p(p+2) \frac{S^i_{\alpha\gamma} S^j_{\gamma\beta} + S^i_{\beta\gamma} S^j_{\gamma\alpha}}{R^{p+4}} + p(p+2)(p+4) \frac{S^i_{\mu\nu} S^j_{\mu\nu}}{R^{p+6}} R_\alpha R_\beta \\
&+ p(p+2)(p+4) \frac{(R_\alpha S^i_{\beta\gamma} + R_\beta S^i_{\alpha\gamma}) S^j_{\gamma\nu} R_\nu + (R_\alpha S^j_{\beta\gamma} + R_\beta S^j_{\alpha\gamma}) S^i_{\gamma\nu} R_\nu}{R^{p+6}}
\end{aligned}$$

$$
\begin{aligned}
&+ p(p+2)(p+4)\Big[\frac{R_\mu(S^i_{\mu\alpha}S^j_{\beta\nu}+S^i_{\mu\beta}S^j_{\alpha\nu})R_\nu}{R^{p+6}} + (p+6)\,\frac{R_\mu S^i_{\mu\gamma}S^j_{\gamma\nu}R_\nu}{R^{p+8}}\,R_\alpha R_\beta\Big] \\
&+ \frac{p(p+2)(p+4)}{2}\,\frac{(R_\alpha S^i_{\beta\gamma}+R_\beta S^i_{\alpha\gamma})R_\gamma Trace(S^j)+(R_\alpha S^j_{\beta\gamma}+R_\beta S^j_{\alpha\gamma})R_\gamma Trace(S^i)}{R^{p+6}} \\
&+ \frac{p(p+2)(p+4)}{2}\,\frac{S^i_{\mu\nu}R_\mu R_\nu S^j_{\alpha\beta}+S^j_{\mu\nu}R_\mu R_\nu S^i_{\alpha\beta}}{R^{p+6}} \\
&- \frac{p(p+2)(p+4)(p+6)}{4}\,\frac{S^i_{\mu\nu}R_\mu R_\nu Trace(S^j)+S^j_{\mu\nu}R_\mu R_\nu Trace(S^i)}{R^{p+8}}\,R_\alpha R_\beta \\
&- \frac{p(p+2)}{2}\Big[\frac{S^i_{\alpha\beta}Trace(S^j)+S^j_{\alpha\beta}Trace(S^i)}{R^{p+4}} - \frac{p+4}{2}\,\frac{Trace(S^i)Trace(S^j)}{R^{p+6}}R_\alpha R_\beta\Big] \\
&- \frac{p(p+2)(p+4)(p+6)}{2}\,\frac{R_\mu R_\nu[S^j_{\mu\nu}(R_\alpha S^i_{\beta\gamma}+R_\beta S^i_{\alpha\gamma})+S^i_{\mu\nu}(R_\alpha S^j_{\beta\gamma}+R_\beta S^j_{\alpha\gamma})]R_\gamma}{R^{p+8}} \\
&+ \frac{p(p+2)(p+4)(p+6)(p+8)}{4}\,\frac{S^i_{\mu\nu}R_\mu R_\nu S^j_{\kappa\lambda}R_\kappa R_\lambda}{R^{p+10}}\,R_\alpha R_\beta
\end{aligned}
\tag{C.124}
$$

Up to T^i and T^j

In addition to terms in E_{F^i,F^j} and E_{S^i,S^j}, we have

$$
\begin{aligned}
E_{T^i,T^j} = &-\frac{p(p+2)(p+4)}{6}\,\frac{(Z^iT^j_{\alpha\beta\gamma}-Z^jT^i_{\alpha\beta\gamma})R_\alpha R_\beta R_\gamma}{R^{p+6}} \\
&+ \frac{p(p+2)}{2}\,\frac{Z^iT^j_{\lambda\lambda\alpha}R_\alpha - Z^jT^i_{\lambda\lambda\alpha}R_\alpha}{R^{p+4}} - \frac{p(p+2)}{2}\,\frac{F^i_\alpha T^j_{\lambda\lambda\alpha}-F^j_\alpha T^i_{\lambda\lambda\alpha}}{R^{p+4}} \\
&+ \frac{p(p+2)(p+4)}{2}\,\frac{R_\alpha R_\beta(F^i_\alpha T^j_{\lambda\lambda\beta}+F^j_\alpha T^i_{\lambda\lambda\beta})}{R^{p+6}} \\
&+ \frac{p(p+2)(p+4)}{2}\,\frac{(F^i_\alpha T^j_{\alpha\beta\gamma}+F^j_\alpha T^i_{\alpha\beta\gamma})R_\beta R_\gamma}{R^{p+6}} \\
&- \frac{p(p+2)(p+4)(p+6)}{6}\,\frac{R_\mu(F^i_\mu T^j_{\alpha\beta\gamma}+F^j_\mu T^i_{\alpha\beta\gamma})R_\alpha R_\beta R_\gamma}{R^{p+8}} \\
&- \frac{p(p+2)(p+4)}{2}\,\frac{(S^i_{\alpha\beta}T^j_{\alpha\beta\gamma}-S^j_{\alpha\beta}T^i_{\alpha\beta\gamma})R_\gamma}{R^{p+6}} \\
&- \frac{p(p+2)(p+4)}{2}\,\frac{R_\alpha(S^i_{\alpha\beta}T^j_{\lambda\lambda\beta}-S^j_{\alpha\beta}T^i_{\lambda\lambda\beta})}{R^{p+6}} \\
&+ \frac{p(p+2)(p+4)(p+6)}{4}\,\frac{(S^i_{\alpha\beta}T^j_{\lambda\lambda\gamma}-S^j_{\alpha\beta}T^i_{\lambda\lambda\gamma})R_\alpha R_\beta R_\gamma}{R^{p+8}} \\
&+ \frac{p(p+2)(p+4)(p+6)}{2}\,\frac{R_\mu(S^i_{\mu\alpha}T^j_{\alpha\beta\gamma}-S^j_{\mu\alpha}T^i_{\alpha\beta\gamma})R_\beta R_\gamma}{R^{p+8}}
\end{aligned}
$$

$$
\begin{aligned}
&- \frac{p(p+2)(p+4)(p+6)(p+8)}{12} \frac{R_\mu R_\nu (S^i_{\mu\nu} T^j_{\alpha\beta\gamma} - S^j_{\mu\nu} T^i_{\alpha\beta\gamma}) R_\alpha R_\beta R_\gamma}{R^{p+10}} \\
&- \frac{p(p+2)(p+4)}{4} \frac{Trace(S^i) T^j_{\lambda\lambda\alpha} R_\alpha - Trace(S^j) T^i_{\lambda\lambda\alpha} R_\alpha}{R^{p+6}} \\
&+ \frac{p(p+2)(p+4)(p+6)}{12} \frac{[Trace(S^i) T^j_{\alpha\beta\gamma} - Trace(S^j) T^i_{\alpha\beta\gamma}] R_\alpha R_\beta R_\gamma}{R^{p+8}} \\
&+ \frac{p(p+2)(p+4)}{6} \frac{T^i_{\alpha\beta\gamma} T^j_{\alpha\beta\gamma}}{R^{p+6}} - p(p+2)(p+4)(p+6) \frac{R_\mu T^i_{\mu\alpha\beta} T^j_{\alpha\beta\nu} R_\nu}{R^{p+8}} \\
&- \frac{p(p+2)(p+4)(p+6)}{4} \frac{R_\alpha R_\beta (T^i_{\alpha\beta\gamma} T^j_{\lambda\lambda\gamma} - T^j_{\alpha\beta\gamma} T^i_{\lambda\lambda\gamma})}{R^{p+8}} \\
&+ \frac{p(p+2)(p+4)(p+6)(p+8)}{4} \frac{R_\alpha R_\beta R_\gamma (T^i_{\alpha\beta\gamma} T^j_{\lambda\lambda\mu} + T^j_{\alpha\beta\gamma} T^i_{\lambda\lambda\mu}) R_\mu}{R^{p+10}} \\
&+ \frac{p(p+2)(p+4)(p+6)(p+8)}{4} \frac{R_\alpha R_\beta T^i_{\alpha\beta\gamma} T^j_{\gamma\mu\nu} R_\mu R_\nu}{R^{p+10}} \\
&- \frac{p(p+2)(p+4)(p+6)(p+8)(p+10)}{36} \frac{T^i_{\alpha\beta\gamma} R_\alpha R_\beta R_\gamma T^j_{\mu\nu\lambda} R_\mu R_\nu R_\lambda}{R^{p+12}}
\end{aligned}
\tag{C.125}
$$

The stress contribution from the above terms can be derived accordingly.

C.6.3 Stress Calculation Based on (μ, Q, O)

Multipole Moments Interactions(up to dipole)

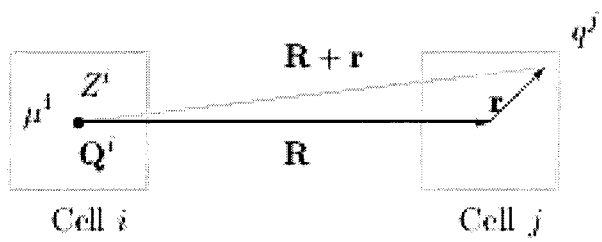

Figure C.6: Multipole moments interaction

We know the field at $\mathbf{r}$ and the energy of a point charge q^j at $\mathbf{r}$; we'll approximate the total energy between point charges within cell j in field of multipole moments of cell j by interaction of multipole moments of the two cells. We'll examine Z^i, μ^i and $\mathbf{Q}^i$ in turn.

Interaction between $\mathbf{Q}^i$ and cell j

$$E_{Z^iq^j} = \frac{Z^iq^j}{(R_\gamma R_\gamma + 2R_\gamma r_\gamma + r_\gamma r_\gamma)^{\frac{p}{2}}} \tag{C.126}$$

$$\left.\frac{\partial E_{Z^iq^j}}{\partial r_\alpha}\right|_{r=0} = -pZ^iq^j\frac{R_\alpha}{R^{p+2}} \tag{C.127}$$

$$\left.\frac{\partial^2 E_{Z^iq^j}}{\partial r_\alpha \partial r_\beta}\right|_{r=0} = -pZ^iq^j\frac{\delta_{\alpha\beta}}{R^{p+2}} + p(p+2)Z^iq^j\frac{R_\alpha R_\beta}{R^{p+4}} \tag{C.128}$$

then,

$$\begin{aligned} E_{Z^ij} &= \sum_j \frac{Z^iq^j}{R^p} + \sum_j -pZ^iq^j\frac{R_\alpha r_\alpha}{R^{p+2}} \\ &\quad + \sum_j \Big[-pZ^iq^j\frac{\delta_{\alpha\beta}r_\alpha r_\beta}{R^{p+2}} + p(p+2)Z^iq^j\frac{R_\alpha R_\beta}{R^{p+4}}r_\alpha r_\beta\Big] \\ &= \frac{Z^iZ^j}{R^p} - \frac{Z^i\mu^j_\alpha R_\alpha}{R^{p+2}} + \frac{Z^iQ^i_{\alpha\beta}R_\alpha R_\beta}{R^{p+4}} \end{aligned} \tag{C.129}$$

Interaction between μ^i and cell j

$$E_{\mu^iq^j} = \frac{\mu_\kappa(R_\kappa + r_\kappa)q^j}{(R_\lambda R_\lambda + 2R_\lambda r_\lambda + r_\lambda r_\lambda)^{\frac{p+2}{2}}} \tag{C.130}$$

$$\left.\frac{\partial E_{\mu^iq^j}}{\partial r_\alpha}\right|_{r=0} = \frac{\mu^i_\alpha q^j}{R^{p+2}} - (p+2)\frac{\mu^i_\lambda R_\lambda q^j}{R^{p+4}}R_\alpha \tag{C.131}$$

$$\begin{aligned} \left.\frac{\partial^2 E_{\mu^iq^j}}{\partial r_\alpha \partial r_\beta}\right|_{r=0} &= -(p+2)\frac{q^j\mu^i_\alpha R_\beta}{R^{p+4}} - (p+2)\frac{q^j\mu^i_\lambda R_\lambda \delta_{\alpha\beta}}{R^{p+4}} - (p+2)\frac{q^j\mu^i_\beta q^j R_\alpha}{R^{p+4}} \\ &\quad + (p+2)(p+4)\frac{\mu^i_\lambda R_\lambda q^j R_\alpha R_\beta}{R^{p+6}} \end{aligned} \tag{C.132}$$

then

$$E_{\mu^ij} = \sum_j \frac{\mu^i_\kappa R_\kappa q^j}{R^{p+2}} + \sum_j \frac{\mu^i_\alpha q^j r_\alpha}{R^{p+2}} - (p+2)\sum_j \frac{\mu^i_\lambda R_\lambda q^j}{R^{p+4}}R_\alpha r_\alpha$$

$$- \frac{p+2}{2} \sum_j \frac{q^j \mu_\alpha^i R_\beta r_\alpha r_\beta}{R^{p+4}} - \frac{p+2}{2} \sum_j \frac{q^j \mu_\lambda^i R_\lambda \delta_{\alpha\beta} r_\alpha r_\beta}{R^{p+4}} - \frac{p+2}{2} \sum_j \frac{q^j \mu_\beta^i q^j R_\alpha r_\alpha r_\beta}{R^{p+4}}$$
$$+ \frac{(p+2)(p+4)}{2} \sum_j \frac{\mu_\lambda^i R_\lambda q^j R_\alpha R_\beta}{R^{p+6}} r_\alpha r_\beta \tag{C.133}$$

Since

$$Q_{\alpha\beta}^j = \frac{p}{2} \sum_j q^j \Big[(p+2) r_\alpha r_\beta - r^2 \delta_{\alpha\beta} \Big] \tag{C.134}$$

we have

$$\frac{p+2}{2} \sum_j \frac{q^j \mu_\alpha^i R_\beta r_\alpha r_\beta}{R^{p+4}} = \frac{1}{p} \frac{Q_{\alpha\beta}^j \mu_\alpha^i R_\beta}{R^{p+4}} + \frac{1}{2} \sum_j \frac{\mu_\alpha^i R_\beta}{R^{p+4}} q^j r^2 \delta_{\alpha\beta} \tag{C.135}$$

$$\frac{p+2}{2} \sum_j \frac{q^j \mu_\beta^i q^j R_\alpha r_\alpha r_\beta}{R^{p+4}} = \frac{1}{p} \frac{Q_{\alpha\beta}^j \mu_\beta^i R_\alpha}{R^{p+4}} + \frac{1}{2} \sum_j \frac{\mu_\beta^i R_\alpha}{R^{p+4}} q^j r^2 \delta_{\alpha\beta} \tag{C.136}$$

$$\frac{p+2}{2} \sum_j \frac{\mu_\lambda^i R_\lambda q^j R_\alpha R_\beta}{R^{p+6}} r_\alpha r_\beta = \frac{1}{p} \frac{\mu_\kappa^i R_\kappa Q_{\alpha\beta}^j R_\alpha R_\beta}{R^{p+6}} + \frac{1}{2} \sum_j \frac{\mu_\kappa^i R_\kappa}{R^{p+6}} R_\alpha R_\beta q^j r^2 \delta_{\alpha\beta} \tag{C.137}$$

$$\frac{p+2}{2} \sum_j \frac{q^j \mu_\lambda^i R_\lambda \delta_{\alpha\beta} r_\alpha r_\beta}{R^{p+4}} = \frac{p+2}{2} \sum_j \frac{q^j \mu_\lambda^i R_\lambda r^2}{R^{p+4}} \tag{C.138}$$

$$R_\alpha R_\beta \delta_{\alpha\beta} r^2 = R^2 r^2 \tag{C.139}$$

$$\mu_\alpha^i R_\beta \delta_{\alpha\beta} r^2 = \mu_\lambda^i R_\lambda \tag{C.140}$$

$$\mu_\beta^i R_\alpha \delta_{\alpha\beta} r^2 = \mu_\lambda^i R_\lambda \tag{C.141}$$

Then finally

$$E_{\mu^i j} = \frac{\mu_\alpha^i R_\alpha Z^j}{R^{p+2}} + \frac{1}{p} \frac{\mu_\alpha^i \mu_\alpha^j}{R^{p+2}} - \frac{p+2}{p} \frac{\mu_\alpha^i R_\alpha \mu_\beta^j R_\beta}{R^{p+4}}$$
$$- \frac{1}{p} \frac{\mu_\alpha^i R_\beta + \mu_\beta^i R_\alpha}{R^{p+4}} Q_{\alpha\beta}^j + \frac{p+4}{p} \frac{\mu_\lambda^i R_\lambda}{R^{p+6}} Q_{\alpha\beta}^j R_\alpha R_\beta \tag{C.142}$$

Interaction between Q^i and cell j

$$E_{Q^i q^j} = \frac{Q^i_{\kappa\lambda} q^j (R_\kappa + r_\kappa)(R_\lambda + r_\lambda)}{(R_\gamma R_\gamma + 2R_\gamma r_\gamma + r_\gamma r_\gamma)^{\frac{p+4}{2}}} \tag{C.143}$$

$$\left.\frac{\partial E_{Q^i j}}{\partial r_\alpha}\right|_{r=0} = \frac{2Q^i_{\kappa\alpha} R_\kappa q^j}{R^{p+4}} - (p+4)\frac{Q^i_{\kappa\lambda} R_\kappa R_\lambda q^j}{R^{p+6}} R_\alpha \tag{C.144}$$

$$\begin{aligned}\left.\frac{\partial^2 E_{Q^i j}}{\partial r_\alpha \partial r_\beta}\right|_{r=0} &= \frac{2Q^i_{\alpha\beta} q^j}{R^{p+4}} - (p+4)\frac{2Q^i_{\lambda\beta} R_\lambda R_\alpha q^j}{R^{p+6}} - (p+4)\frac{Q^i_{\lambda\kappa} R_\lambda R_\kappa \delta_{\alpha\beta} q^j}{R^{p+6}} \\ &\quad + (p+4)(p+6)\frac{Q^i_{\lambda\kappa} R_\lambda R_\kappa q^j}{R^{p+8}} R_\alpha R_\beta \end{aligned} \tag{C.145}$$

then

$$\begin{aligned} E_{Q^i j} = &\sum_j \frac{Q^i_{\kappa\lambda} R_\kappa R_\lambda q^j}{R^{p+4}} + \sum_j \frac{2Q^i_{\kappa\alpha} R_\kappa q^j}{R^{p+4}} r_\alpha - \sum_j (p+4)\frac{Q^i_{\kappa\lambda} R_\kappa R_\lambda q^j}{R^{p+6}} R_\alpha r_\alpha \\ &+ \sum_j \frac{Q^i_{\alpha\beta} q^j}{R^{p+4}} r_\alpha r_\beta - \sum_j (p+4)\frac{Q^i_{\lambda\beta} R_\lambda R_\alpha}{R^{p+6}} q^j r_\alpha r_\beta - \sum_j \frac{p+4}{2}\frac{Q^i_{\lambda\kappa} R_\lambda R_\kappa \delta_{\alpha\beta}}{R^{p+6}} q^j r_\alpha r_\beta \\ &+ \sum_j \frac{(p+4)(p+6)}{2}\frac{Q^i_{\lambda\kappa} R_\lambda R_\kappa}{R^{p+8}} R_\alpha R_\beta q^j r_\alpha r_\beta \end{aligned} \tag{C.146}$$

since

$$\sum_j q^j r_\alpha r_\beta = \frac{2}{p(p+2)} Q^j_{\alpha\beta} + \frac{2}{p+2}\delta_{\alpha\beta}\sum_j q^j r^2 \tag{C.147}$$

we have

$$\begin{aligned} E_{Q^i j} = &\frac{Q^i_{\kappa\lambda} R_\kappa R_\lambda Z^j}{R^{p+4}} + \frac{2Q^i_{\kappa\alpha} R_\kappa \mu_\alpha}{pR^{p+4}} - \frac{p+4}{p}\frac{Q^i_{\kappa\lambda} R_\kappa R_\lambda \mu_\alpha R_\alpha}{R^{p+6}} \\ &+ \frac{2}{p(p+2)}\frac{Q^i_{\alpha\beta} Q^j_{\alpha\beta}}{R^{p+4}} - \frac{2(p+4)}{p(p+2)}\frac{Q^i_{\lambda\beta} R_\lambda R_\alpha Q^j_{\alpha\beta}}{R^{p+6}} \\ &+ \frac{(p+4)(p+6)}{p(p+2)}\frac{Q^i_{\lambda\kappa} R_\lambda R_\kappa R_\alpha R_\beta Q^j_{\alpha\beta}}{R^{p+8}} \\ &+ \frac{2}{p+2}\frac{Q^i_{\alpha\alpha}}{R^{p+4}}\sum_j q^j r^2 + \frac{(p+4)(p+6)}{2(p+2)}\frac{Q^i_{\lambda\kappa} R_\lambda R_\kappa}{R^{p+6}}\sum_j q^j r^2 \end{aligned} \tag{C.148}$$

For $p \neq 1$,

$$\sum_j q^j r^2 = \frac{2}{p(p-1)} Tr[Q^j] \tag{C.149}$$

For $p = 1$, which is Coulomb interaction, by using $Q_{\alpha\beta}$, we lost the information of $\sum_i q^i r^2$, thus the Z, F, S, and T scheme would be a better choice.

Stress Contribution from Monopoles and Dipoles

Up to dipole moments, the total energy between (Z^i, μ^i) and (Z^j, μ^j)

$$E = \frac{Z^i Z^j}{R^p} - \frac{Z^i \mu_\alpha^j R_\alpha}{R^{p+2}} + \frac{Z^j \mu_\alpha^i R_\alpha}{R^{p+2}} - \frac{(p+2)\mu_\alpha^j R_\alpha \mu_\beta^i R_\beta - \mu_\alpha^i \mu_\alpha^j R^2}{pR^{p+4}} \tag{C.150}$$

By using

$$\frac{\partial(\vec{\mu} \cdot \vec{R})}{\partial \epsilon_{\alpha\beta}} = R_\alpha \mu_\beta + R_\beta \mu_\alpha \tag{C.151}$$

$$\frac{\partial(\vec{\mu^i} \cdot \vec{\mu^j})}{\partial \epsilon_{\alpha\beta}} = \mu_\alpha^i \mu_\beta^j + \mu_\beta^i \mu_\alpha^j \tag{C.152}$$

we have

$$\begin{aligned}
-\Omega \Pi_{\alpha\beta} &= \frac{\partial E}{\partial \epsilon_{\alpha\beta}} \\
&= -p\frac{Z^i Z^j R_\alpha R_\beta}{R^{p+2}} + (p+2)\frac{Z^i \mu_\gamma^j R_\gamma R_\alpha R_\beta}{R^{p+4}} - Z^i \frac{\mu_\alpha^j R_\beta + \mu_\beta^j R_\alpha}{R^{p+2}} \\
&- (p+2)\frac{Z^j \mu_\gamma^i R_\gamma R_\alpha R_\beta}{R^{p+4}} + Z^j \frac{\mu_\alpha^i R_\beta + \mu_\beta^i R_\alpha}{R^{p+2}} \\
&+ \frac{(p+2)(p+4)}{p} \frac{\mu_\kappa^i R_\kappa \mu_\lambda^i R_\lambda R_\alpha R_\beta}{R^{p+6}} \\
&- \frac{p+2}{p} \mu_\kappa^i R_\kappa \frac{\mu_\alpha^j R_\beta + \mu_\beta^j R_\alpha}{R^{p+4}} - \frac{p+2}{p} \mu_\lambda^j R_\lambda \frac{\mu_\alpha^i R_\beta + \mu_\beta^i R_\alpha}{R^{p+4}}
\end{aligned} \tag{C.153}$$

C.7 References

1. H.Q. Ding, N. Karasawa and W.A. Goddard III, "Atomic level simulations on a million particles - the cell multipole method for Coulomb and London nonbond interactions," *J. Chem. Phys.* **97(6)**, 1992, 4309-4315.

2. L. Greengard and V. Rokhlin, "A fast algorithm for particle simulations," *J. Comp. Phys.* **73**, 1987, 325-348.

3. H.G. Petersen, D. Soelvason and J.W. Perram, "The very fast multipole method," *J. Chem. Phys.* **101(10)**, 1994, 8870-76.

4. E.R. Smith, "Fast moment methods for general potentials in molecular dynamics," *Mol. Phys.* **86(4)**, 1995, 769-796.

5. J.K. Singer, *The parallel fast multipole method in molecular dynamics*, Ph.D. Thesis, 1995, Univ. of Houston.

Appendix D Ewald Summation

D.1 Introduction

From macromolecular structure, to aqueous biological systems, accurate computation of electrostatic and van der Waals interactions is the most difficult task in computer modeling. Simulations of peptides and membranes as well as of ions in aqueous solutions have provided clear-cut evidence of artifactual behavior due to the use of cutoffs. Works done by Yor[1] have showed using current force field without truncation of Coulombic interactions do not exhibit similar artifactual behavior. The general approach to this problem is the Ewald method.

D.2 Lattice Sums For Inverse Power Of Distance

Consider crystal lattice pairwise sums of the type

$$E_n = \frac{1}{2} C_n \sum_{j \neq k} \frac{q_j q_k}{r_{jk}^n} \tag{D.1}$$

where $n = 1$ for Coulomb interaction and $n = 2$ for shielded Coulomb interaction, while $n = 6$ is the London dispersion term, or the van der Waals attraction sum.

We'll derive the lattice summation formulas used in our program for the case of dispersion interactions as well as for Coulombic interactions. These lattice sums do not in general converge absolutely, so we need to specify the asymptotic order of summation, corresponding to the asymptotic shape of the finite crystal made up of the union of lattice translations of unit cell U.

Let Λ denote the set of all lattice vectors $n = n_1 a_1 + n_2 a_2 + n_3 a_3$. In order to describe the order of summation in R^3, we introduce a closed, bounded region P,

centered on the origin, and for positive integers K let $P_K(\Lambda)$ denote the set of lattice vectors n such that $n/K \in P$. Given N points $r_1, \ldots, r_N$ in the unit cell U, and real constants C_{ij}, we consider

$$E_p(r_1, \ldots, r_N) = \lim_{K\to\infty} \frac{1}{2} {\sum_{n\in P_K(\Lambda)}}' \sum_{i,j} \frac{C_{ij}}{|r_i - r_j + n|^p} \tag{D.2}$$

where the prime denotes that terms with $i = j$ and $n = 0$ are omitted.

Let's start with some identities for the inverse powers $1/|r|^p$, $p > 0$, where r is any nonzero vector in R^3. The following two formulas are used

$$\Gamma(x) = \int_0^\infty t^{x-1} e^{-t} dt = \lambda^z \int_0^\infty t^{x-1} e^{-\lambda t} dt \tag{D.3}$$

and

$$e^{-a^2 w^2} = \frac{\sqrt{\pi}}{a} \int_0^\infty e^{-\frac{\pi^2 u^2}{a^2}} e^{-2\pi i w u} du \tag{D.4}$$

where $\Gamma(x)$ is the Euler gamma function.

Given a 3-dimension vector $\mathbf{r}$, substitute $\lambda = |\mathbf{r}|^2 = \mathbf{r}^2$ and $z = p/2$. For arbitrary positive number β, we then have

$$\frac{\Gamma(\frac{p}{2})}{r^p} = \int_0^{\beta^2} t^{\frac{p}{2}-1} e^{-r^2 t} dt + \int_{\beta^2}^\infty t^{\frac{p}{2}-1} e^{-r^2 t} dt \tag{D.5}$$

In the second term, if we substitute t by s, with $r^2 t = s^2$, we have

$$\int_{\beta^2}^\infty t^{\frac{p}{2}-1} e^{-r^2 t} dt = \frac{1}{r^p} \int_{\beta r}^\infty s^{p-1} e^{-s^2} ds \tag{D.6}$$

For the first term, we write $r^2 = x^2 + y^2 + z^2$ and apply Equation (D.4) in all three dimension; and we have

$$\int_0^{\beta^2} t^{\frac{p}{2}-1} e^{-r^2 t} dt = \pi^{\frac{3}{2}} \int_0^{\beta^2} t^{\frac{p}{2}-\frac{5}{2}} \int_{R^3} e^{-\frac{\pi^2 u^2}{t}} e^{-2\pi i u\cdot r} d^3u\, dt \tag{D.7}$$

Integrate over t first and substituting t with s, where $\pi^2 u^2 = ts^2$, we have

$$\pi^{\frac{3}{2}} \int_0^{\beta^2} t^{\frac{p}{2}-\frac{5}{2}} e^{-\frac{\pi^2 u^2}{t}} dt = 2\pi^{\frac{3}{2}} \beta^{p-3} (\frac{\pi u}{\beta})^{p-3} \int_{\frac{\pi u}{\beta}}^{\infty} s^{2-p} e^{-s^2} ds \tag{D.8}$$

Consider the reciprocal unit cell U^* made up of the points u in R^3 such that $-\frac{1}{2} \leq a_i \cdot u \leq \frac{1}{2}$ and the fact that R^3 can be decomposed as the union of the points sets $U^* + m$, over all reciprocal vectors m, we have

$$\frac{1}{r^p} = \pi^{\frac{3}{2}} \beta^{p-3} \sum_m \int_{U^*} f_p(\frac{\pi|v+m|}{\beta}) e^{-2\pi i(v+m)\cdot r} d^3v + \frac{g_p(\beta r)}{r^p} \tag{D.9}$$

where we have defined

$$f_p(x) = \frac{2x^{p-3}}{\Gamma(\frac{p}{2})} \int_x^{\infty} s^{2-p} e^{-s^2} ds \tag{D.10}$$

and

$$g_p(x) = \frac{2}{\Gamma(\frac{p}{2})} \int_x^{\infty} s^{p-1} e^{-s^2} ds \tag{D.11}$$

also noted

$$\lim_{r\to 0}(\frac{1}{r^p} - \frac{g_p(\beta r)}{r^p}) = \frac{1}{\Gamma(\frac{p}{2})} \int_0^{\beta^2} t^{\frac{p}{2}-1} dt = \frac{2\beta^p}{p\Gamma(\frac{p}{2})} \tag{D.12}$$

For $v \in U^*$ we write $v = w_1 a_1^* + w_2 a_2^* + w_3 a_3^*$ where $w_k = v \cdot a_k$, $k = 1, 2, 3$. For $r \in U$ and any lattice vector $n = n_1 a_1 + n_2 a_2 + n_3 a_3$, such that $r + n \neq 0$, we extend Equation (D.9); changing variables in the integral over U^*, we have

$$\frac{1}{|r+n|^p} = \frac{\pi^{\frac{3}{2}} \beta^{p-3}}{V} \sum_m e^{-2\pi i m\cdot r} \int_{-\frac{1}{2}}^{\frac{1}{2}} \int_{-\frac{1}{2}}^{\frac{1}{2}} \int_{-\frac{1}{2}}^{\frac{1}{2}} h_{p,m,n}(w) e^{-2\pi i w\cdot n} d^3w + \frac{g_p(\beta|r+n|)}{|r+n|^p} \tag{D.13}$$

where

$$h_{p,m,n}(w) = f_p(\frac{\pi|v+m|}{\beta})e^{-2\pi iv\cdot r} \tag{D.14}$$

with $v = w \cdot a^*$

Applying the above formula to Equation (D.2), and using the fact that the sum of the Fourier coefficients of the smooth, bounded function $h_{p,m,r}$, $m \neq 0$ converges to $h_{p,m,r}(0) = f_p(\frac{\pi|m|}{\beta})$, we can write

$$\begin{aligned} E_p(r_1,\ldots,r_N) &= \frac{1}{2}{\sum_n}' \sum_{ij} \frac{C_{ij}g_p(\beta|r_i-r_j+n|)}{|r_i-r_j+n|^p} + \frac{\pi^{\frac{3}{2}}\beta^{p-3}}{2V}\sum_m f_p(\frac{\pi|m|}{\beta})\sum_{ij} C_{ij}e^{-2\pi im\cdot(r_i-r_j)} \\ &\quad -\frac{\beta^p}{p\Gamma(\frac{p}{2})}\sum_i C_{ii} \end{aligned} \tag{D.15}$$

where the last term is the correction term (self-energy) for $r = 0$.

D.3 Coulomb Sums

D.3.1 Energy, Force, Stress

When $p = 1$ which is Coulomb interaction, we have

$$f_1(x) = \frac{e^{-x^2}}{\sqrt{\pi}x^2}, \quad g_1(x) = erfc(x) \tag{D.16}$$

Then we can write

$$\begin{aligned} E_1(r_1,\ldots,r_N) &= \frac{1}{2}{\sum_n}' \sum_{ij} \frac{q_iq_jerfc(\beta|r_i-r_j+n|)}{|r_i-r_j+n|} + \frac{1}{2\pi V}\sum_{m\neq 0}\frac{e^{-\frac{\pi^2m^2}{\beta^2}}}{m^2}S(m)S(-m) \\ &\quad -\frac{\beta}{\sqrt{\pi}}\sum_i q_i^2 + \frac{1}{2\pi}\lim_{K\to\infty}\sum_{n\in P_K(\Lambda)}\int_{U^*}\sum_{ij}\frac{q_iq_je^{-\frac{\pi^2m^2}{\beta^2}}}{v^2}e^{-2\pi iv\cdot(r_i-r_j)}e^{-2\pi iv\cdot n}d^3v \end{aligned} \tag{D.17}$$

where

$$S(m) = \sum_i q_i e^{-2\pi i m \cdot r_i} \tag{D.18}$$

is the Coulomb structure factor. The last term diverges, but when we apply a second-order Taylor series expansion to the function $e^{-\frac{\pi^2 m^2}{\beta^2}} e^{-2\pi i v \cdot (r_i - r_j)}$, expanding about $v = 0$. The zeroth and first-order terms, which account for the singularity in the integral, are cancelled by the double summation over i and j for neutral unit cell. The remainder term, which is of order three, can be written as

$$J(D) = 2\pi \lim_{K \to \infty} \sum_{n \in P_K(\Lambda)} \int_{U^*} \frac{(v \cdot D)^2}{v^2} e^{-2\pi i v \cdot n} d^3 v \tag{D.19}$$

where $D = \sum_i q_i r_i$ is the unit cell dipole moment.

Following the above argument, if we neglect the unit cell dipole moment contribution (which depends on the surface boundary of the bulk material) and replace β by $\eta = 1/\beta$, we have

$$E_{Coulomb} = \frac{1}{2\eta} \sum_{L,i,j} Q_{ij} \frac{erfc(a)}{a} + \frac{2\pi}{\Omega} \sum_h{}' S(h) S(-h) h^{-2} e^{-b^2} - \frac{1}{\eta\sqrt{\pi}} \sum_i Q_{ii} \tag{D.20}$$

where the prime indicates that the term at the origin is excluded,

$$a = \frac{|r_i - r_j - R_L|}{\eta}, \qquad \vec{h} = 2\pi\vec{m} = 2\pi \tilde{H}^{-1} \cdot \vec{n} \tag{D.21}$$

with matrix H contains the real space unit cell vectors in Cartesian coordinates, and

$$b = \frac{h\,\eta}{2}, \qquad \Omega = \det H \tag{D.22}$$

$S(h)$ is the structure factor

$$S(h) = C_1^{\frac{1}{2}} \sum_j q_j \, e^{-ih \cdot r_j} \tag{D.23}$$

It was proved that

$$S(h)S(-h) = C_1 \left\{ \Big[\sum_i q_i \cos(h \cdot r_i) \Big]^2 + \Big[\sum_i q_i \sin(h \cdot r_i) \Big]^2 \right\} \tag{D.24}$$

Since

$$\frac{\partial \phi_1(r)}{\partial r_\alpha} = \frac{\partial}{\partial r_\alpha} \left[\frac{1}{\sqrt{\pi}} \int_{\frac{r^2}{\eta^2}}^{\infty} \frac{e^{-t}}{t^{\frac{1}{2}}} dt \right] = -\frac{1}{\sqrt{\pi}} \frac{e^{-\frac{r^2}{\eta^2}}}{\frac{r}{\eta}} \frac{\partial}{\partial r_\alpha} (\frac{r^2}{\eta^2}) = -\frac{2e^{-\frac{r^2}{\eta^2}}}{\sqrt{\pi}\eta} \frac{r_\alpha}{r} \tag{D.25}$$

and

$$\begin{aligned} \frac{\partial}{\partial r_{p,\alpha}} \Big[S(-h)S(h) \Big] &= 2C_1 q_p \left\{ -\sin(h \cdot r_p) \sum_i q_i \cos(h \cdot r_i) + \cos(h \cdot r_p) \sum_i q_i \sin(h \cdot r_i) \right\} h_\alpha \\ &= 2C_1 h_\alpha \sum_i q_p q_i \sin[h \cdot (r_i - r_p)] \end{aligned} \tag{D.26}$$

The force on each atom p

$$\begin{aligned} F_{p,\alpha} &= -\frac{\partial E_1}{\partial r_{p,alpha}} \\ &= \frac{C_1}{\eta^3} \sum_{L,i} q_p q_i (r_{p,\alpha} - r_{i,\alpha} - R_{L,\alpha}) \Big[\frac{erfc(a_p)}{a_p^3} + \frac{2\, e^{-a_p^2}}{\sqrt{\pi} a_p^2} \Big] \\ &\quad + \frac{4\pi C_1}{\Omega} \sum_h{}' h_\alpha \Big[\sum_i q_p q_i \sin \left[h \cdot (r_p - r_i) \right] \Big] \frac{e^{-b^2}}{h^2} \end{aligned} \tag{D.27}$$

where

$$a_p = \frac{|\vec{r}_p - \vec{r}_i - \vec{R}_L|}{\eta} \tag{D.28}$$

The internal stress can be calculated as

$$\begin{aligned}
\Omega\Pi_{\alpha\beta} &= -\frac{\partial E_1}{\partial \epsilon_{\alpha\beta}} \\
&= \frac{1}{2\eta}\sum_{L,i,j} Q_{ij}\left[\frac{erfc(a)}{a^2}+\frac{2e^{-a^2}}{\sqrt{\pi}a}\right]\frac{\partial a}{\partial \epsilon_{\alpha\beta}} \\
&\quad -2\pi\sum_{h}{}' S(h)S(-h)\Big[\frac{e^{-b^2}}{h^2}\frac{\partial}{\partial\epsilon_{\alpha\beta}}(\frac{1}{\Omega})-\frac{1}{\Omega}\frac{\partial h^2}{\partial\epsilon_{\alpha\beta}}\frac{\partial}{\partial h^2}(\frac{e^{-b^2}}{h^2})\Big] \\
&= \frac{1}{2\eta^3}\sum_{L,i,j} Q_{ij}\left[\frac{erfc(a)}{a^3}+\frac{2e^{-a^2}}{\sqrt{\pi}a^2}\right](r_i-r_j-R_L)_\alpha(r_i-r_j-R_L)_\beta \\
&\quad +\frac{2\pi}{\Omega}\sum_{h}{}' S(h)S(-h)\frac{e^{-b^2}}{h^2}\left[\delta_{\alpha\beta}-2\frac{1+b^2}{h^2}h_\alpha h_\beta\right] \qquad \text{(D.29)}
\end{aligned}$$

where

$$h\cdot r_i = 2\pi\tilde{H}^{-1}_{\gamma\alpha}n_\alpha H_{\gamma\beta}s_{i,\beta} = 2\pi n\cdot s_i \qquad \text{(D.30)}$$

is independent of H matrix, or ϵ, and

$$\begin{aligned}
\frac{\partial a}{\partial\epsilon_{\alpha\beta}} &= \frac{1}{2a}\frac{\partial a^2}{\partial\epsilon_{\alpha\beta}} \\
&= \frac{1}{2a}\frac{\partial}{\partial\epsilon_{\alpha\beta}}\Big[\frac{(s_i-s_j-S_L)_\mu G_{\mu\nu}(s_i-s_j-S_L)_\nu}{\eta^2}\Big] \\
&= \frac{1}{\eta^2 a}(r_i-r_j-R_L)_\alpha(r_i-r_j-R_L)_\beta \qquad \text{(D.31)}
\end{aligned}$$

$$\begin{aligned}
\frac{\partial h^2}{\partial\epsilon_{\alpha\beta}} &= 4\pi^2\frac{\partial}{\partial\epsilon_{\alpha\beta}}(n_\mu G^{-1}_{\mu\nu}n_\nu) \\
&= 4\pi^2 n_\mu\frac{\partial G^{-1}_{\mu\nu}}{\partial\epsilon_{\alpha\beta}}n_\nu \\
&= -4\pi^2 n_\mu G^{-1}_{\mu\kappa}\frac{\partial G_{\kappa\lambda}}{\partial\epsilon_{\alpha\beta}}G^{-1}_{\lambda\nu}n_\nu \\
&= -2h_\alpha h_\beta \qquad \text{(D.32)}
\end{aligned}$$

where

$$\frac{\partial A^{-1}_{\mu\nu}}{\partial B_{\alpha\beta}} = -A^{-1}_{\mu\kappa}\frac{\partial A_{\kappa\lambda}}{\partial B_{\alpha\beta}}A^{-1}_{\lambda\nu} \tag{D.33}$$

was used.

$$\begin{aligned}\frac{\partial}{\partial\epsilon_{\alpha\beta}}\frac{1}{\Omega} &= -\frac{1}{\Omega^2}\frac{\partial\Omega}{\partial G_{\mu\nu}}\frac{\partial G_{\mu\nu}}{\partial\epsilon_{\alpha\beta}} \\ &= -\frac{1}{2\Omega}G^{-1}_{\mu\nu}\frac{\partial G_{\mu\nu}}{\partial\epsilon_{\alpha\beta}} \\ &= -\frac{1}{\Omega}\delta_{\alpha\beta}\end{aligned} \tag{D.34}$$

D.3.2 Accuracy Specified Cutoffs

With η specified there is still an infinite number of terms in the sums over the real space and reciprocal space lattices, and an accuracy criteria is used to specify limits on these sums. This is achieved by specifying a tolerance δ and carrying out the sums until the neglected terms have a total contribution smaller than δ. For structure optimization, the energy based cutoffs is desired, while for dynamics simulation, the force based cutoffs is more appropriate. We'll look at the two cases separately.

Energy Based Cutoffs

Using a cutoff distance R_{cut} introduces an error in the total energy for the real space sum of

$$E_{real} = \frac{1}{2}\sum_{L,i,j} Q_{ij}\frac{erfc(\frac{R_{ijL}}{\eta})}{R_{ijL}}\theta(R_{ijL} - R_{cut}) \tag{D.35}$$

where $\theta(R_{ijL} - R_{cut})$ is the step function.

To estimate this error, we replace the discrete sum by a continous integral. Defin-

ing the average interaction as $<q^2> = \sum_i q_i^2/N$, we have

$$E_{real} \simeq \frac{N^2 <q^2>}{2\Omega} \int_{R_{cut}}^{\infty} 4\pi R^2 \frac{erfc(\frac{R}{\eta})}{R} dR \tag{D.36}$$

By using the inequality

$$erfc(\frac{R}{\eta}) = \frac{1}{\pi^{\frac{1}{2}}} \int_{\frac{R^2}{\eta^2}}^{\infty} t^{-\frac{1}{2}} e^{-t} dt \leq \frac{1}{\pi^{\frac{1}{2}}} \int_{\frac{R^2}{\eta^2}}^{\infty} \frac{\eta}{R} e^{-t} dt = \frac{\eta}{\pi^{\frac{1}{2}} R} e^{-\frac{R^2}{\eta^2}} \tag{D.37}$$

we obtain

$$E_{real} \leq \frac{N^2 <q^2>}{2\Omega} \int_{R_{cut}}^{\infty} 4\pi^{\frac{1}{2}} \eta e^{-\frac{R^2}{\eta^2}} dR = \pi \eta^2 \frac{N^2 <q^2>}{\Omega} erfc(\frac{R_{cut}}{\eta}) \tag{D.38}$$

Using a cutoff H_{cut} in the reciprocal space sum introduces an error in the total energy for the reciprocal space sum of

$$E_{recip} = \frac{2\pi}{\Omega} \sum_{h}{}' S(h)S(-h) \frac{e^{-b^2}}{h^2} \theta(h - H_{cut}) \tag{D.39}$$

Replacing the sum by an intergral and replacing $S(h)S(-h)$ by $N^2 <q^2>$, we obtain

$$E_{recip} \simeq \frac{2\pi}{\Omega} N^2 <q^2> \frac{\Omega}{8\pi^3} \int_{H_{cut}}^{\infty} 4\pi h^2 \frac{e^{-(\frac{h\eta}{2})^2}}{h^2} dh = \frac{N^2 <q^2>}{\pi^{\frac{1}{2}} \eta} erfc(\eta \frac{H_{cut}}{2}) \tag{D.40}$$

Force Based Cutoffs

For the real space sum, the error introduced in force of atom p by R_{cut} can be written as

$$|F_{p,real}| = \frac{1}{\eta^3} \sum_{L,i} |Q_{pi}| R_{piL} \left[\frac{erfc(a_p)}{a_p^3} + \frac{2e^{-a_p^2}}{\sqrt{\pi} a_p^2} \right] \theta(R_{piL} - R_{cut}) \tag{D.41}$$

by using average interaction and replacing the sum with integral, we obtain

$$|F_{real}| \simeq \frac{N<q^2>}{\eta^3\Omega}\int_{R_{cut}}^{\infty} 4\pi R^2 R\left[\frac{erfc(a)}{a^3}+\frac{2e^{-a^2}}{\sqrt{\pi}a^2}\right]dR \tag{D.42}$$

further using Equation (D.37),

$$\begin{aligned}
|F_{real}| &\simeq \frac{4\pi\eta N<q^2>}{\Omega}\int_{\frac{R_{cut}}{\eta}}^{\infty}\left[erfc(a)+\frac{2}{\sqrt{\pi}}ae^{-a^2}\right]da \\
&\leq \frac{4\pi\eta N<q^2>}{\Omega}\int_{\frac{R_{cut}}{\eta}}^{\infty}\left[\frac{1}{\sqrt{\pi}a}e^{-a^2}+\frac{2}{\sqrt{\pi}}ae^{-a^2}\right]da \\
&\leq \frac{4\pi\eta N<q^2>}{\Omega}\int_{\frac{R_{cut}}{\eta}}^{\infty}\left[\frac{\eta}{\sqrt{\pi}R_{cut}}e^{-a^2}+\frac{2}{\sqrt{\pi}}ae^{-a^2}\right]da \\
&= \frac{4\pi\eta N<q^2>}{\Omega}\left[2\sqrt{\pi}erfc(\frac{R_{cut}}{\eta})+e^{-\frac{R_{cut}^2}{\eta^2}}\right]
\end{aligned} \tag{D.43}$$

For reciprocal space sum, the error introduced in force of atom p by R_{cut} is

$$|F_{p,recip}| = \frac{4\pi}{\Omega}\sum_{h}{}'h\Big[\sum_i Q_{pi}\sin(h\cdot r_{pi})\Big]\frac{e^{-b^2}}{h^2}\theta(h-H_{cut}) \tag{D.44}$$

Replacing the sum by integral and replacing $\sum_i Q_{pi}\sin(h\cdot r_{pi})$ by $N^2<q^2>$, we obtain

$$\begin{aligned}
|F_{recip}| &\simeq \frac{4\pi}{\Omega}N^2<q^2>\frac{\Omega}{8\pi^3}\int_{H_{cut}}^{\infty}2\pi h^2 h\frac{e^{-b^2}}{h^2}dh \\
&= \frac{N^2<q^2>}{2\pi}\int_{H_{cut}}^{\infty}e^{-b^2}dh^2 \\
&= \frac{2N^2<q^2>}{\pi\eta^2}e^{-\frac{1}{4}\eta^2H_{cut}^2}
\end{aligned} \tag{D.45}$$

For a given η, by using Equation (D.43) and Equation (D.45) we can evaluate the cutoff distances R_{cut} and H_{cut} to obtain a given accuracy δ_Q. Because of the neutrality of the cell under which Ewald calculation is carried out, there will be a great deal of cancellation when we use the average interaction $<q^2>$. Consequently, Equation (D.43) and Equation (D.45) overestimate the errors.

D.4 Dispersion Sums

D.4.1 Energy, Force, Stress

For $p = 6$, which is the London dispersion interaction, noted

$$f_6(x) = \frac{1}{3}\Big[(1-2x^2)e^{-x^2} + 2x^3\sqrt{\pi}erfc(x)\Big] \tag{D.46}$$

and

$$g_6(x) = (1 + x^2 + \frac{1}{2}x^4)e^{-x^2} \tag{D.47}$$

we can write energy sum as

$$\begin{aligned} E_{London} &= \frac{1}{2\eta^6}\sum_{L,i,j} C_{ij}(a^{-6} + a^{-4} + 12a^{-2})e^{-a^2} \\ &+ \frac{\pi^{\frac{3}{2}}}{24\Omega}\sum_{h}{}' \sum_{i,j} C_{ij}\cos[h\cdot(r_i - r_j)]h^3\left[\pi^{\frac{1}{2}}erfc(b) + \Big(\frac{1}{2b^3} - \frac{1}{b}\Big)e^{-b^2}\right] \\ &+ \frac{\pi^{\frac{3}{2}}}{6\Omega\eta^3}\sum_{i,j} C_{ij} - \frac{1}{12\eta^6}\sum_i C_{ii} \end{aligned} \tag{D.48}$$

where a, b, and h are defined in the previous section. If we assume

$$-C_{ij} = \sqrt{C_{ii}C_{jj}} \tag{D.49}$$

we have

$$\sum_{i,j} C_{ij}\cos[h\cdot(r_i - r_j)] = -\Big[\sum_i \sqrt{|C_{ii}|}\cos(h\cdot r_i)\Big]^2 - \Big[\sum_i \sqrt{|C_{ii}|}\sin(h\cdot r_i)\Big]^2 \tag{D.50}$$

The force on atom p is

$$\begin{aligned} F_{p,\alpha} &= -\frac{\partial E_{London}}{\partial r_{p,\alpha}} \\ &= \frac{1}{\eta^8}\sum_L\sum_i C_{pi}(r_p - r_i - R_L)_\alpha(6a_p^{-8} + 6a_p^{-6} + 3a_p^{-4} + a_p^{-2})e^{-a_p^2} \\ &\quad + \frac{\pi^{\frac{3}{2}}}{12\Omega}\sum_h{}' h_\alpha\Big(\sum_i C_{pi}\sin[h\cdot(r_p - r_i)]\Big)h^3\Big[\sqrt{\pi}erfc(b) + (\frac{1}{2b^3} - \frac{1}{b})e^{-b^2}\Big] \end{aligned} \tag{D.51}$$

The stress

$$\begin{aligned} \Omega\Pi_{\alpha\beta} &= \frac{1}{2\eta^8}\sum_{L,i,j} C_{ij}(6a_p^{-8} + 6a_p^{-6} + 3a_p^{-4} + a_p^{-2})e^{-a_p^2}(r_p - r_i - R_L)_\alpha(r_p - r_i - R_L)_\beta \\ &\quad + \frac{\pi^{\frac{3}{2}}}{24\Omega}\sum_h{}'\sum_{i,j} C_{ij}\cos[h\cdot(r_i - r_j)]h^3\Big[\pi^{\frac{1}{2}}erfc(b) + (\frac{1}{2b^3} - \frac{1}{b})e^{-b^2}\Big]\delta_{\alpha\beta} \\ &\quad + \frac{\pi^{\frac{3}{2}}}{24\Omega}\sum_h{}'\sum_{i,j} C_{ij}\cos[h\cdot(r_i - r_j)]3h\Big[\pi^{\frac{1}{2}}erfc(b) - \frac{e^{-b^2}}{b}\Big]h_\alpha h_\beta + \frac{\pi^{\frac{3}{2}}}{6\eta^3\Omega}\sum_{i,j} C_{ij}\delta_{\alpha\beta} \end{aligned} \tag{D.52}$$

D.4.2 Accuracy Specified Cutoffs

Following section of Coulomb interaction, we'll discuss the energy based accuracy and force based accuracy for London dispersion interaction.

Energy Based Cutoffs

Using a cutoff distance R_{cut} introduces an error in the total energy for the real space sum of

$$E_{real} = \frac{1}{2\eta^6}\sum_{L,i,j} B_{ij}(a^{-6} + a^{-4} + \frac{1}{2}a^{-2})e^{-a^2}\theta(R_{Lij} - R_{cut}) \tag{D.53}$$

By using average interaction strength $< B_{ij} >$ and replacing the sum with integral, we obtain

$$\begin{aligned} E_{real} &\simeq \frac{N^2 < B_{ij} >}{2\eta^6 \Omega} \int_{\frac{R_{cut}}{\eta}}^{\infty} (a^{-6} + a^{-4} + \frac{1}{2} a^{-2}) e^{-a^2} 2\pi R^2 dR \\ &\leq \frac{\pi N^2 < B_{ij} >}{\eta^3 \Omega} (\frac{\eta^4}{R_{cut}^4} + \frac{\eta^2}{R_{cut}^2} + \frac{1}{2}) \int_{\frac{R_{cut}}{\eta}}^{\infty} e^{-a^2} da \\ &= \frac{\pi^{\frac{3}{2}} N^2 < B_{ij} >}{2\eta^3 \Omega} (\frac{\eta^4}{R_{cut}^4} + \frac{\eta^2}{R_{cut}^2} + \frac{1}{2}) erfc(\frac{R_{cut}}{\eta}) \end{aligned} \tag{D.54}$$

Using a cutoff distance H_{cut} introduces an error in the total energy for the reciprocal space sum of

$$E_{recip} = \frac{\pi^{\frac{3}{2}}}{24\Omega} \sum_{h}{}' \sum_{ij} B_{ij} \cos(h \cdot r_{ij}) h^3 \left[\sqrt{\pi} erfc(b) + \left(\frac{1}{2b^3} - \frac{1}{b} \right) e^{-b^2} \right] \theta(h - H_{cut}) \tag{D.55}$$

Replacing the sum with integral, and replacing $\sum_{ij} B_{ij} \cos(h \cdot r_{ij})$ with $N^2 < B_{ij} >$, we obtain

$$\begin{aligned} E_{recip} &\simeq \frac{\pi^{\frac{3}{2}} N^2 < B_{ij} >}{24\Omega} \frac{\Omega}{8\pi^3} \int_{H_{cut}}^{\infty} 2\pi h^2 h^3 \left[\sqrt{\pi} erfc(b) + \left(\frac{1}{2b^3} - \frac{1}{b} \right) e^{-b^2} \right] dh \\ &= \frac{2N^2 < B_{ij} >}{3\sqrt{\pi}\eta^6} \int_{\frac{1}{2}\eta H_{cut}}^{\infty} \left[\sqrt{\pi} b^5 erfc(b) + \left(\frac{1}{2} b^2 - b^4 \right) e^{-b^2} \right] db \end{aligned} \tag{D.56}$$

By using $\sqrt{\pi} erfc(b) \leq e^{-b^2}/b$, we have

$$\begin{aligned} E_{recip} &\simeq \frac{2N^2 < B_{ij} >}{3\sqrt{\pi}\eta^6} \int_{\frac{1}{2}\eta H_{cut}}^{\infty} \frac{1}{2} b^2 e^{-b^2} db \\ &= \frac{N^2 < B_{ij} >}{12\eta^6} \left[\frac{\eta H_{cut}}{\sqrt{\pi}} e^{-\frac{1}{4}\eta^2 H_{cut}^2} + erfc(\frac{1}{2}\eta H_{cut}) \right] \end{aligned} \tag{D.57}$$

Force Based Cutoffs

Using a cutoff distance R_{cut} introduces an error in the force on atom p for the real space sum of

$$|F_{p,real}| \simeq \frac{1}{\eta^8} \sum_L \sum_i B_{pi} r_{piL} (6a_p^{-8} + 6a_p^{-6} + 3a_p^{-4} + a_p^{-2}) e^{-a_p^2} \theta(r_{piL} - R_{cut}) \quad \text{(D.58)}$$

Replacing the sum with integral and using the average interaction $< B_{ij} >$, we have

$$\begin{aligned}
|F_{real}| &\simeq \frac{N < B_{ij} >}{\eta^8 \Omega} \int_{R_{cut}}^{\infty} 2\pi R^2 (6a^{-8} + 6a^{-6} + 3a^{-4} + a^{-2}) e^{-a^2} dR \\
&= \frac{2\pi N < B_{ij} >}{\eta^5 \Omega} \int_{\frac{R_{cut}}{\eta}}^{\infty} (6a^{-6} + 6a^{-4} + 3a^{-2} + 1) e^{-a^2} da \\
&\leq \frac{2\pi N < B_{ij} >}{\eta^5 \Omega} (6\frac{\eta^6}{R_{cut}^6} + 6\frac{\eta^4}{R_{cut}^4} + 3\frac{\eta^2}{R_{cut}^2} + 1) \int_{\frac{R_{cut}}{\eta}}^{\infty} e^{-a^2} da \\
&= \frac{\pi^{\frac{3}{2}} N < B_{ij} >}{\eta^5 \Omega} (6\frac{\eta^6}{R_{cut}^6} + 6\frac{\eta^4}{R_{cut}^4} + 3\frac{\eta^2}{R_{cut}^2} + 1) erfc(\frac{R_{cut}}{\eta}) \qquad \text{(D.59)}
\end{aligned}$$

Using a cutoff distance H_{cut} introduces an error in the force on atom p for the reciprocal space sum of

$$|F_{p,recip}| \simeq \frac{\pi^{\frac{3}{2}}}{12\Omega} {\sum_h}' h \Big[\sum_i B_{pi} \sin(h \cdot r_{pi}) \Big] h^3 \left[\sqrt{\pi} erfc(b) + \Big(\frac{1}{2b^3} - \frac{1}{b} \Big) e^{-b^2} \right] \theta(h - H_{cut}) \quad \text{(D.60)}$$

Replacing the sum with integral and using $\sum_i B_{pi} \sin(h \cdot r_{pi}) \simeq N < B_{ij} >$, we obtain

$$\begin{aligned}
|F_{recip}| &\simeq \frac{\pi^{\frac{3}{2}} N < B_{ij} >}{12\Omega} \frac{\Omega}{8\pi^3} \int_{H_{cut}}^{\infty} 4\pi h^2 h^3 \Big[\sqrt{\pi} erfc(b) + (\frac{1}{2b^3} - \frac{1}{b}) e^{-b^2} \Big] dh \\
&\leq \frac{N < B_{ij} >}{24\sqrt{\pi}} \int_{H_{cut}}^{\infty} \frac{h^5}{2b^3} e^{-b^2} dh \\
&= \frac{4N < B_{ij} >}{3\sqrt{\pi}\eta^6} \int_{\frac{1}{2}\eta H_{cut}}^{\infty} b^2 e^{-b^2} db \\
&= \frac{N < B_{ij} >}{3\sqrt{\pi}\eta^6} \Big[\eta H_{cut} e^{-\frac{1}{4}\eta^2 H_{cut}^2} + \sqrt{\pi} erfc(\frac{1}{2}\eta H_{cut}) \Big] \qquad \text{(D.61)}
\end{aligned}$$

D.5 Particle-Mesh Ewald Sum

Since $n_{cut} = \frac{1}{2\pi} H \cdot h_{cut}$, the cost for reciprocal sum is proportional to $\frac{4\pi}{3} n_{cut}^3 N \sim \Omega N \sim N^2$ for convention computation, where $\frac{4\pi}{3} n_{cut}^3$ is the volume in h space, while N is the cost of structure factor computation.

For given accuracy, optimize *eta* parameter so that the computation cost minimized, we can get a scaling of $N^{\frac{3}{2}} = \sqrt{NN^2}$ where the N and N^2 is the cost in real space sum and reciprocal space sum. It's not practical to perform simulation with $N \sim 1000,000$. To improve speed, Lee Pedersen et al. proposed the so-called particle-mesh Ewald (PME) method[2-4] which is an $N \cdot \log N$ method for the reciprocal space sum.

D.5.1 Theory

The particle-mesh Ewald method involves choosing η sufficiently large that atom pairs for which r_{ij} exceeds a specified cutoff are negligible in the direct space sum which reduces the real space sum to order N. The reciprocal space sum is then approximated by multidimensional piecewise-interpolation. The approximate reciprocal energy and forces are expressed as convolutions and thus can be evaluated quickly using 3D fast fourier transforms (FFTs). The resulting algorithm is of order $N \ln N$. Let's look at the second term in Equation (D.15)

$$E_{recip} = \frac{\pi^{\frac{3}{2}} \beta^{p-3}}{2V} \sum_{m}{}' f_p(\frac{\pi |m|}{\beta}) \sum_{ij} C_{ij} e^{-2\pi i m \cdot (r_i - r_j)} \tag{D.62}$$

Define the reciprocal lattice vector m by $m = m_x a_x^* + m_y a_y^* + m_z a_z^*$ with m_x,m_y,m_z integers not all zero, and the structure factor $S(m)$ by

$$\begin{aligned} \tilde{S}(m) &= \sum_{j=1}^{N} q_j e^{2\pi i m \cdot r_i} \\ &= \sum_{j=1}^{N} q_j exp\Big[2\pi i (m_x s_{xj} + m_y s_{yj} + m_z s_{zj})\Big] \end{aligned} \tag{D.63}$$

where $s_{\alpha j}$, $\alpha = x,\ y,\ z$ are the fractional coordinates of atom j. In order to approximate the above defined structure factor (Coulomb, or London), we'll interpolate the complex exponentials appearing in the above equation. Given positive integers $K_x,\ K_y,\ K_z$ and a point r in the unit cell, denote its fractional coordinates by $u_x,\ u_y,\ u_z$, i.e., $u_\alpha = K_\alpha a_\alpha^* \cdot r$, for $\alpha = x,\ y,\ z$. Due to periodic boundary conditions, we may assume that $0 \leq u_\alpha \leq K_\alpha$. Then

$$exp(2\pi i m \cdot r) = exp(2\pi i \frac{m_x u_x}{K_x}) \cdot exp(2\pi i \frac{m_y u_y}{K_y}) \cdot exp(2\pi i \frac{m_z u_z}{K_z}) \tag{D.64}$$

There are several ways of interpolating the above exponential. Lagrangian interpolation and Cardinal B-splines are the two which get the most attention. Lagrangian weight functions are continuous and therefore give rise to approximate unit cell energies which are continuous as functions of particle positions. But they are only piecewise differentiable, so the approximate reciprocal energy cannot be differentiated to arrive at forces. The forces and stresses have to be interpolated as well. While by using the Euler exponential spline which interpolate exponentials with the Cardinal B-splines, we can differentiate the energy to get forces and stresses, due to several nice properties of the Cardinal B-splines.

For any real number u, let $M_2(u)$ denote the linear hat function given by

$$M_2(u) = \begin{cases} 1 - |u - 1| & 0 \leq u \leq 2 \\ 0 & \text{otherwise} \end{cases} \tag{D.65}$$

For n greater than 2, define $M_n(u)$ by the recursion

$$M_n(u) = \frac{u}{n-1} M_{n-1}(u) + \frac{n-u}{n-1} M_{n-1}(u-1) \tag{D.66}$$

It can be proven that

$$\frac{d}{du} M_n(u) = M_{n-1}(u) - M_{n-1}(u-1) \tag{D.67}$$

Clearly, for $n > 2$, $M_n(u)$ is $n-2$ times continously differentiable. It's also proved when n is even we can write

$$exp(2\pi i\frac{m_\alpha}{K_\alpha}u_\alpha) \simeq b(m_\alpha)\sum_{k=-\infty}^{\infty} M_n(u_\alpha - k)exp(2\pi i\frac{m_\alpha}{K_\alpha}k) \tag{D.68}$$

where again $\alpha = x,\ y,\ z$, and

$$b(m_\alpha) = \frac{exp\left[2\pi i(n-1)\frac{m_\alpha}{K_\alpha}\right]}{\sum_{k=0}^{n-2} M_n(k+1)exp(2\pi i\frac{m_\alpha}{K_\alpha}k)} \tag{D.69}$$

Proceeding as above, we can then approximate the structure factor by

$$\tilde{S}(m) = b(m_x)b(m_y)b(m_z)\sum_{k_x,k_y,k_z=-\infty}^{\infty} Q(k_x,k_y,k_z)exp(2\pi i\frac{m_x}{K_x}k_x)exp(2\pi i\frac{m_y}{K_y}k_y)exp(2\pi i\frac{m_z}{K_z}k_z) \tag{D.70}$$

where

$$Q(k_x,k_y,k_z) = \sum_{j=1}^{N}\sum_{n_x,n_y,n_z} q_j M_n(u_x^j - k_x - n_xK_x)M_n(u_y^j - k_y - n_yK_y)M_n(u_z^j - k_z - n_zK_z) \tag{D.71}$$

Define

$$B(m_x,m_y,m_z) = |b(m_x)|^2 \cdot |b(m_y)|^2 \cdot |b(m_z)|^2 \tag{D.72}$$

and

$$F(Q)(m_x,m_y,m_z) = \sum_{k_x,k_y,k_z=-\infty}^{\infty} Q(k_x,k_y,k_z)exp(2\pi i\frac{m_x}{K_x}k_x)exp(2\pi i\frac{m_y}{K_y}k_y)exp(2\pi i\frac{m_z}{K_z}k_z) \tag{D.73}$$

The approximate reciprocal energy is now given by

$$\begin{aligned} E_{recip} &= \frac{\pi^{\frac{3}{2}}\beta^{p-3}}{2V}{\sum_{m_x,m_y,m_z}}' f_p(\frac{\pi|m|}{\beta})B(m_x,m_y,m_z)F(Q)(m_x,m_y,m_z)F(Q)(-m_x,-m_y,-m_z) \\ &= \frac{1}{2}\sum_{k_x=0}^{K_x-1}\sum_{k_y=0}^{K_y-1}\sum_{k_z=0}^{K_z-1} Q(k_x,k_y,k_z)(\theta_{rec} * Q)(k_x,k_y,k_z) \end{aligned} \tag{D.74}$$

where $\theta_{rec} * Q$ is the convolution of θ_{rec} and Q, and

$$\theta_{rec} = F\Big[\frac{\pi^{\frac{3}{2}}\beta^{p-3}}{V} f_p(\frac{\pi|m|}{\beta})B(m_x,m_y,m_z)\Big] \tag{D.75}$$

We have used the following properties of discrete fourier transform

$$A * B = F\Big[F^{-1}(A * B)\Big] = F\Big[F^{-1}(A)F^{-1}(B)\Big] \tag{D.76}$$

$$F^{-1}(A)(m_x,m_y,m_z) = F(A)(-m_x,-m_y,-m_z) \tag{D.77}$$

$$\sum_m F(A)(m)\,B(m) = \sum_m A(m)F(B)(m) \tag{D.78}$$

Since θ_{rec} does not depend on particle positions, we get

$$\frac{\partial E_{rec}}{\partial r_{\alpha i}} = \sum_{k_x=0}^{K_x-1}\sum_{k_y=0}^{K_y-1}\sum_{k_z=0}^{K_z-1}\frac{\partial Q}{\partial r_{\alpha i}}(k_x,k_y,k_z)(\theta_{rec} * Q)(k_x,k_y,k_z) \tag{D.79}$$

Also, since $m \cdot r_i$ does not depend on the unit cell parameters, we can compute reciprocal contribution of stress as the following two terms:

$$\Omega\Pi_{1,\alpha\beta} = E_{recip}\delta_{\alpha\beta} \tag{D.80}$$

which originate from $\frac{\partial \Omega}{\partial \epsilon_{\alpha\beta}}$ and

$$\Omega\Pi_{2,\alpha\beta} = \frac{1}{2}\sum_{k_x=0}^{K_x-1}\sum_{k_y=0}^{K_y-1}\sum_{k_z=0}^{K_z-1} Q(k_x,k_y,k_z)(\zeta_{\alpha\beta} * Q)(k_x,k_y,k_z) \tag{D.81}$$

with

$$\zeta_{\alpha\beta} = F\Big[\frac{\pi^{\frac{3}{2}}\beta^{p-3}}{V}\frac{\partial^2}{\partial m_\alpha \partial m_\beta} f_p(\frac{\pi|m|}{\beta})B(m_x,m_y,m_z)\Big] \tag{D.82}$$

For the Coulomb case, which is $p = 1$, we have

$$\theta^Q_{rec} = F\Big[\frac{1}{\pi V}\frac{e^{-\frac{\pi^2 m^2}{\beta^2}}}{m^2}B(m_x,m_y,m_z)\Big] \tag{D.83}$$

For van der Waals attraction, or London dispersion interaction, we have $p = 6$, which gives us

$$\theta^L_{rec} = F\left[\frac{\pi^{\frac{3}{2}}\beta^3}{6V}\Big[(1-2\frac{\pi^2\beta^2}{\beta^2})e^{-\frac{\pi^2 m^2}{\beta^2}} + 2\frac{\pi^{\frac{5}{2}}m^3}{\beta^3}erfc(\frac{\pi m}{\beta})\Big]B(m_x,m_y,m_z)\right] \tag{D.84}$$

D.6 References

1. D.M. York, T.A. Darden, and L.G. Pedersen, "The effect of long-range electrostatic interactions in simulations of macromolecular crystals: A comparison of the Ewald and truncated list methods," *J. Chem. Phys.* **99(10)**, 1993, 8345-48.

2. U. Essmann, L. Perera, M.L. Berkowitz, T. Darden, H. Lee, and L.G. Pedersen, "A smooth particle mesh Ewald method," *J. Chem. Phys.* **103(19)**, 1995, 8577-8593.

3. H.G. Petersen, "Accuracy and efficiency of the particle mesh Ewald method," *J. Chem. Phys.* **103(9)**, 1995, 3668-3676.

4. T. Darden, D. York, and L. Pedersen, "Particle mesh Ewald: An $N \cdot \log(N)$

method for Ewald sums in large systems," *J. Chem. Phys.* **98(12)**, 1993, 10089-10092.

Appendix E Structural Optimization

Structural optimization is a necessary tool to get the lowest energy configuration which corresponds to zero temperature in experiments. It's an essential starting point for vibration frequency calculation. We implemented two kinds of optimizers. Before we can proceed with the structural minimization which is multi-dimensional, we have to look at minimization of function with one degree of freedom. These are based on the well-known "Numerical Recipes in C."[1]

E.1 Minimization in One Dimension

Both methods (steepest descent and conjugate gradient) require finding the minimum along a certain direction, thus minimization in one dimension.

E.1.1 Golden Section Search

Given three points, $a, b, andc$ which bracket a minimum, so that for $a < b < c$ (or $a > b > c$), $f(b)$ is less than both $f(a)$ and $f(c)$. The problem can be phrased as find a point x, either between a and b, or between b and c. Let's assume we pick the latter choice. Then we evaluate $f(x)$. If $f(b) < f(x)$, then the new bracketing triplet of points is (a, b, x), otherwise (b, x, c). In all cases the middle point of the new triplet is the abscissa whose ordinate is the best minimum achieved so far. Suppose b is a

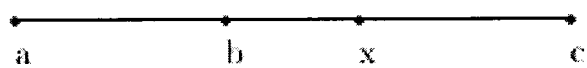

Figure E.1: Golden search

fraction w of the way between a and c, i.e.,

$$\begin{aligned} \frac{b-a}{c-a} &= u \\ \frac{c-b}{c-a} &= 1-u \end{aligned} \tag{E.1}$$

Suppose next trial point x is between b and c, such that

$$\frac{x-b}{c-a} = v \tag{E.2}$$

then the next bracketing triplet would be either (a, b, x), or (b, x, c) with length of $(u+v)(c-a)$, or $(1-u)(c-a)$ respectively. If we want to minimize the worst case possibility, then we will choose v such that

$$(u+v)(c-a) = (1-u)(c-a) \tag{E.3}$$

or

$$v = 1-2u \tag{E.4}$$

If the point x is chosen as optimal, so was the point before it. This scale similarity suggests

$$\frac{v}{1-u} = u \tag{E.5}$$

Finally, by solving the above two equations, we have

$$u = \frac{3-\sqrt{5}}{2} \approx 0.38197 \tag{E.6}$$

Given a bracketing triplet of points, the next point to be tried is that which is a fraction 0.38197 into the larger of the two intervals (measuring from the central point of the triplet).

E.1.2 Parabolic Interpolation and Secant Interpolation of First Derivative

The golden section search is designed to handle, in effect, the worst possible case of function minimization. For function which is nicely parabolic near to the minimum, we can find the minimum in one step by parabola fitting. Assume the bracketing triplet (a, b, c) satisfy the parabolic function

$$f(x) = A\,x^2 + B\,x + C \tag{E.7}$$

which has its minimum at

$$x = -\frac{B}{2\,A} \tag{E.8}$$

By solving the linear equations

$$\begin{aligned} a^2\,A + a\,B + C &= f(a) \\ b^2\,A + b\,B + C &= f(b) \\ c^2\,A + c\,B + C &= f(c) \end{aligned} \tag{E.9}$$

we have the minimum at

$$x = b - \frac{1}{2}\,\frac{(b-a)^2[f(b)-f(c)] - (b-c)^2[f(b)-f(a)]}{(b-a)[f(b)-f(c)] - (b-c)[f(b)-f(a)]} \tag{E.10}$$

Another approach is use the first derivatives, which is readily available in the energy force calculation, to extrapolate to zero first derivative. The sign of the derivative at the central point of the bracketing triplet (a, b, c) indicates uniquely whether the next test point should be taken in the interval (a, b) or in the interval (b, c). We can use the secant method to extrapolate the derivatives of the best point and the second best point. Assume d_a is the derivative of point a, and d_b is the derivative of point b,

then the extrapolated point x is

$$x = \frac{b\, d_a - a\, d_b}{d_a - d_b} \tag{E.11}$$

E.1.3 Brent's Method

The golden section search is reliable, but it's slow to converge. The parabolic interpolation and secant extrapolation of first derivative are faster, but not reliable. Brent's method takes the best of the golden section search and the parabolic interpolation (or extrapolation of first derivative), it relies on a sure-but-slow technique when the function is not cooperative, and switches to a faster method when the function allows.

At any particular stage, it is keeping track of six function points (not necessarily all distinct). (a, b) bracket the minimum, u is the most recent evaluated point, x is the best point, w is the second best point, while v is the previous stage's w.

Figure E.2 is the flow chart. The scheme to detect a cooperative versus noncooperative function has to be robust, the attention must be paid to the convergence test. The bookkeeping is to update the six point at next stage, so that it conforms to the definitions of the six points.

For parabolic interpolation method, the point must fall within the bounding interval (a, b) and imply a movement from the best current value x that is less than half the movement of the step before last.

For secant first derivative extrapolation method, the movement must be consistent with the sign of first derivative at point x and lies within the bracketing interval (a, b).

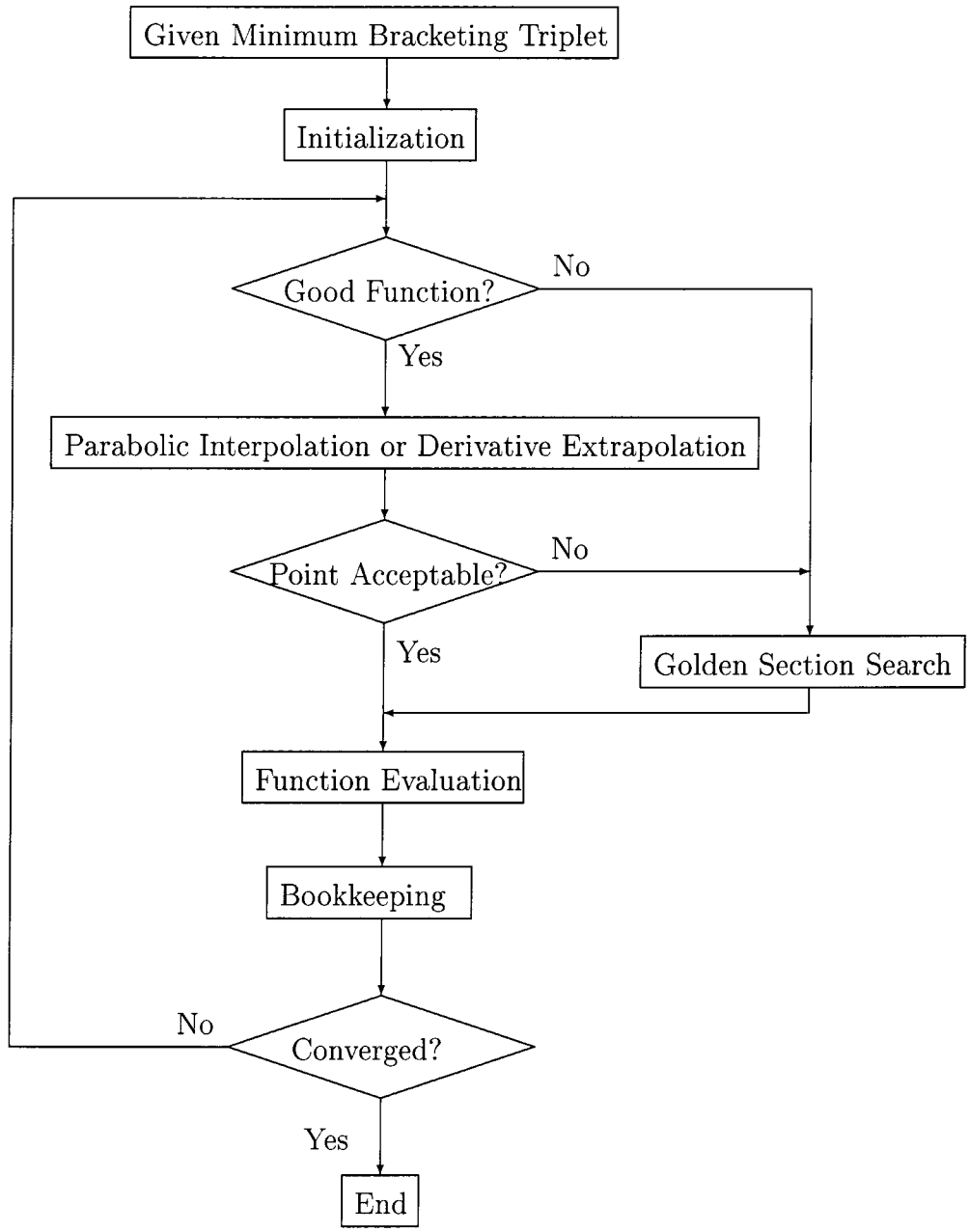

Figure E.2: Brent's flowchart

E.2 Multi-dimensional Minimization

There are many ways of multi-dimension minimization, which include direction set methods; simulated annealing, etc. We implemented two direction set methods, they are steepest descent and conjugate gradient. All direction set methods consist of two tasks, updating the set of directions as the method proceeds, attempting to come up with a set of minimization directions. It is very important for the set of directions to include some very good directions that will take us far along narrow valleys, or minimization along one direction is not spoiled by minimization along other directions within the set. Since the first derivatives are calculated along with energy evaluation in our program, we'll use gradient information.

E.2.1 Steepest Descent Method

The algorithm of steepest descent is the following:

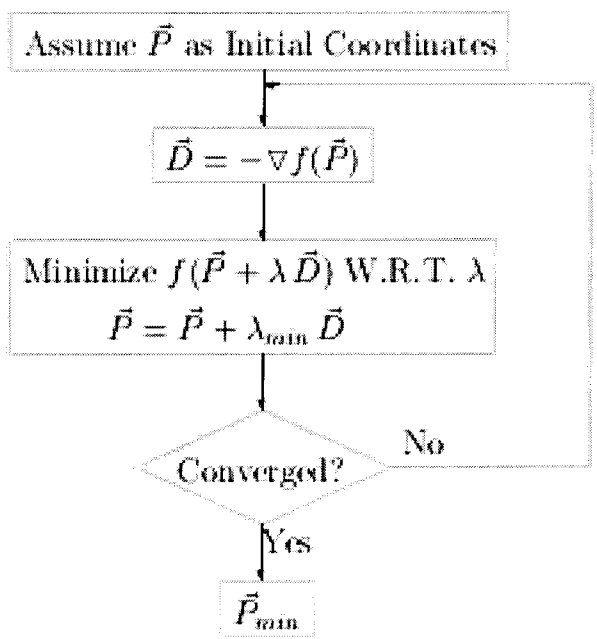

Figure E.3: Steepest descent flowchart

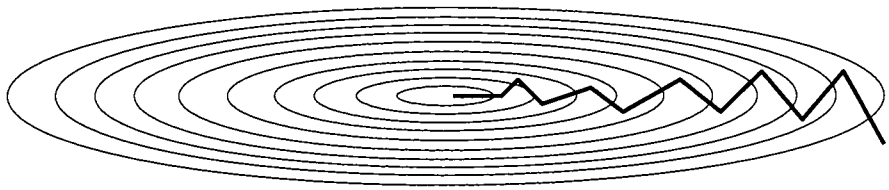

Figure E.4: Steepest descent method in long narrow valley

E.2.2 Conjugate Gradient Method

The problem with steepest descent method is in a long, narrow "valley." It takes many steps to reach the valley as shown in the following figure. We really want to construct the new direction somehow to be conjugate to the old gradient, and, insofar as possible, to all previous directions traversed. Methods that accomplish this construction are called conjugate gradient methods.

Definition of Conjugate

We can Taylor expand function $f(\vec{r})$ around point $\vec{P}$ as

$$f(\vec{r}) = c - \vec{b} \cdot \vec{x} + \frac{1}{2} \vec{x} \cdot A \cdot \vec{x} + \dots \tag{E.12}$$

where

$$\vec{r} = \vec{P} + \vec{x}, \quad c = f(\vec{P}), \quad \vec{b} = -\nabla f(\vec{r})|_{\vec{r}=\vec{P}}\ , \quad A_{ij} = \frac{\partial^2 f}{\partial r_i \partial r_j}\Big|_{\vec{r}=\vec{P}} \tag{E.13}$$

Then

$$\nabla f = A \cdot \vec{x} - \vec{b} \tag{E.14}$$

the change of ∇f when we move along some direction

$$\delta(\nabla f) = A \cdot (\delta \vec{x}) \tag{E.15}$$

Suppose that we have moved along some direction $\vec{u}$ to a minimum and now propose to move along some new direction $\vec{v}$. The condition that motion along $\vec{v}$ not spoil our minimization along $\vec{u}$ is just that the gradient stay perpendicular to $\vec{u}$, i.e., that the change in the gradient be perpendicular to $\vec{u}$. That's

$$\vec{u} \cdot \delta(\nabla f) = \vec{u} \cdot A \cdot \vec{v} = 0 \tag{E.16}$$

When the above equation holds for two vectors $\vec{u}$ and $\vec{v}$, they are said to be conjugate.

Construct a Set of Conjugate Directions

Starting with an arbitrary initial vector $\vec{g}_0$ and letting $\vec{h}_0 = \vec{g}_0$, construct two sequences of vectors from the recurrence

$$\lambda_i = \frac{\vec{g}_i \cdot \vec{g}_i}{\vec{h}_i \cdot A \cdot \vec{h}_i} = \frac{\vec{g}_i \cdot \vec{h}_i}{\vec{h}_i \cdot A \cdot \vec{h}_i} \tag{E.17}$$

$$\vec{g}_{i+1} = \vec{g}_i - \lambda_i A \cdot \vec{h}_i \tag{E.18}$$

$$\gamma_i = \frac{\vec{g}_{i+1} \cdot \vec{g}_{i+1}}{\vec{g}_i \cdot \vec{g}_i} \tag{E.19}$$

$$\vec{h}_{i+1} = \vec{g}_{i+1} + \gamma_i \vec{h}_i \tag{E.20}$$

The vectors satisfy the orthogonality and conjugacy conditions

$$\vec{g}_i \cdot \vec{g}_j = 0\,, \quad \vec{h}_i \cdot A \cdot \vec{h}_j = 0\,, \quad \vec{g}_i \cdot \vec{h}_j = 0 \quad \text{for} \quad i \neq j \tag{E.21}$$

We'll prove it by induction as follows. First let's look at case $i = 1$

$$\begin{aligned} \vec{g}_1 \cdot \vec{g}_0 &= \vec{g}_0 \cdot \vec{g}_0 - \lambda_0 \vec{g}_0 \cdot A \cdot \vec{h}_0 \\ &= \vec{g}_0 \cdot \vec{g}_0 - \lambda_0 \vec{h}_0 \cdot A \cdot \vec{h}_0 = 0 \end{aligned} \tag{E.22}$$

since $\vec{h}_0 = \vec{g}_0$ and $\lambda_0 = \frac{\vec{g}_0 \cdot \vec{g}_0}{\vec{h}_0 \cdot A \cdot \vec{h}_0}$

$$\begin{aligned} \vec{g}_1 \cdot \vec{h}_0 &= (\vec{g}_0 - \lambda_0 A \cdot \vec{h}_0) \cdot \vec{h}_0 \\ &= \vec{h}_0 \cdot \vec{h}_0 - \lambda_0 \vec{h}_0 \cdot A \cdot \vec{h}_0 = 0 \end{aligned} \tag{E.23}$$

$$\begin{aligned} \vec{h}_1 \cdot A \cdot \vec{h}_0 &= (\vec{g}_1 + \gamma_0 \vec{h}_0) \cdot (\vec{g}_0 - \vec{g}_1)/\lambda_0 \\ &= (\gamma_0 \vec{g}_0 \cdot \vec{g}_0 - \vec{g}_1 \cdot \vec{g}_1)/\lambda_0 = 0 \end{aligned} \tag{E.24}$$

since

$$\gamma_0 = \frac{\vec{g}_1 \cdot \vec{g}_1}{\vec{g}_0 \cdot \vec{g}_0} \tag{E.25}$$

Then assume the claim holds for $i \leq n - 1$; let's look at $i = n$

$$\begin{aligned} \vec{g}_{n+1} \cdot \vec{h}_m &= (\vec{g}_n - \lambda_n A \cdot \vec{h}_n) \cdot \vec{h}_m \\ &= \vec{g}_n \cdot \vec{h}_m - \lambda_n \vec{h}_n \cdot A \cdot \vec{h}_m \end{aligned} \tag{E.26}$$

Obviously for $m = 0, 1, 2, \ldots, n - 1, \quad \vec{g}_{n+1} \cdot \vec{h}_m = 0$ holds. For $m = n$, we have

$$\vec{g}_{n+1} \cdot \vec{h}_n = \vec{g}_n \cdot \vec{h}_n - \lambda_n \vec{h}_n \cdot A \cdot \vec{h}_n = 0 \tag{E.27}$$

since

$$\lambda_n = \frac{\vec{g}_n \cdot \vec{h}_n}{\vec{h}_n \cdot A \cdot \vec{h}_n} \tag{E.28}$$

$$\begin{aligned} \vec{g}_{n+1} \cdot \vec{g}_m &= (\vec{g}_n - \lambda_n A \cdot \vec{h}_n) \cdot \vec{g}_m \\ &= \vec{g}_n \cdot \vec{g}_m - \lambda_n \vec{h}_n \cdot A \cdot \vec{g}_m \end{aligned} \tag{E.29}$$

Obviously for $m = 0, 1, 2, \ldots, n-1$, $\vec{g}_{n+1} \cdot \vec{g}_m = 0$ holds. For $m = n$, we have

$$\begin{aligned} \vec{g}_{n+1} \cdot \vec{g}_n &= \vec{g}_n \cdot \vec{g}_n - \lambda_n \vec{g}_n \cdot A \cdot \vec{h}_n \\ &= \vec{g}_n \cdot \vec{g}_n - \lambda_n \vec{h}_n \cdot A \cdot \vec{h}_n + \lambda_n \gamma_{n-1} \vec{h}_{n-1} \cdot A \cdot \vec{h}_n \\ &= 0 \end{aligned} \tag{E.30}$$

$$\vec{h}_{n+1} \cdot \vec{g}_m = \vec{g}_{n+1} \cdot \vec{g}_m + \gamma_n \vec{h}_n \cdot \vec{g}_m \tag{E.31}$$

Obviously for $m = 0, 1, 2, \ldots, n-1$, $\vec{h}_{n+1} \cdot \vec{g}_m = 0$ holds. For $m = n$, we have

$$\begin{aligned} \vec{h}_{n+1} \cdot \vec{g}_n &= \vec{g}_{n+1} \cdot \vec{g}_n + \gamma_n \vec{h}_n \cdot \vec{g}_n \\ &= \gamma_n \vec{h}_n \cdot (\vec{g}_{n-1} - \lambda_{n-1} A \cdot \vec{h}_{n-1}) \\ &= 0 \end{aligned} \tag{E.32}$$

$$\begin{aligned} \vec{h}_{n+1} \cdot A \cdot \vec{h}_m &= (\vec{g}_{n+1} + \gamma_n \vec{h}_n)(\vec{g}_m - \vec{g}_{m+1})/\lambda_m \\ &= \frac{\vec{g}_{n+1} \cdot \vec{g}_m - \gamma_n \vec{h}_n \cdot \vec{g}_{m+1} + \gamma_n \vec{h}_n \cdot \vec{g}_m - \vec{g}_{n+1} \cdot \vec{g}_{m+1}}{\lambda_m} \end{aligned} \tag{E.33}$$

Obviously for $m = 0, 1, 2, \ldots, n-1$, $\vec{h}_{n+1} \cdot A \cdot \vec{h}_m = 0$ holds. For $m = n$, we have

$$\begin{aligned} \vec{h}_{n+1} \cdot A \cdot \vec{h}_n &= (\vec{g}_{n+1} + \gamma_n \vec{h}_n)(\vec{g}_n - \vec{g}_{n+1})/\lambda_n \\ &= \frac{\gamma_n \vec{h}_n \cdot \vec{g}_n - \vec{g}_{n+1} \cdot \vec{g}_{n+1}}{\lambda_n} \\ &= 0 \end{aligned} \tag{E.34}$$

since

$$\gamma_n = \frac{\vec{g}_{n+1} \cdot \vec{g}_{n+1}}{\gamma_n \vec{h}_n \cdot \vec{g}_n} \tag{E.35}$$

This concludes the induction. The above construction of directions requires computation of the second derivatives. In some cases, the second derivatives are not available, even if they can be calculated, the computation is expansive. We implemented the method without using the second derivatives.

Conjugate gradient without matrix A

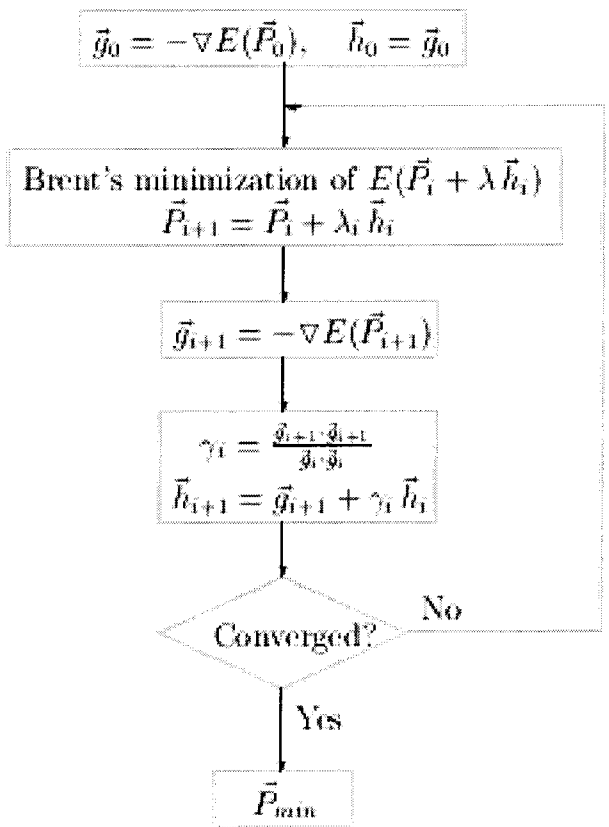

Figure E.5: Conjugate gradient minimization

Figure E.5 shows the flow chart of our structure minimization. Suppose at step i, we have $\vec{g}_i = -\nabla E(\vec{P}_i)$, where point $\vec{P}_i$ is the minimum of f along $\vec{h}_{i-1}$. Find

minimum point $\vec{P}_{i+1}$ along $\vec{h}_i$, so that

$$\vec{P}_{i+1} = \vec{P}_i + \lambda_i \vec{h}_i \tag{E.36}$$

Since

$$\begin{aligned} \nabla E(\vec{P}_i) &= A \cdot \vec{P}_i - \vec{b} && \text{(E.37)} \\ \nabla E(\vec{P}_{i+1}) &= A \cdot \vec{P}_{i+1} - \vec{b} \\ &= A \cdot \vec{P}_i - \vec{b} + \lambda_i A \cdot \vec{h}_i \\ &= -\vec{g}_i + \lambda_i A \cdot \vec{h}_i && \text{(E.38)} \end{aligned}$$

we have

$$\vec{g}_{i+1} = -\nabla E(\vec{P}_{i+1}) \tag{E.39}$$

which is the force at $\vec{P}_{i+1}$.

E.3 References:

1. W.H. Press, S.A. Teukolsky, W.T. Vetterling and B.P. Flannery, *Numerical Recipes in C*, 1992, Cambridge University Press.

Appendix F Molecular Dynamics

F.1 Introduction

In this chapter, we deal with the theories and techniques used in molecular dynamics simulation. The fundamental dynamics equations of any system is the Lagrangian equation of motion

$$\frac{d}{dt}(\frac{\partial L}{\partial \dot{q}_k}) = \frac{\partial L}{\partial q_k} \tag{F.1}$$

where the Lagrangian function $L(q, \dot{q})$ is defined in terms of kinetic and potential energies

$$L = K - V \tag{F.2}$$

F.2 NVE Dynamics

For an isolated system, we have Lagrangian as

$$L = \sum_i \frac{1}{2} m_i \dot{r_i}^2 - V(r_1, r_2, \dots, r_i, \dots) \tag{F.3}$$

and dynamics equations

$$\ddot{r_i} = \frac{F_i}{m_i} \tag{F.4}$$

To solve numerically the equation of motion, we use the velocity Verlet or leap frog algorithm.

$$\dot{V}_n^i = \frac{F_n^i}{m_i} \tag{F.5}$$

For time step δ, we approximate

$$\dot{V}_n^i = \frac{V_{n+\frac{1}{2}}^i - V_{n-\frac{1}{2}}^i}{\delta} \tag{F.6}$$

leading to

$$V_{n+\frac{1}{2}}^i = V_{n-\frac{1}{2}}^i + \delta \frac{F_n^i}{m_i} \tag{F.7}$$

and

$$X_{n+1} = X_n + \delta V_{n+\frac{1}{2}}^i \tag{F.8}$$

The problem with these two equations is that the velocities and coordinates are not from the same time step. Thus the KE and PE are available only for different time steps. To obtain equations involving V_n and X_n at the same time step, we start with Eq. (F.7) and estimate V_n by

$$V_n^i = \frac{1}{2}(V_{n+\frac{1}{2}}^i + V_{n-\frac{1}{2}}^i) \tag{F.9}$$

Then we have

$$V_{n+\frac{1}{2}}^i = V_n^i + \frac{1}{2}\delta \frac{F_n^i}{m_i} \tag{F.10}$$

and

$$V_n^i = V_{n-\frac{1}{2}}^i + \frac{1}{2}\,\delta\,\frac{F_n^i}{m_i} \tag{F.11}$$

F.3 NVT Dynamics

F.3.1 Theory

There are many ways of doing molecular dynamics simulations under constant temperature. Among them, the extended system method originally formulated by Nosé[1] and Hoover[2] is most important. An additional degree of freedom corresponding to a heat bath is introduced. The total energy of the physical system is allowed to fluctuate by a thermal contact with a heat bath. In Nosé's original formulation, two frames of variables, real variables corresponding to realistic motion of particles and virtual variables, are introduced. The relations between these two kinds of variables are derived from an assumption of time scaling $dt' = dt/s$, t' is a real time, t is a virtual time, and the scaling factor s corresponds to a heat bath variable. The canonical distribution is realized in a physical system if we choose the Lagrangian as the following

$$L = \sum_i \frac{1}{2}\,m_i\,s^2\,\dot{r_i}^2 - V(r_1, r_2, \ldots, r_i, \ldots) + \frac{1}{2}\,Q_s\,\dot{s}^2 - g k_B T_B \ln s \tag{F.12}$$

Equation for particles

$$\frac{d}{dt}(m_i\,s^2\,\dot{r}_i) = 2\,m_i\,s\,\dot{s}\,\dot{r}_i + m_i\,s^2\,\ddot{r}_i \tag{F.13}$$

Convert the equation to real time by

$$\dot{A} = \frac{1}{s}\,\frac{dA}{dt} \tag{F.14}$$

$$2m_i\frac{ds}{dt}\frac{dr^i}{dt} + m_i s(\frac{1}{s}\frac{d^2r^i}{dt^2} - \frac{1}{s^2}\frac{ds}{dt}\frac{dr^i}{dt}) = F^i \tag{F.15}$$

Define

$$\zeta^s = \frac{1}{s}\frac{ds}{dt} \tag{F.16}$$

we have

$$\frac{d^2r^i}{dt^2} = \frac{F^i}{m_i} - \zeta^s\frac{dr^i}{dt} \tag{F.17}$$

Equation for s

$$\frac{d}{dt}(Q_s\,\dot{s}) = \sum_i m_i\,s\,\dot{r}_i^2 - gk_BT_B\frac{1}{s} \tag{F.18}$$

Convert to real time we have

$$\frac{1}{s}Q_s\frac{d\zeta^s}{dt} = s\sum_i m_i\,\dot{r}_i^2 - gk_BT_B\frac{1}{s} \tag{F.19}$$

Since

$$\sum_i m_i\,s^2\,\dot{r}_i^2 = 2KE = fk_BT \tag{F.20}$$

where f is the degree of freedom. If we choose g as degree of freedom also, we have

$$\frac{d\zeta^s}{dt} = \frac{gk_BT_B}{Q_s}(\frac{T}{T_B} - 1) \tag{F.21}$$

F.3.2 Numerical Integration

Let's consider a general form of dynamics equation with velocity dependent forces, or friction forces

$$\frac{\partial V}{\partial t} = \frac{F}{M} - f\,V \tag{F.22}$$

where f indicates a frictional term. The numerical equation thus becomes

$$V_{n+\frac{1}{2}} = V_{n-\frac{1}{2}} + \delta\,\frac{F_n}{M} - \delta\,f_n\,V_n \tag{F.23}$$

approximate V_n by

$$2\,V_n = V_{n+\frac{1}{2}} + V_{n-\frac{1}{2}} \tag{F.24}$$

Then we have

$$V_{n+\frac{1}{2}} = \frac{1-\frac{1}{2}\delta f_n}{1+\frac{1}{2}\delta f_n} V_{n-\frac{1}{2}} + \frac{\delta}{1+\frac{1}{2}\delta f_n}\frac{F_n}{M} \tag{F.25}$$

It is often convenient to break the leap frog algorithm into two half steps

$$V_{n-\frac{1}{2}} \longrightarrow V_n$$

which is

$$V_{n+\frac{1}{2}} = (1-\frac{1}{2}\delta f_n)V_n + \frac{1}{2}\delta\frac{F_n}{M} \tag{F.26}$$

and

$$V_n \longrightarrow V_{n+\frac{1}{2}}$$

which is

$$V_n = \frac{1}{1+\frac{1}{2}\delta f_n} V_{n-\frac{1}{2}} + \frac{\frac{1}{2}\delta}{1+\frac{1}{2}\delta f_n}\frac{F_n}{M} \tag{F.27}$$

Replacing f by ζ^s, we have

$$V^i_{n+\frac{1}{2}} = (1-\frac{1}{2}\delta\zeta_n)V^i_n + \frac{1}{2}\delta\frac{F^i_n}{m_i} \tag{F.28}$$

$$V^i_n = \frac{1}{1+\frac{1}{2}\delta\zeta_n} V^i_{n-\frac{1}{2}} + \frac{\frac{1}{2}\delta}{1+\frac{1}{2}\delta\zeta_n}\frac{F^i_n}{m_i} \tag{F.29}$$

and

$$\zeta_n = \zeta_{n-1} + \frac{gk_BT_B}{Q_s}(\frac{T_{n-\frac{1}{2}}}{T_B} - 1) \tag{F.30}$$

F.4 NPT(Gibbs) Dynamics Formulation

F.4.1 Constant Temperature and Constant Stress Ensemble

Constant temperature and constant stress ensemble is one of the most important ensemble being studied, because most of the experiments are done under such condition. Results from molecular dynamics simulation of constant temperature and constant constant stress ensemble can be directly related to experimental results. Andersen[3] has shown how MD calculations can be modified to study systems under constant pressure by introducing the volume of the system as an additional variable. Later on, Parrinello and Rahman[4] extended the variable to simulation cell parameters which results the constant stress ensemble. By combining the Hamiltonian of Nosé-Hoover formulation and that of Parrinello-Rahman, we get a constant temperature and constant stress ensemble. Parrinello-Rahman's original formulation used cell transformation matrix $H = (a, b, c)$ which is not invariant under rotation. This

may introduce artificial effects into the dynamics systems, lead to instable systems. In our implementation, we take the metric tensor $G = H^T H$ as our variable, which may gave us better stability.

F.4.2 Coordinates Transformation

Let $e_x, e_y, e_z = \{e_\alpha\}$ be a set of orthogonal unit vectors and write the primitive vectors for the unit cell as $a, b, c = H$. Then we can write the coordinates of particle i as

$$R_\alpha^i = H_{\alpha\beta}\rho_\beta^i \tag{F.31}$$

where R_α^i is the α coordinate of particle i, ρ_β^i is the scaled α coordinate of particle i. From equation (F.31), we have

$$\dot{R_\alpha^i} = H_{\alpha\beta}\dot{\rho_\beta^i} \tag{F.32}$$

The inner product becomes

$$(R^i \cdot R^j) = R_\gamma^i R_\gamma^j = H_{\gamma\alpha}H_{\gamma\beta}\rho_\alpha^i\rho_\beta^j = G_{\alpha\beta}\rho_\alpha^i\rho_\beta^j \tag{F.33}$$

where the metric tensor

$$G_{\alpha\beta} = H_{\gamma\alpha}H_{\gamma\beta} = H_{\alpha\gamma}^T H_{\gamma\beta} = (H^T H)_{\alpha\beta} \tag{F.34}$$

or

$$G = \begin{pmatrix} H_{11}^2 + H_{21}^2 + H_{31}^2 & H_{21}H_{22} + H_{31}H_{32} & H_{31}H_{33} \\ H_{21}H_{22} + H_{31}H_{32} & H_{22}^2 + H_{32}^2 & H_{32}H_{33} \\ H_{31}H_{33} & H_{32}H_{33} & H_{33}^2 \end{pmatrix} \tag{F.35}$$

while

$$H = \begin{pmatrix} \sqrt{G_{11} - H_{21}^2 - H_{31}^2} & 0 & 0 \\ (G_{21} - H_{31}H_{32})/H_{22} & \sqrt{G_{22} - H_{32}^2} & 0 \\ G_{31}/H_{33} & G_{32}/H_{33} & \sqrt{G_{33}} \end{pmatrix} \tag{F.36}$$

The H matrix is calculated in the order of

$$H_{33} \rightarrow H_{32} \rightarrow H_{31} \rightarrow H_{22} \rightarrow H_{21} \rightarrow H_{11}$$

F.4.3 Strain Tensor

Consider a homogeneous distortion

$$H_0 \longrightarrow H \tag{F.37}$$

in which the unit cell change size but the scaled particle coordinates remain fixed. The new particle coordinates are given by

$$R_\alpha^i = H_{\alpha\beta} H_{0,\beta\gamma}^{-1} R_{0,\gamma}^i \tag{F.38}$$

Thus the displacement of each particle is given by

$$\vec{u} = \vec{R} - \vec{R}_0 = (HH_0^{-1} - 1)R_0 \tag{F.39}$$

Using the Landau-Lifschitz definition of finite strain

$$\epsilon_{\alpha\beta} = \frac{1}{2}\left(\frac{\partial u_\alpha}{\partial x_\beta} + \frac{\partial u_\beta}{\partial x_\alpha} + \frac{\partial u_\gamma}{\partial x_\alpha}\frac{\partial u_\gamma}{\partial x_\beta}\right) \tag{F.40}$$

leads then to

$$\epsilon = \frac{1}{2}(\tilde{H}_0^{-1} G H_0^{-1} - 1) \tag{F.41}$$

where the tilde indicates transpose of a matrix and H_0 refers to the reference state of the cell in terms of which the external stress is defined.

F.4.4 Lagrangian for Particles and Cell

Kinetic Energy

For particle kinetic energy, we have

$$KE_{particle} = \frac{1}{2}s^2 \sum_i M_i \dot{R}^i_\gamma \dot{R}^i_\gamma = \frac{1}{2}s^2 \sum_i M_i \dot{\rho}^i_\alpha G_{\alpha\beta} \dot{\rho}^i_\beta \tag{F.42}$$

For *nosé* parameter s

$$KE_{nosé} = \frac{1}{2}Q\dot{s}^2 \tag{F.43}$$

For cell kinetic energy, we have

$$KE_{cell} = \frac{1}{2}Ws^2 \dot{G}_{\alpha\beta}\dot{G}_{\alpha\beta} \tag{F.44}$$

Potential Energy

Particles potential energy $PE_{particle}$ includes all valence and nonbond interactions. while the *nosé* potential energy is defined as

$$PE_{nosé} = gk_BT_B \log s \tag{F.45}$$

The total potential energy for the stresses system is

$$PE_{cell} = p(\Omega - \Omega_0) + \Omega_0(-S + p)_{\alpha\beta}\epsilon_{\alpha\beta} \tag{F.46}$$

where Ω is the unit cell volume, $p = \frac{1}{3}Trace(S)$ is the pressure and S is the external stress tensor.

Defining the transformed stress tensor as

$$\sigma = \Omega_0 H_0^{-1}(-S+p)\tilde{H}_0^{-1} \tag{F.47}$$

we have

$$PE_{cell} = p(\Omega - \Omega_0) + \frac{1}{2}\sigma_{\alpha\beta}G_{\alpha\beta} \tag{F.48}$$

Lagrangian

The above results leads to a Lagrangian

$$\begin{aligned} L &= \frac{1}{2}s^2\sum_i m_i\dot{\rho}_\alpha^i G_{\alpha\beta}\dot{\rho}_\beta^i - V(\vec{r}_1,\vec{r}_2,\ldots,\vec{r}_i,\ldots) \\ &+\frac{1}{2}Qs^2 - gk_BT_B\log s \\ &+\frac{1}{2}W\dot{G}_{\alpha\beta}\dot{G}_{\alpha\beta}s^2 - p(\Omega-\Omega_0) - \frac{1}{2}\sigma_{\alpha\beta}G_{\alpha\beta} \end{aligned} \tag{F.49}$$

F.4.5 Dynamics Equations

Internal Coordinates

Since

$$\frac{\partial L}{\partial \rho_\alpha^i} = \frac{\partial R_\beta^i}{\partial \rho_\alpha^i}\frac{\partial L}{\partial R_\beta^i} = H_{\alpha\beta}F_\beta^i \tag{F.50}$$

$$\frac{\partial}{\partial t_s}\left(\frac{\partial L}{\partial \dot{\rho}_\alpha^i}\right) = \frac{\partial}{\partial t_s}(m_i s^2 G_{\alpha\beta}\dot{\rho}_\beta^i) = 2m_i s\dot{s}G_{\alpha\beta}\dot{\rho}_\beta^i + m_i s^2 G_{\alpha\beta}\ddot{\rho}_\beta^i + m_i s^2\dot{G}_{\alpha\beta}\dot{\rho}_\beta^i \tag{F.51}$$

By using

$$\frac{\partial}{\partial t_s}\left(\frac{\partial L}{\partial \dot{\rho}_\alpha^i}\right) = \frac{\partial L}{\partial \rho_\alpha^i} \tag{F.52}$$

we have

$$m_i s^2 G_{\alpha\beta} \ddot{\rho}^i_\beta = H_{\alpha\beta} F^i_\beta - 2 m_i s \dot{s} G_{\alpha\beta} \dot{\rho}^i_\beta - m_i s^2 \dot{G}_{\alpha\beta} \dot{\rho}^i_\beta \quad \text{(F.53)}$$

$$m_i s^2 G^{-1}_{\gamma\alpha} G_{\alpha\beta} \ddot{\rho}^i_\beta = G^{-1}_{\gamma\alpha} H_{\alpha\beta} F^i_\beta - 2 m_i s \dot{s} G^{-1}_{\gamma\alpha} G_{\alpha\beta} \dot{\rho}^i_\beta - m_i s^2 G^{-1}_{\gamma\alpha} \dot{G}_{\alpha\beta} \dot{\rho}^i_\beta \quad \text{(F.54)}$$

$$\ddot{\rho}^i_\gamma = \frac{1}{m_i s^2} H^{-1}_{\gamma\beta} F^i_\beta - 2 \frac{\dot{s}}{s} \dot{\rho}^i_\gamma - G^{-1}_{\gamma\alpha} \dot{G}_{\alpha\beta} \dot{\rho}^i_\beta \quad \text{(F.55)}$$

where we have used

$$G^{-1}_{\gamma\alpha} G_{\alpha\beta} = \delta_{\gamma\beta} \quad \text{(F.56)}$$

$$G^{-1}_{\gamma\alpha} H_{\alpha\beta} = H^{-1}_{\gamma\beta} \quad \text{(F.57)}$$

Convert *nosé* time to real time

$$\dot{A} = \frac{\partial A}{\partial t_s} = \frac{1}{s} \frac{\partial A}{\partial t} \quad \text{(F.58)}$$

then

$$\frac{1}{s} \frac{\partial}{\partial t} \left(\frac{1}{s} \frac{\partial \rho^i_\gamma}{\partial t} \right) = \frac{1}{s^2} \frac{\partial^2 \rho^i_\gamma}{\partial^2 t} - \frac{1}{s^3} \frac{\partial s}{\partial t} \frac{\partial \rho^i_\gamma}{\partial t} \quad \text{(F.59)}$$

Define

$$\zeta^s = \frac{1}{s} \frac{\partial s}{\partial t} \quad \text{(F.60)}$$

$$\zeta^P_{\gamma\beta} = G^{-1}_{\gamma\alpha} \frac{\partial G_{\alpha\beta}}{\partial t} \quad \text{(F.61)}$$

Finally we have

$$\frac{\partial^2 \rho^i_\gamma}{\partial^2 t} = H^{-1}_{\gamma\alpha} \frac{F^i_\alpha}{m_i} - \zeta^s \frac{\partial \rho^i_\gamma}{\partial t} - \zeta^P_{\gamma\beta} \frac{\partial \rho^i_\beta}{\partial t} \quad \text{(F.62)}$$

Nosé **Parameter**

$$\frac{\partial L}{\partial s} = \sum_i m_i s \rho_\alpha^i G_{\alpha\beta} \rho_\beta^i - g k_B T_B \frac{1}{s} + W\, s\, \dot{G}_{\alpha\beta} \dot{G}_{\alpha\beta} \tag{F.63}$$

$$\frac{\partial L}{\partial \dot{s}} = Q\, \dot{s} \tag{F.64}$$

$$\ddot{s} = \frac{1}{s} \frac{\partial}{\partial t} (\frac{1}{s} \frac{\partial t}{\partial t}) = \frac{1}{s} \frac{\partial \zeta^s}{\partial t} \tag{F.65}$$

Put them together, and we have

$$\begin{aligned} Q \frac{\partial \zeta^s}{\partial t} &= \sum_i m_i\, s^2\, \rho_\alpha^i G_{\alpha\beta} \rho_\beta^i - g k_B T_B + W\, s^2\, \dot{G}_{\alpha\beta} \dot{G}_{\alpha\beta} \\ &= 2(KE_{particles} + KE_{cell}) - g k_B T_B \\ &= g k_B (T - T_B) \end{aligned} \tag{F.66}$$

where we have used $KE_{particles} + KE_{cell} = g k_B T$ with T as the system temperature. Defining

$$Q = g k_B T_B \tau_s^2 \tag{F.67}$$

we have

$$\frac{\partial \zeta^s}{\partial t} = \frac{1}{\tau_s^2} (\frac{T}{T_B} - 1) \tag{F.68}$$

Metric $G_{\alpha\beta}$

Since

$$-\frac{\partial V}{\partial \epsilon_{\kappa\lambda}} = \Omega\, P^{pe}_{\kappa\lambda} \tag{F.69}$$

$$\frac{\partial V}{\partial G_{\alpha\beta}} = \frac{\partial V}{\partial \epsilon_{\kappa\lambda}} \frac{\partial \epsilon_{\kappa\lambda}}{\partial G_{\alpha\beta}} \tag{F.70}$$

$$\begin{aligned} \frac{\partial \epsilon_{\kappa\lambda}}{\partial G_{\alpha\beta}} &= \frac{1}{2}\tilde{H}^{-1}_{0\kappa\mu}\frac{\partial G_{\mu\nu}}{\partial G_{\alpha\beta}}H^{-1}_{0\nu\lambda} \\ &= \frac{1}{2}\tilde{H}^{-1}_{0\kappa\mu}[\frac{1}{2}(\delta_{\mu\alpha}\delta_{\nu\beta}+\delta_{\mu\beta}\delta_{\nu\alpha})]H^{-1}_{0\nu\lambda} \\ &= \frac{1}{4}(\tilde{H}^{-1}_{0\kappa\alpha}H^{-1}_{0\beta\lambda}+\tilde{H}^{-1}_{0\kappa\beta}H^{-1}_{0\alpha\lambda}) \end{aligned} \tag{F.71}$$

So

$$\begin{aligned} \frac{\partial V}{\partial G_{\alpha\beta}} &= -\frac{1}{4}\Omega(\tilde{H}^{-1}_{0\kappa\alpha}H^{-1}_{0\beta\lambda}+\tilde{H}^{-1}_{0\kappa\beta}H^{-1}_{0\alpha\lambda})P^{pe}_{\kappa\lambda} \\ &= -\frac{1}{2}\,\Omega_0\, H^{-1}_{0\alpha\kappa}P^{pe}_{\kappa\lambda}\tilde{H}^{-1}_{0\lambda\beta} \end{aligned} \tag{F.72}$$

where we have used the symmetry property of $P^{pe}_{\kappa\lambda}$. Similarly

$$\frac{\partial KE_{particle}}{\partial G_{\alpha\beta}} = \frac{1}{2}\,\Omega_0\, H^{-1}_{0\alpha\kappa}P^{ke}_{\kappa\lambda}\tilde{H}^{-1}_{0\lambda\beta} \tag{F.73}$$

Since

$$\det H = \epsilon_{\alpha\beta\gamma}\epsilon_{ijk}H_{i\alpha}H_{j\beta}H_{k\gamma} \tag{F.74}$$

$$\frac{\partial \det H}{\partial H_{i\alpha}} = \epsilon_{\alpha\beta\gamma}\epsilon_{ijk}H_{j\beta}H_{k\gamma} \tag{F.75}$$

$$H_{i\lambda}\frac{\partial \det H}{\partial H_{i\alpha}} = \epsilon_{\alpha\beta\gamma}\epsilon_{ijk}H_{i\lambda}H_{j\beta}H_{k\gamma} = \delta_{\lambda\alpha}\det H \tag{F.76}$$

$$\frac{\partial \det H}{\partial H_{\alpha\beta}} = \tilde{H}^{-1}_{\alpha\beta} \det H \tag{F.77}$$

$$\Omega = \vec{a} \cdot (\vec{b} \times \vec{c}) = \epsilon_{ijk} H_{i1} H_{j2} H_{k3} = \det H \tag{F.78}$$

$$\det G = \det \tilde{H} \det H = (\det H)^2 = \Omega^2 \tag{F.79}$$

$$\frac{\partial \Omega}{\partial G_{\alpha\beta}} = \frac{1}{2} \Omega \tilde{G}^{-1}_{\alpha\beta} = \frac{1}{2} \Omega G^{-1}_{\alpha\beta} \tag{F.80}$$

By using the above equations, we have

$$\begin{aligned} \frac{\partial L}{\partial G_{\alpha\beta}} &= \frac{1}{2} \Omega_0 H^{-1}_{0\alpha\kappa} (P^{pe}_{\kappa\lambda} + P^{ke}_{\kappa\lambda}) \tilde{H}^1_{0\lambda\beta} - \frac{1}{2} P_{ext} \Omega G^{-1}_{\alpha\beta} - \frac{1}{2} \sigma_{\alpha\beta} \\ &= \frac{1}{2} \Omega_0 H^{-1}_{0\alpha\kappa} (P^{internal}_{\kappa\lambda} - S^{external}_{\kappa\lambda}) \tilde{H}^1_{0\lambda\beta} - \frac{1}{2} P_{ext} \Omega G^{-1}_{\alpha\beta} \end{aligned} \tag{F.81}$$

$$\frac{\partial L}{\partial \dot{G}_{\alpha\beta}} = W s^2 \dot{G}_{\alpha\beta} \tag{F.82}$$

$$\ddot{G}_{\alpha\beta} = \frac{1}{2W} \left[\Omega_0 H^{-1}_{0\alpha\kappa} (P^{internal}_{\kappa\lambda} - S^{external}_{\kappa\lambda}) \tilde{H}^1_{0\lambda\beta} - P_{ext} \Omega G^{-1}_{\alpha\beta} \right] - 2 s \dot{s} \dot{G}_{\alpha\beta} \tag{F.83}$$

In Hoover formulation (real time)

$$\frac{\partial^2 G_{\alpha\beta}}{\partial^2 t} = \frac{1}{2W} \left[\Omega_0 H^{-1}_{0\alpha\kappa} (P^{internal}_{\kappa\lambda} - S^{external}_{\kappa\lambda}) \tilde{H}^1_{0\lambda\beta} - P_{ext} \Omega G^{-1}_{\alpha\beta} \right] - \zeta^s \dot{G}_{\alpha\beta} \tag{F.84}$$

F.4.6 About Cell Mass

From the above derivation, $W\dot{G}^2$ has unit of $\frac{WL^4}{T^2}$ while the kinetic energy usually has unit of $\frac{ML^2}{T^2}$. We propose

$$W = f\, M_{cell}\Omega^{-\frac{2}{3}} \tag{F.85}$$

with f a scale factor and

$$M_{cell} = \sum_{i}^{n} m_i \tag{F.86}$$

F.4.7 Numeric Integration

Two Step Leap-frog for TPN

Following are the equations used in our integration

$$\frac{\partial^2 \rho_\gamma^i}{\partial^2 t} = H_{\gamma\alpha}^{-1}\frac{F_\alpha^i}{m_i} - \zeta^s\frac{\partial \rho_\gamma^i}{\partial t} - \zeta_{\gamma\beta}^P\frac{\partial \rho_\beta^i}{\partial t} \tag{F.87}$$

$$\frac{\partial^2 G_{\alpha\beta}}{\partial^2 t} = \frac{1}{2W}\Big[\Omega_0\, H_{0\alpha\kappa}^{-1}(P_{\kappa\lambda}^{internal} - S_{\kappa\lambda}^{external})\tilde{H}_{0\lambda\beta}^{-1} - P_{ext}\,\Omega\, G_{\alpha\beta}^{-1}\Big] - \zeta^s\,\dot{G}_{\alpha\beta} \tag{F.88}$$

and

$$\frac{\partial \zeta^s}{\partial t} = \frac{1}{\tau_s^2}(\frac{T}{T_B} - 1) \tag{F.89}$$

The $n-1 \longrightarrow n-\frac{1}{2}$ equation for internal velocites of particles

$$V_{n-\frac{1}{2}} = [1 - \frac{1}{2}\delta(\zeta^P + \zeta^s)]V_{n-1} + \frac{1}{2}\delta\frac{F_{n-1}^{atm}}{M} \tag{F.90}$$

The $n-1 \longrightarrow n-\frac{1}{2}$ equation for velocity of metric parameters

$$\dot{G}_{n-\frac{1}{2}} = (1 - \frac{1}{2}\delta\zeta^s)\dot{G}_{n-1} + \frac{1}{2}\delta\frac{F^{cell}_{n-1}}{W} \tag{F.91}$$

Nosé parameter

$$\zeta^s_n = \zeta^s_{n-1} + \frac{1}{\tau^2_s}\delta\,(\frac{T_{n-\frac{1}{2}}}{T_B} - 1) \tag{F.92}$$

Internal coordinates of particles

$$X_n = X_{n-1} + \delta\, V_{n-\frac{1}{2}} \tag{F.93}$$

Metric parameters

$$G_n = G_{n-1} + \delta\, \dot{G}_{n-\frac{1}{2}} \tag{F.94}$$

The $n-\frac{1}{2} \longrightarrow n$ equation for internal velocity of particles

$$V_n = \frac{1}{1+\frac{1}{2}\delta(\zeta^P_n + \zeta^s_n)}\, V_{n-\frac{1}{2}} + \frac{\frac{1}{2}\delta}{1+\frac{1}{2}\delta(\zeta^P_n + \zeta^s_n)}\,\frac{F^{atm}_n}{M} \tag{F.95}$$

The $n-\frac{1}{2} \longrightarrow n$ equation for velocity of metric parameters

$$\dot{G}_n = \frac{1}{1+\frac{1}{2}\delta\zeta^s_n}\,\dot{G}_{n-\frac{1}{2}} + \frac{\frac{1}{2}\delta}{1+\frac{1}{2}\delta\zeta^s_n}\,\frac{F^{cell}_n}{W} \tag{F.96}$$

since ζ^P_n and F^{cell}_n depends on V_n and $\dot{G}_n$, we have to solve these two equations self-consistently. Following is the flowchart of an integration circle.

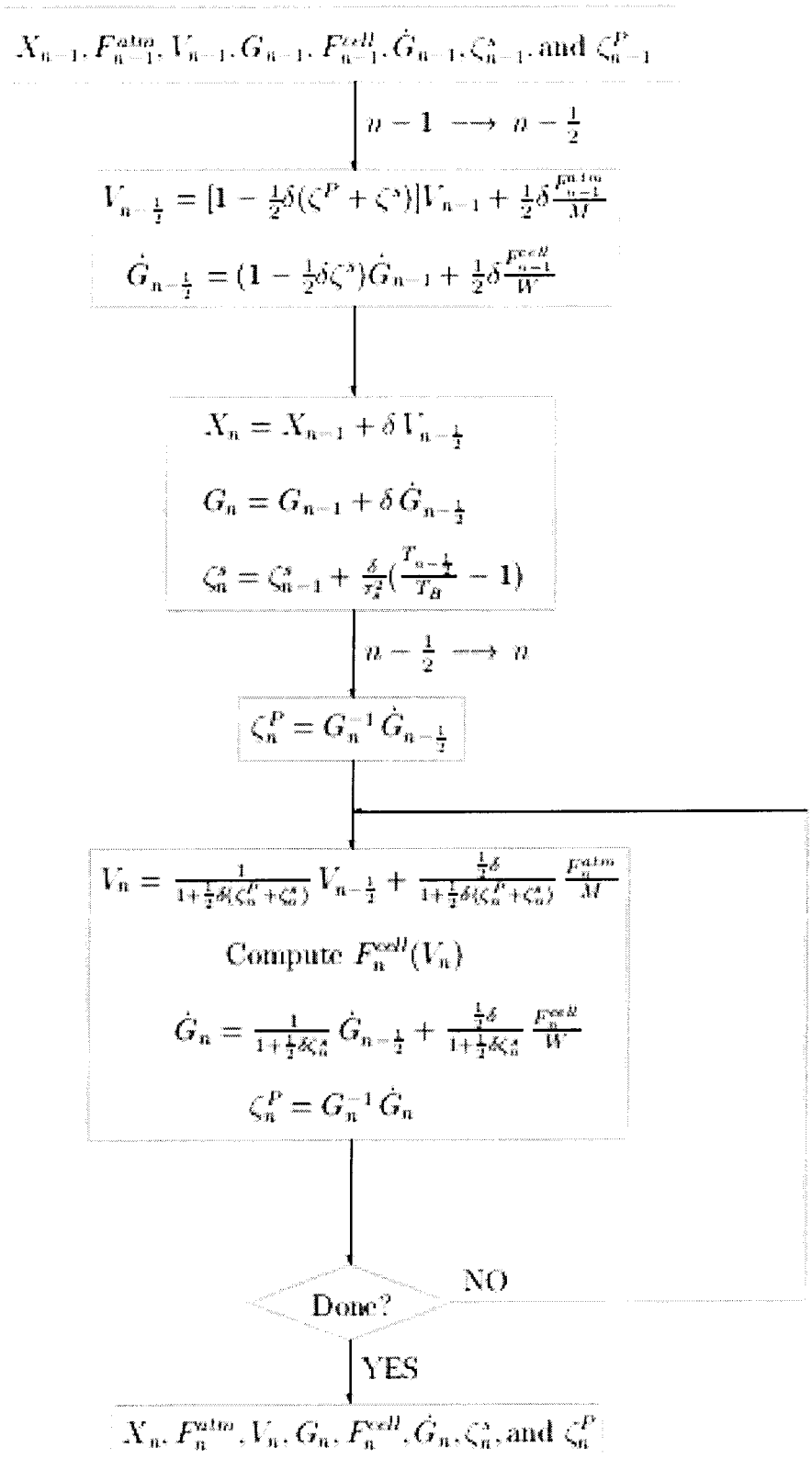

Figure F.1: NPT dynamics flowchart

F.5 Rigid Dynamics

In general, atomistic molecular dynamics of various ensemble can handle most of the molecular systems; however treating some of the molecules as rigid can decrease the degree of freedoms and increase dynamics time-step, and thus, can simulate larger systems longer.

F.5.1 Partition of dynamics equations

Consider the motions of a rigid molecule M interacting with other atoms or molecules. For a nonlinear molecule there are 6 degrees of freedom (3 translation, 3 rotation). The forces on the atoms of M are calculated and combined to obtain the net forces and torques on the body

$$F_\alpha^M = -\sum_{i \in M} \frac{\partial V}{\partial r_\alpha^i} \tag{F.97}$$

$$T_\alpha^M = -\sum_{i \in M} \epsilon_{\alpha\beta\gamma}(r_\beta^i - R_\beta^{cm}) \frac{\partial V}{\partial r_\gamma^i} \tag{F.98}$$

These calculations are carried out in normal space-fixed coordinates. We introduce a coordinate system attached to the center of mass with the same orientation as the space-fixed system at the initial time. The particle position

$$r_\alpha^i(t) = R_\alpha^{cm}(t) + A_{\alpha\beta}(t)\,[r_\beta^i(0) - R_\beta^{cm}(0)] \tag{F.99}$$

where $A_{\alpha\beta}(t)$ is the rotation matrix. The particle velocities are then given by

$$v_\alpha^i(t) = V_\alpha^{cm}(t) + \epsilon_{\alpha\beta\gamma}\,\omega_\beta(t)[r_\gamma^i(t) - R_\gamma^{cm}(t)] \tag{F.100}$$

where ω is the angular velocity

Define

$$r^i_{cm}(t) = r^i(t) - R^{cm}(t) \tag{F.101}$$

Using equation (F.100) in KE, we have

$$\begin{aligned} KE &= \frac{1}{2}\sum_{i\in M} m_i v^i v^i \\ &= \frac{1}{2}MV^{cm}V^{cm} + \frac{1}{2}\sum_{i\in M} m_i\Big[\omega(t)\times r^i_{cm}(t)\Big]^2 \\ &= KE_{cm} + KE_{rot} \end{aligned} \tag{F.102}$$

So we can partition equation of motion into center of mass translation and rotation with respect to center of mass coordinates. It's the angular motion which needs further study.

F.5.2 Dynamics Equation for Angular Motion

We can write the rotational kinetic energy as

$$KE_{rot} = \frac{1}{2}\sum_{i\in M} m_i \epsilon_{\alpha\beta\gamma}\epsilon_{\alpha\mu\nu}\omega_\beta r^i_{cm,\gamma}\omega_\mu r^i_{cm,\nu} \tag{F.103}$$

By using

$$\epsilon_{\alpha\beta\gamma}\epsilon_{\alpha\mu\nu} = \delta_{\beta\mu}\delta_{\gamma\nu} - \delta_{\beta\nu}\delta_{\gamma\mu} \tag{F.104}$$

we have

$$\begin{aligned} KE_{rot} &= \frac{1}{2}\sum_{i\in M} m_i[\omega_\beta\omega_\mu\delta_{\beta\mu}r^i_{cm,\gamma}r^i_{cm,\gamma} - \omega_\beta\omega_\mu r^i_{cm,\beta}r^i_{cm,\mu}] \\ &= \frac{1}{2}\sum_{i\in M} m_i\omega_\beta(\delta_{\beta\mu}r^{i^2}_{cm} - r^i_{cm,\beta}r^i_{cm,\mu})\omega_\mu \\ &= \frac{1}{2}I_{\beta\mu}\omega_\beta\omega_\mu \end{aligned} \tag{F.105}$$

where

$$I_{\beta\mu} = \sum_{i \in M} m_i (\delta_{\beta\mu} r^{i^2}_{cm} - r^i_{cm,\beta} r^i_{cm,\mu}) \tag{F.106}$$

is defined as the moment of inertia tensor.

The angular momentum

$$J_\alpha = \frac{\partial KE_{rot}}{\partial \omega_\alpha} = I_{\alpha\beta}\omega_\beta \tag{F.107}$$

We can rewrite KE_{rot} as

$$KE_{rot} = \frac{1}{2} I^{-1}_{\alpha\beta} J_\alpha J_\beta \tag{F.108}$$

Then for micro-canonical ensemble

$$L = L_{NVE} + \frac{1}{2}\sum_M M_{cm} V^i_{cm} V^i_{cm} + \frac{1}{2}\sum_M I^M_{\alpha\beta}\omega^M_\alpha \omega^M_\beta \tag{F.109}$$

and for canonical ensemble we have Lagrangian as

$$L = L_{NVT} + \frac{1}{2}\sum_M M_{cm} s^2 V^i_{cm} V^i_{cm} + \frac{1}{2}\sum_M s^2 I^M_{\alpha\beta}\omega^M_\alpha \omega^M_\beta \tag{F.110}$$

and for Gibbs ensemble we have Lagrangian as

$$L = L_{NPT} + \frac{1}{2}\sum_M M_{cm} s^2 V^i_{cm} V^i_{cm} + \frac{1}{2}\sum_M s^2 I^M_{\alpha\beta}\omega^M_\alpha \omega^M_\beta \tag{F.111}$$

noted, there are no coupling between cell deformation and rotation of rigid molecules. For rotational degree of freedom, the dynamics equation takes the form of

$$\dot{J}_\alpha = T_\alpha - f\, J_\alpha \tag{F.112}$$

where $T_\alpha = -\frac{\partial V}{\partial \theta_\alpha}$, $f = \zeta^s$ for canonical and Gibbs ensembles, $f = 0$ for micro-

canonical ensemble.

The two-step numerical integration equations are:

$$J_{n-\frac{1}{2}} = (1 - \frac{1}{2}\,\delta\, f_{n-1})J_{n-1} + \frac{1}{2}\,T_{n-1} \tag{F.113}$$

and

$$J_n = \frac{1}{1 + \frac{1}{2}\,\delta\, f_{n-1}}\,J_{n-\frac{1}{2}} + \frac{\frac{1}{2}\,\delta}{1 + \frac{1}{2}\,\delta\, f_{n-1}}\,T_n \tag{F.114}$$

The above equation is in space-fixed coordinates. In order to solve for the new angular coordinates, we must transform from space-fixed (J) to body-fixed (J^B) coordinates by applying

$$J^B_\alpha = A_{\alpha\beta}(t)J_\beta \tag{F.115}$$

where $A_{\alpha\beta}(t)$ takes the current space-fixed coordinates transform back to the body-fixed coordinates at $t = 0$. Since

$$J_{\alpha\beta} = I_{\alpha\beta}\omega_\beta \tag{F.116}$$

where $I_{\alpha\beta}$ is evaluated in the original body-fixed coordinate system at $t = 0$. Thus

$$\omega^B(t) = I^{-1}J^B(t) = I^{-1}A(t)J \tag{F.117}$$

F.5.3 Solving the Equation Using Quaternions

Since the potential energy and forces (thus torques) are evaluated in space-fixed coordinate systems, while the moment of internia is most easily expressed in a body-fixed coordinate system, we have to relating the coordinates of a moving-body to a space fixed coordinate system. The most common approach is in terms of Euler angles:θ, ϕ, ψ, where θ and ϕ give the orientation of a body axis relative to the space-

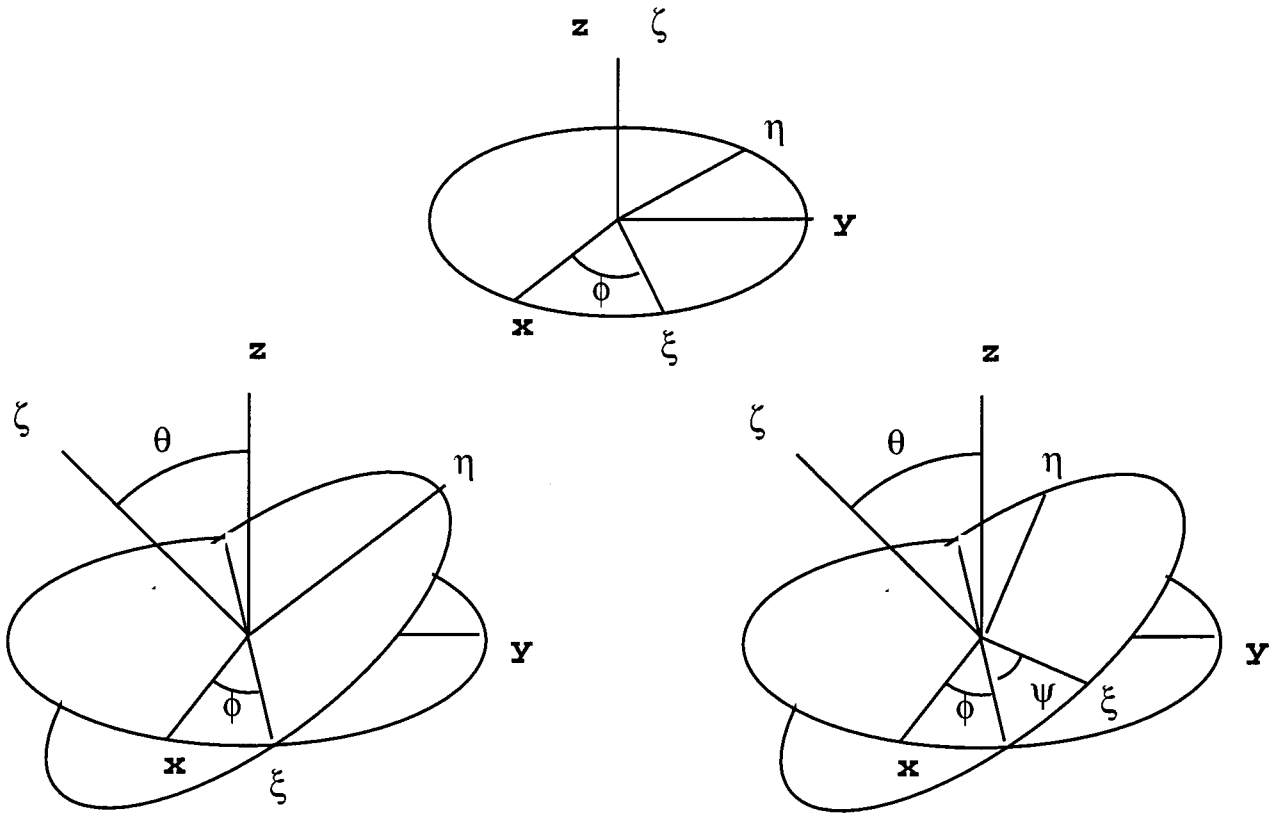

Figure F.2: The rotations defining the Euler angles

fixed frame and ψ is the rotation of the body about this axis. The transformation tensor is

$$A = \begin{pmatrix} \cos\psi\cos\phi - \cos\theta\sin\phi\sin\psi & \cos\psi\sin\phi + \cos\theta\cos\phi\sin\psi & \sin\psi\sin\theta \\ -\sin\psi\cos\phi - \cos\theta\sin\phi\cos\psi & -\sin\psi\sin\phi + \cos\theta\cos\phi\cos\psi & \cos\psi\sin\theta \\ \sin\theta\sin\phi & -\sin\theta\cos\phi & \cos\theta \end{pmatrix} \tag{F.118}$$

However, Euler angles lead to singularities whenever the equation of motion takes θ too close to 0^o or 180^o. The using of four variable quaternions rather than the three variable Euler angles can by-pass the singularity problems.

The quaternions are defined in terms of Euler angles as

$$Q_x = \sin\frac{\theta}{2}\cos\frac{\phi-\psi}{2} \tag{F.119}$$

$$Q_y = \sin\frac{\theta}{2}\sin\frac{\phi-\psi}{2} \tag{F.120}$$

$$Q_z = \cos\frac{\theta}{2}\sin\frac{\phi+\psi}{2} \tag{F.121}$$

$$Q_4 = \cos\frac{\theta}{2}\cos\frac{\phi+\psi}{2} \tag{F.122}$$

where the normalization condition is

$$\sum_{\alpha=1}^{4} Q_\alpha^2 = 1 \tag{F.123}$$

The relation between A and Q is

$$A_{ii} = Q_4^2 + Q_i^2 - \sum_{j\neq i} Q_j^2 \tag{F.124}$$

$$A_{ij} = 2Q_iQ_j + \epsilon_{ijk}Q_4Q_k \quad \text{if } i \neq j \tag{F.125}$$

where $i = 1, 2, 3$. In matrix form

$$A = \begin{pmatrix} Q_x^2 - Q_y^2 - Q_z^2 + Q_4^2 & 2Q_xQ_y + 2Q_4Q_z & 2Q_xQ_z - 2Q_4Q_y \\ 2Q_xQ_y - 2Q_4Q_z & -Q_x^2 + Q_y^2 - Q_z^2 + Q_4^2 & 2Q_yQ_z + 2Q_4Q_x \\ 2Q_xQ_z + 2Q_4Q_y & 2Q_yQ_z - 2Q_4Q_x & -Q_x^2 - Q_y^2 + Q_z^2 + Q_4^2 \end{pmatrix} \tag{F.126}$$

the quaternions change smoothly in time with no singualr points. The relation between $\dot{Q}$ and ω is

$$\dot{Q}_i = \frac{1}{2}(Q_4\omega_i + \epsilon_{ijk}Q_j\omega_k) \quad , i = 1,2,3 \tag{F.127}$$

$$\dot{Q}_4 = -\frac{1}{2}Q_i\omega_i \tag{F.128}$$

If we define $\omega_4 = 0$, in matrix form

$$\dot{Q}_\alpha = S_{\alpha\beta}\omega_\beta \tag{F.129}$$

we have

$$S = \begin{pmatrix} Q_4 & -Q_z & Q_y & Q_x \\ Q_z & Q_4 & -Q_x & Q_y \\ -Q_y & Q_x & Q_4 & Q_z \\ -Q_x & -Q_y & -Q_z & Q_4 \end{pmatrix} \tag{F.130}$$

Note that $\tilde{S}\,S = 1$

Let's partition the equation

$$Q_n = Q_{n-1} + \delta\,\dot{Q}_{n-\frac{1}{2}} \tag{F.131}$$

into

$$Q_{n-\frac{1}{2}} = Q_{n-1} + \frac{1}{2}\,\delta\,\dot{Q}_{n-\frac{1}{2}} \tag{F.132}$$

$$Q_n = Q_{n-\frac{1}{2}} + \frac{1}{2}\,\delta\,\dot{Q}_{n-\frac{1}{2}} \tag{F.133}$$

Then following is the flowchart of one dynamics step

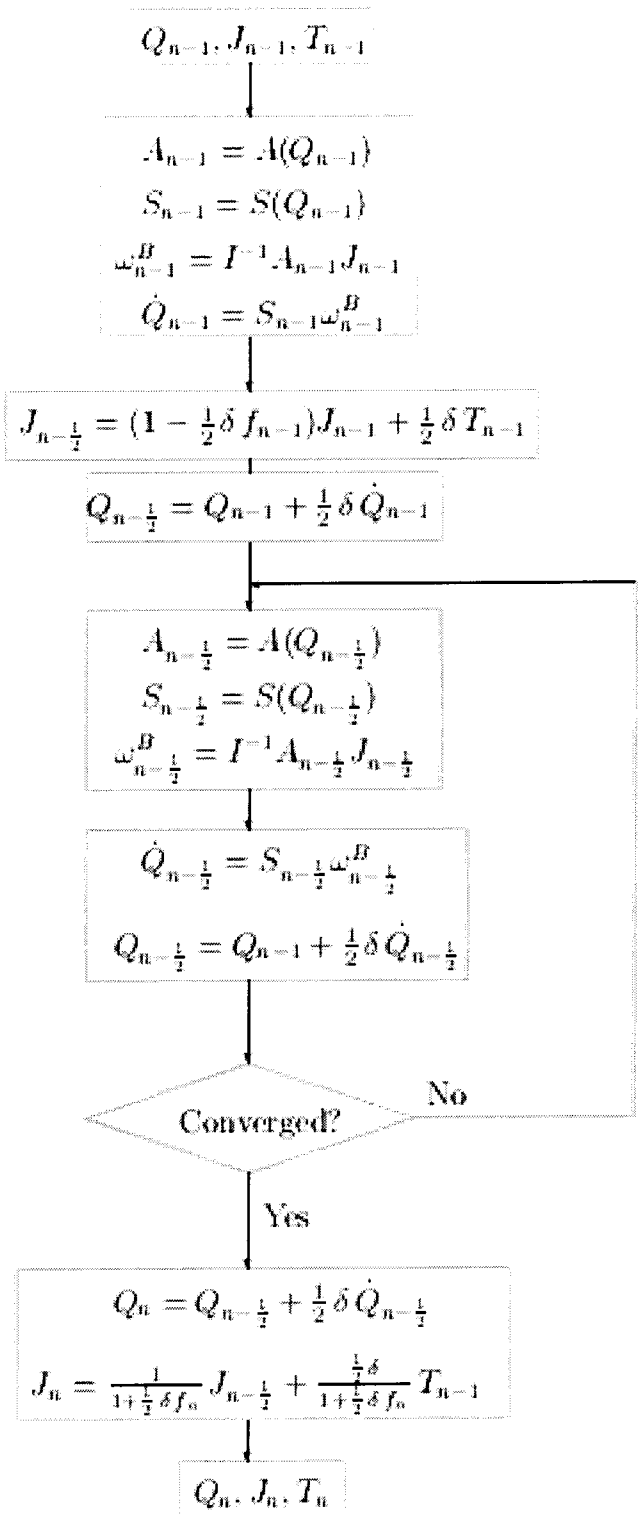

Figure F.3: Rigid dynamics flowchart

F.5.4 Linear Molecule

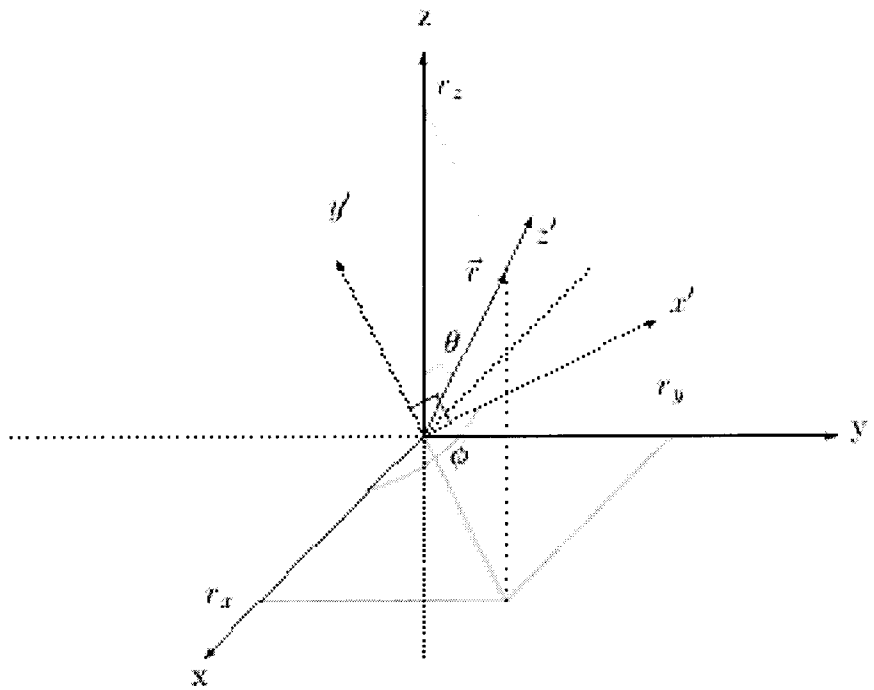

Figure F.4: Orientation of linear molecule

Let's assume the bond axis of a linear molecule as $\vec{r}$ as in the above figure; we can diagnolize the inertia tensor by transformation coordinate system (x, y, z) into (x', y', z')

$$I' = A\, I\, A^T = \begin{pmatrix} a & & \\ & a & \\ & & 0 \end{pmatrix} \tag{F.134}$$

Since the inverse is singular, we have to pay special attention to linear molecule. We require angular momentum J be orthogonal to the bond axis. Denoting the unit vector along the molecule as e_a, we must have

$$J \cdot e_a = 0 \tag{F.135}$$

Then rewrite I as proportional to the unit matrix

$$I = \begin{pmatrix} a & & \\ & a & \\ & & a \end{pmatrix} = a1 \tag{F.136}$$

The kinetic energy becomes

$$KE_{rot} = \frac{1}{2}\frac{J \cdot J}{I} \tag{F.137}$$

To ensure angular momentum J be orthogonal to linear molecule bond axis, we Schmit orthogonalize each iteration by applying

$$J^{new} = J^{old} - (e_a \cdot J^{old})e_a \tag{F.138}$$

The inverse of inertia tensor I^{-1} can be calculated as

$$I^{-1} = A \begin{pmatrix} \frac{2}{TraceI} & & \\ & \frac{2}{TraceI} & \\ & & \frac{2}{TraceI} \end{pmatrix} \tilde{A} \tag{F.139}$$

where transformation matrix A can be calculated with Euler angle (ϕ, θ, ζ) as

$$\begin{aligned} \theta &= \arccos\frac{r_z}{r} \\ \phi &= \pi - \arccos\frac{r_y}{\sqrt{r_x^2 + r_y^2}} \\ \zeta &= 0 \end{aligned} \tag{F.140}$$

The quantities specified are defined in Fig. F.4

F.6 References

1. S. Nosé, *J. Chem. Phys.* **81**, 1984, 511.

2. W.H. Hoover, *Phys. Rev. A* **31**, 1985, 1695.

3. H.C. Andersen, *J. Chem. Phys.* **72**, 1980, 2384.

4. M. Parrinello and A. Rahman, *Phys. Rev. Lett.* **45(14)**, 1980, 1196-1199.